Katharina Lilith Quade

Aging Diagnostics for a Commercial Sodium-Ion Cell: Experimental and Simulation-Based Transfer from Lithium-Ion Systems

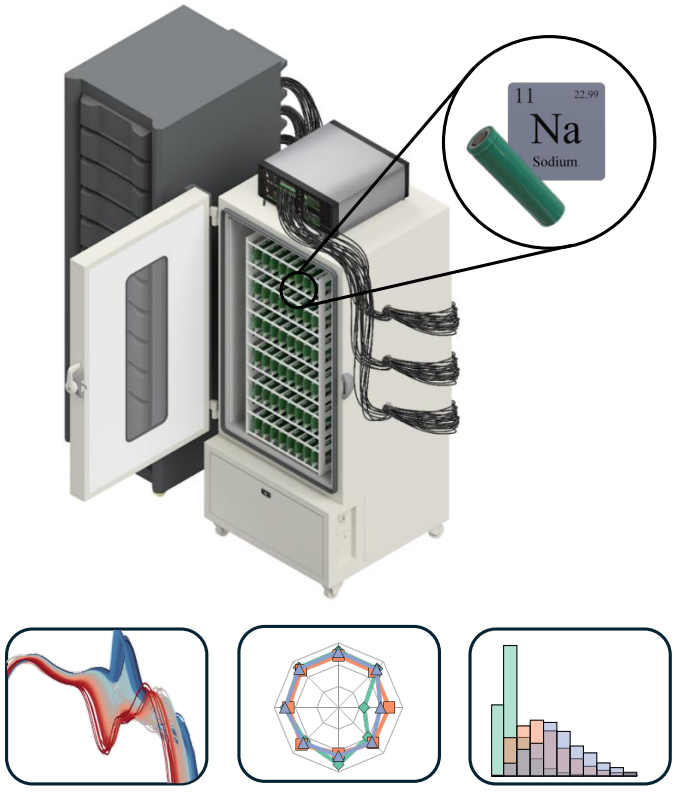

Aachener Beiträge des ISEA Band 202

Aging Diagnostics for a Commercial Sodium-Ion Cell: Experimental and Simulation-Based Transfer from Lithium-Ion Systems

Von der Fakultät für Elektrotechnik und Informationstechnik der Rheinisch-Westfälischen Technischen Hochschule Aachen zur Erlangung des akademischen Grades eines Doktors der Ingenieurwissenschaften genehmigte Dissertation

vorgelegt von
Katharina Lilith Quade, M.Sc.
aus München

Berichter:
Univ.-Professor Dr. rer. nat. Dirk Uwe Sauer
Professor Scott Moura, Ph. D., University of California, Berkeley, USA

Tag der mündlichen Prüfung: 19.12.2025

AACHENER BEITRÄGE DES ISEA
Vol. 202

Editor:
Univ.-Prof. Dr. ir. Dr. h. c. Rik W. De Doncker
Director of the Institute for Power Electronics and Electrical Drives (ISEA)
RWTH Aachen University

ISSN 1437-675X

Institute for Power Electronics and Electrical Drives (ISEA)
RWTH Aachen University
Campus-Boulevard 89 • 52074 Aachen • Germany
Tel: +49 (0)241 80-96920
post@isea.rwth-aachen.de

Preface

I have always been interested in batteries and research, which is why I decided early on to write both my Bachelor's and Master's thesis at the Institute for Power Electronics and Electrical Drives at RWTH Aachen University. I am deeply grateful to Prof. Dirk Uwe Sauer for giving me the opportunity to continue with a PhD at his chair. Thank you very much for the freedom I had during this time, for the trust you placed in me as a chief engineer, and for your continuous support and encouragement. During my PhD, the Center for Ageing, Reliability, and Lifetime Prediction of Electrochemical and Power Electronic Systems (CARL) provided excellent research opportunities. Thanks to its infrastructure I was able to carry out a large part of my work here. CARL also created an environment that made collaboration with PhD students from other fields very accessible, which allowed me to broaden my perspective and benefit greatly from interdisciplinary exchange. Life at the institute was never boring. For this, I would like to sincerely thank all my colleagues, as well as my Bachelor's and Master's students and student assistants. Without their help and dedication, this dissertation would not have been possible. Furthermore, I am very thankful for the warm welcome I received as a visiting student at the University of California, Berkeley, from Prof. Scott Moura and his group. My time in the US gave me the chance to fully focus on my research and, ultimately, further strengthened my passion for science and research. Finally, I want to thank my family, boyfriend and friends for their unconditional support. A special thanks goes to my parents, who sparked my enthusiasm for technology at a young age and always encouraged me to keep going.

Abstract

Sodium-ion batteries are gaining attention as a cost-effective and sustainable complementary technology to their lithium counterpart. However, fully realizing their drop-in potential and integrating them into applications requires a deeper understanding of their aging behavior, as well as the implications for the overall system, particularly for management strategies. A high-power, cost-sensitive application is selected, where lithium-ion cells could potentially be replaced by a cheaper complementary technology with similar power characteristics and energy density. An extensive field dataset from this application is then analyzed to determine the operational requirements that such a technology must meet in terms of lifetime and management. Following this analysis, a unique aging study on 81 commercial 18650 sodium-ion cells with layered-oxide cathode and hard-carbon anode is conducted giving insights into their degradation behavior. The results show that while there are distinct aging patterns in the sodium-ion cells, particularly capacity loss predominantly occurring at low State of Charge, the lifetime of the sodium-ion cells is high with an average capacity loss of 2.8 % after approximately 4000 equivalent full cycles across different operating conditions. The parameterized models, derived from experimental data, and application-specific requirements are implemented in a simulation framework to evaluate real-time algorithms commonly used for lithium-ion batteries. The results show low algorithm errors, indicating high transferability of existing management strategies to the investigated sodium-ion cells in the target application. Furthermore, we analyze that the favorable voltage range and steep open-circuit voltage curve of the investigated sodium-ion cells allow the use of simpler models and lower-cost sensors without significantly affecting algorithm performance. By quantifying degradation and algorithm performance, this work guides the integration of sodium-ion batteries into applications, shortening the time to market for these technologies as viable alternatives to lithium-ion batteries when economic or political factors make it necessary.

Contents

1 Introduction

The escalating threat of global warming, already evident in increasingly frequent and severe natural disasters [1], highlights the urgent need for rapid and widespread decarbonization. At the same time, global modernization and digitalization are driving a growing demand for energy. Balancing these two developments requires a major expansion of renewable energy and storage solutions. Batteries play a crucial role in this transition, enabling emission reductions across different applications from powering electric vehicles to supporting grid stability through stationary storage systems [2, 3]. Over the past decades, lithium-ion batteries (LIBs) have dominated the market due to their favorable trade-off between energy and power density, which has been instrumental in advancing electrification across various sectors [4–6]. Additionally, economies of scale and progress in battery science have driven down LIB costs by more than 97 % since their first commercial use in 1991 [7–9]. However, for the first time, lithium-ion cell costs increased in 2022, largely due to rising raw material prices [4, 10], although these spikes have so far been intermittent. The scarcity of important materials and concerns about future price volatility as well as geopolitical and economic dependencies in terms of energy security related to lithium supply have led industry and academia to intensify the search for cost-effective and sustainable alternatives to conventional LIBs [6, 7].

In recent years, sodium-ion batteries (SIBs) have emerged as a promising commercial alternative. With similar electrochemical characteristics to lithium-based systems, they offer potential as a drop-in replacement for certain applications [11, 12]. Sodium is approximately 1,000 times more abundant than lithium, which could enable substantial cost savings and greater price stability [7, 11]. The growing relevance of SIBs is reflected in recent industrial announcements and production efforts [11, 13–15]. Nonetheless, as a relatively new battery technology with distinct storage mechanisms, the suitability of SIBs for energy transition applications remains to be fully demonstrated. Differences in energy density, and voltage characteristics may require system-level adaptations for electric mobility and stationary storage. In particular, aging behavior under diverse operating conditions, which strongly impacts battery operation and therefore costs, must be understood and analyzed to enable optimal operation and system integration [5], and ultimately shorten the time to market. Most existing studies about SIB aging focus on fundamental electrochemical behavior and are based on small sample sizes in aging experiments. This lack of comprehensive aging data makes it difficult to draw statistically robust conclusions about the long-term performance of SIBs.

This limited understanding of aging also creates uncertainty about how to monitor and

manage degradation during battery operation. Efficient, safe, and long-lasting operation in real-world applications relies heavily on effective diagnostic methods. While such methods are well established for lithium-based systems and widely used in both research and industry, their applicability to SIBs is unclear, and it remains necessary to quantify the limitations that may occur [13, 16].

Rapid deployment of new battery technologies as drop-in replacements requires a clear understanding of their lifetime and appropriate management strategies, which are essential to reduce time to market. Current high-power applications often rely on NMC/LTO cells, which provide high performance but come with significant costs. This motivates the search for more cost-effective and sustainable alternatives that can deliver comparable power densities while maintaining similar energy densities. To evaluate whether SIBs can serve as such an alternative, this work focuses on a representative automotive high-power use case, defining the system-level and lifetime requirements that a replacement technology must satisfy. Commercial SIBs are experimentally investigated under these application-relevant operating conditions to analyze their degradation behavior and longevity. Then, the performance of diagnostic algorithms originally developed for lithium-based systems is systematically quantified, evaluating the algorithms' accuracy, robustness, and adaptability for SIBs. By combining experimental aging data with simulation-based analyses, this work evaluates both the suitability of SIBs for real-world applications and the applicability of existing diagnostic methods to this emerging technology.

Outline of this Work

Following this introductory chapter, Chapter 2 establishes the methodological foundations by elaborating on the electrochemical and aging behavior of both LIBs and SIBs. It further introduces the fundamentals and requirements of a battery management system (BMS) as well as the statistical methods used to analyze field, experimental, and simulation data throughout this work. The three main chapters, which are depicted in Figure 1.1, build upon these foundations. Finally, the work concludes with a summary of the main findings and an outlook on future research directions.

To assess whether SIBs can represent an alternative to LIBs, it is first necessary to define a representative application. A high-power automotive use case is chosen that relies on costly lithium-based NMC/LTO cells, making it an ideal scenario to evaluate more cost-effective replacement technologies. Using field data from more than 600,000 vehicles and over 12 million readouts, we analyze in Chapter 3 the impact of diverse operating conditions, such as temperature and State of Charge (SOC), on aging behavior. Outliers are identified based on industrial tolerance thresholds, offering insights into abnormal degradation. Moreover, our anomaly detection framework helps to guide manufacturer in rapidly obtaining feedback on the aging of cells under operation using statistical methods, ultimately supporting predictive maintenance strategies.

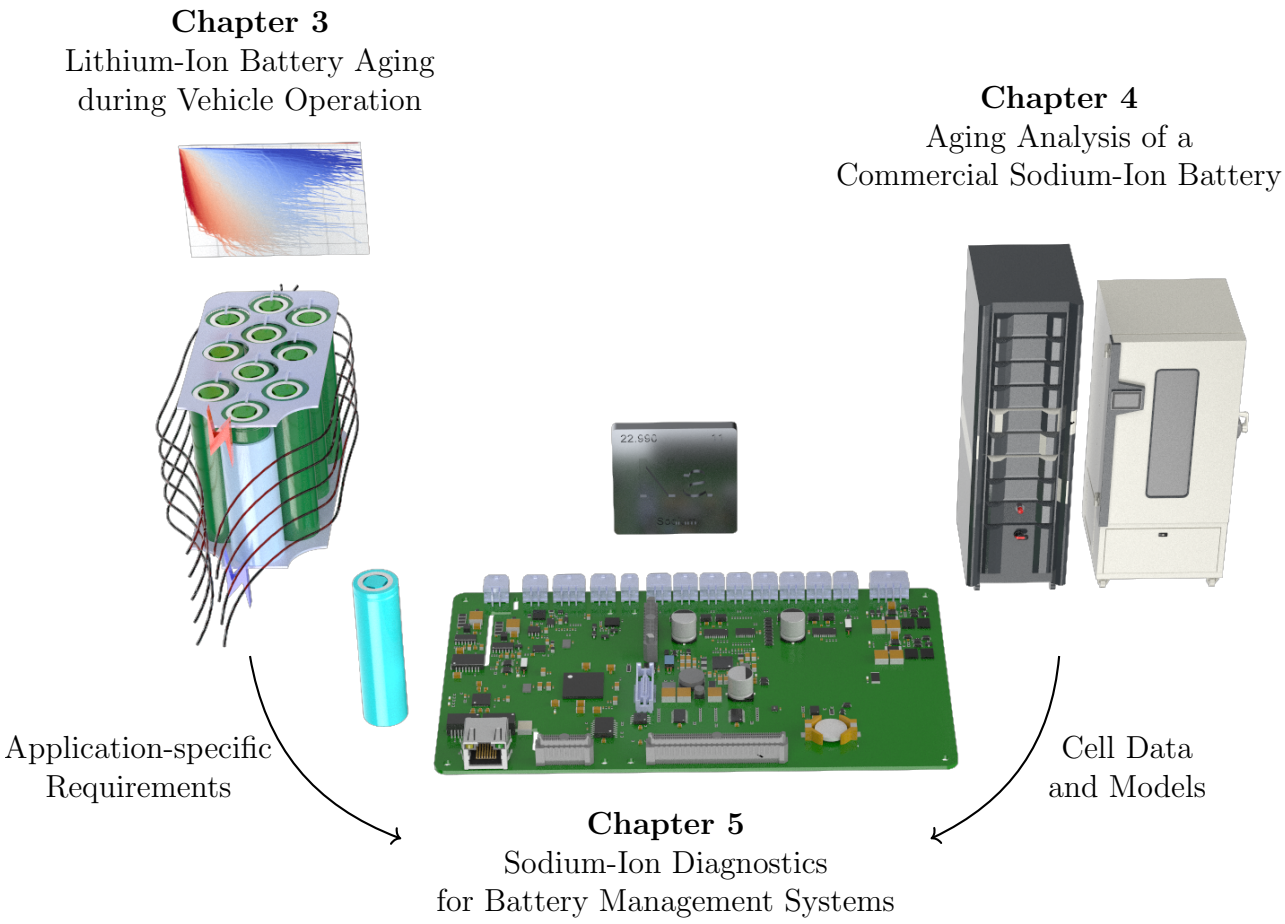

Figure 1.1: Overview of this work's structure. To evaluate the transferability of real-time diagnostic methods from lithium-based to sodium-based systems in high-power applications, an understanding of both aging and application-specific requirements is essential. We therefore analyze aging in lithium vehicle batteries using an extensive field dataset and, moreover, conduct a comprehensive sodium-ion aging study for degradation analysis. Together, these investigations provide a foundation for evaluating the practical feasibility of SIBs in the high-power use case, assessing their lifetime, and identifying management strategies to accelerate deployment and reduce time to market.

To evaluate whether SIBs can serve as a viable drop-in replacement in the high-power application, we first need to investigate whether the cells can meet the lifetime requirements under realistic operating conditions. Therefore, Chapter 4 presents an extensive aging study conducted on commercial sodium-ion cylindrical cells with a layered-oxide cathode and hard carbon (HC) anode. A total of 81 cells were cycled under six defined conditions, systematically varying SOC and depth of discharge (DOD), for up to more than 4,000 equivalent full cycles (EFC). Aging diagnostics methods, such as differential

voltage analysis (DVA), are performed to generate a deeper understanding of the relevant degradation mechanisms.

Building on this, in Chapter 5, we introduce two electrical models and one semi-empirical aging model, all fitted to the experimental data. These models are integrated into a BMS simulation framework to quantify the accuracy, robustness, and adaptability of real-time SOC and State of Health (SOH) estimators under realistic operating conditions of the high-power application. By simulating the sodium-ion cell within the targeted use case, we evaluate how well SIBs can be integrated into existing BMS architectures and assess their practical potential as a drop-in replacement, considering both performance and lifetime requirements.

2 Fundamentals

This chapter provides an overview of the fundamental electrochemical principles necessary to understand the functionality and performance of batteries. Following this, materials, specific aging mechanisms, and degradation modes of LIBs and SIBs are introduced. Moreover, we explain the importance of a BMS within a battery system, with a particular focus on real-time diagnostic methods. Finally, this chapter introduces the concepts of statistics, applied to analyze the field, experimental, and simulation data in the following chapters.

2.1 Electrochemical Fundamentals and Definitions

Electrode potential
When a metal is in contact with an electrolyte, the partial dissolution of metal atoms into the solution leads to an electrode potential at the interface. This potential arises from the redistribution of electrons in the metal and ions in the electrolyte, continuing until electrochemical equilibrium is reached. The electrode potential can be described by the Nernst equation where E^0 is the electrode potential at standard conditions, A_P denotes the activity of the relevant products, A_R indicates the activity of the reactants, R is the universal gas constant, F is the Faraday constant, n the number of transferred electrons, and T the temperature in Kelvin:

$$E = E^0 + \frac{RT}{nF} ln \left(\frac{A_P}{A_R} \right) \tag{2.1}$$

The equation shows the dependency of the electrode potential on temperature and molar concentration of ions in the solution. [17]

The electrode potential cannot be measured directly. To address this, a reference potential is used to define a scale for half-cell or standard potentials. By convention, the standard hydrogen electrode serves as the reference, with all other potentials expressed relative to it. [18, 19] When working with batteries we typically refer to a either a Li/Li+ or Na/Na+ reference electrode.

Cell voltage
In the thermodynamic equilibrium state, the cell voltage corresponds to the potential

difference between the anode and cathode. It depends on the change in free energy of the electrochemical couple and is defined as $U_{OCV} = E_c - E_a = -\frac{\Delta G}{nF}$, where U_{OCV} describes the so-called open-circuit voltage (OCV) [18–21]. The voltage that is additional needed to drive a reaction during operation is called polarization or overpotential and is the difference between the OCV and the terminal cell voltage U_T [19, 20]. When a current i is drawn by an external load (here, i is positive during cell discharge), U_T can be expressed as follows:

$$U_T = U_{OCV} - [(\eta_{ct})_a + (\eta_{con})_a] - [(\eta_{ct})_c + (\eta_{con})_c] - iR_i \tag{2.2}$$

$(\eta_{ct})_a$ and $(\eta_{ct})_c$ describe the activation polarization at anode and cathode, $(\eta_{con})_a$ and $(\eta_{con})_c$ the concentration polarization at anode and cathode and R_i the internal resistance [18, 19]. By convention, the negative electrode is called the anode and the positive electrode the cathode. From an electrochemical standpoint, the designation is based on the electrode with the lower thermodynamic equilibrium voltage relative to the other, and is strictly accurate only for the discharge direction. When no current is applied and the chemical reactions are leveled out, the cell voltage equals the U_{OCV}, which is also a function of temperature.

Concentration overpotential occurs due to mass transport limitations during operation, primarily caused by restricted diffusion of active species to and from the electrode surface. When diffusion within the electrolyte solution is constrained, a concentration gradient forms, resulting in polarization. [19] This effect can be described by the following equation:

$$\eta_{con} = \frac{RT}{n} ln \left(\frac{C}{C_0} \right) \tag{2.3}$$

where C is the concentration at electrode surface and C_0 is the bulk concentration in the solution.

Activation polarization arises from kinetic hindrances to the charge-transfer reaction at the electrode/electrolyte interface. In this context, the Butler-Volmer equation shown in Equation (2.4) describes how the current density depends on the potential difference between the electrode and the electrolyte [22], where i_0 is the exchange current density, η the overpotential relative to equilibrium, and α the charge transfer coefficient. [19] The current density i is expressed in units of A/m^2.

$$i = i_0 \cdot \left[\exp\left(\frac{\alpha z F}{RT} \eta \right) - \exp\left(-\frac{(1-\alpha) z F}{RT} \eta \right) \right] \tag{2.4}$$

Ohmic polarization arises from the resistance of various cell components, including the electrolyte, conductive additives, electrodes, current collectors, terminals, and contact between active material particles as well as between different cell components. [19] Tracking the cell voltage is one of the key methods used to monitor degradation effects and attribute them to the individual electrodes, as detailed in Chapter 4.

Capacity
The theoretical capacity is determined by the amount of active materials, i.e. the number of ions that can (de-)intercalate in electrodes, the stability of the active material, and the overall cell design [23].

In practical applications, the available capacity of a battery C_{act} corresponds to the maximum electrical charge Q_{max} that can be extracted from a fully charged battery under specific conditions [24]. Q_{max} is defined according to Equation (2.5):

$$C_{act} = Q_{max} = \int_{t_{start}}^{t_{end}} i(\tau) d\tau \tag{2.5}$$

t_{start} is the time when the battery is fully charged. If the cell is fully discharged, the time t_{end} is reached. The nominal capacity C_{nom} is usually specified by the cell manufacturer and corresponds to the amount of charge that can be drawn from a fresh, fully charged cell under nominal conditions. In contrast to the available capacity C_{act}, C_{nom} is not dependent on the aging condition of the cell.

Coulombic Efficiency
During cycling of a battery, various parasitic side reactions occur, including Solid Electrolyte Interphase (SEI) growth and electrolyte oxidation. These reactions consume additional charge so that the amount of discharged Q is less than the charged Q. The coulombic efficiency is therefore a measure of the reversibility of the redox reaction and is defined according to Equation (2.6) [25].

$$\eta_C = \frac{Q_{dch}}{Q_{cha}} = \frac{\int_{t_{start,dch}}^{t_{end,dch}} i(\tau) d\tau}{\int_{t_{start,cha}}^{t_{end,cha}} i(\tau) d\tau} \tag{2.6}$$

$t_{start,dch}$ and $t_{start,cha}$ indicate the start time of discharging or charging, respectively. $t_{end,dch}$ describes the time of complete discharging according to the cell's specification, where $t_{end,cha}$ indicates the time of complete charging according to the manufacturer specification. The coulombic efficiency η_C thus represents the ratio of the discharged to the charged Q in one cycle [26].

2.2 Lithium-Ion Batteries

LIBs are key enablers for the energy transition, significantly impacting a wide range of sectors. While batteries were historically used primarily in consumer electronics, stationary storage, and automotive applications, recent literature highlights the growing expansion of their use across various other industries [27–30]. LIBs offer notable advantages, including high power and energy densities, coupled with long lifetime capabilities, posing favorable attributes for the adoption of electric vehicles. From a chemical viewpoint, the

advantage of LIBs lies in lithium's light atomic weight ($M = 6.94\,\mathrm{g\,mol^{-1}}$) and very negative reduction potential ($-3.04\,\mathrm{V}$ versus the standard hydrogen electrode), making LIBs particularly well-suited for applications demanding high energy densities [31, 32].

2.2.1 Basic Principles

LIBs are electrochemical devices that convert chemical energy into electrical energy and vice versa [18, 33, 34]. In general, electrical energy is generated by electrochemical redox reactions occurring at the electrode/electrolyte interface.

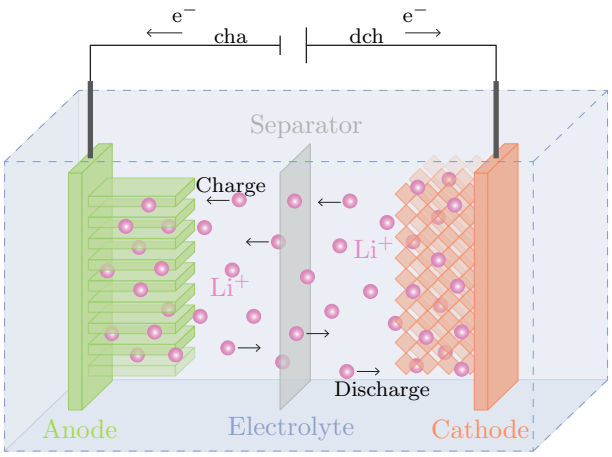

Figure 2.1: Working principle of a LIB, adapted from [35]. The functionality of LIBs is based on the intercalation of lithium ions into active materials, the so-called rocking-chair mechanism.

The working principle of a LIB is depicted in Figure 2.1. A LIB consists of two electrodes made of a different material separated by a thin separator soaked into an ion-conducting electrolyte. The cathode is equipped with a current collector typically made out of aluminum [36–38]. Since aluminum can react with lithium at high cell voltages (i.e. low anode potentials), the anode current collector is usually made of copper [36, 37]. The electrolyte serves as the medium for ion transfer between the anode and cathode, and is typically in liquid form [18], although solid electrolytes, as used in solid-state batteries, are also an active subject of research.

The functionality of LIBs relies on the migration of lithium ions between two electrodes and the reversible intercalation of these ions into the active materials. This so-called rocking-chair mechanism allows for the transfer of lithium ions without altering the macroscopic structure of the electrodes [33]. During the discharge process, the electrons flow from the anode to the cathode through an external circuit, equivalent to a current i at a voltage V. This electron flow is compensated by the migration and intercalation

of lithium ions through the electrolyte and separator into the cathode. The reaction is reversed during the charging process where lithium ions transfer back to the anode. [37]

The electrochemical reactions occur at the interface of active material and electrolyte and depend on the specific materials. The redox reaction can be divided into two half-cell reactions and can be described at a cobalt-oxide based cathode as follows:

$$LiCoO_2 \underset{\text{discharge}}{\overset{\text{charge}}{\rightleftharpoons}} Li_{1-x}CoO_2 + xLi^+ + xe^- \tag{2.7}$$

Usually, a carbon-based anode is employed, which absorbs lithium ions through intercalation of the ions into the anode during charging [39].

$$xLi^+ + 6C + xe^- \underset{\text{discharge}}{\overset{\text{charge}}{\rightleftharpoons}} Li_xC_6 \tag{2.8}$$

Not all of the theoretically stored energy can be converted into usable energy. [18, 37] The losses stem from (i) activation polarization, (ii) concentration polarization, and (iii) ohmic resistance as described in Section 2.1 [18]. These effects reduce the amount of extractable energy, with some energy dissipated as heat and some temporarily stored in concentration gradients.

2.2.2 Materials

The selection of active material plays a fundamental role in the characteristics of a battery cell, including its energy and power density, as well as its cycling performance under different environmental conditions. A cell's lifetime is influenced by the interfaces between the electrodes and the electrolyte, while its safety mostly depends on the stability of both the active materials and the electrolyte [31]. Usually, the quest for best-performing materials is driven by maximizing the energy density requiring high potentials and high specific capacity. Figure 2.2 depicts a selection of commercial and researched anode and cathode materials highlighting their specific capacity and corresponding potential. In addition to achieving high energy densities, active materials must exhibit sufficient electronic and ionic conductivity as well as high stability throughout the redox reaction to ensure reliable performance [37].

Widely used LIB anode and cathode combinations along with their resulting full cell voltage, determined as the difference between cathode and anode potential, are illustrated in Figure 2.3. It is visible that the voltage window for NMC/LTO is significantly lower compared to that of NMC/C. Furthermore, the full cell voltage of LFP/C is considerably flatter than that of NMC/C. The anode and cathode materials as well as their properties are discussed in more detail in the following section.

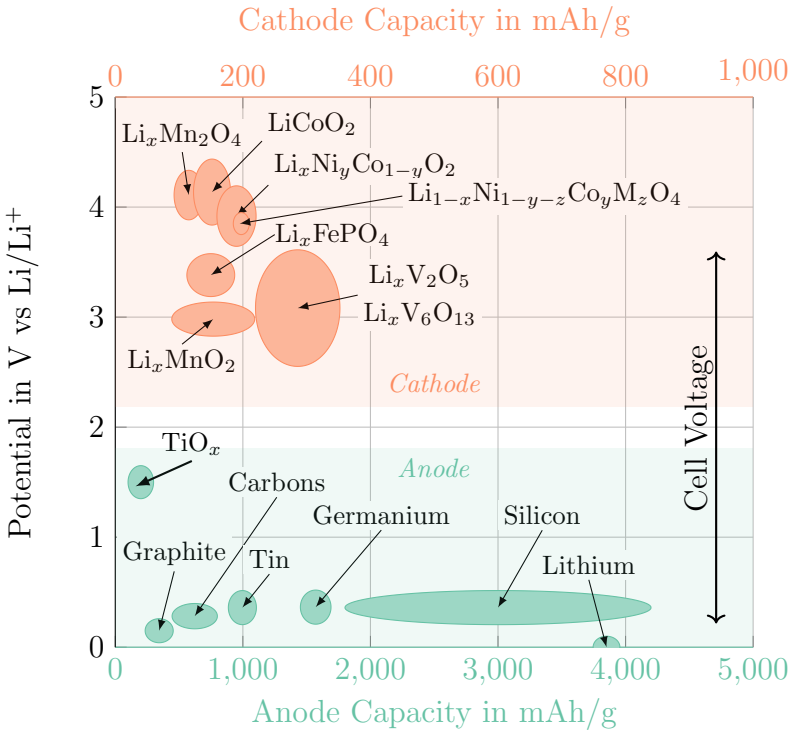

Figure 2.2: Potential vs. specific capacity for anode and cathode materials. [31, 37, 40, 41]. The ellipses illustrate characteristic trends that may correspond to different lithiation states. The cell voltage is determined as the difference of anode (green area) and cathode (orange area) potential.

2.2.2.1 Anode

Theoretically, pure metals would serve as the best anode materials due to their ability to achieve the highest possible energy density (approximately 3860 mAh/g), allowing for a greater number of metal atoms to be stored in a compact space [38, 42]. However, the practical use of pure lithium metal as anode material is hindered by the challenge of dendrite formation [43]. This limitation is still one of the reasons of the widespread adoption of lithium intercalation materials as anode materials [38]. Hereby, **graphite** has emerged as the dominant anode material [44] as it demonstrates good cycle lifetime, mitigates dendrite formation, and is cost-effective. However, challenges remain, including low rate capability and irreversible capacity losses caused by electrolyte decomposition at low potentials and the formation of the so-called SEI. This passivating, protective layer is formed on the surface of the anode due to the reaction between electrolyte solution and the anode [40, 45–47]. It acts as an ionic conductor while blocking electron flow, and is ideally insoluble in the electrolyte [45, 46]. The SEI is formed during the first charge cycle of a cell and leads to an initial loss of reversible capacity as the lithium ions are bound and no longer available for cycling. Once established, the SEI prevents direct contact between the active material, therefore mitigating the further decomposition of the electrolyte [38, 47]. But it continues to grow at a rate depending on the operating

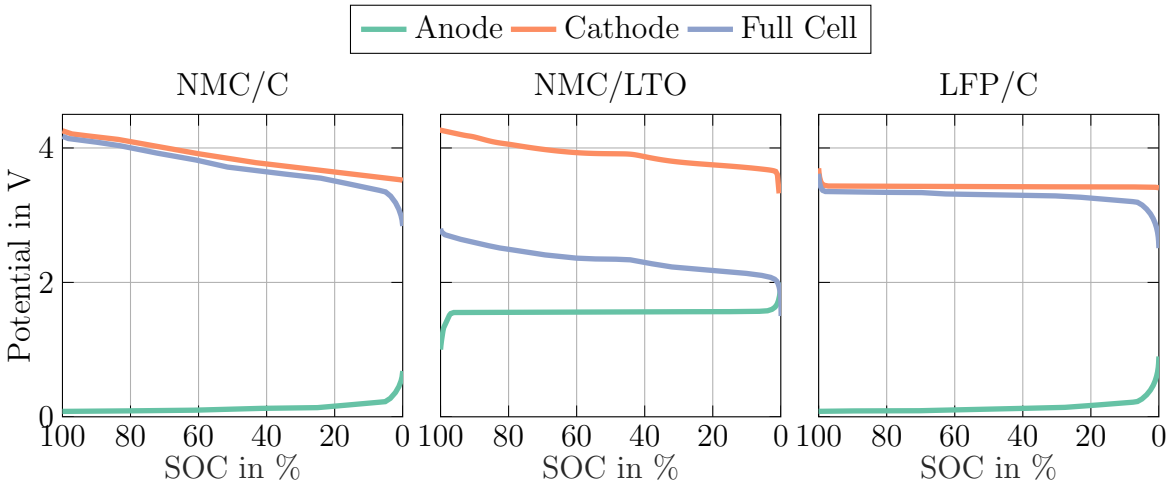

Figure 2.3: Mean anode, cathode and full cell potentials of an NMC/C, NMC/LTO, and LFP/C cell over SOC. The material composition is denoted as (cathode material/anode material), where NMC stands for $Li_{1-x}Ni_{1-y-z}Mn_yCo_zO_2$, C for graphite, LTO for $Li_4Ti_5O_{12}$, and LFP for $LiFePO_4$.

conditions throughout the whole lifetime. This is a main reason for the continuous loss of capacity and increase of internal resistance. As the SEI is critical to durability, battery performance and safety, optimizing SEI formation and mitigating growth through the selection of suitable electrolyte materials remains a focus of ongoing research [45, 46].

The pursuit of higher energy densities has led researchers to explore alternative materials, with **silicon** emerging as a promising active material [44]. Silicon offers significantly higher specific capacity compared to graphite, as shown in Figure 2.2, while simultaneously maintaining a low voltage potential. However, during lithiation and delithiation silicon suffers from an immense volume change of approximately 300 % [44] (compared to graphite with approximately 11 % [48]). This expansion can cause mechanical stress, fractures and deformation of the electrode through swelling impacting performance and safety. Furthermore, silicon is prone to enhanced side reactions with the electrolyte solution, resulting in excessive formation of the SEI. To leverage the advantages of both materials while mitigating their respective shortcomings, a combination of silicon and graphite is favorable, allowing for increased energy density while moderating the volume expansion. [49]

Another anode material is the spinel $\mathbf{Li_4Ti_5O_{12}}$. Compared to graphite, LTO generates a higher potential (1.5 V vs. Li/Li^+), as shown in Figure 2.2, avoiding the formation of SEI that typically forms at lower potentials (approximately 0.7 V vs. Li/Li^+) [32, 50]. This higher voltage also contributes to increased safety, as lithium is stored in a less reactive state, minimizing the risk of reactions with air or moisture [32]. Furthermore, LTO is structurally stable, exhibiting minimal volume change during lithium intercalation and deintercalation. This stability, together with the absence of SEI formation, allows LTO to maintain long cycle life and high durability [38, 50]. Unlike graphite, which is

limited by SEI growth on small particles, LTO can be synthesized with small crystal sizes, improving lithium ion diffusion and supporting high current rate (C-Rate) applications. However, LTO's higher potential lowers the overall energy density of the cell, which can be a limitation for high-energy applications [50]. Additionally, the material's low intrinsic electrical conductivity [50] necessitates the use of conductive carbon coatings to achieve better performance levels [38].

2.2.2.2 Cathode

The cathode is by convention the positive electrode of the cell and acts as the source of Li^+ during charging. The cathode materials can be grouped into different classes based on their crystal structure [51].

In **layered oxides**, composition is denoted as $LiMO_2$, where M corresponds to the elements Co, Ni, Mn and/or Al. Since the first introduction of rechargeable batteries, LCO has been widely used as a cathode material and is characterized by high energy density, but has shortcomings when it comes to safety, chemical stability, and costs. Furthermore, dissolution of cobalt ions can lead to capacity and thus performance loss. To address this, cobalt is increasingly replaced by the cheaper nickel, that still offers high reversible capacity and good ionic, and electrical conductivity. To further improve stability, aluminum is often added, resulting in the cathode material $LiNi_{1-x-y}Co_xAl_yO_2$ (NCA) [43, 52]. Another widely used cathode material is NMC, which can have different stoichiometries, typically ranging from NMC111 ($LiNi_{0.33}Mn_{0.33}Co_{0.33}O_2$) to NMC811 ($LiNi_{0.8}Mn_{0.1}Co_{0.1}O_2$). Higher Ni content increases energy density, while Co and Mn contribute to structural stability and cycle lifetime [53].

For a **spinel**, composition is denoted as $LiMn_2O_4$. While it provides higher thermal, structural stability, and good rate capability [32] as well as safety, spinels suffer from poor cycling behavior and reduced performance for high temperature, especially in acid environments where water can react with conducting salt [38].

Olivine $LiFePO_4$ (LFP) cathodes are characterized by their minimal structural and mechanical changes during (de-)intercalation and good stability, resulting in a significantly higher safety level compared to layered-oxide cathode materials and typically long lifespans. However, a main disadvantage is, first, the material's low average potential [51], the flat charging and discharging plateau which is problematic for battery diagnostics, and, second, their poor electrical and ionic conductivity [54]. To address this, the surface is often carbon coated [51]. LFP can also sustain high discharge currents [51]. The olivine structure is not only stable for LFP but also for other lithium transition metal phosphates, which offer higher voltage and energy density, but suffer poor conductivity [51]. Current trends in olivine material research include developing mixed iron-manganese phosphates, which aim to further improve performance and energy density [55, 56].

2.2.3 Aging Mechanisms

The characteristics of a battery change over its lifetime as a consequence of complex chemical and physical mechanisms leading to a decline in performance [57–60]. This degradation occurs during usage as well as storage and results in lower available capacity and increased internal resistance.

The major modes of degradation can be classified as follows [57, 61]:

- **loss of lithium inventory (LLI)**: Lithium ions are no longer available for the (de-)intercalation. Causes can include the formation and growth of the SEI, lithium plating and electrolyte decomposition.

- **loss of active material (LAM)**: This involves the reduction in the capacity of active materials and can be caused by structural changes, particle isolation, or dissolution of active materials. In literature, it is often differentiated between loss of active material of the anode $\mathrm{LAM_{NE}}$ and cathode $\mathrm{LAM_{PE}}$.

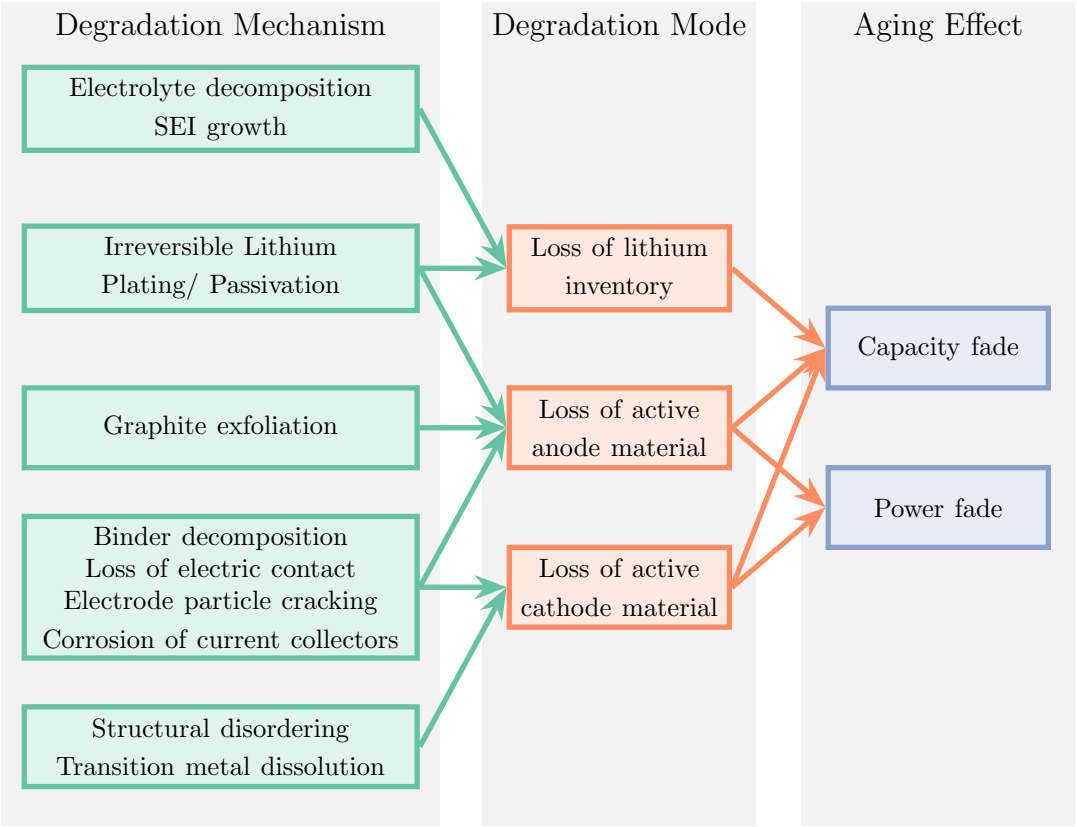

Figure 2.4: Interconnection of degradation mechanisms that contribute to the three investigated degradation modes LLI, $\mathrm{LAM_{NE}}$, and $\mathrm{LAM_{PE}}$ adapted from [57]. The resulting aging effects are highlighted in purple.

As illustrated in Figure 2.4, the degradation modes stem from various underlying mecha-

nisms that ultimately result in diminished power and energy capabilities. The degradation mechanisms, highlighted in green, have various causes, such as high and low temperatures, high and low voltages, high currents, or mechanical stress. The mechanical and chemical side reactions are influenced by an array of co-interpendent factors. Some of them are the chosen cell chemistry, the environmental conditions, and volumetric dimension, such as cell and pack design. The consequence of these side reactions is a reduction in lithium inventory, and active material, which is indicated in orange. [57, 61]

Figure 2.5 shows systematically the influence of the degradation modes on the single electrode potentials and the resulting cell voltage of an NMC/C cell.

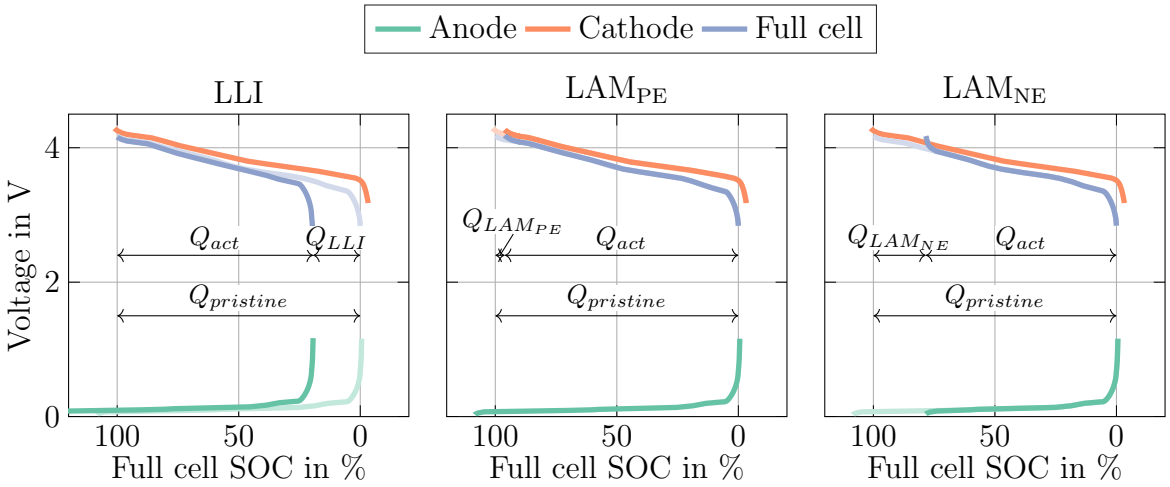

Figure 2.5: Simplified schematic representation of degradation modes with corresponding electrode potentials and full cell voltage for an NMC/C cell, adapted from [57]. The pristine cell is depicted in faded colors, while the aged cell is shown in full colors. In reality, multiple degradation mechanisms can occur simultaneously [61]. The degradation modes for the sodium-ion cell and the influence on the OCV for the sodiated and desodiated states are discussed in detail in Chapter 4.

During charging, the cathode potential increases and acts as the limiting factor, while during discharging, the anode becomes the limiting factor, determining the end-of-discharge voltage. The charge extractable from the cell, i.e. the capacity, corresponds to the cyclable lithium within it and is represented as Q_{act}. In the cell's pristine state, this charge equals $Q_{pristine}$. [57] In the case of LLI, the anode potential curve is shifted resulting in a shifted full cell voltage. Even though less lithium is available for the cycling, LLI can also mitigate the occurrence of lithium plating [62] as negative anode potentials may not occur. In the case of LAM$_{PE}$ (lithiated state), the OCV of the aged cell shrinks since a smaller amount of active material is available in the cathode. As the cathode looses more active material, it must operate at higher potentials, which can destabilize the active cathode material. [57] In the case of LAM$_{NE}$ (delithiated state), the capacity of the anode shrinks. Initially, the excess of anode material (anode overhang) can mask

the impact of active material loss. With progressive aging, the effects of LAM_{NE} become more evident, and the limitation during charging gradually shifts to the cathode, reducing the end-of-charge voltage. Since the cell is still operated up to its maximum voltage, the anode may be forced into negative potentials, increasing the risk of lithium plating and dendrite formation. [57]

The degradation mechanisms at the anode differ significantly from those at the cathode. Consequently, the degradation mechanisms are discussed individually for each electrode in the following sections.

2.2.3.1 Anode

In the literature, mainly the aging of graphite-based anodes has been investigated and is described in this section. Generally, aging at the anode is largely driven by changes in the electrode/electrolyte interface. Beyond reactions of the anode with the electrolyte and the changes of composite electrodes, structural changes in the active material also contribute to aging. Graphite exfoliation (separation of graphene layers), particle cracking (caused by mechanical stress of volume change), electrolyte reduction, and gas evolution (caused by electrolyte decomposition) within the graphite can accelerate degradation. [59]

A major aging mechanism is the reaction of the anode with the electrolyte. Since the graphite anode operates outside the electrochemical stability window [61, 63], electrolyte decomposition and the irreversible consumption of lithium ions can occur, leading to the growth of the SEI. This effect is particularly pronounced at higher temperatures, where the SEI continues to grow [61]. As a result, the SEI can grow into the pores of the anode, reducing the active surface area available for lithium intercalation. Additionally, corrosion may occur, further promoting SEI growth during cycling and storage. The formation and growth of the SEI can lead to contact loss within the electrode, while volume changes in the anode may cause mechanical stress. As a result, electrode porosity is reduced, limiting electrolyte infiltration. Moreover, binder materials can react with the anode, further degrading the mechanical properties of the electrode. At low temperatures, lithium plating can occur, especially during charging with high current [64]. This process describes the deposition of metallic lithium on the surface of the anode and can only occur when the anode potential drops below 0 V vs. Li/Li^+. Lithium plating can be categorized into reversible and irreversible lithium deposition [65]. A large part is reversible, meaning that the plated lithium is either reincorporated into the graphite through subsequent intercalation or dissolves during the following discharge (so-called stripping) [64, 65]. For irreversible plating, the lithium is passivated in the SEI and is no longer available for electrochemical cycling. The metallic lithium can lead to dendrite formation that can penetrate the separator and lead to short circuits [65]. In the worst case, these short circuits can trigger high temperatures, ultimately leading to a thermal runaway [65]. Inhomogeneous current and potential distributions increase the risk of lithium metal reacting with the electrolyte leading to accelerated aging [59]. Selecting suitable electrolyte materials and binders with

beneficial properties can help slow down SEI aging processes [59].

2.2.3.2 Cathode

On the cathode side, lifetime degradation is primarily driven by the oxidation of electrolyte components and the formation of a surface layer known as the Cathode Electrolyte Interphase (CEI). Additional degradation mechanisms include the dissolution of electrode materials, gas generation, irreversible phase transitions, and mechanical stress. These effects are co-dependent, vary with the cathode material used and are strongly influenced by operation, such as cycling conditions and SOC [59].

Oxidative decomposition of the electrolyte can lead to the formation of the CEI on certain cathode materials. While the CEI is usually not as thick as the SEI, it can significantly influence the available Li^+ inventory, contributing to accelerated aging. Elevated temperatures further influence its growth. As the CEI grows, more lithium ions are bound, reducing the number of ions available for the (de-)intercalation process [66]. Similar to the SEI, the CEI consists of both inorganic and organic components [66]. These components of both the SEI and CEI are often soluble in electrolyte solvents and may transfer onto the counter electrode surface. To mitigate aging effects caused by the CEI, a suitable choice of electrolyte components can help improve its properties. Additionally, aging due to the CEI can be slowed down through the incorporation of additives or by applying a coating. [67] Furthermore, during cycling at high voltage and temperature, the transition metals can be dissoluted, where metal ions from the cathode material migrate into the electrolyte. This issue can be mitigated to some extent by applying cathode coatings. [67] Mechanical stress can result from volume changes in materials, which induce stress within the particles and the electrode. This can lead to inhomogeneous chemical reactions and expose particle surfaces to further deterioration through reactions with the electrolyte [59]. Additionally, volume changes during phase transitions contribute to these mechanical stresses, further accelerating degradation [67]. Irreversible phase transitions within the bulk are accompanied by the dissolution and dislocation of transition metals, as well as oxygen loss, which results from cation mixing between transition metals and lithium ions. This process increases and hinders the transport of the ions, leading to further degradation. To mitigate this effect, again, coating and doping methods are used. [67]

2.3 Sodium-Ion Batteries

While the pursuit of higher energy densities has long driven innovations in battery technology, costs and sustainability are gaining increasing importance [37]. In this context, SIBs offer a promising alternative to the dominant LIB technology. Research on SIBs began alongside LIBs in the 1980s, but due to their lower theoretical capacity and slow

reaction kinetics, LIBs became the preferred technology [15]. However, rising costs of raw materials for LIBs have renewed interest in the SIB technology. One major factor driving the costs is the scarcity of lithium, which contributes to price fluctuations in LIBs [68]. In contrast, sodium is abundant, as it can be extracted from seawater and sodium carbonates [15, 68], making it a cost-effective alternative that is less vulnerable to raw material supply risk [34]. Besides raw material availability, certain design-related aspects of sodium-ion cells offer additional advantages: Unlike LIBs, where aluminum would alloy with lithium at low anode potentials, aluminum is generally stable in the low-potential range of sodium-ion anodes. Therefore, aluminum can often be used as current collector for both electrodes in SIBs [14, 68]. This not only reduces costs but also enhances safety, as SIBs can be stored at 0 V. Additionally, aluminum is lighter than copper, which improves the overall energy density of the battery [68].

Generally, lithium and sodium exhibit similar chemical characteristics, and therefore, SIBs operate similarly to LIBs, following the rocking-chair mechanism as discussed in Section 2.2.1 [15, 17, 68]: During discharge, sodium ions migrate from the anode through the electrolyte and separator to the cathode, where they intercalate into the active material. Simultaneously, electrons flow from the anode to the cathode through an external circuit to maintain charge balance. This process is reversed for charging. [23] However, as illustrated in Table 2.1, sodium's higher relative atomic mass (6.94 for Li and 22.99 for Na) and bigger size (0.76 Å for Li and 1.02 Å for Na) has a negative influence on the electrochemical performance of SIBs when compared to LIBs [17]: lower (volumetric and gravimetric) theoretical capacity, lower solubility in the solid state, lower cell voltage, slow transport kinetics, more severe structural damage, and volume change. [68]

Category	**Lithium**	**Sodium**
Relative atomic mass	6.94	22.99
Cation radius (Å)	0.76	1.02
E^0 vs. standard hydrogen elecrode (V)	-3.04	-2.71
Melting point (°C)	180.5	97.7
First ionization energy (kJ mol^{-1})	520.2	495.8
Abundance in the earth crust (mg kg^{-1})	20	23.6×10^3
Distribution	70 % in South America	Everywhere
Theoretical capacity (mAh g^{-1})	3861	1166
Theoretical capacity (mAh cm^{-3})	2062	1131

Table 2.1: Comparison of lithium and sodium properties. [17, 69]

2.3.1 Materials

Most of the electrode materials that are commonly used for LIBs cannot be directly applied to SIBs due to the larger radius of sodium ions [17]. An overview of researched anode and cathode materials with their characteristics is given in Figure 2.6.

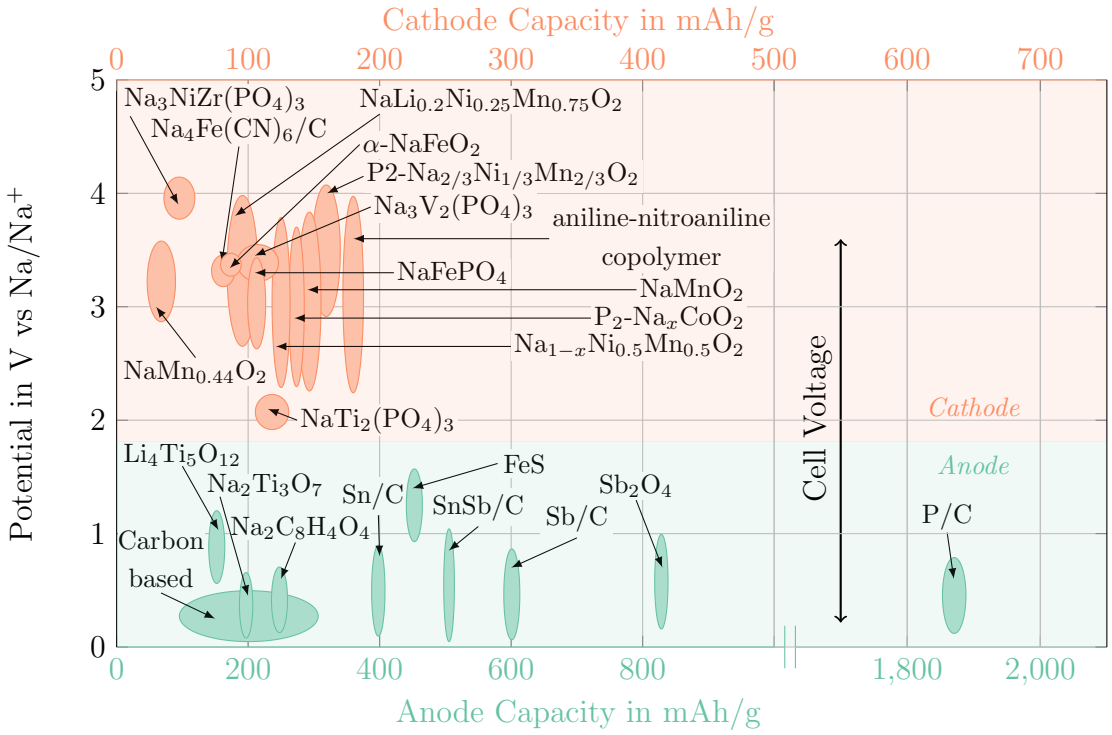

Figure 2.6: Potential vs. specific capacity for some anode and cathode materials used for SIBs. [70] The ellipses illustrate characteristic trends that may correspond to different sodiation states. The cell voltage is determined as the difference between cathode and anode potential of the used materials.

2.3.1.1 Anode

In contrast to LIBs, graphite is not commonly used as anode material in SIBs, since graphite is thermodynamically unfavorable to intercalate sodium [71]. Therefore, instead of intercalating, metallic sodium can deposit on the graphite surface, negatively influencing safety and electrochemical performance. [17] Similar to LIBs, metallic sodium as an anode material remains an area of research due to the risk of dendrite formation. However, dendrite formation is less pronounced for SIBs due to sodium's larger ionic radius and higher surface diffusion energy, which promotes more uniform deposition during plating-like behavior. [17] As a result research focuses on intercalation anodes, especially carbon-based, titanium-based, and alloy-based materials.

Within the literature **carbon-based** anode materials are typically categorized into three types: graphite, soft carbon, and HC [72]. Among these, graphite shows the lowest sodium storage capability [68]. In contrast to graphite, that shows a crystalline form, soft carbon and HC materials exhibit disordered structure and increased interlayer spacing [68]. Since the sodium-graphite intercalation compounds are less stable, graphite achieves a reversible capacity of merely $40\,\mathrm{mAh\,g^{-1}}$, significantly lower compared to $350\,\mathrm{mAh\,g^{-1}}$ in LIBs [68]. As a result, HC has become much attention as anode material for SIBs. HC

consists of crystalline and disordered domains with structural defects [73]. In between the disordered and ordered domains, HC has closed pores [73]. Its high porosity and large interlaying spacing provide more sodium diffusion pathways and numerous active sites to store sodium ions [68, 74] enabling a reversible capacity of approximately $300\,\mathrm{mAh\,g^{-1}}$ [23]. However, the sodium storage mechanism is still focus of ongoing research [71]. Current literature suggests that sodium ions can be stored by the adsorption of sodium ions on defects, the intercalation of sodium ions into graphite layers, and the filling of sodium ions in nanopores. [74] In contrast, soft carbon has a less disordered graphitic structure compared to HC. While it generally exhibits a lower specific capacity and higher operating potentials resulting in lower energy density it offers good rate capability making it an interesting anode material for high-power applications [68].

Besides carbon-based anode materials, **alloy-based** anodes are also promising candidates as they have very good sodium storage capabilities and high theoretical capacities. However, they often exhibit an excessive volume change during (de)sodiation and usually suffer from low electrical conductivity. Therefore, those materials are typically combined with carbon to mitigate the volume expansion and enhance conductivity. [17] Interestingly, silicon, which is a very promising candidate in LIBs, is practically inactive in SIBs [73].

Another family that is suitable for SIB anodes are **titanium-based** anode materials. Similar to their lithium counterparts, they exhibit advantageous characteristics, including favorable structural dynamics, non-toxicity, and 2D diffusion channel for sodium ions that facilitate the sodium-ion transport [68]. Their relatively high operating voltage can hinder metallic sodium plating; however it also reduces the overall energy density [73, 75]. Recently, literature and research have mainly focused on titanium dioxide, lithium titanate, sodium titanate, and sodium titanium phosphate [23]. The storage of sodium ions in these materials occurs through a (de-)insertion mechanism [73]. Despite their advantages, titanium-based anode materials face challenges, including poor electronic conductivity, and sluggish kinetics resulting in poor rate capability and cycling stability. Additionally, their high operating voltage limits the overall energy density [73]. In contrast to LTO anode materials, an SEI may be formed on the surface of NTO anodes [73, 75].

2.3.1.2 Cathode

Similar to LIBs, the cathode material of SIBs mainly determines the cell costs, lifetime, safety and performance, including energy and power density [17]. Since sodium ions are larger, the cathode materials for LIBs cannot directly be applied for SIBs [23]. The cathode materials for SIBs can be roughly grouped into three different categories, namely (i) layered transition metal oxides, (ii) polyanion compounds and (iii) prussian blue analogs (PBA) [76].

The general chemical formula for **layered transition metal oxides** is $\mathrm{Na}_x\mathrm{M}_y\mathrm{O}_2$ where M denotes a transition metal [17, 70, 76]. The most commonly used layered transition metal

oxides crystallize in O3, P2, or P3 structures. O and P denote octahedral and trigonal prismatic coordination environment, respectively, while the numbers 2 or 3 describe the number of transition metal layers in a repeated stacking unit of the crystal [70]. Due to the larger radius of sodium, transition metal oxides undergo more complex phase transitions during the removal of sodium ion compared to their LIB counterparts. [17] Among the structures, P2 allows for more facile sodium-ion mobility resulting in better kinetics and rate capability. [17] However, less sodium ions can be accommodated compared to the O3 environment leading to a lower theoretical capacity [76]. In contrast, O3 offers higher energy densities but undergoes more complex phase transitions.

Polyanionic materials have the chemical formula $Na_xM_y(XO_4)_n$, where M denotes a transition metal and X=S,P,Si,B [17]. These materials are composed of anionic $(XO_4)^{n-}$ tetrahedra and the polyhedra MO_x [17]. Polyanionic compounds include phosphates, such as $NaFePO_4$, sulfates, such as $NaMSO_4F$ and other oxysalts [17]. The advantages of polyanionic compounds include higher thermal stability compared to layered transition metal oxides, enhanced ionic diffusion kinetics, stable 3D structure and restricted volume changes during (de-)sodiation [17, 23]. Additionally, these compounds exhibit an improved redox potential, leading to higher energy densities [17]. However, several challenges remain, including limited capacity (due to the high molecular weight of polyanionic material), restricted ion mobility, and low electronic conductivity. Therefore, research focuses on the investigation of materials with a suitable balance of voltage and capacity. [76]

Prussian blue analogs (PBA) describes a broad family of transition-metal hexacyanometallates [17]. Their general chemical formula is $A_xM_a[M_b(CN)_6]_y \cdot nH_2O$, where M_a and M_b denote transition metal ions, and A denotes an alkali metal such as sodium. [17] The large channel structure of PBA cathode materials allows for facile transportation of the large sodium ions. However, their structure contains several vacancies, which can lead to structural instability, potentially even collapse, and reduced electrochemical performance [17, 76]. Additionally, the vacancies can decrease the electrical conductivity resulting in poor rate capability [17]. Furthermore, three discrete forms of water exist in the PBA structures which can negatively influence capacity and rate capability. The water molecules hinder the sodium-ion transport, promote side reactions, and destabilize the structure, ultimately leading to a reduced cycle stability [17, 76]. The vacancies further introduce water reducing sodium content and lowers capacity [17]. PBA may be a promising cathode material for SIBs due to their low cost, facile synthesis, and high theoretical capacity [17]. However, practical challenges remain, including poor conductivity, low structure stability and low energy density through inherent water and vacancies [17].

2.3.2 Aging Mechanisms

As for LIBs, the degradation of SIBs strongly depends on the choice of anode, cathode and electrolyte materials. The electrolyte degradation in SIBs is mainly driven by moisture as water can react with $NaPF_6$ to form toxic hydrofluoric acid (HF). HF can then react with sodium materials and form NaF on the electrode surface and dissolve transition metals from the cathode. These dissolved metals can migrate to the anode causing dendrite formation and an increased risk of short circuits. [74] Figure 2.7 illustrates the various aging mechanisms occurring in SIBs. The HC anode is shown in green, and the layered-oxide cathode in blue. Unlike LIBs, SIBs can generally use aluminum for both current collectors, as it is stable even at low potentials of the anode [68]. However, the cell investigated in Chapter 4 uses copper on the anode side and aluminum on the cathode side. Apart from this, the cell design and aging mechanisms in SIBs generally closely resemble those of lithium-based systems.

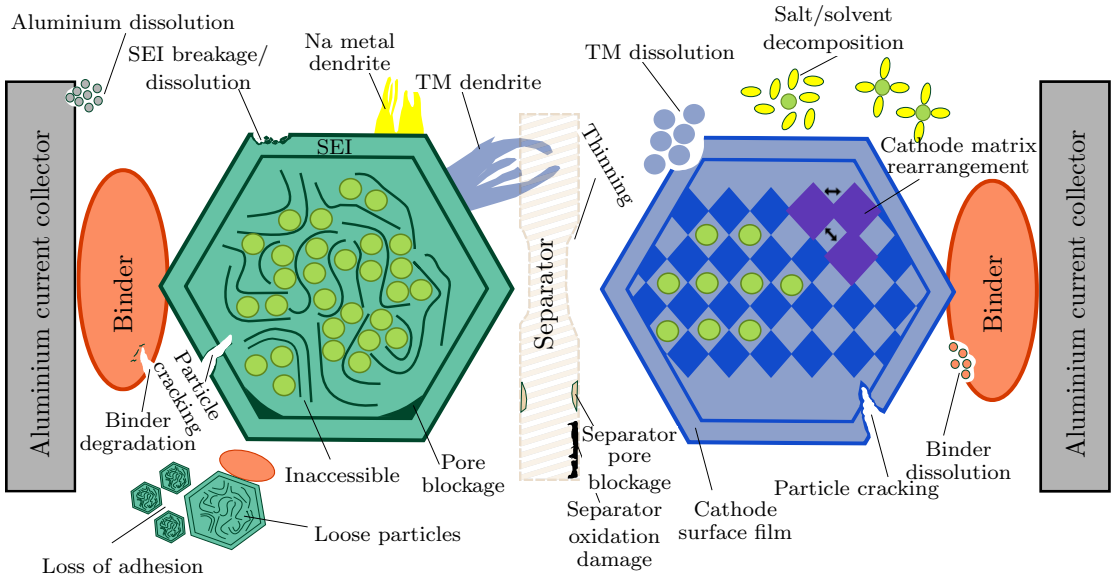

Figure 2.7: Aging mechanisms in SIBs based on [57, 74]. TM stands for transition metal.

In the following, degradation is categorized into anode and cathode aging. Since the underlying mechanisms are similar to those in LIBs and have already been discussed, we provide only a summary of the most relevant differences between SIBs and LIBs.

2.3.2.1 Anode

The anode degradation is primarily driven by reactions at the electrode/electrolyte interface. Similar to LIBs, a passivation layer, i.e. SEI, forms on the surface of the anode

during the first cycle due to reactions of the electrolyte with the electrode. The presence of a stable SEI is advantageous for cell performance as it hinders further electrolyte decomposition; however, it also reduces the number of sodium ions available for cycling. The SEI typically forms at approximately 0.8 V vs. Na/Na^+. Usually, the SEI in SIBs exhibits reduced stability, and increased solubility compared to the SEI of LIBs [46]. As a result, the SEI is more prone to breakdown even at lower temperatures. The susceptibility to breakdown can expose the electrode and thereby facilitate further SEI growth and, consequently, an increase in resistance. Additionally, an exothermic breakdown may generate heat and in extreme cases, trigger a thermal runaway. The increased solubility of the SEI necessitates continuous replenishment, leading to an increased inefficiency in cycling and further utilization of salt and electrolyte solvent which can ultimately deplete the electrolyte. [74] Besides the SEI formation, growth and breakdown, mechanical stress of the materials also contributes to anode degradation. During sodiation, the active material expands as sodium ions are inserted, inducing mechanical strain. Since sodium ions have a larger radius than lithium ions volume expansion is more severe in SIBs [17]. However, HC expands less than graphite and does so in 3D rather than 2D, which is beneficial for the stress. In contrast, alloy-based anode materials experience significant expansion. This can ultimately result in particle and electrode cracking, exposing the electrode to the electrolyte which accelerates SEI growth. If the SEI continues to grow, electrode pores can block, increasing the resistance and potentially causing the particles to lose contact to the current collector. Detached particles might move through the cell, damaging the separator and block its pores. This can create inhomogeneous current distribution and localized high current density, increasing the risk of overcharge and overdischarge as well as dendrite formation. [74] Inhomogeneous current distribution, structural changes [74] as well as an interfacial overpotential near 0 V vs. Na/Na^+ can cause sodium plating to occur [17]. Sodium plating can lead to additional SEI, electrolyte decomposition and an increased resistance accelerating degradation. [74] Additionally, dendrites can be formed that may lead to short circuits. Other consequences of volume change of particles are pulverization and delamination stemming from loss of electronic contact [17].

2.3.2.2 Cathode

The degradation of cathode is driven by material degradation, phase changes, mechanical stress, and foreign molecule insertion [17]. Transition metals can dissolute in the electrolyte resulting in loss of capacity and the destabilization of the SEI [17]. Additionally, the redox potentials of layered-oxide materials lie outside the upper limit of the electrolyte stability window, causing electrolyte oxidization at the cathode, resulting in decomposition and the formation of the CEI. Beyond CEI formation and growth that directly influence cathode degradation, the species from the anode SEI can also influence the stability of the CEI when the species from the SEI migrate to the cathode or react through the electrolyte similar to LIBs. To mitigate this effect, protective coatings can be applied to the cathode to reduce electrolyte decomposition, preventing transition metal dissolution and inhibiting structural degradation [74]. When it comes to layered transi-

tion metal oxides, at elevated temperatures, active cathode materials can undergo thermal runaway as the high temperatures release oxygen from the structure and accelerate the oxidation [17]. Besides the material degradation, phase changes during cycling impact cathode stability. During overcharging, where too many sodium ions are extracted, the structure can collapse leading to cell failure [17]. The structural changes of sodium-layered compounds differ fundamentally from their lithium-ion counterparts. Sodium-ion cathode materials usually are more stable which is due to the lower number of sites suitable for sodium storage [17]. However, the larger ionic radius of sodium can lead to more pronounced volumetric changes during cycling in certain cathode materials. This expansion and contraction introduces mechanical stress, which at high voltages may cause particle cracking and electrode exposure, as also observed for the anode [74]. An additional degradation mechanism observed in some SIB cathodes is the insertion of foreign molecules such as water or carbon dioxide into sodium sites [17]. These species usually originate from precursor impurities or exposure to air during manufacturing [17]. The presence of these molecules reduces capacity and cyclability of the cathode material [17].

2.4 Battery Management System

A battery system consists of a number of in series and parallel connected cells, the wiring, the housing, and the BMS. The latter is the central processing unit managing the whole battery system. Depending on the cell design and intended application, the exact requirements regarding the management of the battery differ [77–80]. The BMS itself can be thought of as a gatekeeper, supervising the energy flow and ensuring the safe and efficient operation of the battery. Moreover, the BMS consists of processing units containing algorithms to calculate internal battery states [80]. A BMS is often organized using a hierarchical topology referred to as controller-responder. Within this topology, the responder units are responsible for collecting measurement data from individual battery cells or modules and the energy management. The collected data is then transmitted to the control unit (CU), where it is interpreted, temporarily stored, and forwarded to the vehicle's system via a Controller Area Network (CAN) bus. This hierarchical structure ensures efficient data acquisition, monitoring, and management within the BMS. [77]

As illustrated in Figure 2.8, the responsibilities of a BMS can be categorized into protection, monitoring, state estimation, and energy management. These interconnected tasks share their specific outputs with other CUs. For example, the engine controller in a car relies on the BMS to determine how much power the battery can provide, enabling optimal power delivery to the wheels.

During operation, voltage, current, and temperature are monitored non-invasively at both cell and pack levels, with temperature measurements typically focused on specific locations such as hotspots rather than every individual cell [79]. The selection of digital or analog sensors for these measurements depends on various application-specific requirements,

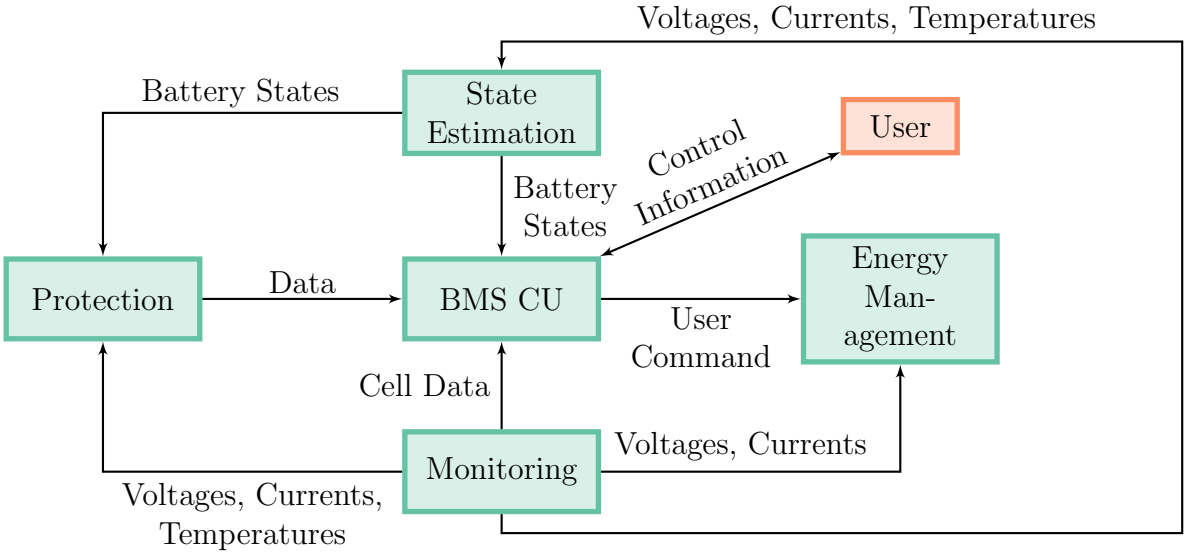

Figure 2.8: Simplified overview of the interconnection of different BMS responsibilities. In the center is the BMS CU that manages critical tasks such as state estimation, protection, monitoring, and energy management. The CU acts as the controller and hosts a computing unit which calculates the internal battery states. The monitoring and parts of the energy management are carried out by the responder. This part of the BMS, directly connected to the cells, is sending the cell data to the controller and supervises the cell energy management. A fuse box contains the main protections and connection fuses to the consumer.

including cost, bandwidth, accuracy, measurement range, and size. This data collection plays a crucial role in ensuring the battery's safe operation within its defined safe operating area (SOA). Battery protection encompasses both electrical and thermal aspects. Electrical protection involves actively bounding current and voltage during operation to prevent excessive currents, overcharging, and deep discharging, with limits typically specified by the manufacturer. Thermal protection, on the other hand, maintains the battery's temperature within an appropriate range to mitigate risks such as lithium or sodium plating, an effect that, as already described, can occur at low temperatures and high currents. To mitigate this, the BMS manages the heating or cooling mechanisms. In the case that the limits defined by the SOA are violated, the BMS is able to trigger active circuit breakers to stop the operation.

Based on the sensor measurements, internal states such as SOC and SOH are estimated by diagnostic algorithms as described in Section 2.4.1. These estimates not only provide valuable insights into the battery's condition but also contribute to maintaining operation within the SOA, for example, by preventing overcharging. The configuration of these algorithms needs to be adapted to the cells and the sensor hardware. [77]

Due to production tolerances and varying operational and environmental conditions, cells

can exhibit different characteristics, manifesting in variations of voltage and SOC [81]. An imbalance leads to limitations of the maximum of chargeable energy or the capacity of the whole pack, as the cell with the lowest SOC should not be discharged below the boundary and the cell with the highest SOC should not be overcharged [81]. Furthermore, in an unbalanced system, some cells are subjected to higher loads, which results in uneven aging and thus negatively impacts the lifetime of the overall system [81]. The energy management is aiming at balancing the voltages or SOCs of the cells to mitigate this and optimize energy and capacity of the system. There are two common approaches, namely active and passive balancing: An active balancing system transfers the excess charge from one cell to another, whereas a passive system dissipates the charge from all cells that have accumulated an excessive amount of charge. [77]

2.4.1 Battery Diagnostics

Battery diagnostics aim to estimate the internal states of cells within a battery system that cannot be directly measured. Depending on the use case, different states are estimated using methods of varying complexity [77]. In this work, we focus on the widely used states SOC and SOH. The estimation methods for these states range from direct approaches [82, 83] to model-based [84–86] and data-driven [87–91] methods. Here, we concentrate on direct and model-based methods, as they are suitable for real-time implementation in a BMS. Specifically, we analyze the transferability of direct methods as well as Kalman filter-based and least-squares-based algorithms.

2.4.1.1 Internal Battery States

State of Charge
The SOC is a state parameter correlating with the remaining charge in a battery cell. In existing literature, there are numerous definitions [24, 77]. However, one of the most commonly used definitions is the ratio between the charge currently stored in the battery, represented by the variable $Q_{residual}(t)$, and the battery's capacity, represented by C in Equation (2.9), where C is either the nominal or the actual capacity considering the aging of the cell. The initial SOC at time t_0 is denoted as $SOC(t_0)$. i is positive during charge and negative during discharge. The coulombic efficiency η_c, defined in Equation (2.6), is included in the definition to account for side effects. However, for this work, the parameter is set to 1.

$$SOC(t) = \frac{Q_{residual}(t)}{C} = SOC(t_0) + \eta_C \cdot \frac{1}{C} \cdot \int_{t_0}^{t} i(\tau) d\tau \tag{2.9}$$

State of Health
The performance of batteries deteriorates over time and with increasing usage. To quantify this aging, the indicator SOH is estimated by the BMS. Wile several definitions for the

SOH exist in literature, the SOH usually reflects the decrease of capacity, State of Health capacity (SOH_C), or the increase in internal resistance, State of Health resistance (SOH_R) [92]. A commonly used definition to quantify capacity degradation is shown in Equation (2.10), where C_{act} represents the remaining, actual capacity, and C_{nom} denotes the nominal capacity of the pristine cell. For the SOH_R, we use Equation (2.11), where R_i denotes the current resistance and $R_{i,nom}$ a nominal value given by the manufacturer. Typically, the End-of-Life is reached when the capacity C_{aged} is 80 % of the nominal capacity C_{nom} or the resistance $R_{i,aged}$ doubles compared to the nominal resistance of the fresh cell $R_{i,nom}$. This threshold is commonly used as a reference for warranty-related performance, not as a limit of cell usability.

$$SOH_C = \frac{C_{act}}{C_{nom}} \tag{2.10}$$

$$SOH_R = \frac{R_{i,act}}{R_{i,nom}} \tag{2.11}$$

2.4.1.2 Direct State Estimation

Direct state estimation is an open-loop approach, meaning that the state is determined solely based on measurements, without any correction. For both SOC and SOH estimation, the definition of SOC from Equation (2.9) is applied. The estimation involves integrating the measured current over time. While this method has low computational effort, it comes with the drawbacks that current measurement errors accumulate during integration and that initial state errors cannot be corrected [77, 92, 93].

2.4.1.3 Model-based State Estimation with Kalman Filters

Model-based methods for state estimation emulate the behavior of a system using a model and connect the non-observable internal system state with the observable output. An observer or filter, such as a Kalman Filter (KF), is then used to minimize the discrepancy between the model's estimated value and the observable but noisy output.

For linear systems with uncorrelated, mean-free, Gaussian distributed, white noise, the KF provides an optimal estimate with minimum mean squared error. [94] Figure 2.9 illustrates the steps of the KF. Each estimated state consists of an expected value $\hat{\mathbf{x}}$ and an associated probability distribution, which is characterized by its covariance matrix $\mathbf{P}$. [94] The KF relies on two equations that describe the relationship between the system's internal state and the measurable quantities. These equations are defined in Equations (2.12) and (2.13), where $\mathbf{A}$ is the state transition matrix and $\mathbf{B}$ is the input matrix, describing how the input $\mathbf{u}$ affects the state transition. $\mathbf{H}$ is the observation matrix, describing how the measured value is derived from the state $\mathbf{x}$. The vectors $\mathbf{w}$ and $\mathbf{v}$ describe the

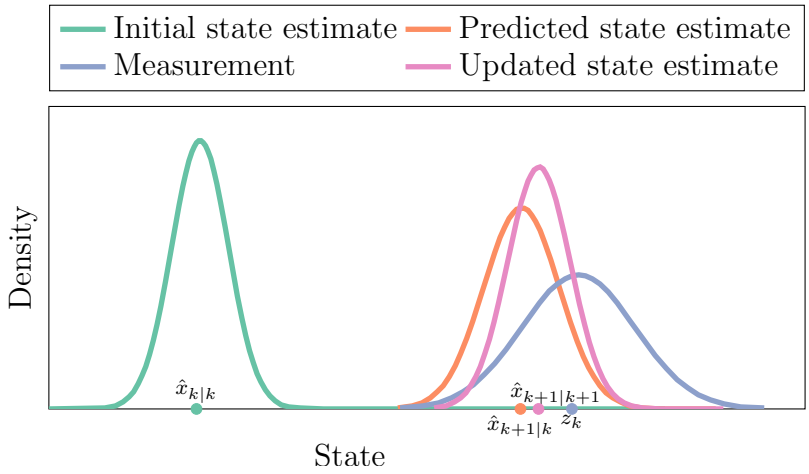

Figure 2.9: Illustration of the estimation of a new state in the KF based on an initial state estimate and a measurement adapted from [95]. The pink curve represents the updated distribution after combining prediction and measurement.

uncorrelated, mean-free, Gaussian, white noise. $\mathbf{z}$ is the measured output [94].

$$\mathbf{x}_{k+1} = \mathbf{A}\mathbf{x}_k + \mathbf{B}\mathbf{u}_k + \mathbf{w}_k \tag{2.12}$$

$$\mathbf{z}_k = \mathbf{H}\mathbf{x}_k + \mathbf{v}_k \tag{2.13}$$

The filter operates in two successive steps, prediction and update. These steps are described mathematically in Supplementary Material A.1 and are thoroughly discussed in literature.

If a Gaussian-distributed state were to be transferred to the next state using a non-linear function, the state would generally not remain Gaussian-distributed. As a result, it would no longer be sufficient to characterize the state using only an expected value and a covariance matrix. To ensure that the principle of the KF is nevertheless also applicable for non-linear systems, a linearization of the model is necessary [93, 95].

The Extended Kalman Filter (EKF) linearizes the model in each step by a first-order Taylor expansion at the position of the expected value of the previous estimate. The probability distribution around the expected value is transferred to the next state using the linearized function. The necessary linearization results in an additional error and the filter is no longer optimal. The computational effort increases for the EKF, since the Jacobian matrices have to be calculated at every iteration [95].

The Unscented Kalman Filter (UKF) describes the Gaussian distribution of the state not by an expected value and a covariance matrix, as it is the case in the KF or EKF, but by a few selected sample points. These sample points, also known as sigma points, are then transferred to the next state with the non-linearized model using an unscented

transformation. The transformed sigma points describe the new probability distribution of the state. [96]

2.5 Statistics

Statistical analysis employs various indicators to gain a comprehensive understanding of the characteristics of the underlying data distributions. First, the metrics associated with the probability distributions of discrete random variables with finite values are introduced, followed by an introduction of different goodness-of-fit tests. Throughout this work, we use the statistical analysis to gain insights into our field data in Chapter 3, aging data in Chapter 4, and simulation data in Chapter 5.

2.5.1 Statistical Indicators

Mean
When considering a finite sample set with N elements, the mean value, also known as the arithmetic mean, is calculated using Equation (2.14). [97–99]

$$\mu = \bar{x} = \frac{1}{N} \sum_{i=1}^{N} x_i \tag{2.14}$$

Median
The median $\tilde{x}$ is the value that divides an ordered set of data points into two equal halves so that 50 % of the values are less than or equal to and 50 % greater than or equal to the median. For odd sample sizes, the median is the central value in the ordered list, while for even samples it is the arithmetic mean of the two central values as shown in Equation (2.15). [98, 99]

$$\tilde{x} = \begin{cases} x_{(N+1)/2}, & \text{if } N \text{ is odd,} \\ \frac{1}{2}(x_{N/2} + x_{N/2+1}), & \text{if } N \text{ is even.} \end{cases} \tag{2.15}$$

Variance and standard deviation
The variance, as defined in Equation (2.16), measures the spread of the values of a distribution or a data set around its mean value. It describes how much the individual values deviate on average from their mean value [99]. The unit of variance is the square of the unit of the original variable. The standard deviation (σ), as shown in Equation (2.17), is defined as the square root of the variance. Its unit is identical to that of the original variable and the mean value, which is why it is often preferred for statistical analyses, as it can be interpreted more intuitively.

$$\sigma_x^2 = \frac{1}{N}\sum_{i=1}^{N}(x_i - \bar{x})^2 \tag{2.16}$$

$$\sigma_x = \sqrt{\sigma_x^2} \tag{2.17}$$

Equation (2.16) describes the population variance, valid when the entire dataset is available. For a sample, however, the denominator is instead $N - 1$ (Bessel's correction) to obtain an unbiased estimate of the population variance.

Quantile
An α-quantile, is defined as the value $Q_\alpha(x)$ for which at least one proportion αN of the data is less than or equal to $Q_\alpha(x)$ and at least one proportion $(1-\alpha)\cdot N$ of the data is greater [98]:

$$Q_\alpha(x) = \begin{cases} x_{\lfloor \alpha N \rfloor + 1} & \text{if } \alpha \cdot N \notin \mathbb{N}, \\ \frac{1}{2}\left(x_{\alpha N} + x_{\alpha N + 1}\right) & \text{if } \alpha \cdot N \in \mathbb{N}. \end{cases} \tag{2.18}$$

The median $\tilde{x}$ can also be referred to as the 0.5 quantile $Q_{0.5}(x)$. [98]

Skewness and kurtosis
Skewness and kurtosis are two indicators that provide insights into the shape and symmetry of distributions [100]. The skewness, which is defined according to Equation (2.19), quantifies the extent of asymmetry around the mean value in a distribution, indicating whether it is skewed to the left or right [98, 99].

$$\gamma_1[x] = \langle (\frac{x - \bar{x}}{\sigma_x})^3 \rangle \tag{2.19}$$

Positive skewness indicates that the distribution possesses a longer tail on the right side, whereas negative skewness signifies a longer tail on the left side [98, 99]. Symmetric distributions, such as the normal distribution, have a skewness of 0. Kurtosis measures the degree of peakedness or flatness of a distribution in comparison to a normal distribution and is defined according to Equation (2.20) [99, 100].

$$\beta_1[x] = \langle (\frac{x - \bar{x}}{\sigma_x})^4 \rangle \tag{2.20}$$

Confidence interval
A confidence interval is a range of values within which a population parameter is likely to fall, with the level of confidence representing the percentage of intervals that would contain the parameter if the sampling process were repeated numerous times. For instance,

a confidence interval of (1-α)·100 % means that when taking many random samples from the population, approximately (1-α)·100 % of the resulting intervals would contain the true population parameter. A confidence interval consists of two so-called confidence limits, between which the population parameter is expected to lie [101].

2.5.2 Probability Density Functions

Frequency distributions can be represented visually using bar charts or histograms. In probability theory, a probability mass function indicates the likelihood of a discrete random variable assuming specific values. For continuous random variables, the probability of falling within a specific range is represented by the area under the probability density function (pdf). [98] Generally, the pdf p_X is defined as follows, where F_X is the culumative distribution function (cdf) [98]:

$$F_X(u) = \int_{-\infty}^{u} p_X(\xi) d\xi \tag{2.21}$$

In practice, the exact shape of a pdf is often unknown and must be estimated from data. A common non-parametric approach is the kernel density estimation (kde), which provides a smooth estimate of the underlying probability density. For bandwidths $h_1, \ldots, h_N \in (0, \infty)$, the kde is defined as [98]:

$$p_{h_1,\ldots,h_N}(u) = \sum_{n=1}^{N} \frac{1}{N h_n} K\left(\frac{u - x_n}{h_n}\right) \tag{2.22}$$

Here, K is the kernel, a nonnegative, even function whose integral from $-\infty$ to ∞ equals 1. In this work, we use a Gaussian kernel, which is defined as [98]:

$$K(u) = \frac{1}{\sqrt{2\Pi}} exp[-0.5u^2] \tag{2.23}$$

While the kde is flexible and does not assume a specific parametric form, it is inherently descriptive, thus it reproduces the observed data but is not easily used for analytical calculations, or integrated into models. Therefore, in addition to kde, field data is also fitted to standard theoretical distributions such as normal, lognormal, Weibull, exponential, gamma, and beta distributions. These parametric functions provide interpretable parameters, and allow generalization beyond the observed data. Figure 2.10 provides an overview of the shapes of these theoretical distributions dependent on different parameter configurations. The mathematical definitions are provided in the following based on Lista [97] and Mouais et al. [102].

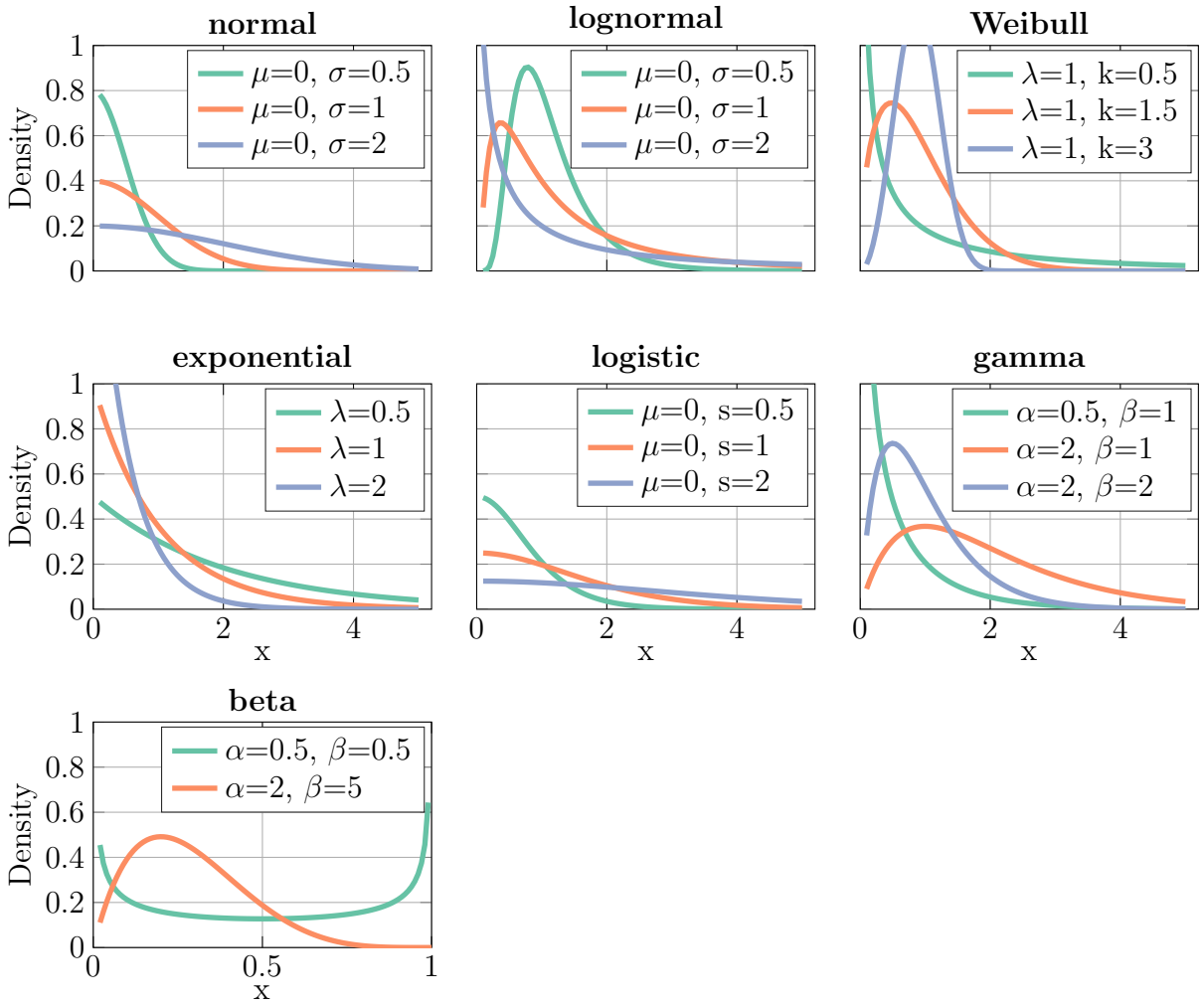

Figure 2.10: Exemplary parameter variation for the considered pdfs.

The normal distribution is defined for $x \in (-\infty, \infty)$, where $\mu \in \mathbb{R}$ and $\sigma > 0$ represent the arithmetic mean and σ, respectively:

$$p_n(x; \mu, \sigma) = \frac{1}{\sigma\sqrt{2\pi}} exp[-\frac{(x-\mu)^2}{2\sigma^2}] \tag{2.24}$$

The normal distribution is symmetric around its mean and has two inflection points at $x = \mu \pm \sigma$. It is commonly used to model symmetric variations around a mean, such as differences in initial battery performance.

The lognormal distribution p_{ln} has the following pdf for $x > 0$ where $Y = ln(X)$ follows a normal distribution:

$$p_{ln}(x;\mu,\sigma) = \frac{1}{x\sigma\sqrt{2\pi}} exp[-\frac{(ln(x)-\mu)^2}{2\sigma^2}] \tag{2.25}$$

Here, μ and σ denote the mean and standard deviation of the variable $Y = ln(X)$. The lognormal distribution has been commonly employed for product lifetime analysis [102].

Especially in the scope of failure analysis, the Weibull distribution is a common model and has been analyzed for the lifetime modeling of batteries [103]. The pdf of the Weibull distribution is defined for $x > 0$ as described in Equation (2.26), where the scale parameter $\lambda > 0$ and the shape parameter $\beta > 0$:

$$p_w(x;k,\lambda) = \frac{\beta}{\lambda}\left(\frac{x}{\lambda}\right)^{\beta-1} exp[-\left(\frac{x}{\lambda}\right)^{\beta}] \tag{2.26}$$

The scale parameter λ determines the steepness of the failure density distribution curve, and β affects the geometric shape of the pdf [102].

The exponential distribution for $x \geq 0$ is expressed as follows where λ describes a constant, positive normalization factor:

$$p_e(x;\lambda) = \lambda exp[-\lambda x] \tag{2.27}$$

It models positive data with a constant hazard rate, meaning that the probability of an event occurring is independent of the elapsed time.

The logistic distribution has the following pdf for the scale factor $s > 0$:

$$p_l(x;\mu,s) = \frac{exp[\frac{-(x-\mu)}{s}]}{s(1+exp[\frac{-(x-\mu)}{s}])^2} \tag{2.28}$$

The logistic distribution models data with a symmetric distribution that has heavier tails than the normal distribution.

The gamma distribution is defined for $x > 0$ as follows, where α and β are positive values:

$$p_g(x;\alpha,\beta) = \frac{\beta^\alpha x^{\alpha-1} exp[-\beta x]}{\Gamma(\alpha)} \tag{2.29}$$

The gamma distribution models positive and right-skewed quantities, such as accumulated capacity loss, and can represent varying levels of skewness.

The beta distribution can be described as follows, where $x \in [0,1]$ and the shape factors $\alpha,\beta > 0$:

$$p_b(x;\alpha,\beta) = \frac{x^{\alpha-1}(1-x)^{\beta-1}}{B(\alpha,\beta)} \tag{2.30}$$

$B(\alpha,\beta)$ is the Beta function, which serves as a normalization factor. The beta distribution is symmetric for $\alpha = \beta$. The beta distribution models data constrained to a finite interval, such as normalized SOH and can capture symmetric or skewed behaviors.

2.5.3 Goodness of Fit

As a complement to graphical analyses of a distributional fit, goodness-of-fit tests assess the deviations between data points and density curves, generating characteristic values that allow for a comparison of different fitting methods. We use these tests in Chapter 3 to analyze the fitting results of SOH values to different theoretical distribution functions.

The residual sum of squares (RSS) is defined as the sum of the squared deviation of the expected probability and the accurate probability that a specific SOH value occurs:

$$RSS = \sum_{i=1}^{n} (y_i - \hat{y}_i)^2 \tag{2.31}$$

In our application example of assessing the fit of distribution functions to our SOH field data, y_i represents an observed SOH value, and $\hat{y}_i$ the corresponding value predicted by the fitted distribution.

With the Kolmogorov-Smirnov test (KS), we assess the hypothesis that the empirical data is compatible with being randomly extracted from a given theoretical pdf. We then state the null hypothesis $H_0 : F_N(x) = F(x)$ and the alternative hypothesis $H_1 : F_N(x) \neq F(x)$, where $F_N(x)$ is the empirical cdf of the observed SOH values for a cluster, and $F(x)$ is the cdf of a fitted theoretical distribution (e.g., normal, lognormal). The KS statistic represents the largest vertical difference between the empirical and theoretical cdf and is defined as:

$$D_N = \sup_x |F_N(x) - F(x)| \tag{2.32}$$

D_N is then compared to a critical value that depends on the number of values and the significance level. The critical value can be calculated according to Rithatgi and Saleh [104]. If the supremum is higher than the critical value, the null hypothesis is rejected, and it can be assumed that the observed data does not belong to the respective theoretical distribution. If the supremum is lower than the critical value, the null hypothesis is not rejected based on a significance level and it can be assumed that the empirical distribution follows the specific theoretical distribution function. However, it's essential to consider the potential impact of a Type II error that arises when we fail to reject a false null hypothesis [101]. This means that despite the empirical distribution not adhering to the

theoretical distribution function under consideration, our hypothesis test fails to detect this deviation, resulting in a false non-rejection of the null hypothesis.

Other goodness-of-fit tests, such as the Cramér-von-Mises [105] and Chi-Square [106, 107] tests, are also commonly employed to evaluate the agreement between empirical and theoretical distributions. In this work, we focus on the KS test, which provides a robust measure of the maximum deviation between the empirical and theoretical cdfs, together with the RSS, which quantifies the overall squared deviations.

3 Lithium-Ion Battery Aging during Vehicle Operation

To evaluate the drop-in potential of SIBs as possible replacements for LIBs within a specific application, it is first necessary to understand the specific requirements of the intended use case and assess whether a specific SIB can meet them. Early adoption will likely occur in applications where cost reduction is particularly relevant, such as systems currently relying on expensive high-power NMC/LTO batteries. Commercial SIBs typically offer high power capability [12] and have the potential for lower costs, making them a promising alternative for these applications. Accordingly, this chapter establishes the foundation for evaluating SIBs in such contexts by identifying and analyzing the operational conditions (e.g., current, SOC, and temperature ranges) and lifetime requirements encountered in a high-power mobile application. In Chapter 4, we then investigate whether a commercial SIB can fulfill these lifetime requirements under application-relevant conditions and discuss specific aging characteristics that must be considered before integration. The identified operating conditions additionally serve as the basis for Chapter 5, where the on-board diagnostic performance of SIBs is evaluated under application-relevant scenarios.

Operational data is rarely publicly available, even though it forms the foundation for understanding system requirements. To bridge this gap, we collaborated with a car manufacturer to analyze an entire global vehicle fleet equipped with LIB NMC/LTO systems. Our analysis is based on an extensive field dataset of 600,000 batteries in a 48 V application. Moreover, we introduce an anomaly detection framework for SOH values, which identifies batteries with atypical aging and provides manufacturers with a systematic way to rapidly assess in-field battery degradation and support reliability decisions.

The subsequent analyses have been published as a peer-reviewed article in the Journal *Cell Reports Physical Science* under the title "Detection of abnormal SOH estimates in battery field data using statistical learning"[108].

3.1 Variability in Battery Aging

Field observations show that the aging behavior of individual cells varies significantly. This so-called cell-to-cell variance can stem from an array of influencing factors, encompassing

distinct operating conditions, environmental variables, usage patterns, production-related inconsistencies [109–111], and the presence of corrupted software versions.

The production of battery cells involves a long and complex process chain as described in [112]. In principle, any manufacturing-related variation in cells results from fluctuations in process or material parameters [113]. Depending on the extent of these fluctuations, the impact on battery performance can range from slightly accelerated aging to severe and safety-critical cell failures [111, 114]. To mitigate these risks, End-of-Line tests are implemented to ensure a quality standard for battery cells. Common tests include measurements of voltage, voltage drop over time, capacity, and impedance [113, 115]. However, a certain degree of statistical variation in cell quality remains unavoidable, manifesting in differences in initial performance as well as aging behavior over time [111]. For instance, Ank et al. [113] demonstrated that even under highly consistent process conditions, an initial standard deviation of approximately 25 % in internal resistance and 10 % in capacity can still occur. Notably, this study did not include any cells that were rejected based on End-of-Line tests. Beyond initial performance variation, further differences emerge over time. Baumhöfer et al. aged 48 cells under nearly identical environmental and cycling conditions [116]. Their study revealed substantial inter- and intra-cycle differences. Similar to Ank et al., an initial variation in quality was observed, but with capacity deviations below 1 %. It is important to note that these were commercial cells subjected to End-of-Line quality testing and sorting. However, as aging progressed, variance increased significantly. Particularly striking was the lack of a clear correlation between initial capacity and the value after 1200 cycles, highlighting the complexity and sensitivity of battery aging.

Cells age differently not only due to inherent manufacturing variations but also because of multiple degradation mechanisms occurring simultaneously [62]. These mechanisms are strongly influenced by external conditions and usage patterns, such as temperature, SOC, C-Rate, and DOD [58]. Temperature is a significant factor affecting battery aging [117]: At low temperatures, graphite-based cells are susceptible to lithium plating, which negatively impacts both degradation and safety [117]. In contrast, high temperatures accelerate SEI growth and structural changes [117]. Beyond SEI growth, elevated temperatures also accelerate cathode degradation and the breakdown of inactive materials, such as binders. Schmalstieg et al. demonstrated that high temperatures are the primary external factor driving calendar aging [118]. Typically, battery degradation occurs up to ten times faster at elevated temperatures compared to operation at 25 °C [60]. Additionally, high current rates accelerate aging, primarily due to the anode's capacity limitations, which can lead to lithium plating and structural deterioration [59, 60]. Furthermore, ohmic losses and temperature might increase which can accelerate degradation [119]. This effect is particularly relevant for high-power applications, where batteries are exposed to extremely high currents. While high currents and elevated temperatures drive battery degradation, the way a battery is cycled also plays a crucial role in its longevity. Von Geslin et al. observed lifespan extensions of up to 38 % for dynamic cycling compared to constant current tests, despite identical average current and voltage limits [120]. This suggests that laboratory-based battery lifetime assessments tend to be highly con-

servative. The impact of DOD on cycle life varies significantly depending on the cathode material used [60]. According to the Wöhler curve, the lifetime increases with decreasing DOD [121].

In addition to environmental conditions and production tolerances, variation in battery aging can also arise from faulty estimations. Therefore, field data based on measured and estimated BMS values may be inaccurate if the models or estimator are flawed, potentially leading to misinterpretation of aging data.

3.2 Vehicle Field Data

As the advent of the information age, the advancement of big data technologies opens up opportunities for precise monitoring of the battery pack health status [122, 123]. Consequently, car manufacturers collect real-world customer field data by accessing the BMS memory, specifically the estimated SOH and relevant characteristics such as charge throughput, and transmitting it to a centralized data pool for subsequent processing and analysis. This systematic collection of periodic readouts facilitates thorough monitoring of battery operation [124], encompassing various measured signals like temperature, voltage, and current, as well as estimated states such as SOH and SOC.

In the following, we undertake an in-depth examination of a substantial real-world dataset spanning from July 2020 to June 2023 to gain insights into estimated battery aging and system requirements. The dataset comprises 12 million readouts originating from 600,000 customer and prototype vehicles, all equipped with 48 V LIB systems. As a transitional technology, these low-voltage batteries find utility in various vehicle applications, offering fuel economy gains in mild-hybrid vehicles by assisting the combustion engines through boosting and recuperation. Additionally, 48 V batteries play a vital role by providing high current peaks to support systems like roll stabilization, notably alleviating the load on the conventional 12 V battery [125]. In one battery system 20 individual cells are connected in series. The characteristics of the system's lithium-ion cell are depicted in Table 3.1.

Each readout encapsulates a snapshot of the vehicle's load history, comprising an array of vehicle-specific variables, including a hashed identification number, mileage, and the order country, as well as storage variables obtained from the BMS of the LIB. Therefore, this comprehensive battery dataset is constructed from a fusion of measured signals, such as current, temperature, and voltage, alongside estimated variables like SOC and SOH derived from on-board BMS estimation models. The variables encompass both single-value metrics and histogram data. Single-value metrics offer instantaneous insights into accumulating variables, such as energy throughput, (dis)charge counts, and SOH. Conversely, histogram variables are used to characterize time-series data. This compressed representation, driven by hardware limitations and storage constraints, enables efficient storage and analysis of the battery's load history. Examples of histogram variables include

Table 3.1: Specifications of the underlying cell in the dataset [119].

Specification	Unit	Value
Nominal capacity	Ah	10.6
Material cathode	–	NMC
Material anode	–	LTO
Nominal voltage	V	2.2
Upper voltage limit	V	2.65
Lower voltage limit	V	1.9
Max. pulse discharge current (1s)	A	760 (≈72 C)
Max. pulse charge current (1s)	A	520 (≈49 C)
Allowed temperature range	°C	[-30, 70]

the time spent within estimated SOC ranges or charge counts within specific temperature ranges. An initiation of a readout occurs via one of two methods: either during vehicle operation, where it is transmitted over the air, or when the customer visits a service facility. Consequently, the readouts from individual customers exhibit uneven sampling intervals, with an average time span of 28 days between consecutive readouts. Figure 3.1 illustrates the SOH behavior provided by the readouts of three exemplary vehicles.

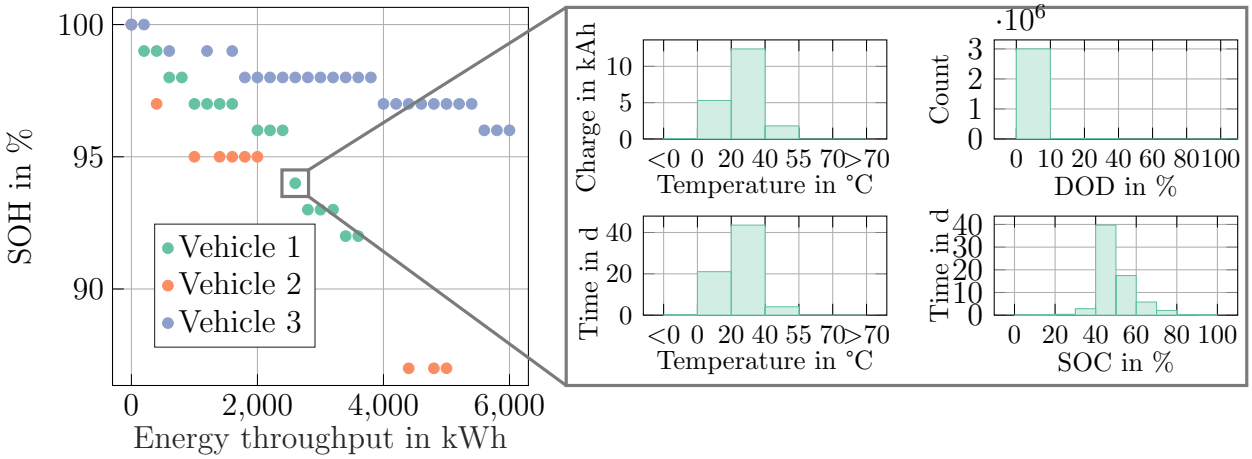

Figure 3.1: Estimated SOH values for three exemplary vehicles across various energy throughputs (left). Each data point corresponds to a singular readout, with SOH values presented as integers. For each readout, the operating conditions in the form of singular values or histograms are recorded (right). The histogram represents counts of values within a range without distinguishing the exact magnitude of each individual value.

Each readout comprises an integer SOH value (left) associated with a set of single and histogram value variables which characterize the load history and operation conditions of

the battery (right). Bank et al. already presented a detailed analysis of the environmental and operational factors for this dataset such as temperature, C-Rate, SOC, and DOD [119] revealing that most values follow an approximately normal distribution within defined operating ranges: Temperatures predominantly range from 10 °C to 40 °C, although values up to 60 °C may occur in warmer regions. The SOC mostly remains between 40 % and 80 %, C-Rate generally stays below 10 C, although occasional higher peaks are observed, and DODs are predominantly under 10 %. These conditions form the basis for the operational assumptions and modeling approaches developed in Chapter 5.

Figure 3.2 shows the trajectories of SOH values for 100 thousand exemplary vehicles.

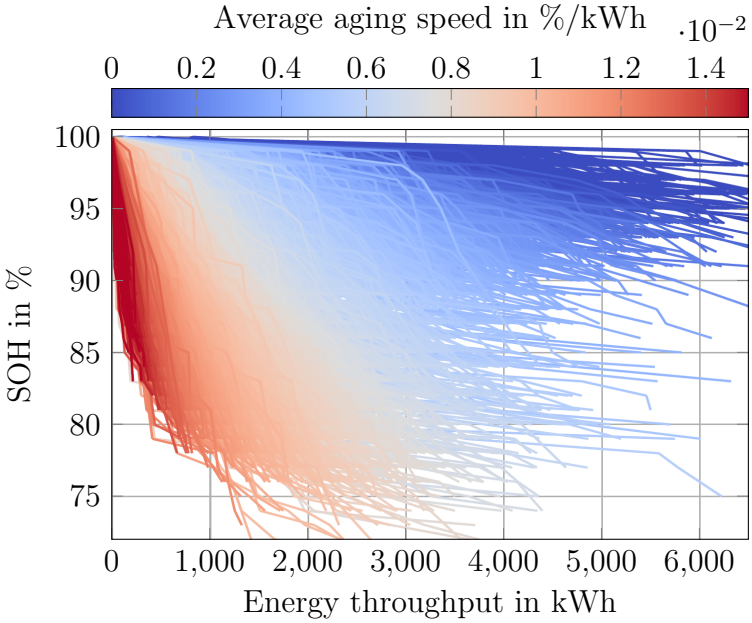

Figure 3.2: SOH trajectories of 100 thousand exemplary batteries over energy throughput. The whole dataset comprises 12 million readouts from 600 thousand vehicles. It is essential to emphasize that the collected SOH values are discrete integers. Thus, we employ linear interpolation for the visualization of continuous SOH values.

While the majority of these trajectories reveal a relatively slow average aging speed, certain trajectories exhibit a notably accelerated aging pace based on the estimated aging values. As described in Section 3.1, this diversity in aging rates can be attributed to an array of influencing factors, encompassing distinct operating conditions, environmental variables, usage patterns, production-related inconsistencies, and the presence of corrupted software versions. Furthermore, there is a noticeable correlation between an increased energy throughput and a broader dispersion of aging trajectories, signifying the impact of usage intensity on battery aging patterns.

In Figure 3.3A, we employ the Gaussian kde, defined in Equation (2.22), to derive prob-

ability curves at predefined energy throughput intervals of 200 kWh. Since SOH values progressively spread over time, the distribution characteristics undergo an evident transformation. They evolve from steep and narrow distributions associated with new batteries to progressively broader distributions characteristic of older batteries. Furthermore, it is noteworthy that all these distributions exhibit a left-skewed asymmetry, reflecting the natural degradation of battery SOH over time and use. The change of distribution characteristics can be quantified with the help of the coefficient of variation [109]. This metric enables to assess variations in the context of a dataset's mean, making it particularly useful for comparing the standard deviation of datasets with differing means. Figure 3.3B shows the deviation of maximum and minimum SOH values in orange and the coefficient of variation, defined as the ratio of σ and μ, in green across different energy throughputs. Generally, the deviation increases with higher energy throughput, considering a decreasing mean. The difference between the minimum and maximum SOH remains relatively constant with increasing energy throughput indicating that for all energy throughputs we have some batteries that exhibit low SOH values.

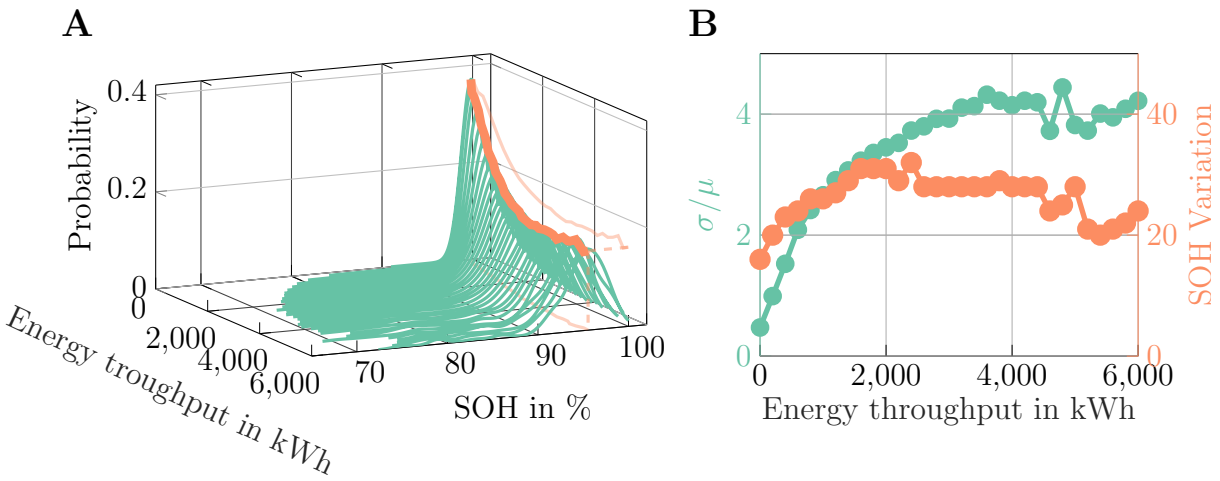

Figure 3.3: Statistical properties of the field dataset.
A: The kdes of SOH values across different energy throughputs exhibit varying distributional characteristics as energy throughput increases.
B: The coefficient of variation, i.e., the ratio of σ to μ, is depicted in green for different energy throughputs. The difference between maximum and minimum SOH is illustrated in orange.

Overall, the batteries can sustain an energy throughput of more than 6,000 kWh over their lifetime in our application, corresponding to approximately 6,000 EFC. At this point, the batteries reach an estimated SOH between 75 % and 98 %. In addition, all batteries exhibit a distinct aging behavior that cannot be explained solely by calendar or cycle aging, highlighting the need to analyze degradation in the context of specific operating conditions.

3.3 Aging Anomaly Detection Framework

Anomaly detection of SOH values enables manufacturers to identify batteries exhibiting atypical aging. By detecting outliers without removing vehicles from service and without requiring prior knowledge, we introduce an anomaly detection framework that is particularly valuable when deploying new battery technologies, offering a systematic and reliable approach for early identification of potential issues. In addition, we use this framework to evaluate the sensitivity of detection performance to the SOH threshold, providing a foundation for assessing whether comparable diagnostic accuracy can be achieved for the investigated SIB. We validate our statistical framework by introducing pseudo SOHs as known outlier data points and by using data from a corrupted prototype software version. An overview of our anomaly detection framework is given in Figure 3.4.

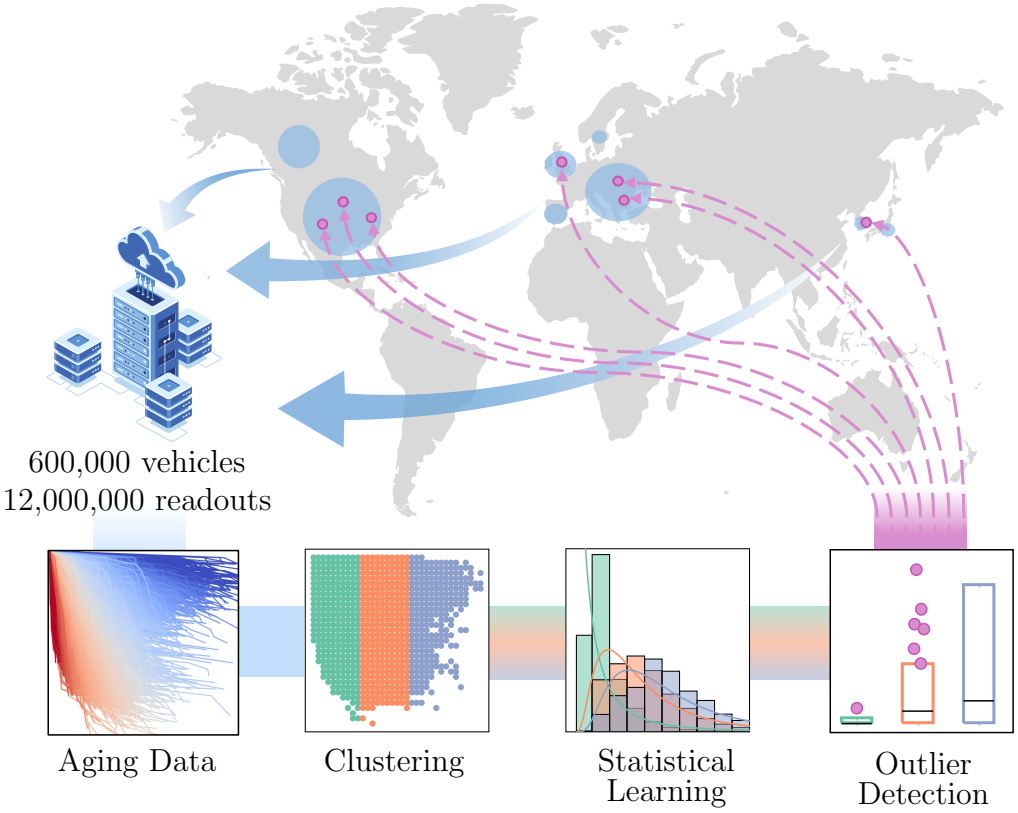

Figure 3.4: Overview of aging anomaly detection framework based on the extensive aging dataset.

The literature provides valuable research on anomaly detection, outlier detection and statistical fault diagnosis, all of which are relevant to battery safety [126–129], quality control [130, 131] and predictive maintenance [132, 133]. Furthermore, researchers analyze real-world vehicle data to build upon insights gained from controlled battery experiments and employ statistical methods for advanced diagnosis [124, 134]. In particular, the field of

statistical learning, which focuses on inferring statistical properties from data, has seen increased adoption in the analysis of battery data [103, 135, 136]. However, existing research does not focus on real-world aging-related data, instead, it investigates algorithms designed for outlier detection through the analysis of measured time-series data [137]. Such data fundamentally differs from field aging data by a high sample frequency and the characterization of variables in the time domain. In contrast, field data contains a relatively low number of readouts per vehicle and includes compression of time-series variables to the histogram and single-value data. Hence, the adoption of existing algorithms on field aging data appears impractical. Moreover, conventional statistical outlier detection methods tend to isolate data within individual vehicles, treating each one as a distinct experiment. Consequently, there exists a need for an unsupervised method that thrives on the increasing volume of data it encounters. Such a method can fulfill the role of a robust monitoring system for field battery aging data, serving as a foundational component of predictive maintenance strategies.

3.3.1 Load-History-Related Clustering

To account for various operation conditions and usage-patterns in our field data, we conduct a load-history-related clustering. Clustering, in general, is an unsupervised learning task that aims to find distinct groups in data called clusters. Instead of density-based clustering methods, we utilize a grid-based approach to account for physical aspects with regard to battery aging instead of quantitative accumulations of SOH values. Such a grid-based approach groups data points within the same value range of clustering variables irrespective of the proximity of neighboring data points. In contrast, DBSCAN or DENCLUE, both representatives of unsupervised density-based clustering methods, group data points that share the same area of akin data density [138]. While those methods can be applied to directly detect outliers by localizing isolated data points, detections do not necessarily exhibit anomalous battery aging but also unique operational behavior [139, 140]. Moreover, density-based constructed clusters would not ensure comparability over the load history since no spatial restriction is given. Consequently, values within the same cluster would not necessarily provide a similar load history with regard to battery aging. Therefore, we apply a spatially restricted grid-based approach.

Previously, the representation of SOH distributions in Figure 3.3A solely accounts for the variability of SOH values with respect to the energy throughput by neglecting potential influences from temperature or SOC on battery aging. To account for further relevant operation conditions, Table 3.2 lists available BMS variables from the field data readouts. Notably, histogram variables encompass multiple values within corresponding bin ranges and are pre-determined by the car or BMS manufacturer.

For instance, the histogram variable *time_soc_x* incorporates ten values to represent the time spent in SOC ranges such as 0 %-10 %, 10 %-20 %, ..., 90 %-100 %. To streamline the clustering process, we extract the most relevant information from all bin values by

Table 3.2: Available clustering features from field data readouts. Histogram variables comprise multiple bins for the respective variable range.

Name	Description	Unit
energy_throughput	Total battery energy throughput until readout	kWh
mileage	Driven mileage until readout	km
$time\_soc\_x_1, \ldots,$ $time\_soc\_x_{10}$	Time spent in SOC range $x \in [0, 10, 20, \ldots, 100]$ %	d
$time\_temp\_x_1, \ldots,$ $time\_temp\_x_6$	Time spent in temperature range $x \in [< 0, 0, 20, \ldots, > 70]$ °C	d
$charge\_temp\_x_1, \ldots,$ $charge\_temp\_x_6$	Charge throughput in temperature range $x \in [< 0, 0, 20, \ldots, > 70]$ °C	kAh

employing Principal Component Analysis (PCA) on each histogram variable. PCA applies a linear transformation on the data, aligning the first component of the new coordinate system with the direction of maximum variance of the data. The transformation of the PCA can be derived from the following assumptions: Consider a data matrix X of dimensions $n \times m$, where each row signifies a variable, and each column represents a sample from that variable. The covariance matrix C_X captures both the variance of individual variables along its diagonal and the covariances between pairs of variables in its off-diagonal elements. Variances indicate the degree of dispersion within a variable, while covariances denote the linear relationship between pairs of variables. Ideally, the covariance matrix of transformed variables should possess exclusively diagonal values. This configuration maximizes the information content along the axis directions while minimizing redundant information. By that, the dimensionality of the data can be reduced by selecting the first n principal components with maximum variance.

To illustrate the use of PCA for clustering our battery field data, we consider a simplified and schematic example for the histogram variable *time_soc_x* comprising ten bins. Each bin represents the time spent in a specific SOC range. First, the data are centered by subtracting the mean of each SOC bin. Next, the covariance matrix is computed to quantify how SOC bins co-vary, revealing patterns such as which ranges tend to increase or decrease simultaneously. Eigenvalue decomposition of the covariance matrix then defines the principal components, with the first component (PC1) capturing the largest variation in the dataset. Conceptually, this can be seen as a rotation of the original axes, aligning the new axis along the direction of maximum variance. Each battery can be represented by a single score along PC1, which summarizes its overall SOC-time behavior for the variable *time_soc_x*. Batteries with similar scores for this variable exhibit similar operational patterns, while differences in the scores highlight distinctions in SOC usage that are not evident from the original histogram bins. We represent each histogram variable from a battery readout exclusively using its first principal component. It is important to emphasize that principal components lack physical interpretations and, therefore, cannot be expressed in units corresponding to their original variables. To validate the quality of

the data reduction process, the amount of information covered in the original data has to be analyzed. Since the size of the eigenvalue represents the degree of dispersion along the corresponding eigenvector, the quotient of the i^{th} eigenvalue and the sum of all remaining eigenvalues quantifies the amount of explained variance of the considered eigenvector. As shown in Figure 3.5A, the amount of explained variance ranges from 0.72 to 0.82 when employing only the first principal component.

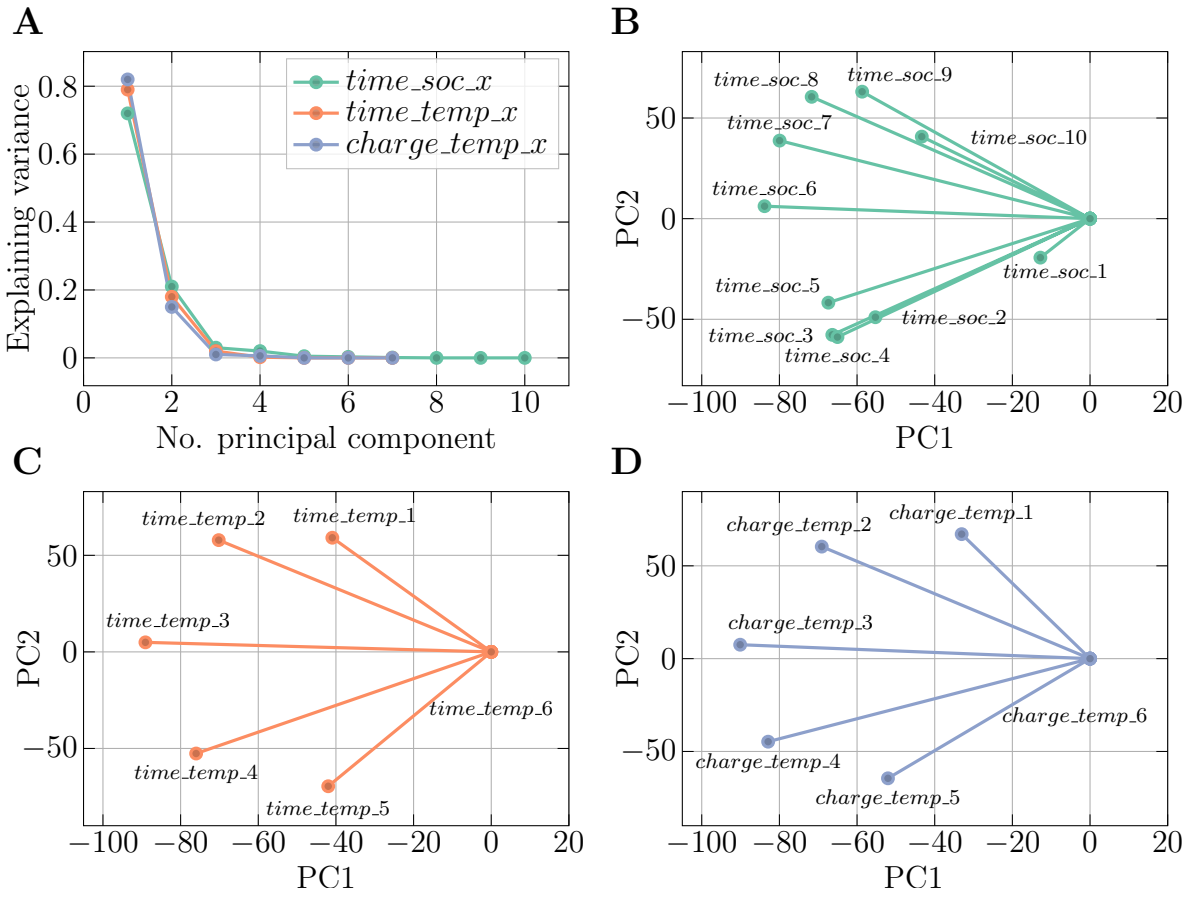

Figure 3.5: Features of the PCA.
A: Explaining variance over the number of principal components. The first principal component provides an explaining variance of around 0.8 for all variables.
B-D: Loading plots of the original data for the first two principal components PC1 and PC2. Main operating points (operation between 50 and 60 % SOC, 20 °C to 40 °C) of the 48 V battery have higher absolute loadings on PC1. Table 3.2 lists the definitions of the variables.

As the histogram variable *time_soc_x* comprises ten bin ranges, its first principal component provides the least explaining variance with 0.72, in contrast to *time_temp_x* and *charge_temp_x* which both comprise six bin ranges and therefore reach an explaining variance of around 0.8. Furthermore, we investigate the influence of original variables on the

principal components by computing the loading matrix $\boldsymbol{L}$ defined as the covariance of the principal components and the original data. The loading of an original variable can be computed by the product of the eigenvectors times the square root of the eigenvalues, which denote the weight of their corresponding eigenvector: $\boldsymbol{L} = \boldsymbol{V}\sqrt{\boldsymbol{\Lambda}}$. Now, selecting the i^{th} row of the loading matrix yields the loadings of the i^{th} original variable for all principal components. The results can be found in Figure 3.5B-D where a greater absolute value of the original variable loading represents a stronger influence of that variable on the respective principal component. This unveils a dominant influence of primary operating points of the 48 V battery, such as an SOC range of 50 % – 60 % on the first principal component.

Overall, we identified the features in our field dataset that characterize the load history, consisting of both single values and histogram-based features with multiple bins. To reduce the dimensionality of the histogram features, we applied PCA and demonstrate that the first principal component captures sufficient information for subsequent clustering.

3.3.1.1 Set of Cluster Variables

To account for similar operating conditions within a cluster, it is necessary to identify suitable clustering variables and assign each an optimal step size that defines how continuous values are discretized. This ensures that readouts falling within the same grid cell share comparable conditions and can be meaningfully analyzed together. Ideally, for such an approach, a cluster variable with an appropriate step size should yield evenly sized clusters across the entire value range of that variable. In contrast, a poor clustering variable would provide a few clusters that contain the majority of data points and an abundance of empty clusters. To assess the quality of a clustering variable, we investigate the distribution of cluster sizes for a given step size of that variable with the number of resulting clusters n, the mean of cluster sizes μ and the standard deviation of cluster sizes σ. In this context, the cluster size refers to the number of readouts a cluster contains but not to the range of SOH values it comprises. Since we opt for evenly distributed cluster sizes, a small standard deviation is desired as it indicates a low dispersion of cluster sizes around their mean. The tree diagram in Figure 3.6 illustrates the number of resulting clusters n, along with the mean μ and σ of cluster sizes for all possible variable combinations.

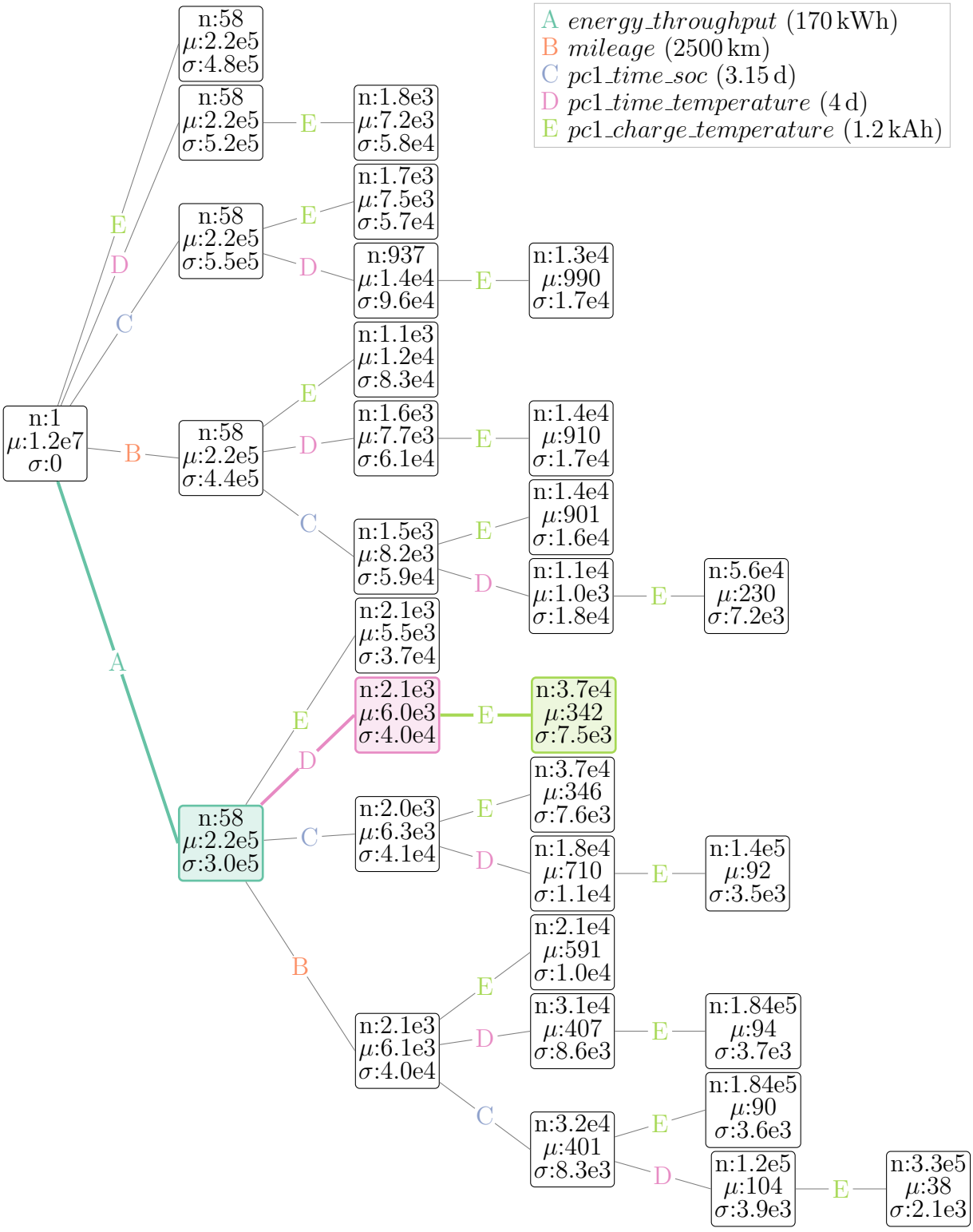

Figure 3.6: Number of resulting clusters n as well as mean μ and σ of cluster sizes for all feature variable combinations. To ensure an equal distribution of cluster sizes, we opt for a small σ, meaning we want clusters with a high number of readouts. Consequently, we choose the variable combination A-D-E for the clustering of vehicle readouts.

We selected a step size of 170 kWh for energy throughput, 2500 km for mileage, 3.15 days for *pc1_time_soc*, 4 days for *pc1_time_temp* and 1.2 kAh for *pc1_charge_temp* so that each variable yields the same number of clusters ($n = 58$) in the first step. Since we consider a total of five cluster variables, five stages of combinations are possible where duplicates have been omitted for the sake of clarity. The root node of the tree diagram represents all available readouts before clustering. Hence, it comprises one cluster ($n = 1$), which holds all available readouts ($\mu = 1.2e7$). In the first stage, readouts get clustered by one variable only to assess the clustering performance of each individual variable. It shows that *pc1_time_soc* (C) yields the highest σ of cluster sizes whereas *energy_throughput* provides the lowest one and therefore ensures a more even distribution of cluster sizes around the mean μ. To identify the top three clustering variables, we follow the path of minimum standard deviation and select the combination A–D–E (order irrelevant), corresponding to *energy_throughput*, *pc1_time_temp*, and *pc1_charge_temp*. These variables ensure that the resulting clusters are as balanced in size as possible.

3.3.1.2 Step Size of Cluster Variables

In addition to the feature set selection, a feasible step size for each variable has to be determined so that readouts within that value range are grouped together. To ensure physically meaningful step sizes for the PCA variables we first round each histogram variable to the nearest multiple of its step size before applying the PCA. Since battery readouts within a cluster are assumed to share comparable load histories with respect to the feature variable, an excessively large step size may lead to the clustering of inconsistent vehicle readouts, while choosing an overly small step size can result in narrow clusters that contain insufficient readouts for the statistical validity of our model.

In order to determine the optimal selection of step sizes quantitatively, we apply an iterative method that continuously decreases the step size of each cluster variable and checks the acceptance of a robustness condition across all data points. Based on the 1 % integer sampling of SOH values, we define the 95 % confidence interval range W around the estimated mean of each cluster to be less than 0.5 % as a condition for statistical robustness, given as follows:

$$W = \frac{t_{95}\sigma}{\sqrt{n}} < 0.5\%. \tag{3.1}$$

with t_{95} as the 95 % T-score from the Student's t distribution, σ as the estimated standard distribution and n as the sample size from each cluster. Here, we use the Student's t distribution instead of the Gaussian since both the variance and the mean are estimated from each cluster. As given by Equation (3.1), the confidence range W increases with a higher σ of a cluster and decreases with a larger cluster size. Next, we iteratively decrease the stepsize from each cluster variable starting at 500 kWh for *energy_throughput*, 20 d for *pc1_time_temp*, and 5 kAh for *pc1_charge_temp* respectively, as long as the above condition is met for 99 % of all data points. Table 3.3 lists an excerpt for the resulting condition acceptance when varying the step size of each cluster variable.

Table 3.3: Excerpt of resulting acceptance from Equation 3.1 across all data points for different step sizes. The chosen step sizes across the features are colored in .

energy_throughput	*pc*1_*time_temp*	*pc*1_*charge_temp*	acceptance
500 kWh	20 d	5 kAh	99.37 %
500 kWh	15 d	4 kAh	99.05 %
400 kWh	20 d	3 kAh	99.10 %
400 kWh	15 d	2 kAh	98.67 %
300 kWh	20 d	3 kAh	98.95 %
300 kWh	15 d	1 kAh	98.53 %
200 kWh	15 d	1 kAh	98.26 %

The smallest cluster configuration that would yield a 99 % acceptance across all data points of a total of 949 resulting clusters is 300 kWh for *energy_throughput*, 15 d for *pc*1_*time_temp*, and 1 kAh for *pc*1_*charge_temp* and will therefore be used for the grid clustering.

With this clustering approach, the field data can now be assessed in the context of the operating conditions. To this end, we identified three features for clustering the data, namely *energy_throughput*, *pc*1_*time_soc*, and *pc*1_*charge_temp*. For each feature, an appropriate step size was determined to group the data accordingly.

3.3.2 Statistical Modeling Considering Usage Patterns

To capture the statistical characteristics of battery aging across the fleet, it is essential to select a pdf that closely matches the observed empirical distributions within each cluster. We assess the suitability of several pdfs, including normal, lognormal, Weibull, exponential, gamma, and beta distributions, which are detailed in Section 2.5.2. To fit these theoretical distribution functions, we employ General Maximum-Likelihood-Estimates.

While many theoretical distribution functions typically exhibit a right-skewed pattern, our battery field data presents distinct left-skewed distributional characteristics stemming from the decreasing SOH values upon aging. To ensure an appropriate fit, we perform fitting and assess pdfs for the ΔSOH values defined as follows:

$$\Delta SOH = 100\,\% - SOH. \tag{3.2}$$

Figure 3.7 showcases the empirical data alongside fitted distribution functions for ΔSOH, considering two exemplary energy throughput scenarios at 600 kWh and 6,000 kWh respectively.

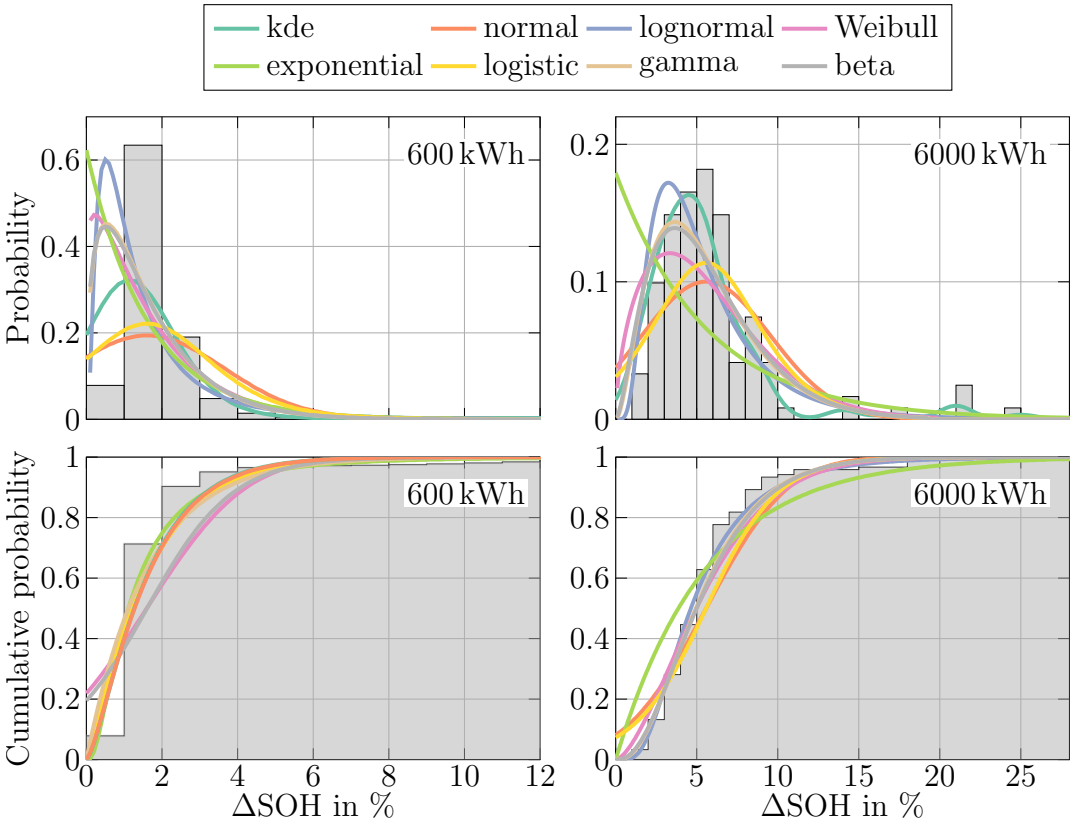

Figure 3.7: Various distribution functions are fitted to the empirical data, which is represented by the histogram in gray. As the majority of the theoretical pdfs are right-skewed, we analyze the pdfs and cdfs for ΔSOH values.

Notably, at lower energy throughputs, a majority of batteries exhibit high SOH values, implying a low ΔSOH. However, as the SOH decreases, the empirical data becomes increasingly diverse, resulting in a broader spectrum of SOH values and a more favorable fit for pdfs. This shift in distributional characteristics with progressive aging underscores the inherent diversity in the aging behaviors of batteries within the field data. Nevertheless, it's important to acknowledge that the field data's aging values are estimated and are susceptible to estimator inaccuracies.

The Cullen-Frey diagram is widely used to visually compare the distributional characteristics of the dataset and evaluate its fit to specific distribution functions. Figure 3.8 illustrates the Cullen-Frey graph for the seven distribution functions described in Section 2.5.2. Each data point represents the kurtosis and squared skewness of the empirical distribution of SOH values for a given energy throughput. By evaluating the placement of these data points within the Cullen-Frey diagram, we visually assess the goodness of fit between the observed data and the particular pdf, gaining insights into the underlying distributional properties. While the normal, logistic, and exponential distribution functions exhibit constant skewness and kurtosis values, the beta, lognormal, gamma, and Weibull distributions introduce varying shape parameters that yield different kurtosis and skew-

ness values. It is visible that the underlying empirical distribution has a diverse range of distributional shapes. Hence, a pdf is necessary that allows for flexible modeling of the different empirical distributions across various energy throughput scenarios.

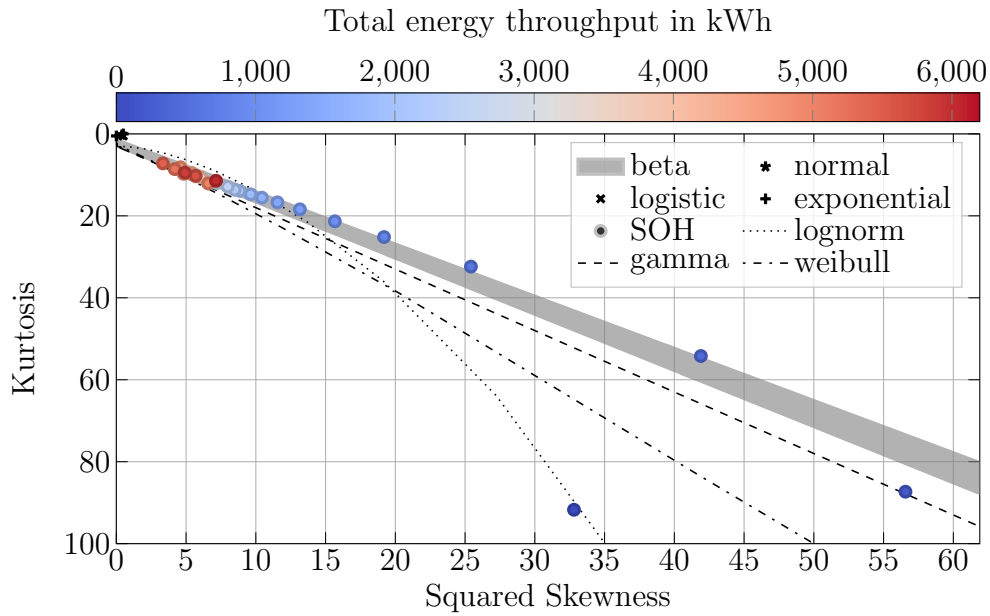

Figure 3.8: Cullen-Frey graph showing the distributional character of different pdfs and the dataset. The points represent the dataset, while the lines indicate the relationships between squared skewness and kurtosis for the theoretical distributions. The position of the dataset points relative to these lines provides an indication of which distribution function may best describe the data.

As a complementary approach to the graphical examination of the distributional fit, we employ analytical methods to assess the goodness of fit. To quantitatively evaluate how well the empirical distribution fits with various pdfs, we employ two statistical metrics: the RSS and the KS test, both described in Section 2.5.3. The results of these two goodness-of-fit assessments are depicted in Figure 3.9. In Figure 3.9A, the RSS for each fitted pdf is displayed, with scatter points illustrating RSS values across different energy throughput scenarios. Notably, the RSS values for lognormal, Weibull, gamma, and beta distributions are lower compared to the other distribution functions. Table 3.4 confirms this by additionally revealing that the mean and the median RSS values for various energy throughput scenarios are lowest for the lognormal distribution. Figure 3.9B presents the KS test results for different theoretical distributions, considering varying energy throughputs. Remarkably, for lower energy throughput scenarios ($< 1000\,\mathrm{kWh}$), it becomes apparent that none of the given distribution functions can feasibly fit the distributional characteristics of the empirical data. Consequently, for all pdfs, the null hypothesis that the data follows the respective distribution is rejected at a significance level of $\alpha = 0.1$. However, as we move to higher energy throughput scenarios, the null hypothesis is not rejected for the lognormal, Weibull, gamma, and beta functions.

The lognormal distribution consistently exhibits superior fitting performance when com-

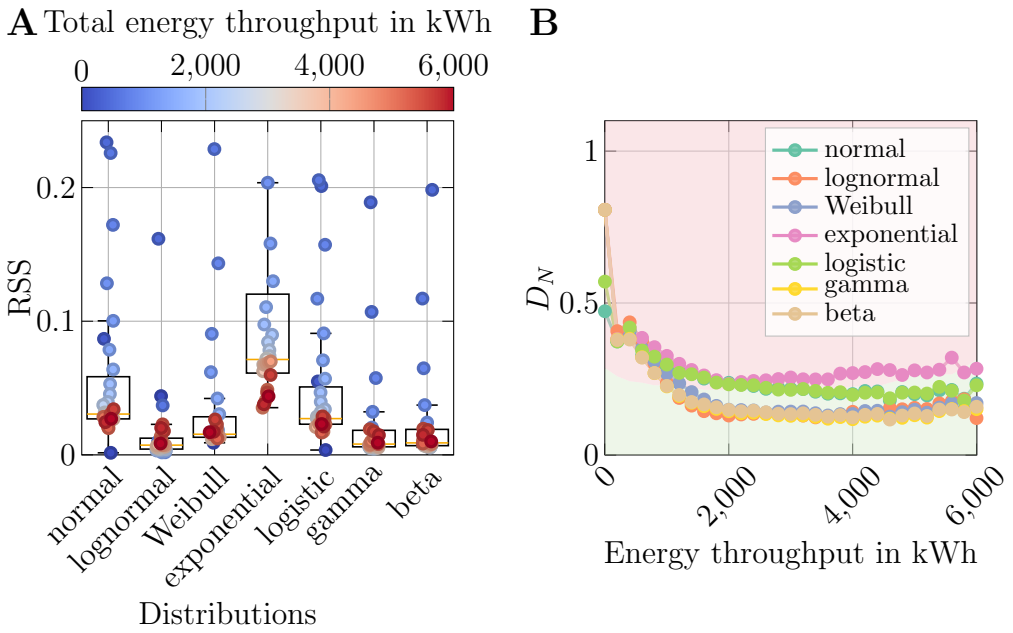

Figure 3.9: Results of goodness-of-fit tests.
A: Boxplot that visualizes the RSS for the different theoretical distributions. The data points depict the RSS for different energy throughputs.
B: Results of the KS test for the different theoretical distribution functions with a significance level of $\alpha = 0.1$. If $D_N = \sup_x |F_N(x) - F(x)|$ is smaller than the critical value it falls within the green area, indicating that the observed data aligns with the respective distribution. In case that D_N is greater than the critical value, it falls in the red area, indicating that the null hypothesis is rejected. The critical value is calculated dependent on the number of SOH values and the significance level.

pared to the other theoretical distributions across a range of energy throughput scenarios. This is evident from its lowest total RSS sum, mean RSS, and median RSS. The results from the KS test align with the RSS analysis, with the null hypothesis not being rejected for energy throughputs above 1000 kWh, providing strong support for the selection of the lognormal distribution to fit the field data. Considering both the RSS analysis and the KS test results, the lognormal distribution emerges as the most suitable choice for fitting the empirical data across a spectrum of energy throughput scenarios for diverse operation conditions. Its ability to reliably represent distributional characteristics, especially in the context of higher energy throughputs, justifies its selection for our battery dataset.

3.3.3 Anomaly Detection

Having selected the lognormal function as the most suitable pdf to describe the SOH value distribution within each operation-specific cluster and identified the optimal cluster vari-

Table 3.4: Analysis and quantization of the goodness of fit according to the error measure RSS. The best-case statistical metrics for RSS are colored in .

Error measure		Distribution functions						
		normal	lognormal	weibull	exponential	logistic	gamma	beta
RSS	total sum	1.76	0.86	1.74	11.6	1.53	3.91	3.94
	mean	0.057	0.027	0.056	0.37	0.049	0.13	0.13
	median	0.031	0.0073	0.015	0.071	0.027	0.0081	0.009
	σ	0.057	0.076	0.1	1.30	0.051	0.49	0.49
	max. value	0.23	0.41	0.46	7.41	0.21	2.76	2.74

ables for achieving well-distributed cluster sizes, we proceed to determine the parameters μ and σ^2 of the lognormal function for each cluster containig the readouts as follows:

$$\mu = \frac{\sum_i^n ln(x_i)}{n} \tag{3.3}$$

$$\sigma^2 = \frac{\sum_i^n (ln(x_i) - \mu)^2}{n-1}. \tag{3.4}$$

To ensure a right-skewed empirical distribution, x denotes the Δ SOH= 100 %-SOH values. Additionally, since the logarithm is only defined for positive numbers, we set all ΔSOH values that are zero to 0.1. This approximation is considered sufficiently close to zero, given that the collected SOH values are integers. In this work, we focus on the detection of contextual anomalies, often referred to as conditional outliers, within the presented field data. These anomalies are values that distinctly deviate from other SOH values within the same cluster of batteries sharing a similar load history, but are not necessarily outliers when considering the overall data. We employ statistical learning methods and utilize percentile techniques for the identification of those anomalies. Percentiles divide a dataset into 100 equal parts, with the xth percentile representing the value below which x % of observations fall, and (100-x) % are greater [141]. They form the basis for calculating the two-sided confidence interval, which delineates the range of permissible SOH values for a cluster. In our approach, we calculate the $\alpha/2$ and $1-\alpha/2$ percentiles of the cdf and apply the following condition to detect a data point as an outlier:

$$is\_outlier(x) = x < \lfloor p_{\alpha/2} \rfloor \ \vee \ x \geq \lceil p_{1-\alpha/2} \rceil \tag{3.5}$$

In the first part of Equation (3.5), a floor rounding operation to the nearest integer is employed, along with a less-than condition, to account for the zero value replacement. This operation aims to identify potential outliers characterized by slower estimated aging compared to all other SOH values within the cluster. In the subsequent part of Equation (3.5), we apply an equal or greater condition after rounding up the (1-$\alpha/2$) percentile

value. This condition is applicable to identify batteries exhibiting accelerated estimated aging. The choice of the significance level α determines the probability of detecting false-positive outliers. Therefore, it represents a trade-off between detecting an outlier and the certainty that identified data points are actual outliers. Hence, a smaller confidence interval results in a higher percentage of identified outliers, accompanied by an increased likelihood of false-positive detection.

Figure 3.10A provides an overview of the resulting clusters of SOH values at a fixed energy throughput of 300 kWh and illustrates the graph of the lognormal pdf based on the distributions of ΔSOH=100 %-SOH values from one exemplary cluster.

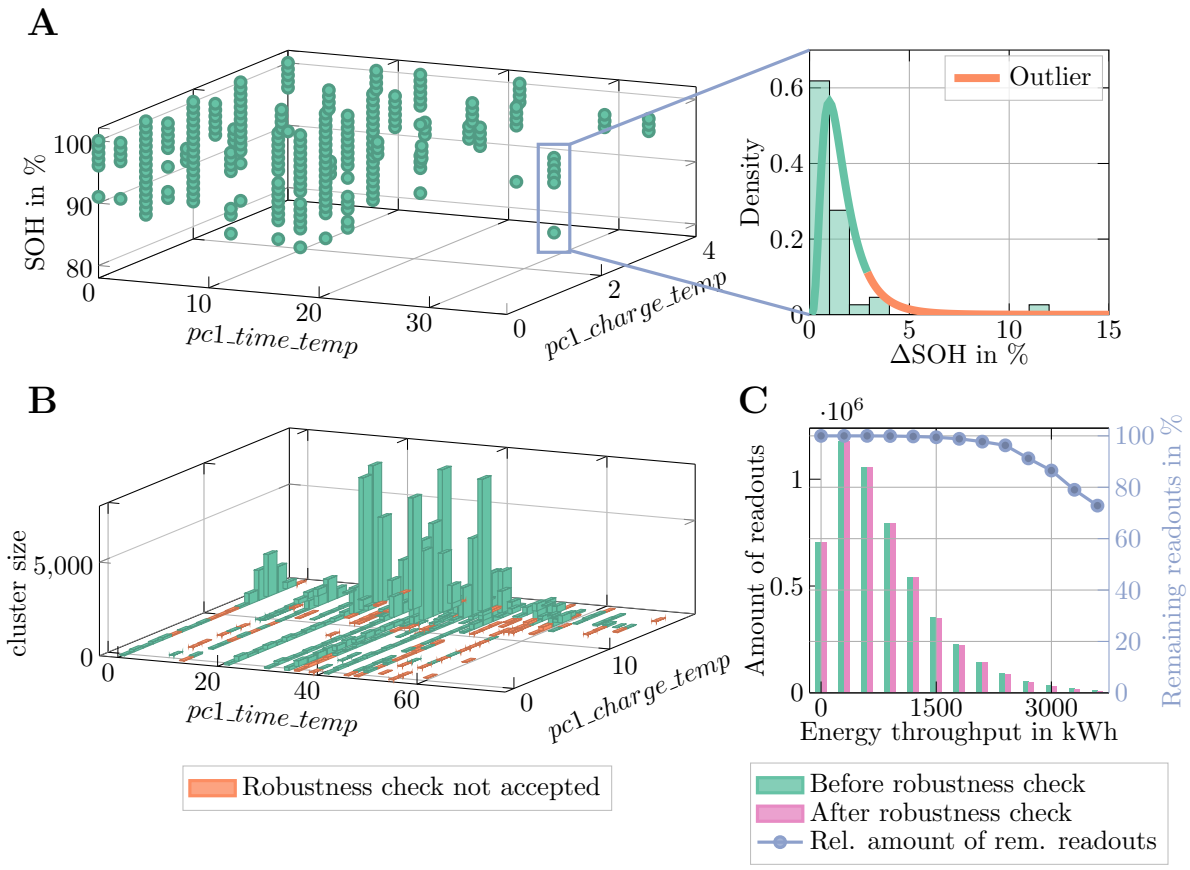

Figure 3.10: Overview of cluster properties.
A: Available SOH data for a fixed energy throughput of 300 kWh across all clusters (left). Distribution of ΔSOH values in the exemplary cluster (right). Values falling under the orange segment of the distribution function are flagged as outliers within the specified confidence interval.
B: Cluster sizes for a fixed energy throughput of 900 kWh. The orange clusters are omitted since the robustness condition is not accepted.
C: Amount of readouts before and after the robustness check. The relative amount of readouts is depicted in purple.

It shows a clear majority of lower ΔSOH values with a decreasing tendency towards higher values. In this case, the estimations of the logarithmic mean μ and variance σ^2 as given in Equations (3.3) and (3.4) are accurate due to the cluster size and the evident trend of the data. In contrast, smaller clusters with a comparable spread of SOH values could not ensure a robust parameter estimation and, hence, not guarantee a valid result for the outlier detection. Consequently, to account for too small cluster sizes with respect to the σ of SOH values, we again apply Equation (3.1) to check for the statistical robustness of a cluster so that the estimations of function parameters are not distorted by outlier data points. Therefore, we define the range of the 95 % symmetric confidence interval of the mean to be less than 0.5 % points. Those clusters that do not satisfy the robustness condition will not be considered for the outlier detection. Figure 3.10B illustrates all clusters at a fixed energy throughput of 900 kWh and also those that do not pass the robustness check. As can be seen, only clusters with a small cluster size are affected by the robustness filter and, therefore, do not substantially influence the total database size as shown in Figure 3.10C.

3.3.4 Validation

Since the outlier detection model represents an unsupervised approach with no target values to be trained on, the validation step requires labeled data of SOH values that are considered outliers. Afterward, the detected and the considered true outlier values can be compared to assess the quality of the model. To obtain those true outlier values, we apply two different approaches for the validation of our framework. The first one utilizes pseudo aging values, which are appended to each cluster to check for the detection sensitivity of our method. By defining the relative SOH drop or rise for each artificial value of a cluster, we can ensure validation for known outlier values and test the sensitivity of our method for single data points that could have resulted from unusual battery aging. The second approach employs the data of a corrupted development software version, which is known to comprise under-estimated SOH values. Hence, we employ real driving data with a high percentage of outlier values to investigate the detection rate of the model.

3.3.4.1 Validation with Pseudo Values

This validation step introduces pseudo SOH values, which are considered actual outliers, and checks for the detection of those values. Hence, to validate the performance of the outlier detection model, we add one artificial SOH value to each cluster i according to the following equation:

$$SOH_{add,i} = C_{pseudo} \cdot \overline{SOH_i} \tag{3.6}$$

with $\overline{SOH_i}$ as the mean SOH value of cluster i and C_{pseudo} as the rate representing the outlier magnitude of the added value $SOH_{add,i}$. As given by Equation (3.6), the added SOH value is the product of the mean SOH of the respective cluster and the constant

C_{pseudo}, which determines the distance of the pseudo value to the mean SOH of the cluster. As an example, a C_{pseudo} of 0.99 would add an artificial SOH value of 99 % to the cluster if its mean was 100 %. Since SOH values usually increasingly spread over time and usage, the magnitude of an outlier considered in an early cluster would not represent an outlier in an older cluster due to a wider spread of SOH values. Hence, we increase the pseudo-rate C_{pseudo} for clusters that comprise older battery readouts to guarantee the generation of actual outlier values considering variations. Afterward, we filter all clusters based on the robustness check from Equation (3.1) and apply the outlier detection framework to the resulting data.

Figure 3.11 illustrates the detection of the pseudo SOH values at three energy throughputs 300 kWh, 2100 kWh and 3900 kWh and a significance level of $\alpha = 10$ %. Hence, we accept a 5 % probability of incorrectly classifying a valid value as an outlier on either side of the distribution. To account for the increasing spread of older SOH values, we apply a pseudo-rate C_{pseudo} of 0.97, 0.94 and 0.92, respectively, following an industry-standard acceptance threshold. These values define the acceptable range for aging-related deviations [116] and ensure a balanced approach to anomaly detection: If the pseudo-rate were set too high, minor cell-to-cell variations could be misclassified as anomalies, potentially leading to warranty claims and increased costs. Conversely, if the pseudo-rate were too low, critical aging might go undetected, potentially resulting in battery failures in the field. By aligning with industry standards, our framework provides a practical trade-off between early fault detection and avoiding excessive warranty cases. The left panels of Figure 3.11 show the clusters at the fixed energy throughputs, where green indicates a successfully detected pseudo SOH ('1') value and orange a failed detection of the artificial value ('0'). The right panels of Figure 3.11 illustrate the distribution characteristics when fitting the lognormal distribution function on the ΔSOH values of each cluster. Thereby, the two outer gray circles depict the upper and lower limit of the two-sided 90 % confidence interval and the middle circle is the mean of ΔSOH values. Moreover, the circle marks show the pseudo SOH values of each cluster with the same color scheme as of the left plot. One can see that for the energy throughput scenario at 300 kWh, all pseudo SOH values lie outside the defined confidence range and are thus detected as outliers providing a too high ΔSOH value with respect to the remaining ΔSOH values of the cluster. At an energy throughput of 2100 kWh, four SOH values with a pseudo-rate of 0.94 are not detected. The right plot shows a wider confidence range of ΔSOH values resulting from a higher dispersion of SOH values in those clusters. The same applies to the not detected pseudo SOH value at an energy throughput of 3900 kWh and a pseudo-rate of $C_{pseudo} = 0.92$. The resulting detection rates for the three scenarios are 100 %, 97.8 % and 96.2 %, respectively. The sensitivity of anomaly detection to different SOH deviations is discussed in the Supplementary Material A.2.

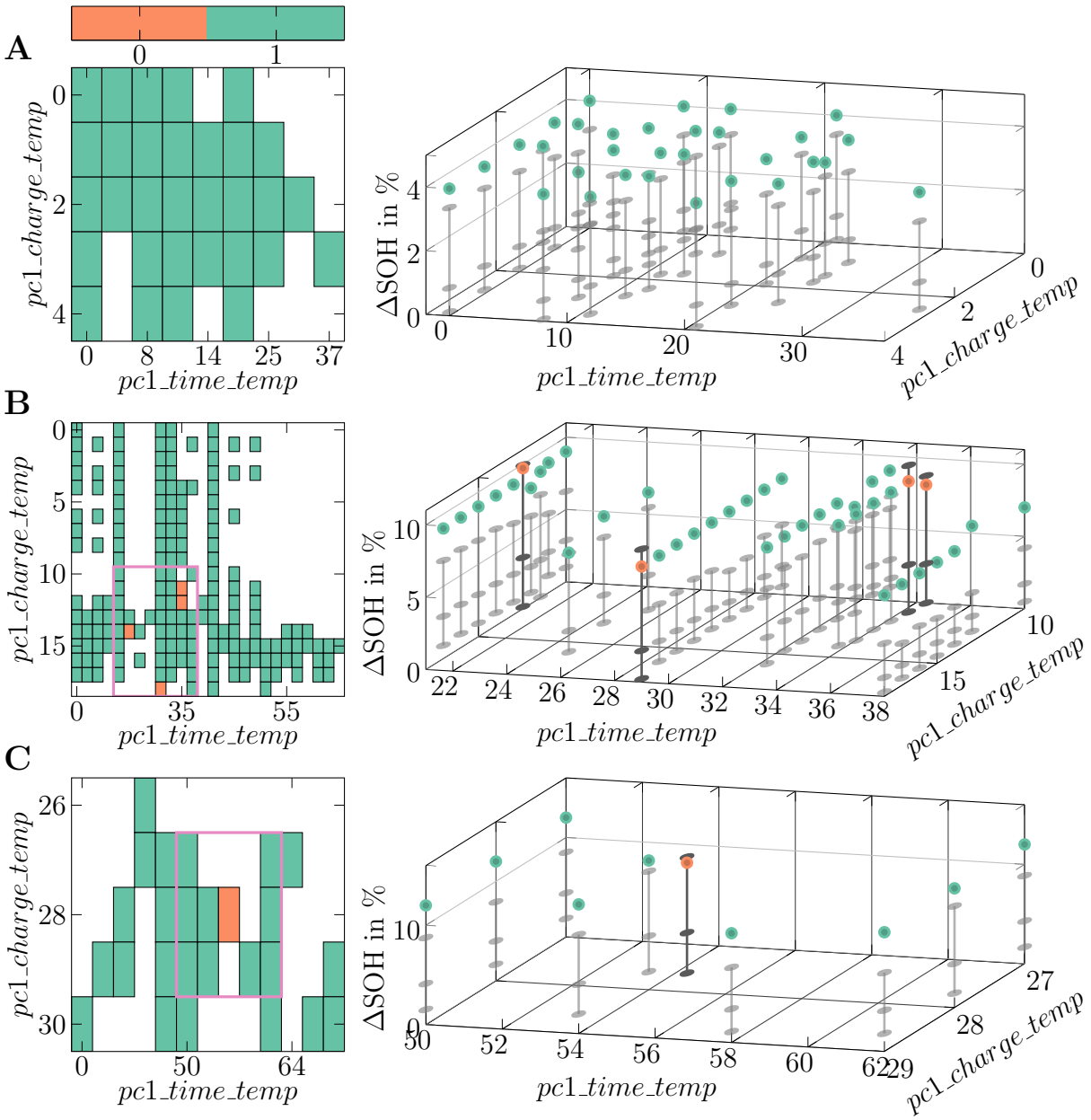

Figure 3.11: Pseudo-SOH validation for different energy throughput scenarios. 1 indicates a successfully identified artificial SOH value and 0 is not detected. (a) Detection of outliers C_{pseudo} = 0.97 across all clusters at *energy_throughput*=300 kWh. The overall detection rate is 100 %. (b) Detection of outliers C_{pseudo} = 0.94 across all clusters at *energy_throughput*=2100 kWh. The overall detection rate is 97.8 % (c) Detection of outliers C_{pseudo} = 0.92 across all clusters at *energy_throughput*=3900 kWh. The overall detection rate is 96.2 %

.

3.3.4.2 Validation with Field Data

In addition to the validation with artificial SOH values across different clusters, we employ data points obtained from a corrupted software version deployed on batteries in prototype vehicles to validate our framework. This specific software version is known for generating underestimated SOH values, as depicted in Figure 3.12.

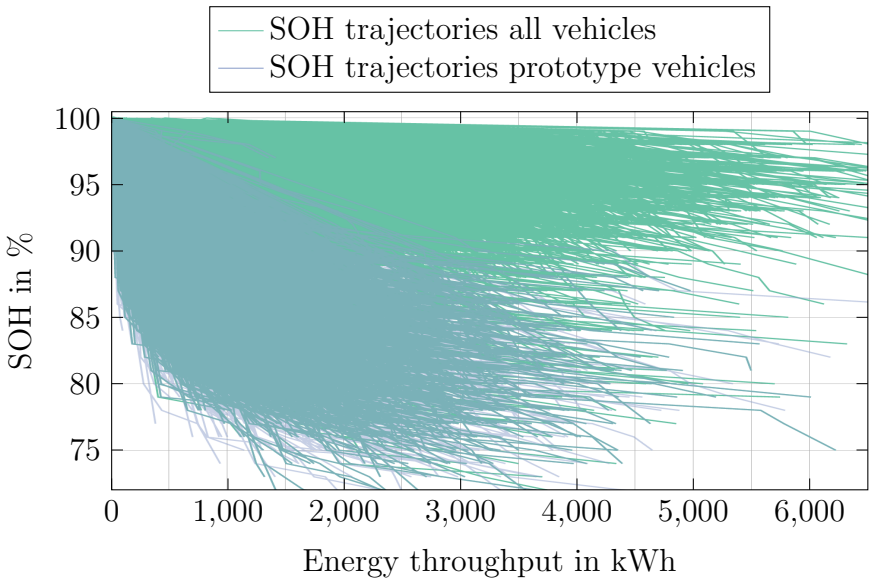

Figure 3.12: SOH trajectories of 100 thousand exemplary vehicles and corrupted prototype vehicles.

Figure 3.13A shows the congruence for each cluster variable based on the 90 % confidence interval. Purple-outlined, orange-filled circles signify successful outlier detection of SOH values from the corrupted software version. Conversely, purple-outlined, green-filled circles indicate that the SOH value from the validation software version has not been identified as an anomaly. To analyze the detection rate of the validation software version, Figure 3.13B shows the ratio of detected outliers within the corrupted software version for all clusters of the respective cluster variable. Moreover, the histograms illustrate the quantity of validation data for each specific SOH cluster related to the three selected features. The corrupted software version is consistently identified across the entire range of cluster variables with a total of 79 % of detected validation data points as anomalies. However, significant drops of the detection rate in Figure 3.13B are noticeable. These drops result from a higher number of corrupted data points within a cluster. This is confirmed by the green line showing the relative number of corrupt data points within a cluster where higher percentages perfectly correlate to a drop in the detection rate. For further analysis, Figure 3.14 shows two exemplary clusters to illustrate the distortion of probability functions together with a shift of the confidence interval due to a higher percentage of corrupt data points.

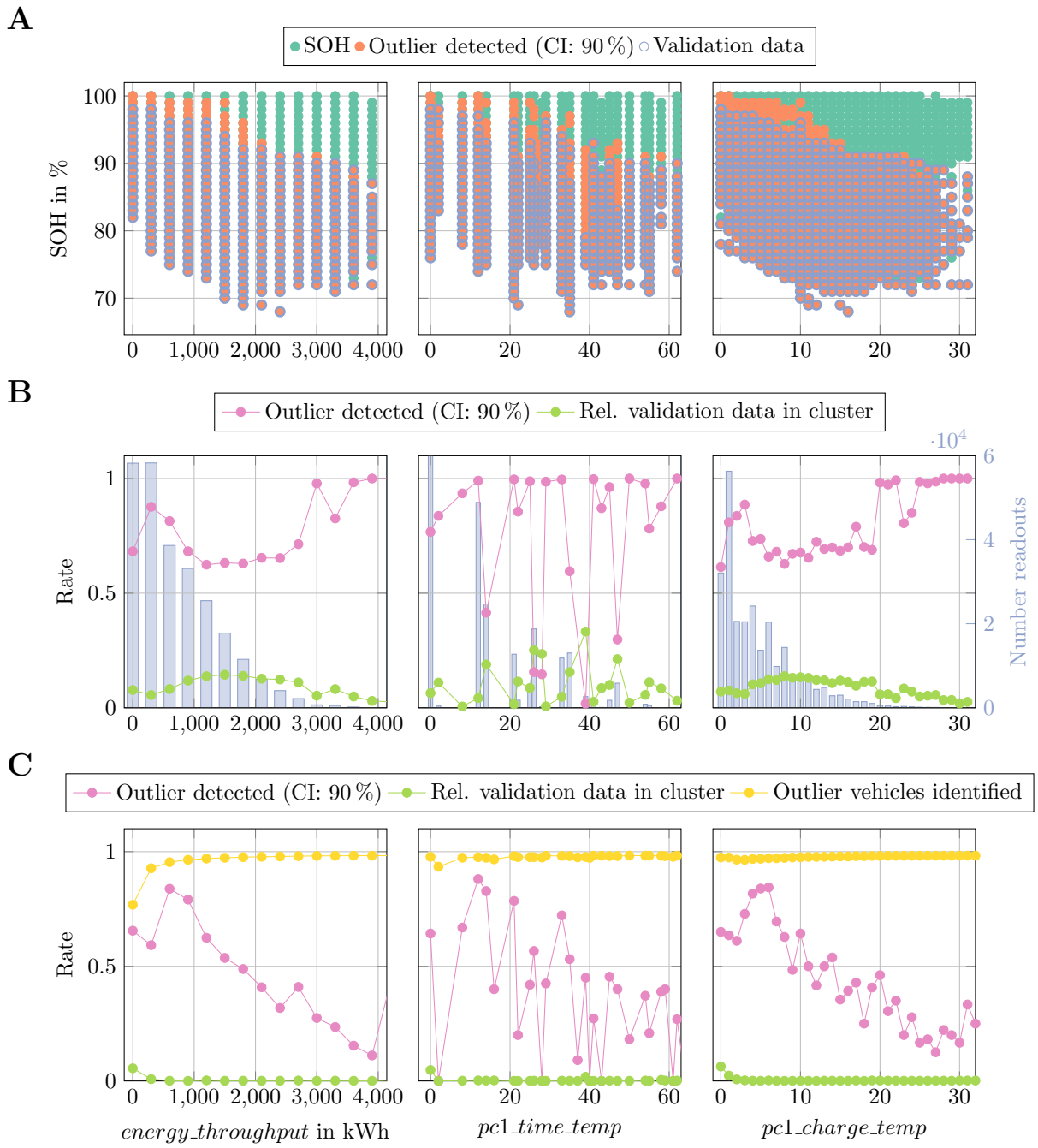

Figure 3.13: Validation of the statistical framework with battery field data.
A: Validation of outlier detection based on a 90 % confidence interval for the three features. The data points outlined in purple are from a faulty software version that should be identified with the developed framework.
B: Relative number of outlier detection of faulty SOH values. The histograms show the count of data points within each cluster of the validation data.
C: Relative number of identified vehicles with a corrupted software version. Once a vehicle has been detected with an anomalous battery aging, its later readouts will be ignored to mitigate the distortion of distribution functions.

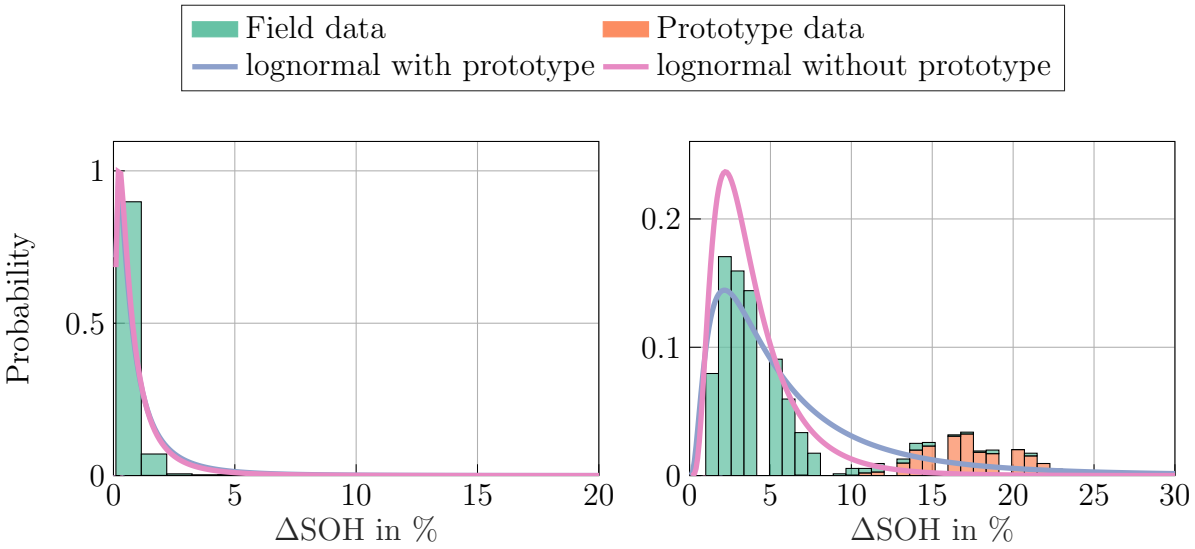

Figure 3.14: Distortion of probability distribution functions in clusters with a high percentage of corrupted data points.

In order to evaluate the effectiveness of our framework to detect vehicles with an anomalously aging battery, we investigate the number of detected vehicles from the prototype fleet. Therefore, we will only account for vehicles with more than one available readout. Furthermore, we will ignore later readouts of a vehicle once it has been detected with an anomalous SOH value to mitigate the distortion of fitted probability functions. Figure 3.13C shows the resulting ratio of detected vehicles from the prototype fleet with a corrupt software version which reaches a final value of 98 %. Thereby, the detection rate shows a decreasing trend due to fewer and fewer detectable vehicles remaining in the prototype fleet.

3.4 Conclusion

Battery field data collection provides valuable insights into battery system performance over their operational lifetimes, serving as a key resource for understanding real-world behavior. In this work, we utilize an extensive dataset comprising over 12 million readouts from 600,000 prototype and customer vehicles equipped with LIBs to identify relevant operational behavior and degradation patterns in a high-power application. This data is essential for defining the operational requirements that a new cell chemistry, like a SIB, must meet when considered as a drop-in replacement for that application. Significantly, the field data provides a detailed picture of the operational demands in the target high-power mobile application. Batteries are regularly exposed to high C-Rates of 10 C and typically operate within a temperature range of 10 °C to 40 °C. DODs are usually below 10 %. Even though some batteries have an operational energy throughput of 6,000 kWh, most batteries sustain an energy throughput of 4,000 kWh while retaining an SOH above

95 %. At the same time, degradation behavior shows notable variability across the fleet, with SOH values differing by up to 30 % in extreme cases.

We introduce a framework for detecting batteries with anomalous estimated aging, which may result from either atypical degradation or a faulty vehicle software version. This framework enables the analysis of in-field aging data without requiring prior knowledge of the specific battery type, making it particularly valuable when deploying new technologies. Identifying batteries with unusual aging patterns can guide manufacturer decisions, such as battery replacements or software updates, and provides a systematic approach to assess reliability directly in the field. For this analysis, we first grouped batteries with similar usage histories based on carefully selected feature variables. These feature variables play a crucial role in clustering batteries with comparable aging characteristics while distinguishing those with distinct load patterns. We chose three BMS variables, considering charge throughput, temperature range, and SOC range, to ensure balanced cluster sizes while providing sufficient data for robust statistical analysis. For detecting irregular SOH values within the individual clusters, we fit theoretical distribution functions to these clusters, ultimately selecting the lognormal distribution function as the best-fitting representation for our data. Then, we identified outliers for each cluster using a two-sided confidence interval. To experimentally validate our statistical framework, we introduced individual pseudo SOH values that represent known outlier data points. We conducted a sensitivity analysis for an array of pseudo SOHs to account for different aging trajectories that have been observed in literature [116]. For three given scenarios, our framework successfully detected 98 % of outliers across all clusters. Additionally, we used a corrupted software version applied to prototype vehicles, deliberately underestimating the SOH. With our methodology, we identified an average of 79 % of data points and a total of 98 % of vehicles from the corrupted software as outliers. Importantly, across various SOH clusters, data points from the corrupted software were recognized as anomalies, highlighting the framework's robustness across various battery operations. However, its effectiveness hinges on the accuracy of the SOH estimates provided by the BMS. Consequently, if the framework is to be applied to replacement technologies such as SIBs, their SOH must be estimated with comparable precision under real-world conditions.

4 Aging Analysis of a Commercial Sodium-Ion Battery

High-power applications, such as the automotive case discussed in Chapter 3, currently rely on NMC/LTO cells, which provide excellent power capability and long cycle life but are limited by low energy density and high cost. These limitations make them suitable candidates for replacement. Recent studies further indicate that SIBs can achieve comparable power performance at substantially lower cost [12]. To successfully introduce SIBs into such high-power applications, however, their lifetime under realistic operating conditions must be well understood. Chapter 3 showed that temperature, current, and SOC strongly influence the aging of high-power systems, which in field operation sustain up to 6,000 EFC. If SIBs are to replace NMC/LTO-based systems, they must demonstrate a comparable lifetime behavior. Understanding the influence of operating parameters on degradation is a crucial prerequisite for assessing the technology's suitability and enabling reliable lifetime prediction [58, 142, 143]. However, most existing studies on SIBs remain limited to fundamental electrochemical analyses or small datasets involving only a few cells [144, 145]. This lack of statistically robust aging data for commercial cells restricts insights into long-term performance and complicates the identification of major degradation modes relevant to practical applications.

This chapter addresses this gap by presenting the experimental setup and results of an extensive aging study on a commercial SIB using a layered-oxide cathode and HC anode. The study systematically investigates the influence of cycling conditions, particularly DOD and mean SOC, on capacity fade and impedance growth within operating ranges that are relevant to the high-power application. Diagnostic techniques such as DVA and electrochemical impedance spectroscopy (EIS) are applied to track aging-related changes. Finally, we perform a feature importance analysis to identify which parameters most strongly correlate with capacity fade within the tested conditions. While not intended as a complete aging study, this chapter provides an important foundation for gaining initial indications of dominant aging mechanisms for the early-commercial SIB.

4.1 Experimental Data

4.1.1 Commercial Sodium-Ion Battery

Within the aging study we age 81 commercial 18650-format sodium-ion cells produced by Shenzhen Mushang Electronics Co., Ltd. The cells feature a layered-oxide ($NaMO_2$) cathode and a HC anode. Specifications are summarized in Table 4.1, where the main characteristics are a nominal capacity of 1.2 Ah, a specific energy density of 97 Wh kg^{-1}, and a specific power density of 810 W kg^{-1}, with an operating voltage range between 1.5 V and 3.8 V. The cells were comprehensively characterized in a previous publication [12], which provides the foundation for the experimental design presented in this chapter.

Table 4.1: Cell specification and material characteristics based on the post-mortem analysis conducted by Laufen et al. [12].

Cell specifications		
Nominal capacity	1.2 Ah	
Nominal voltage	3.0 V	
Unit price	1.1 US$ (0.31 US$/Wh)	
Dimensions (Ø × H)	18 × 65 mm	
Weight	37 g	
Internal resistance	≤25 mΩ (1 kHz for 50 % SOC)	
Voltage range	1.5 – 3.8 V	
Current limits (charge)	0.6 A (0.5C) for 0 °C – 10 °C	
	1.2 A (1C) for 10 °C – 20 °C	
	3.6 A (3C) for 15 °C – 25 °C	
	6.0 A (5C) for 20 °C – 45 °C	
Current limits (discharge)	9.6 A (8C) for 10 °C – 50 °C	
Post-Mortem analysis		
Separator		
Material	Polymer without coating	
Thickness	15 µm	
Porosity	40.6 % (Hg-Intrusion)	
Electrolyte		
Solvent	DMC:EMC:EC:PC:EP	
Solvent mass	3.4 g	
	Positive electrode	**Negative electrode**
Active material	Layered oxide ($NaMO_2$)	hard carbon (HC)
Porosity	29.9 % (Hg-Intrusion)	31.4 % (Hg-Intrusion)
Coating weight	31.61 mgcm^{-2}	16.02 mgcm^{-2}
Coating surface	798.10 cm^2	857.86 cm^2
Number of layers	1 (double coated)	1 (double coated)
Dimensions (L × B × D)	70 × 57.5 × 0.111 mm	76.9 × 59 × 0.154 mm
Thickness of current collectors	17 µm (aluminum)	6 µm (copper)

Figure 4.1 presents the quasi open-circuit voltage (qOCV) of a pristine cell, measured at a low current rate (C/20) at 25 °C. The voltage curve exhibits a distinct hysteresis, i.e. a difference between charge and discharge curve, in the lower SOC range, while the remainder of the curve shows a comparably steep slope with low hysteresis.

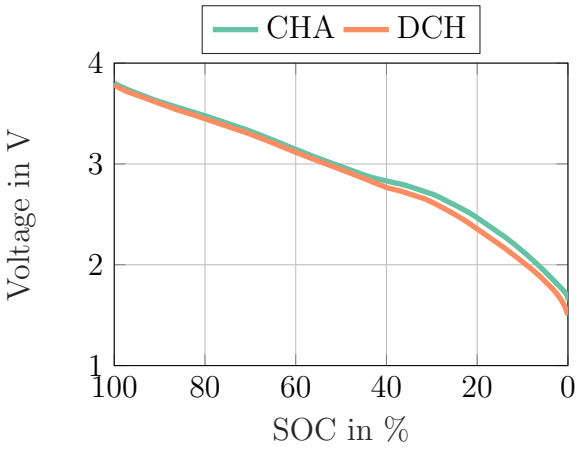

Figure 4.1: The qOCV of the investigated SIB. The curves are determined by discharging and charging the cell at 25 °C within their voltage range using a C/20 current [12].

4.1.2 Initial Cell-to-Cell Variance

Cell-to-cell variation affects system design, aging behavior, and safety aspects [109, 111, 146]. These variations either result from differing operating conditions or from inherent electrochemical differences between individual cells, often traceable to production inconsistencies [109], as discussed in Section 3.1. According to the manufacturer, all investigated cells originate from the same production batch. Figure 4.2 shows the distributions of the initial capacity and resistance for each cell, based on the initial reference performance test (RPT). The green line represents the kde, while the orange line indicates the respective σ intervals. Capacity was determined from a full discharge at 0.5 C, and resistance refers to the 10 s pulse resistance measured at 50 % SOC.

The mean initial capacity is 1.162 Ah, with a standard deviation of 0.028 Ah, resulting in a coefficient of variation of 2.41 %. For resistance, the mean value is 53.1 mΩ, with a standard deviation of 1.83 mΩ, yielding a coefficient of variation of 3.44 %. These values are slightly higher than those reported in the literature: For example, Rumpf et al. [109] observed a coefficient of variation of 0.41 % for capacity and 1.43 % for pulse resistance. Given that SIBs have only been commercialized recently, the results still indicate relatively low initial variation, particularly with regard to capacity.

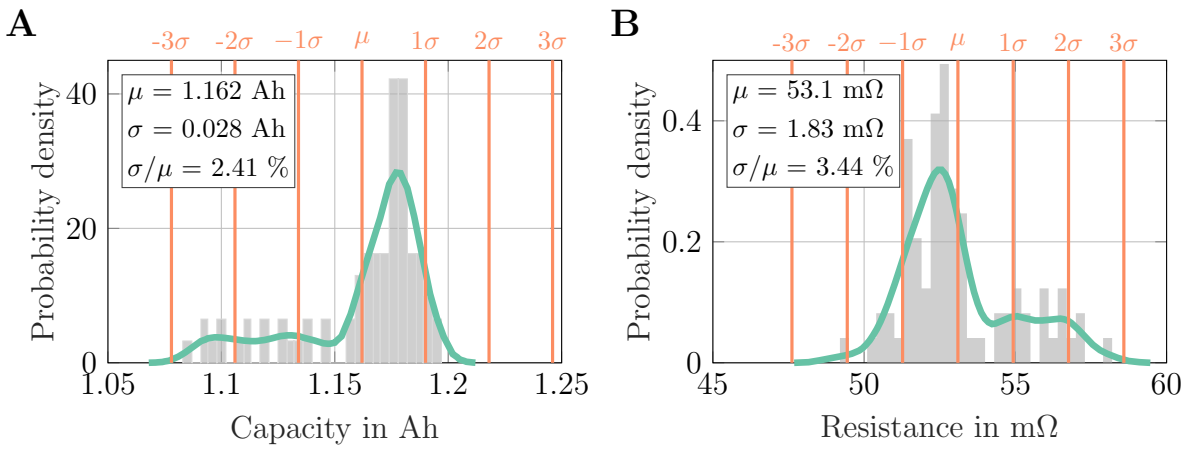

Figure 4.2: Frequency distribution and kde for initial capacity and 10 s pulse resistance at 50 % SOC for all 81 cells. The orange lines indicate the σ intervals and the mean for capacity and resistance.

4.1.3 Design of Experiment

The test bench used for the aging experiments is shown in Figure 4.3. Inside a climate chamber maintained at 25 °C, a rack holds eight main boards arranged in rows, each accommodating four cells connected via four-wire measurement. Besides the overall temperature control of the chamber, the cell temperature is not individually regulated; instead, the cells remain in constant contact with the surrounding air. The maximum current per cell is 10 A, corresponding to a C-Rate of approximately 8 C. Adjacent to the chamber is the cycler unit, which controls the charge and discharge of each cell, while an Inspectrum device mounted on top of the chamber performs EIS measurements. The hardware used in this study is summarized in Table 4.2. A fixture consisting of a motherboard and piggyback printed circuit board (PCB) ensures temperature homogeneity within the chamber by positioning the cells in the direction of the airflow. This leads to a temperature variation of no more than 1 K. For EIS, 12 out of the 81 cells are characterized using the multi-sine excitation method from the manufacturer, which allows multiple frequencies to be measured simultaneously. 32 evenly spaced frequency points between 10 mHz and 10 kHz are used to capture sufficient data on electrochemical processes while optimizing measurement time.

To design the cycling conditions for this aging study, we first determine the voltage limits based on the qOCV curve shown in Figure 4.1. By selecting voltage windows centered around DVA peaks we aim to cycle the cells near phase transitions that are hypothesized to trigger specific aging mechanisms enabling us to distinguish between individual degradation effects [147]. Using these defined voltage windows, we cycle 81 SIBs in a climate chamber at 25 °C with a 2C/2C rate under six different conditions that vary in mean SOC and DOD, as shown in Figure 4.4.

Table 4.2: Accuracy of the measured signals for the devices used in this aging study.

Instrument	Name	Variable	Precision	Range
Cycler	MCT 10-6-384(360) HD	Voltage	±3 mV	0 V - 6 V
		Current	±0.5 mA	0.01 A - 1 A
			±1.25 mA	0.025 A - 2.5 A
			±2.5 mA	0.05 A - 5 A
			±5 mA	0.1 A - 10 A
		Temp. measurement	±0.5 K	−55 °C - 125 °C
Temp. Chamber	LabEvent T/500/30/3	Temp. control	±1 K	−60 °C - 130 °C
EIS Galvanostat	Inspectrum.10-5 HD	Impedance ampl.	≤ 1%	0.1 mΩ - 100 mΩ
		Impedance phase	≤ 0.5°	−90° - 90°

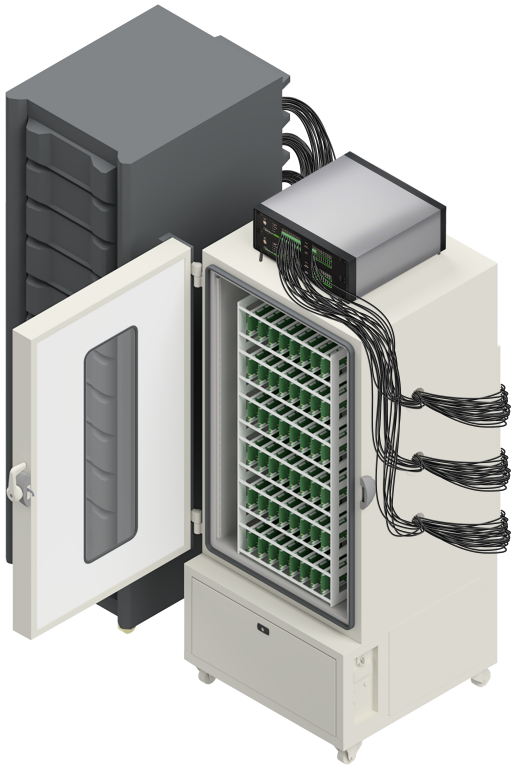

Figure 4.3: Testbench for the conducted aging tests. The cells are cycled in a temperature chamber at 25 °C. For 12 cells, we additionally perform EIS measurements. The device is placed on the top of the chamber. The cycler, responsible for charge and discharge of each cell, is next to the temperature chamber.

During aging, we account for cell hysteresis by discharging to the voltage on the discharge curve and charging to the voltage on the charge curve, ensuring cycling occurs within a consistent SOC range. For simplicity, we introduce the notation meanXDODY, where X

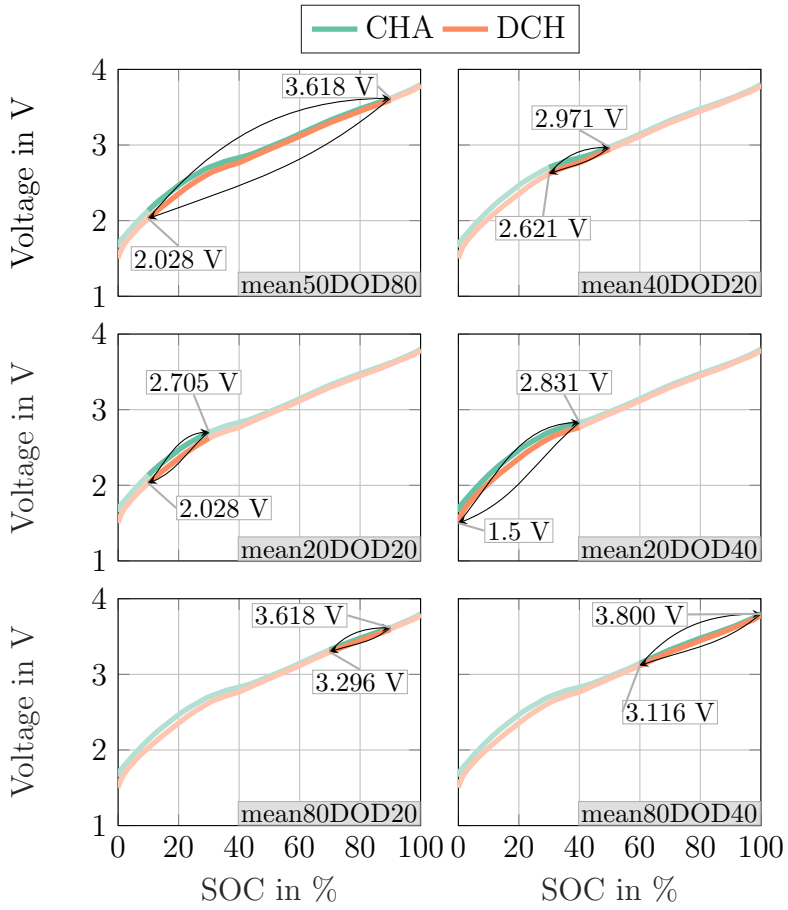

Figure 4.4: Design of Experiment for the aging study We focus on six conditions, where we vary DOD and mean SOC.

denotes the mean SOC and Y the DOD, corresponding to an SOC range from $(X - Y/2)$ to $(X + Y/2)$. To ensure statistical significance and to properly analyze aging variations, the following number of cells were cycled for each condition:

- For the conditions mean20DOD20, mean20DOD40, mean40DOD20, and mean80DOD40, 8 cells were cycled.
- For the condition mean50DOD80, 40 cells were cycled, following the statistical approach of Baumhöfer et al. [116].
- For the condition mean80DOD20, 9 cells were cycled.

4.1.3.1 Reference Performance Test

To monitor cell degradation consistently, each cell undergoes a RPT after reaching the equivalent of 400 EFC, in line with values commonly reported in the literature [148]. This interval balances diagnostic resolution with minimal interruption to the cycling process. However, because the cells are cycled within fixed voltage windows, the actual charge throughput per cycle can vary depending on the cell's internal resistance and aging state. At higher C-Rates such as 2C/2C, increased overpotentials can cause the voltage limits to be reached more quickly, reducing the effective capacity utilized in each cycle and thereby lowering the actual charge throughput. To account for this variation, we calculate the average charge throughput per cell during cycling and estimate how many cycles correspond to 400 EFC. Based on this mapping, each cell is scheduled for an RPT at the cycle count that aligns with this charge-equivalent threshold. The detailed test protocol of the RPT is shown in Figure 4.5. The capacity is determined by fully discharging the fully charged cell and determining the charge throughput by integrating the measured discharge current. The pulse tests consist of 10 second pulses in both charge and discharge directions, followed by charge balancing after each pulse. To capture current and SOC dependency, pulse tests are conducted for several C-Rates at 90 %, 50 %, and 10 % SOC. However, to reduce analytical complexity and focus on the core aspects of this work, we limit the evaluation to the results obtained at 1 C and 50 % SOC and calculate the resistance according to Equation (4.1), whereas t represents the current time.

$$R = \left| \frac{V(t + 10\ \mathrm{s}) - V(t)}{I} \right| \tag{4.1}$$

The qOCV measurement involves a full charge and discharge cycle using a C/20 current. Besides capacity, pulse, and qOCV measurements, the EIS spectra for 12 cells are measured.

4.1.4 Overview Aging

Figures 4.6, 4.7, and 4.8 summarize the results of the aging study, which serve as the foundation for all subsequent analyses. The SIBs are grouped according to their respective aging conditions, with the color scale representing the aging rate. The capacity-based aging rate is defined by Equation (4.2), where t denotes the time of evaluation (i.e., the most recent RPT) and C_{BOL} the initially measured capacity.

$$aging\_speed_C = \frac{\frac{C_{BOL} - C(t)}{C_{BOL}} \cdot 100\ \%}{Ah\ throughput(t)} \tag{4.2}$$

The resistance-based aging rate is defined analogously in Equation (4.3), with R_{BOL} representing the initial resistance. Negative values indicate an increase in internal resistance, while positive values reflect a decrease. Because the charge throughput differs across cells

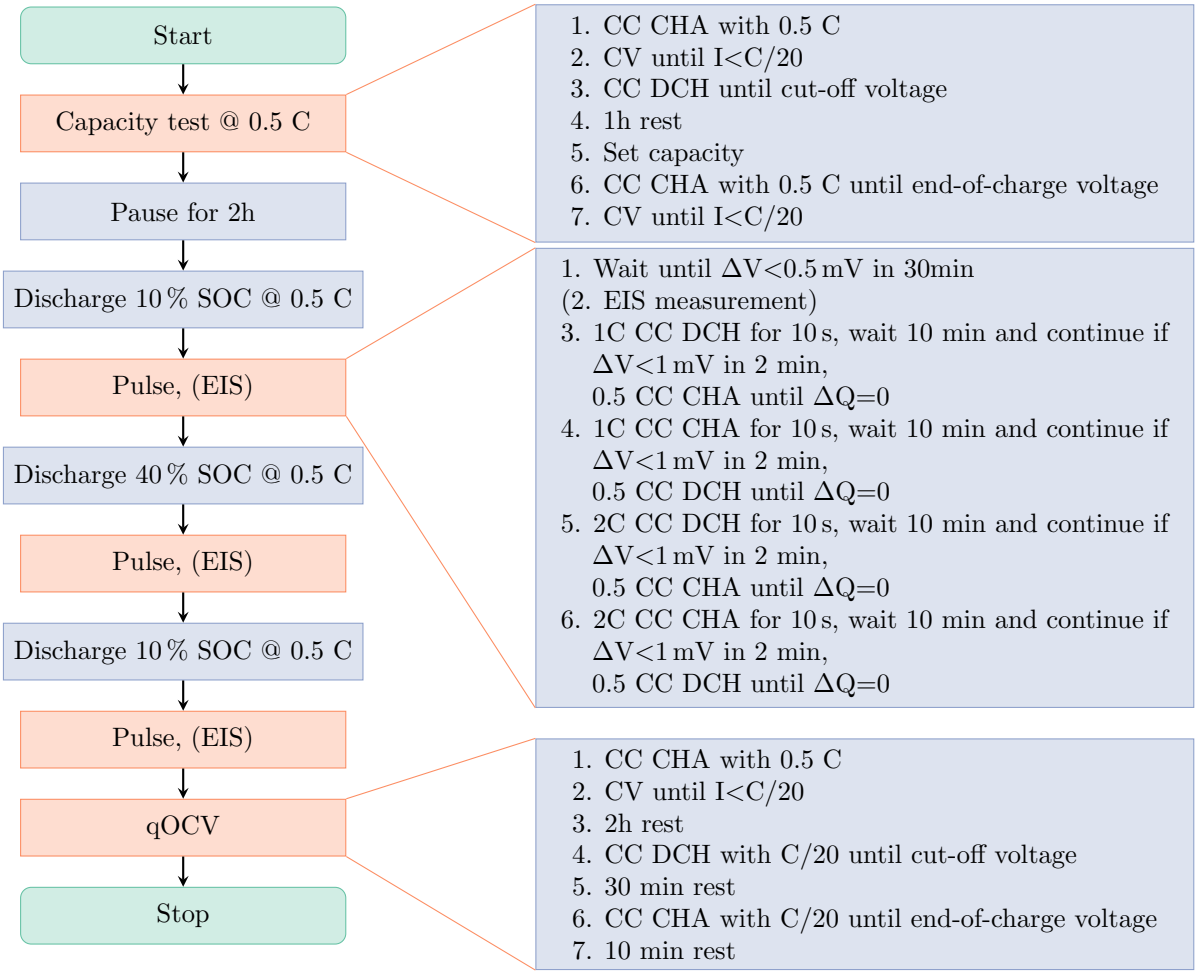

Figure 4.5: The test protocol for the RPT. Each cell undergoes this test approximately every 400 EFC to determine its current state and identify aging indicators. CC stands for constant current, whereas CV denotes constant voltage.

due to condition-dependent cycling, the aging rate provides a more meaningful comparison than relative capacity loss alone, as it normalizes degradation by the charge throughput. Using these metrics makes it possible to directly compare cells aged under different conditions and test durations.

$$aging\_speed_R = \frac{\frac{R_{BOL}-R(t)}{R_{BOL}} \cdot 100\ \%}{Ah\ throughput(t)} \tag{4.3}$$

Figure 4.6 shows the result of capacity loss across all conditions and reveals significantly different aging behaviors depending on the operating conditions. Based on experience with lithium-based aging, it was expected that the aging would increase with higher DOD [118]. However, the aging for the mid mean SOC with a high DOD is surprisingly low. As shown in Figure 4.7, the capacity loss in mean50DOD80 is only 1 % (median) after more than 4,000 EFC. The maximum relative capacity loss is below 6 %. Furthermore, we observe two distinct behaviors which may be due to variations in cell batches or different initial

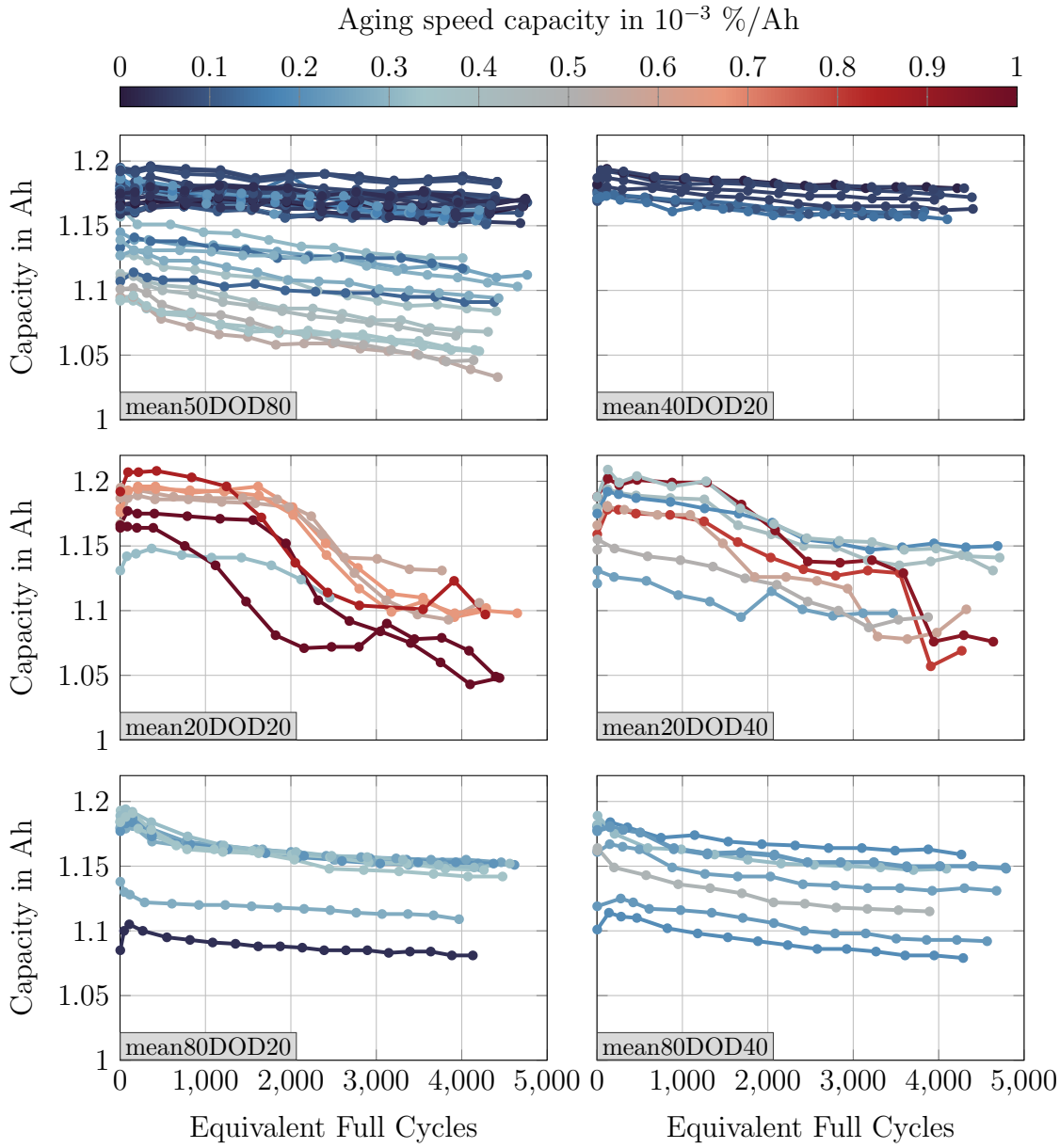

Figure 4.6: Overview of capacity results of the SIB aging data grouped into the six operating conditions. Each point corresponds to a specific capacity value resulting from the capacity test during RPT. The color represents the aging speed defined by Equation (4.2).

aging states. For cycling in the range from 30 % to 50 %, i.e., the condition mean40DOD20, the capacity loss remains also remarkably low. In both categories, the variation in aging speed at Begin-of-Life (BOL) and over the aging process are minimal. For lower mean SOC values, i.e., the conditions mean20DOD20 and mean20DOD40, a different aging pattern is visible. Figure 4.7 shows that the median relative capacity loss in both categories exceeds 4 %, with the maximum relative capacity loss reaching approximately 10 % in the mean20DOD20 category. In the upper SOC range, the aging is low but still higher than

in the first two categories, with a median of over 2 % and the variation in aging speed within this condition is small.

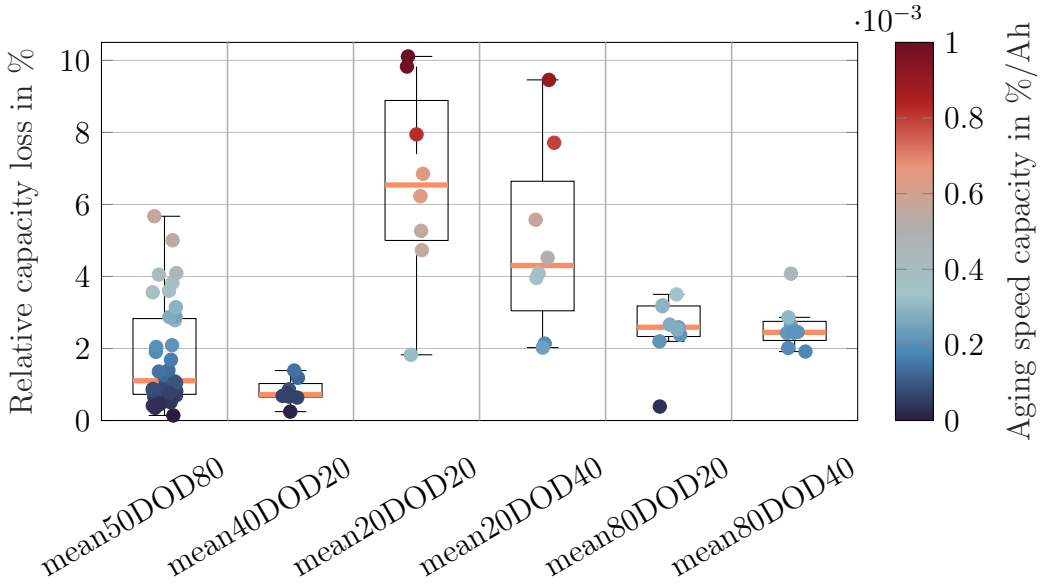

Figure 4.7: Relative capacity loss across each cycling condition. The relative capacity loss is the highest for lower mean SOC. The DOD merely has small influence on the relative capacity loss. The color represents the aging speed defined by Equation (4.2).

The resistance trends shown in Figure 4.8 also reveal a highly variable pattern depending on the condition. For the mean50DOD80 condition, the resistance increases moderately, with two distinct trends observed. In the mean40DOD20 condition, the trend in the resistance data is generally decreasing. In the two conditions with a mean SOC of 20 %, resistance shows a general increasing trend, though some cells exhibit a decrease. Under the mean80DOD20 and mean80DOD40 conditions, the trend is difficult to interpret, as the cells fall into two categories: those with little to no change in resistance and those showing a slight increase in resistance with cycling. In summary, we observe that changes in cell resistance are much more heterogeneous compared to changes in capacity for the investigated SIB.

The correlation between resistance and capacity is shown in Figure 4.9, where each point represents a cell's RPT. The colorbar represents the aging speed according to the capacity for a specific cell. Under the mean50DOD80 condition a linear trend can be observed, where the cells that have low resistance and high capacity correspond to a lower aging speed. In general, we observe that cells exhibiting faster aging speed tend to develop higher internal resistances, likely due to the snowballing nature of degradation mechanisms prevalent at high SOCs, such as sodium plating [149]. However, this relationship is less evident under certain cycling conditions. For example, in the mean40DOD20 case, capacity decreases slightly with increasing EFC, while resistance remains largely stable. This trend is further corroborated by the individual resistance evolution presented in

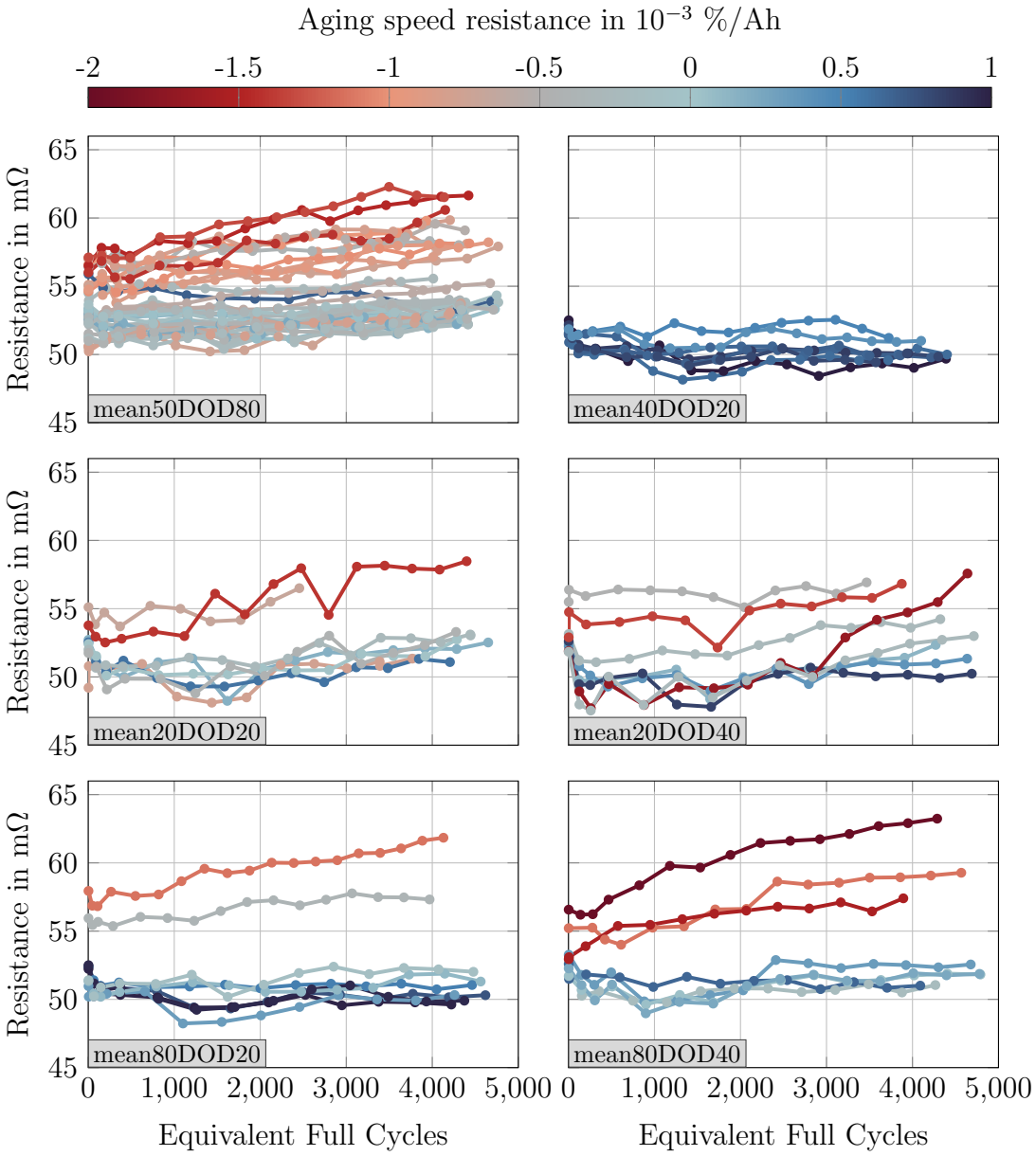

Figure 4.8: Overview of resistance results of the SIB aging data grouped into the six operating conditions. The color represents the aging speed defined by Equation (4.3). A positive aging speed indicates that the resistance is decreasing over cycling, whereas a negative aging speed indicates an increase in resistance.

Figure 4.8. In other cases, the aging speed appears largely uncorrelated with changes in resistance or capacity. Interestingly, cells cycled around an SOC of 20 % can exhibit both high aging speed and simultaneously high capacity and low resistance. This implies that although a cell may degrade quickly over time, it can retain a relatively high capacity and low resistance in the early or intermediate stages of aging. Notably, the approximately linear relationship between capacity and resistance observed for the mean50DOD80 con-

dition is not evident under the mean80DOD20 condition. This may be attributed to the lower DOD, resulting in reduced effective charge throughput due to increased overpotentials. In contrast, the mean80DOD40 condition follows a similar but less distinct trend than mean50DOD80, indicating a combination of different aging mechanisms.

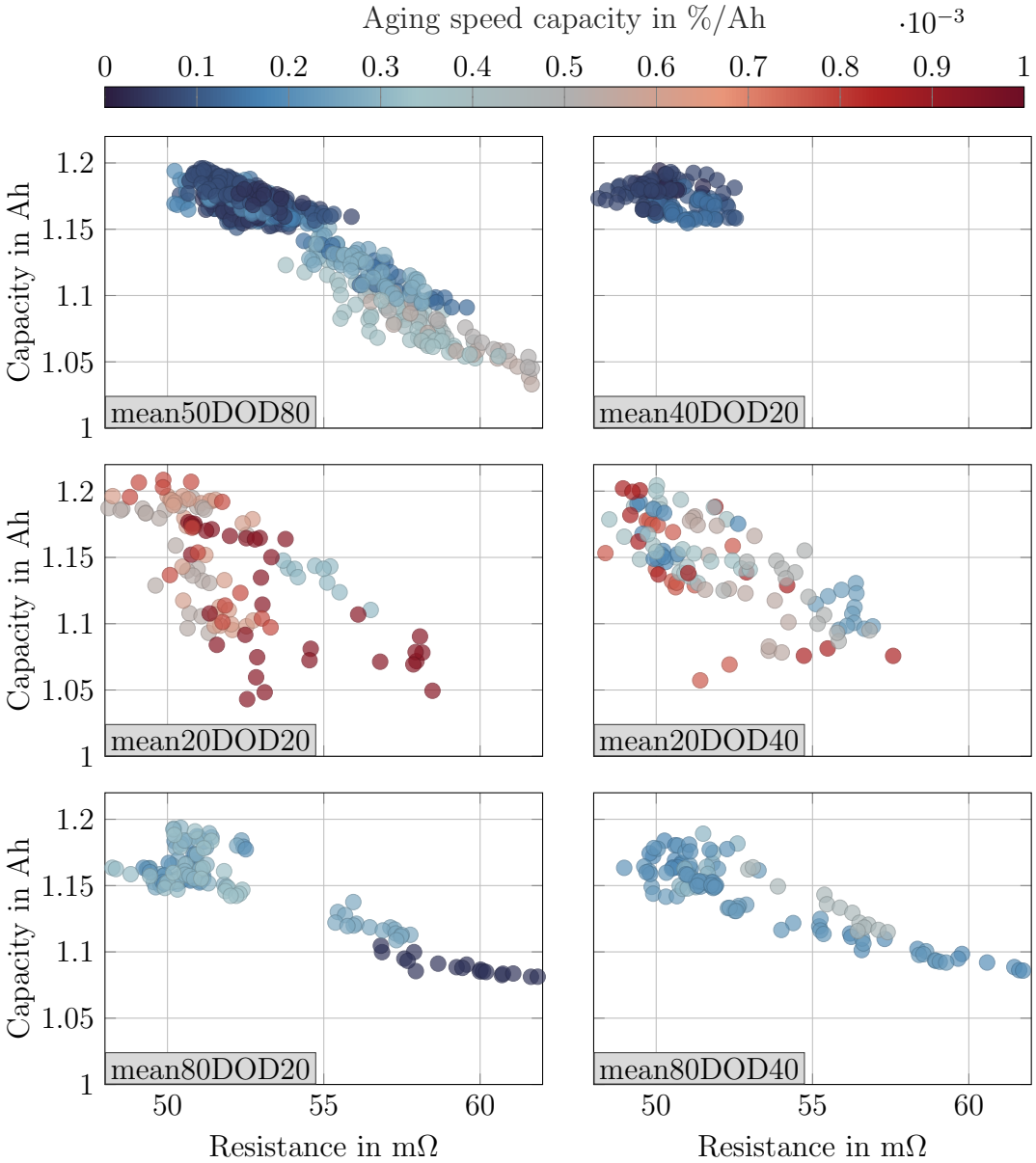

Figure 4.9: Relationship between capacity and resistance over lifetime across all six cycling conditions. Every point reflects a cell's RPT value. The color of the point reflects the aging speed with regards to capacity.

4.1.5 Voltage Behavior

Figure 4.10 illustrates the qOCV curves across all 81 cells and RPTs as a function of capacity, independent of the cycling condition.

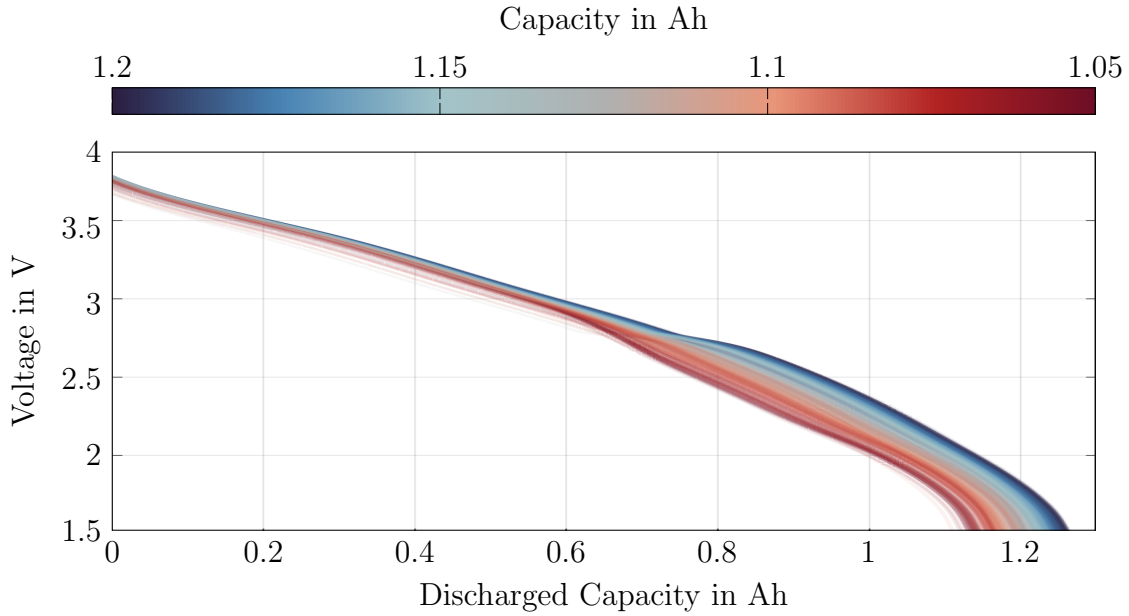

Figure 4.10: Discharge qOCV curves across all cells and RPTs without accounting for the specific cycling condition. The colorbar indicates the capacity of the respective RPT.

At first glance, the color gradient of the qOCVs over aging might suggest that OCV can be approximated as a function of specific capacity alone, without accounting for different aging modes. This simplification, in which OCV is assumed to depend exclusively on capacity, leading to a compression of the OCV curve, is commonly used in SOH estimation models. However, this approach introduces approximation errors when applied to our dataset. For example, the disappearance of the qOCV plateau around 0.8 Ah with progressive aging cannot be fully explained by resistance-induced overpotentials, as is commonly assumed in on-board SOH estimation methods. A more detailed analysis of these errors and their implications is provided in Section 5.2.2. Additionally, differences between qOCVs at a fixed capacity value are apparent, reflecting the influence of different underlying degradation mechanisms. These differences will be further analyzed in the following section providing insights into the specific causes of aging.

The features that we use for the degradation analysis based on qOCV measurements (DVA and qHysteresis) are summarized in Table 4.3. Features derived from EIS measurements are also included and will be analyzed in Section 4.2.2. For improved clarity, the selected characteristics are additionally illustrated in Figure 4.11.

Table 4.3: Selected features for the degradation analysis of the SIB. indicates DVA features, indicates qHysteresis features, and indicates EIS features

Name	Description
HPX	Height of HP X
LPX	Height of LP X
HPX/LPX_{loc}	SOC position of HPX/LPX
Diff HPX/LPX	SOC difference between two HPs/LPs
HP/LP	Height of HP/LP in the qHysteresis curve
HP/LP_{loc}	SOC position of the HPX/LPX in the qHysteresis
HP/LP	Imaginary part of HP or LP in the EIS Nyquist plot
$ZC/HP/LP_{loc}$	Real part of the impedance at ZC/HP/LP
Diff LPZC	Difference in real part of the impedance between LP and ZC

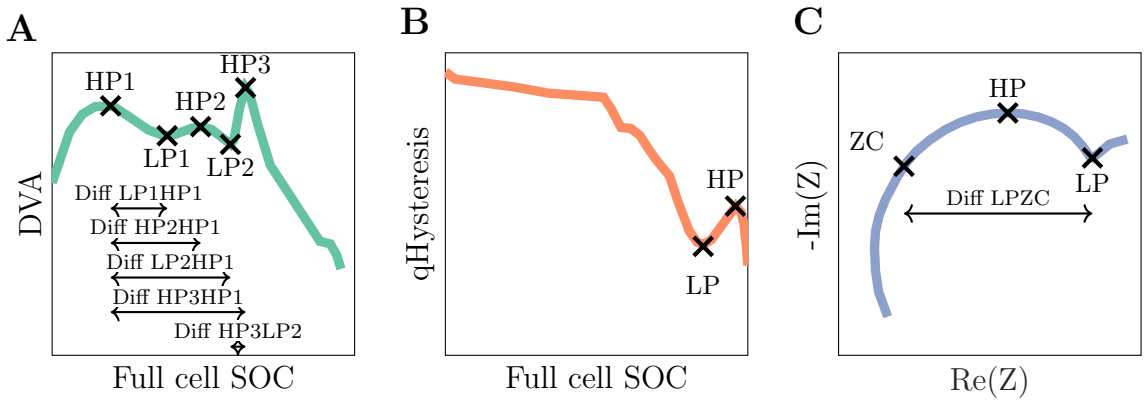

Figure 4.11: For the different measurement and analysis methods we employ a wide array of features based on the qOCV measurements. High point is denoted as HP, low point as LP and zero crossing as ZC, respectively. Every characteristic point is defined with its x-value (location) and y-value. The full cell SOC is defined as the charge normalized to the actual capacity value.
A: DVA.
B: qHysteresis.
C: EIS.

4.2 Degradation Analysis

In the following, we first gather all observations related to the features of the DVA, EIS, and qHysteresis, and then discuss their correlation across all RPTs with capacity loss in Section 4.3.

4.2.1 Differential Voltage Analysis

DVA is a widely used, non-destructive method for analyzing specific battery degradation modes [150–152]. The method analyzes the differential full cell voltage under quasi-equilibrium conditions, expressed as the superposition of the anode and cathode potentials, as shown in Equation 4.4 [153]. Systematic shifts in these voltage profiles enable the identification of degradation phenomena, including LAM and loss of sodium inventory (LSI). A plateau in the DVA indicates that two phases co-exist, whereas the distance between two peaks corresponds to the capacity change between phase transition [151]. When conducting DVA we typically track the location and height of the peaks as indicated in Figure 4.11A that represent the material being in a single phase [151]. A key distinction between DVA and the incremental capacity analysis (ICA) is how they represent electrochemical processes: While ICA peaks correspond to phase equilibria, DVA peaks indicate phase transitions [154]. Additionally, ICA does not allow for the linear separation of individual electrode contributions, whereas DVA preserves this separation.

$$\left(\frac{dV}{dQ}\right)_{fullcell} = \left(\frac{dV}{dQ}\right)_{cathode} - \left(\frac{dV}{dQ}\right)_{anode} \tag{4.4}$$

To investigate degradation mechanisms under varying conditions, the full cell voltage must be separated into its anode and cathode contributions. This requires a balancing procedure, in which the full cell voltage is reconstructed from the anode and cathode half-cell curves and adjusted to minimize deviations from the measured qOCV. Schütte et al. [155] previously conducted the qOCV fitting for the investigated SIB, which serves as the foundation for our DVA. They first disassembled the full cell, extracted the electrode materials, and reassembled them into coin cells with a sodium metal counter electrode. To determine the anode's half-cell potential, they used a coin cell setup. For the cathode, they employed a three-electrode set-up, where the cathode functioned within the full cell with an additional sodium reference electrode. The resulting anode and cathode qOCV curves were then fitted to the full cell qOCV. The reference qOCV was measured using low-current (C/20) charge and discharge cycles without rest phases. Applying the algorithm by Li et al. [156], Schütte et al. minimized the root mean square error (RMSE), achieving an accuracy of 5.4 mV [155]. However, it should be noted that the anode was charged only up to the cell's nominal capacity, and the potential behavior beyond this range remains unclear. In this work, as a remedy, we extrapolate the behavior at the end of the anode's open-circuit potential (OCP). Figure 4.12A illustrates the resulting relationship between the full cell qOCV and the OCPs of the anode and cathode. It presents the full cell discharge qOCV (purple line), the simulated qOCV (dashed black line), and the individual OCPs of the cathode (orange line) and anode (green line), respectively. The fitting parameters θ_{EOC} and θ_{EOD} define the limits at the end of charge and discharge, outlining the operating range of both electrodes. [155]

In Figure 4.12B, the differential voltage ($\partial V/\partial$SOC, DV) is plotted against the full cell

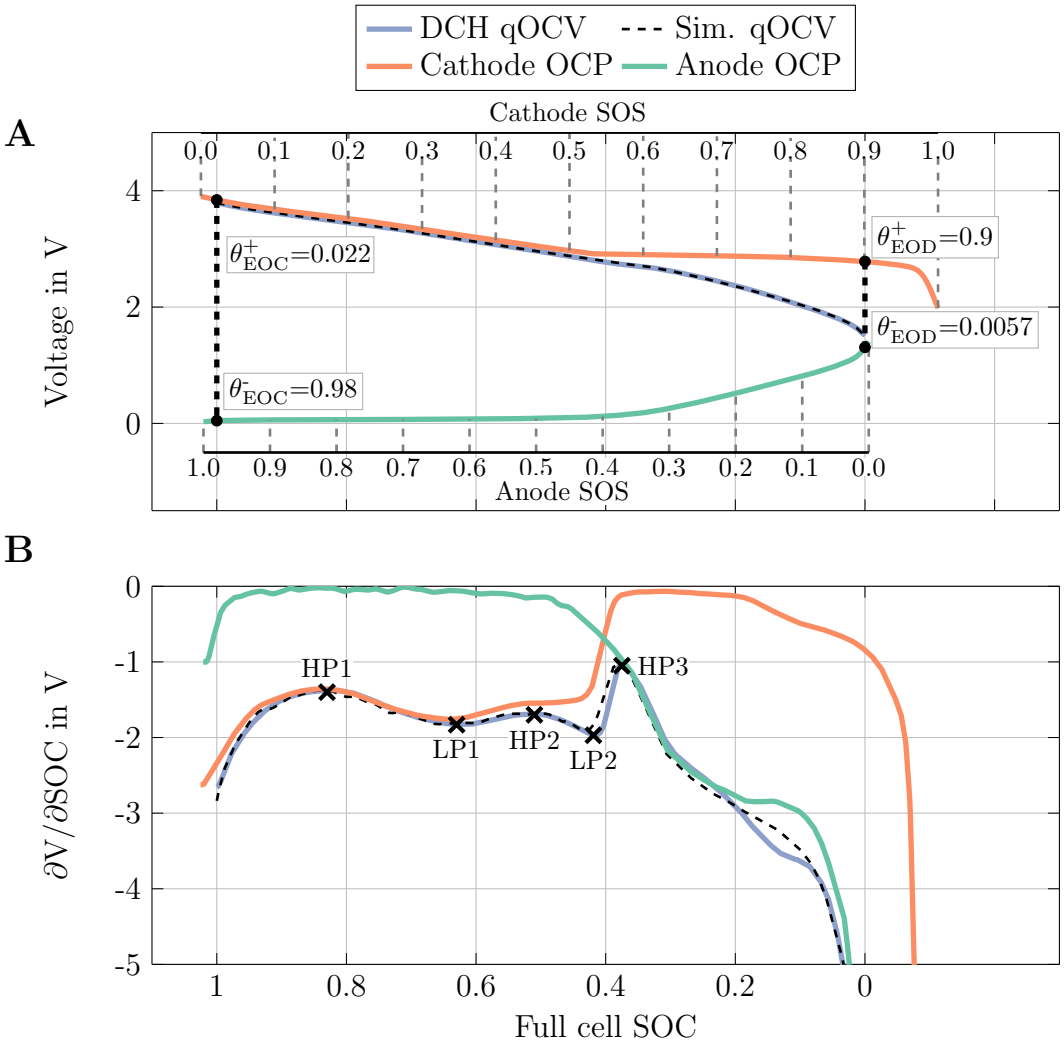

Figure 4.12: Balancing of the commercial SIB conducted by Schütte et al. [155].
A: Anode and cathode OCP and resulting full cell voltage, with SOS indicating the state of sodiation.
B: Anode, cathode, and full cell differential voltage (measured and simulated). We analyze five characteristic peaks to track the degradation modes.

SOC, highlighting voltage plateaus and phase transitions. For our analysis, we identify five peaks that are characteristic for the investigated SIB with their x and y value, i.e. HP1, LP1, HP2, LP2, HP3 as described in Table 4.3.

As battery cells age, the OCPs of their individual electrodes undergo characteristic shifts [5, 157]. Figure 4.13 illustrates the simulated electrode potential shifts associated with the degradation mechanisms LSI, LAM_{NE}, and LAM_{PE}, for both the sodiated and desodiated states, based on the half-cell balancing of the SIB. Figure 4.13A depicts a 10 % LSI, corresponding to a 10 % loss of cyclable sodium. As sodium inventory decreases, the

electrodes are no longer fully utilized, causing the anode potential to rise. In the sodiated state of the negative electrode, this higher anode potential results in a slight capacity increase, illustrated by the light green region. This occurs because more cathode capacity can now be used while still reaching the upper end-of-charge voltage of 3.8 V. In the DVA, this anode shift is primarily reflected in a reduction of LP2 and HP3. Figure 4.13B shows a 10 % loss of active material in the negative electrode in its desodiated state. This loss reduces the amount of sodium that can be stored and released, causing the anode OCP to compress. While the relative shape of the anode potential itself remains unchanged, the compression results in a lower anode potential at higher SOCs, meaning the end-of-discharge voltage is reached more quickly. Since the cell continues to operate at 3.8 V, negative anode potentials may occur, increasing the risk of sodium plating. However, as already noted, the anode curve was not determined beyond the half-cell balancing shown in Figure 4.12A. To still illustrate the degradation mode, we use extrapolation, but emphasize that the actual course of the DV at high SOCs cannot be accurately represented as a result. If sodiated active material is lost at the anode, two effects emerge: First, less sodium is available for cycling, and, second, the anode's reduced capacity further lowers its potential curve (Figure 4.13C). Although the charge potential remains unchanged for both electrodes, the anode's end-of-discharge voltage, and consequently that of the full cell, shift, similar to the LSI scenario in Figure 4.13A. Figure 4.13D illustrates the loss of 10 % desodiated active material in the positive electrode. Here, the cathode potential at the end of charge remains unchanged, but the cathode curve is compressed, leading to a lower potential at the end of discharge. In our targeted SIB, this is associated with a pronounced potential drop. In the case of sodiated cathode material loss in Figure 4.13E, the discharge potential of the electrodes remains unchanged compared to the pristine state. At the end of charge, the anode potential is higher, which results in a higher cathode potential to maintain the 3.8 V end-of-charge voltage.

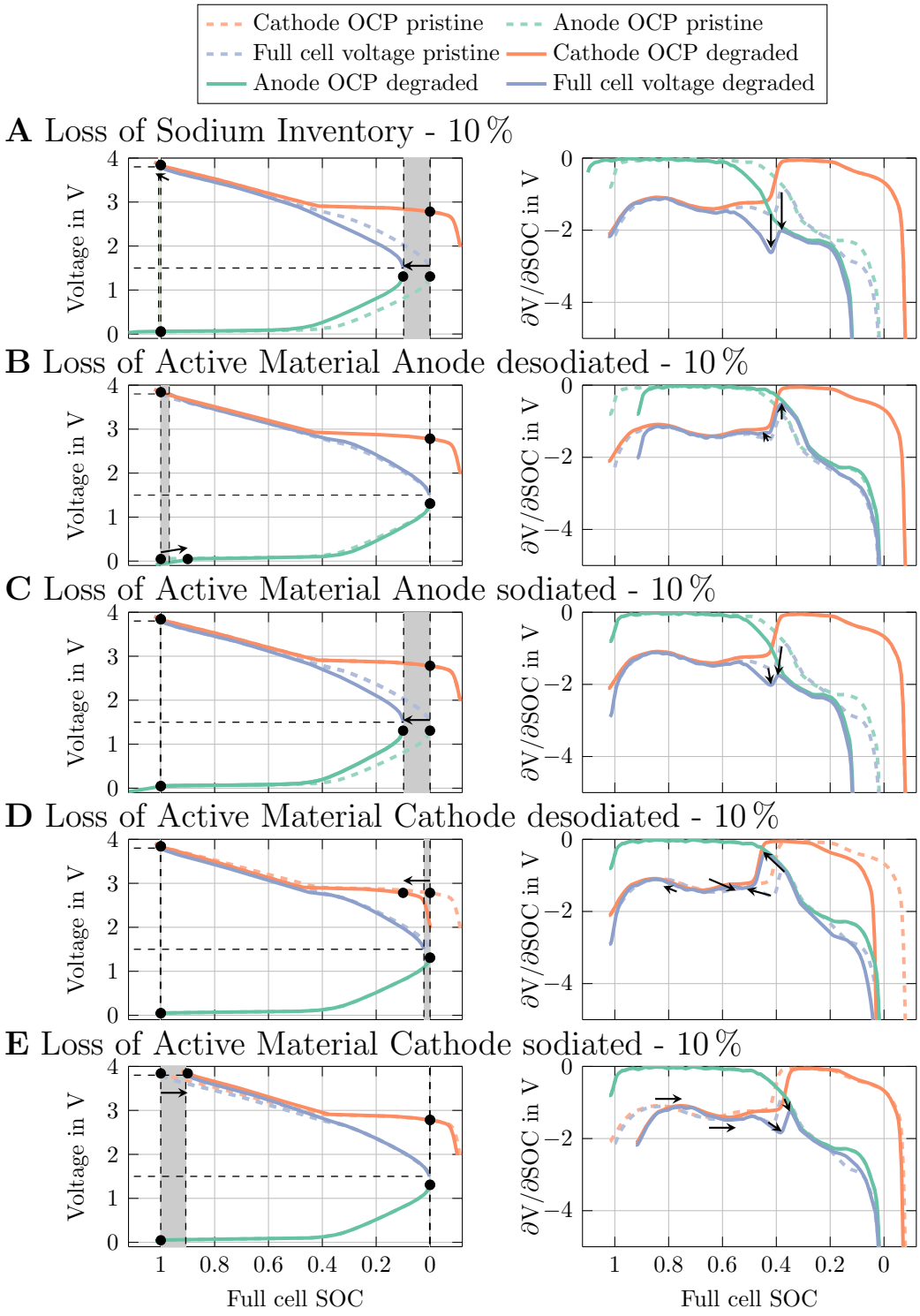

Figure 4.13: Different degradation modes and their impact on full cell voltage through half-cell potential variations are illustrated. The gray area represents capacity loss, while the light green area indicates a stochiometric offset that results in capacity gain. The black dots indicate shifts in the OCP and full cell OCV. The horizontal dashed lines mark the operating range of the full cell. The right panel displays DV curves for both half cells and the full cell.

To facilitate the analysis of the DV curves, we shift the curves in Figure 4.13B and Figure 4.13E so that they start at a full cell SOC of 1. This adjustment is consistent with the common practice in the literature of performing DVA on the discharge curves, which is also followed in this work. Importantly, we note that the shifted DVA (from Figure 4.13B) in Figure 4.14A, is the only case where HP3 rises and HP2 has an nearly horizontal shift.

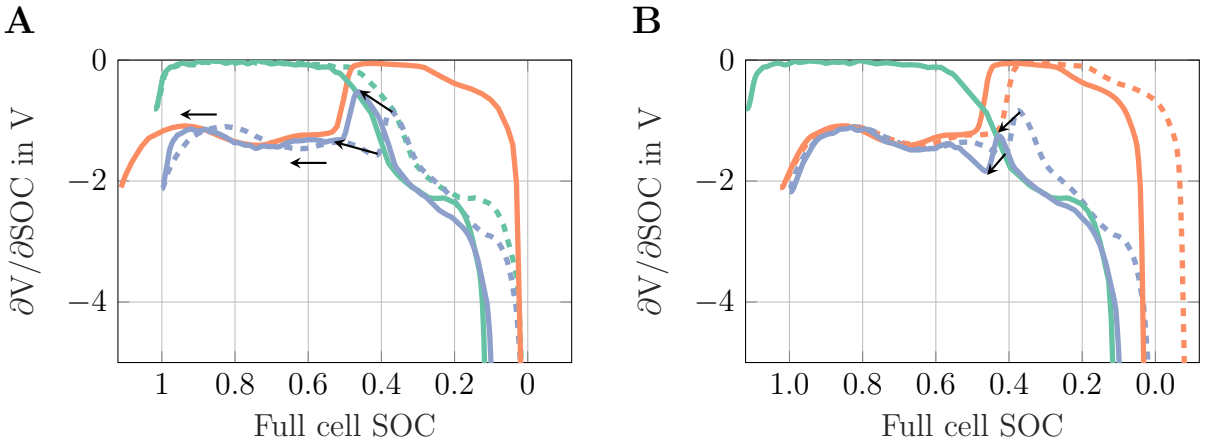

Figure 4.14: Adjusted DV curves from
A: 4.13B (loss of active material anode desodiated).
B: 4.13E (loss of active material cathode sodiated).
Shifting the curves to an initial SOC of 1 ensures their comparability in the subsequent analysis.

After discussing the theoretically occurring shifts in the DVA, we now consider the measured DVs across the RPTs for different conditions. To determine the DV, the gradient of the discharge voltage curve is calculated with respect to the charge throughput, after it was smoothed using the MATLAB `smooth` function with a smoothing factor of 500. For the feature analysis and feature importance analysis, as discussed, we identify five relevant peaks in the DV curves. These peaks are determined using the MATLAB function `findpeaks`, where we specify a minimum height and peak prominence for clearer identification.

Figure 4.15 shows the change in the DVs over the course of the RPTs with respect to the capacity. Given the previously described heterogeneity in aging rates, three representative cells are presented in each row: In the first panel, a cell with a relatively low relative capacity loss is shown; in the second, one with a moderate relative capacity loss; and in the third, a cell with a high relative capacity loss compared to the other cells under the same cycling condition. The comparison is intended to illustrate whether, as aging progresses, the peaks in the DV curves shift and start to overlap, which could make it increasingly challenging to clearly identify and separate individual peaks.

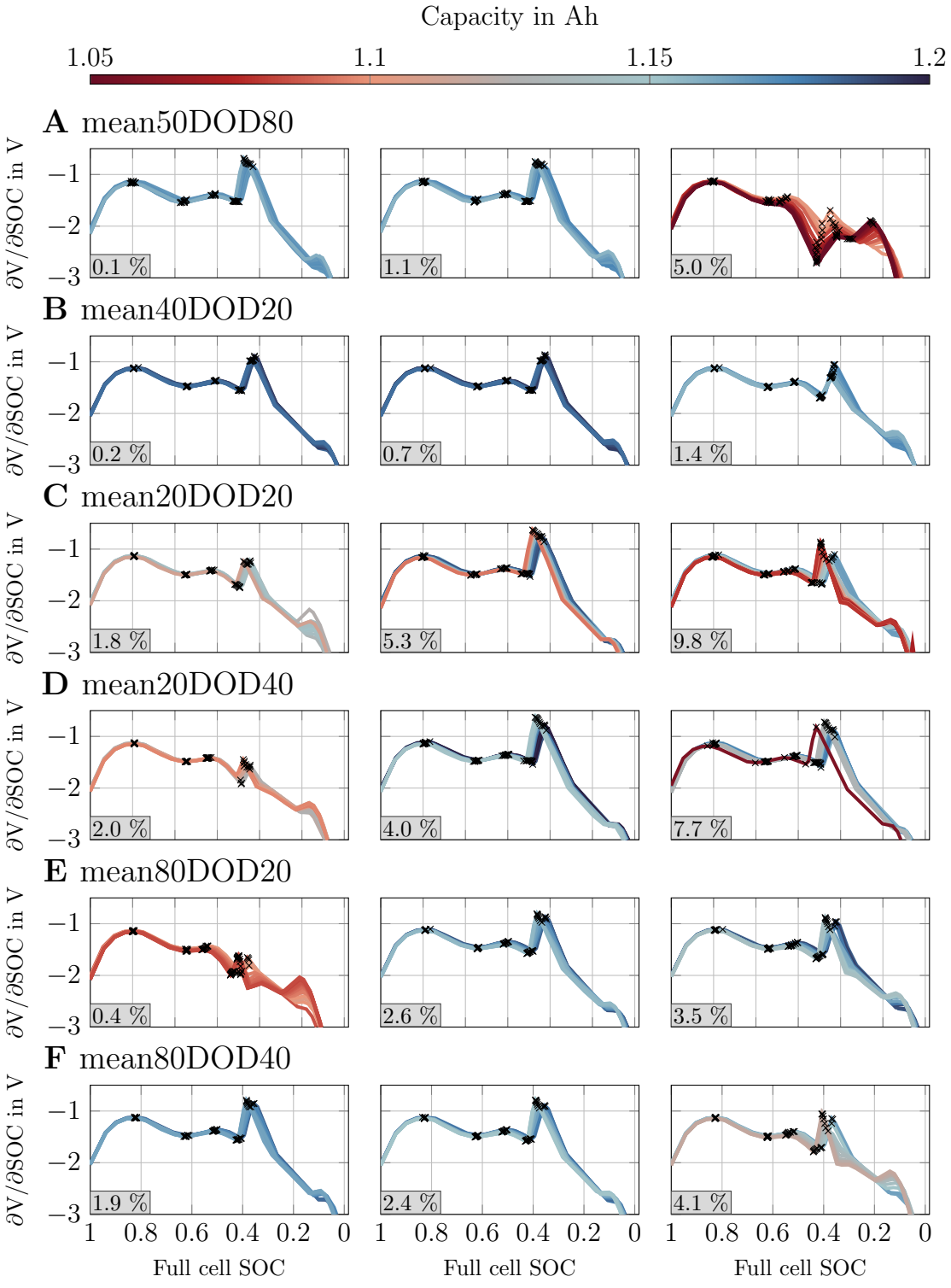

Figure 4.15: DVA for three representative cells within each cycling condition. The first panel reflects a cell with low relative capacity loss, the second panel a cell with moderate relative capacity loss, and the third panel a cell with high relative capacity loss. The relative capacity loss is shown in gray in the lower left corner for each panel.

It is first noticeable that cells in the first and third panels of Figure 4.15 often show a relatively different DV shape and evolution compared to the middle panel. We suspect this heterogeneity arises from the suggested variations in initial aging states or manufacturing differences [113]. To ensure comparability and a clearer analysis of typical degradation behavior, we focus on the cells in the middle panel.

Under the condition mean50DOD80, shown in Figure 4.15A, we observe a slight leftward shift of all DVA features across all aging rates. Additionally, for the first two panels HP3 shifts slightly upward. For the right panel, HP3 decreases significantly. For the condition mean40DOD20, shown in Figure 4.15B, a similar overall trend is observed, though HP3 shifts slightly downward and to the left instead of upward, and the overall leftward drift of all peaks is less pronounced. In the cases with low mean SOC, i.e., mean20DOD20 and mean20DOD40, shown in Figure 4.15C and D, a different pattern emerges: the steepness of the increase of HP3 and the extent of the leftward shift are much more pronounced. Additionally, we observe the previously mentioned distinct horizontal left shift of HP2. For the right panel we see that HP3 first decreases and then increases in height with progressive aging. In the cases with high average SOC (mean80DOD20 and mean80DOD40), shown in Figure 4.15E and Figure 4.15F, all peaks, except for HP3, shift slightly downward and to the left or remain consistent in height. HP3 initially moves downward and to the left, then shifts upward and to the left, resulting in only a minimal increase in the peak. Overall, it is noticeable that HP2 exhibits a similar downward-leftward movement in almost all conditions, with the exceptions being mean20DOD20 and mean20DOD40. In contrast, HP1 appears relatively static across all conditions.

Based on our preliminary investigations in Figures 4.13 and 4.14, the cycling conditions offer insights into the underlying degradation mechanisms. Notably, an increase in the most prominent peak (HP3) occurs only in the case of loss of active material in a desodiated anode and loss of active material in a desodiated cathode. In the cycling conditions with low SOC (mean20DOD20 and mean20DOD40), where the cathode is almost fully charged, the dominant degradation mechanism is likely the loss of active material in the desodiated anode. This is further supported by the observed horizontal movement of HP2. At these low SOCs, the low-potential plateau region of sodium storage is primarily active, implying that sodium ions are predominantly intercalated rather than adsorbed on the surface [158]. In contrast to the predominant SEI formation observed at higher SOCs, which would lead to a decrease in HP3, these cycling conditions suggest mechanical degradation of the anode materials, as reported in the literature [159, 160]. Under conditions with high SOC (mean80DOD20 and mean80DOD40), based on the preliminary investigations, the loss of active material in the sodiated anode is a plausible mechanism for the declining flank, followed by loss of desodiated cathode material for the increasing flank. Additionally, the decrease in LP2 can be attributed to LSI (Figure 4.13A). This is supported by the electrochemical states of the cell under these conditions, where the cathode is desodiated and the anode sodiated. It is plausible that one electrode is initially limiting, followed by the other, as observed in the literature [149]. The literature also confirms that, especially at high SOCs,

there is a growth of the SEI, which further supports the hypothesis of additional LSI [161].

For intermediate SOCs (mean40DOD20 and mean50DOD80), slightly different characteristics emerge in the DVA peak evolution. In the condition with a high DOD, where low SOCs are also reached, the aging effect due to the loss of active material in the anode (desodiated) possibly dominates, which is observed through an increase in the HP3 peak, albeit with a lower amplitude than in the low mean SOC cases. This is particularly interesting because, in this case, various SOC ranges are included in the cycling triggering different aging effects. In the mean40DOD20 condition, both loss of active material on the sodiated electrodes as well as LSI emerge as relevant degradation mechanisms. This is due to the fact that, during cycling, both electrodes are periodically in a similarly sodiated state, which promotes aging processes on both electrodes.

Overall, our results indicate that loss of active anode material, particularly at low SOCs, is possibly a dominant aging effect. Correlating these findings with other non-destructive measurement methods, as discussed in Section 4.3, may help substantiate this hypothesis. A detailed ex-situ analysis of the cells to confirm the hypotheses will be conducted in the future.

4.2.2 EIS Measurements

EIS is an increasingly established method for the non-destructive analysis of cells. It has already been demonstrated in the literature that the impedance of a battery correlates with temperature, SOC, and aging [162, 163]. With measurement times on the order of seconds, EIS enables rapid evaluation of cell behavior with minimal impact on total testing duration. In addition, EIS provides information on processes at different frequencies, whereas DVA reflects the DC behavior of a battery cell.

EIS is based on perturbing a system at equilibrium by applying a small sinusoidal signal, either an AC voltage (potentiostatic excitation) or an AC current (galvanostatic excitation). By analyzing the system's behavior across different frequencies, EIS provides a simplified representation of complex electrochemical processes. Slow processes dominate at low frequencies, while fast processes appear at high frequencies. The method requires the system to be a linear and time-invariant (LTI) system, meaning three conditions must be met: First, the output signal is solely caused by the input signal. Second, the relationship between input and output is linear. And last, the system's properties do not change over time. EIS models the system's response, with voltage as the output in galvanostatic excitation, and characterizes it using a transfer function. The electrochemical behavior is then often represented by equivalent circuit models (ECMs). [163] The complex impedance is calculated as the ratio of the complex output voltage to the complex input current. The applied current is given by:

$$i(t) = i_0 \sin(\omega t) \tag{4.5}$$

The measured output voltage is:

$$v(t) = v_0 \sin(\omega t + \phi) \tag{4.6}$$

The impedance Z is calculated by dividing the measured voltage by the current at each excitation frequency during the EIS measurement. Due to the lack of literature on the use of EIS-based aging analysis in SIBs, we adopt a data-driven approach by selecting and evaluating relevant features directly from the measurements. We extract three characteristic points from the Nquist plots, each defined by its real and imaginary parts. To identify local extrema, we apply MATLAB's `findpeaks` function, as previously used in the feature analysis of the DVA. The first point is the ZC, which marks the intersection of the impedance curve with the real axis, i.e., the point where the imaginary part of the impedance is zero and the cell behavior is purely ohmic [116]. Next, we examine the HP, which corresponds to the peak of the semi-circle in the Nyquist plot. This point represents a local maximum in the absolute imaginary part and was previously used by Baumhöfer et al. [116] in the context of aging analysis. The third point is the LP, which marks the transition between charge transfer and diffusion effects. The distance between ZC and LP corresponds to the charge transfer resistance and possibly an SEI resistance and is thus also included in our evaluation [163]. The diffusion processes represented in the EIS spectrum by a straight branch towards higher imaginary and real parts of the impedance is not shown in the presented data, because the multi-sine method we used in our measurements is not generating information at frequencies as low as e.g. mHz. In general, inferring aging effects from EIS measurements is a relatively challenging area of research. This is particularly true for 18650-type cells, where geometric factors at the cell level can overshadow the electrochemical signature, potentially causing misleading results. This limitation must be taken into account when analyzing the results presented in this section. [164]

Figure 4.16 illustrates the evolution of the complex impedance over aging in the Nyquist diagram. In contrast to the DVA, a different set of cells is used here, specifically the 12 cells for which EIS measurements were conducted. The following numbers of cells were subjected to EIS measurements during RPT:

- Five cells for the mean50DOD80 condition.
- One cell each for the mean40DOD20, mean20DOD20, and mean80DOD20 conditions.
- Two cells each for the mean20DOD40 and mean80DOD40 conditions.

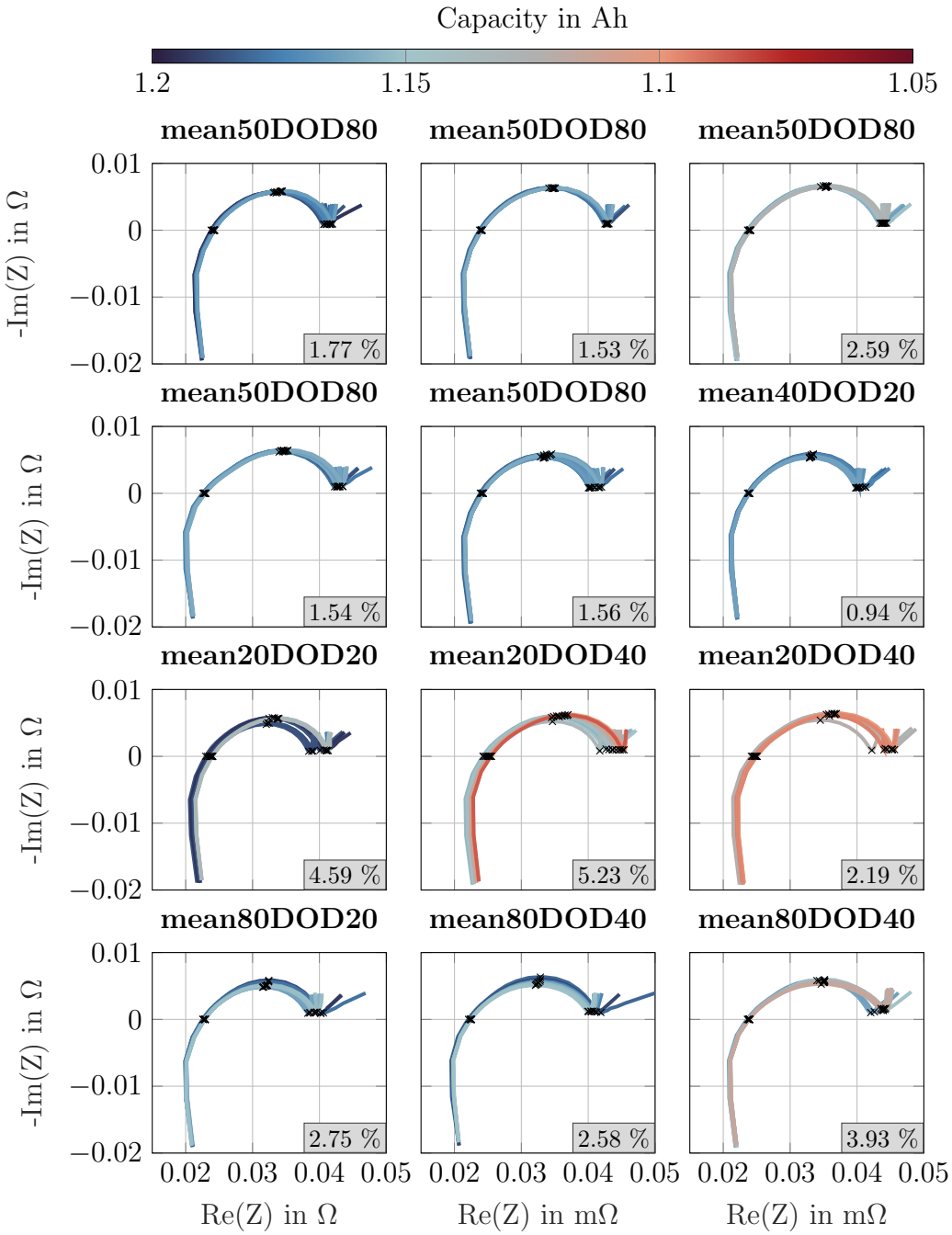

Figure 4.16: EIS measurements over aging for different cells. The relative capacity loss of the specific cell is shown in the lower right corner of each panel. It is evident that the width of the semi-circle generally increases with aging except for the conditions with high mean SOC.

In all cases, the Nyquist plots exhibit a broad semi-circle rather than a clearly defined semi-circle or two distinct circles. This suggests that the resistance contribution from the SEI is relatively small and superimposes with the charge transfer arc, resulting in a single,

flattened circle [165]. To separate these contributions, we analyze the evolution of the HP relative to the ZC: a horizontal shift of HP with a stable ZC can indicate an increase in the SEI resistance. In contrast, a vertical upward shift of HP points to additional charge transfer resistance from electrode degradation mechanisms, such as particle isolation or electrode cracking [165].

Within the mean50DOD80 condition, it is noticeable that despite very similar capacities and aging rates the changes in EIS behavior do not follow a consistent pattern. A slight but reproducible rightward shift of the spectrum is observed, which becomes more pronounced at lower frequencies (i.e., higher values of the real part of the low point, LP). This trend, an increase in the real part of LP with progressive aging, is generally observed across all cycling conditions, although the absolute position of LP varies and is not consistently reproducible between conditions. Typically, an increase in the real part of ZC is associated with electrolyte degradation, assuming the conductivity of the current collectors and tab welds remains constant [165]. In contrast, for the cell cycled under the mean40DOD20 condition, no significant ZC shift is observed. Instead, we note a slight decrease in the imaginary component of HP and a small reduction in the real part of LP. Although these changes are subtle, they suggest that SEI formation is likely not a dominant aging process in this case, which is consistent with earlier discussion. While somewhat unusual, such behavior may indicate an extended stabilization or break-in phase for this specific cell [166]. For the low SOC conditions (mean20DOD20 and mean20DOD40), we observe a pronounced increase in ZC, along with increases in both the real and imaginary components of HP, as well as in the real part of LP. The horizontal shifts of LP, HP, and ZC are of similar magnitude, indicating that SEI growth is not the dominant degradation mechanism in these cases. Instead, the observed impedance behavior points to a different aging process, possibly related to mechanical degradation such as particle fracture, as discussed in [165]. In contrast, under high SOC conditions (mean80DOD20 and mean80DOD40), the position of the HP and LP peaks does not change uniformly with aging. Instead, it initially decreases before gradually increasing. This trend is consistent with the shift in aging behavior previously inferred from the DVA results. The decrease in the imaginary component of HP and in the real part of LP may further suggest post-manufacturing break-in or a delayed stabilization process, sometimes observed after cell formation or for sodium plating [167].

A more detailed, quantitative correlation analysis of these EIS features with capacity loss will be presented in Section 4.3.

4.2.3 qHysteresis

Figure 4.1 illustrates the voltage difference between the C/20 discharge and C/20 charge curves, a phenomenon referred to as hysteresis that can persist even after relaxation. This path-dependent effect arises because the OCV is influenced by the recent current history. [168] The underlying causes of voltage hysteresis include mechanical stress, thermody-

namic entropy effects, and microscopic distortions within the active material particles. Thermodynamic hysteresis results from variations in intercalation rates among individual particles, which can also induce mechanical stress through volume changes and surface tension [169]. Furthermore, hysteresis is linked to cell expansion, as well as rate and power capability [168]. A detailed investigation of these mechanisms is beyond the scope of this work. Instead, our focus lies in tracking the change of peaks as an indicator of aging, similar to DVA and EIS.

In our work, we determine the voltage not based on the fully relaxed state of the cell, but during a C/20 discharge and charge in the RPT. To clarify this distinction, we refer to the hysteresis in the following as qHysteresis. In the qHysteresis plots, we identify two prominent extrema, denoted as the LP and HP, using MATLAB's `findpeaks` function.

Figure 4.17 illustrates the qHysteresis over aging for different cycling conditions across the same cells as for the DVA. Under all conditions, qHysteresis increases with progressive aging. Notably, the LP consistently shifts leftward, corresponding to higher SOCs, while the HP either remains stable or shifts to the left, depending on the cycling condition. The observed shifts in qHysteresis are partly aligned with those seen in the DVA. Whether the LP or HP is more relevant to capacity loss will be further examined in Section 4.3.

A notable observation appears in the third panel of Figure 4.17D, where qHysteresis is significantly more pronounced and coincides with a lower remaining capacity. In this case, our peak detection algorithm also struggles to reliably identify the extrema. A more detailed interpretation would require a better understanding of the underlying mechanisms of hysteresis and cell-specific factors influencing its change with aging, which is beyond the scope of this work. The cause of this change in qHysteresis over aging is not further investigated within the scope of this work and will be discussed in future work.

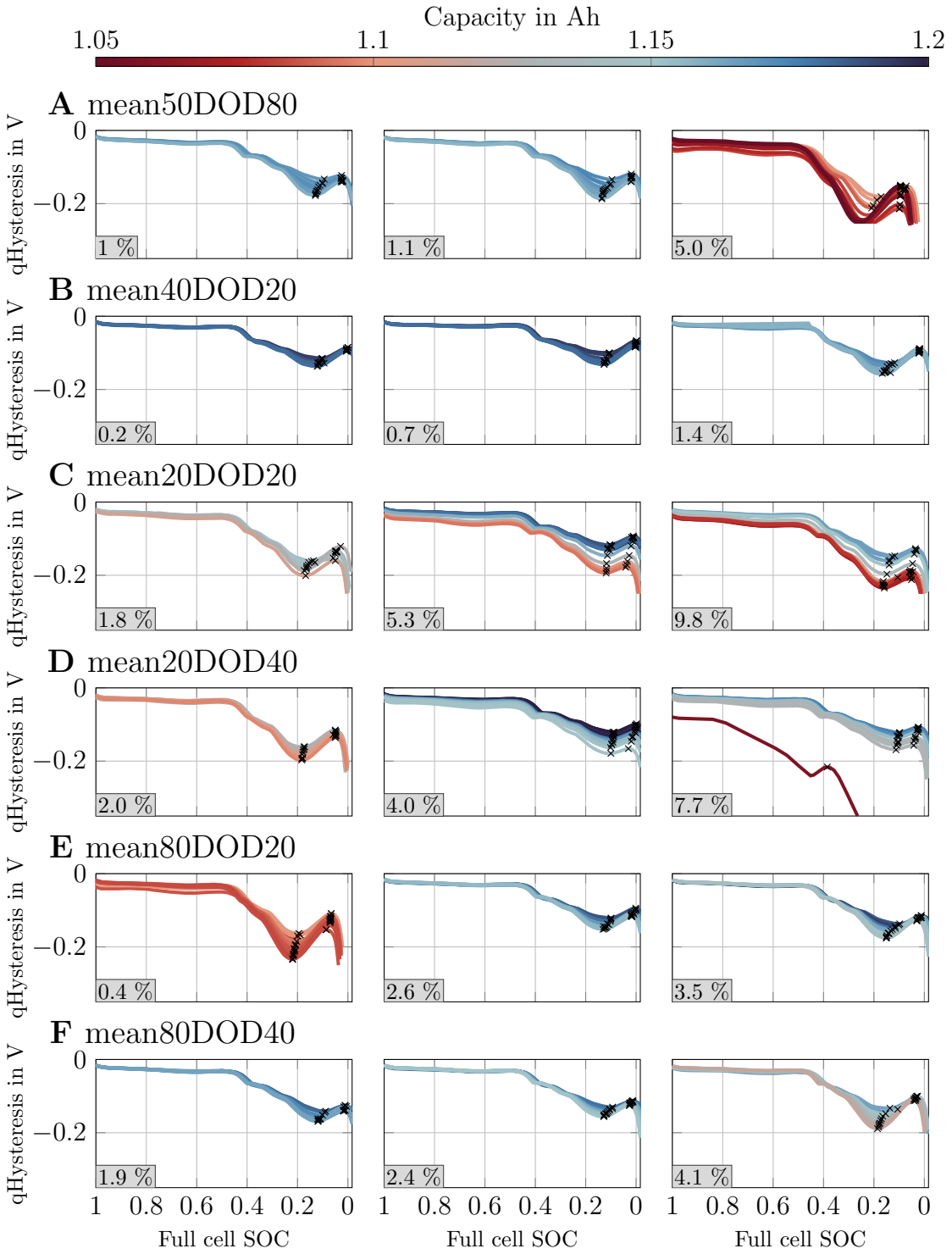

Figure 4.17: Exemplary qHysteresis curves over aging across all six conditions. The first panel represents a cell with low relative capacity loss, the second with medium and the third with high loss. The relative capacity loss is indicated in the left corner of each panel.

4.3 Correlation and Discussion

Based on the observations from DVA, EIS, and qHysteresis, we now aim to identify which features show the strongest correlation with capacity loss across the various cycling conditions. Therefore, we conduct a correlation analysis between the extracted feature values and the capacity loss.

Figure 4.18 presents the Pearson correlation coefficients between the features listed in Table 4.3 and the absolute capacity loss in Ah observed during the RPTs. In this analysis, the capacity loss due to aging is counted as a positive value. The Pearson correlation coefficient is calculated according to Equation (4.7).

$$r_{xy} = \frac{\sum_{i=1}^{n}(x_i - \bar{x})(y_i - \bar{y})}{\sqrt{\sum_{i=1}^{n}(x_i - \bar{x})^2}\sqrt{\sum_{i=1}^{n}(y_i - \bar{y})^2}} \tag{4.7}$$

$X = \{x_1, \ldots, x_n\}$ represents the capacity loss values measured over RPT, while $Y = \{y_1, \ldots, y_n\}$ represents the corresponding values of the specific feature. $\bar{x}$ and $\bar{y}$ are the means of the respective samples. The resulting $r_{XY} \in [-1, 1]$ indicates the direction and strength of the linear relationship between the capacity loss and the considered feature. A positive value suggests that larger feature values are associated with a higher capacity loss, while a negative value indicates an inverse relationship. As common in literature, we assume that correlation is high if $|r_{XY}| \geq 0.8$, which is indicated in Figure 4.18 by the black dotted lines.

We can see that the correlation coefficient for the condition mean50DOD80 does not show a clear relationship between different feature values and the capacity loss, as most of the correlation values are outside the significance boundaries. This is likely because at high DOD, multiple aging effects are triggered simultaneously, and thus, feature shifts in the OCV-based measurements, i.e., DVA and qHysteresis, overlap. Only the ZC from the EIS measurements shows a comparably high and positive correlation, indicating that higher ZC values are generally associated with greater capacity loss across many cells, which in turn suggests that LSI may be a dominant degradation mode contributing to the cells' overall aging. For conditions with smaller and medium DOD, i.e., the conditions mean40DOD20, mean20DOD20, mean20DOD40, mean80DOD20, mean80DOD40, the value of HP2, as well as LP1, and the location of HP2 and HP3 ($HP2_{loc}$ and $HP3_{loc}$), show a consistently high correlation under almost all cycling conditions. This is likely due to their direct correlation with the loss of sodium inventory (see Figure 4.13A). The generally low correlation of the difference between two DVA peaks (Diff HPX/LPX) indicates that aging is primarily associated with loss of desodiated electrode material, as strong relationships are typically absent in such cases (see Figure 4.13B and D).

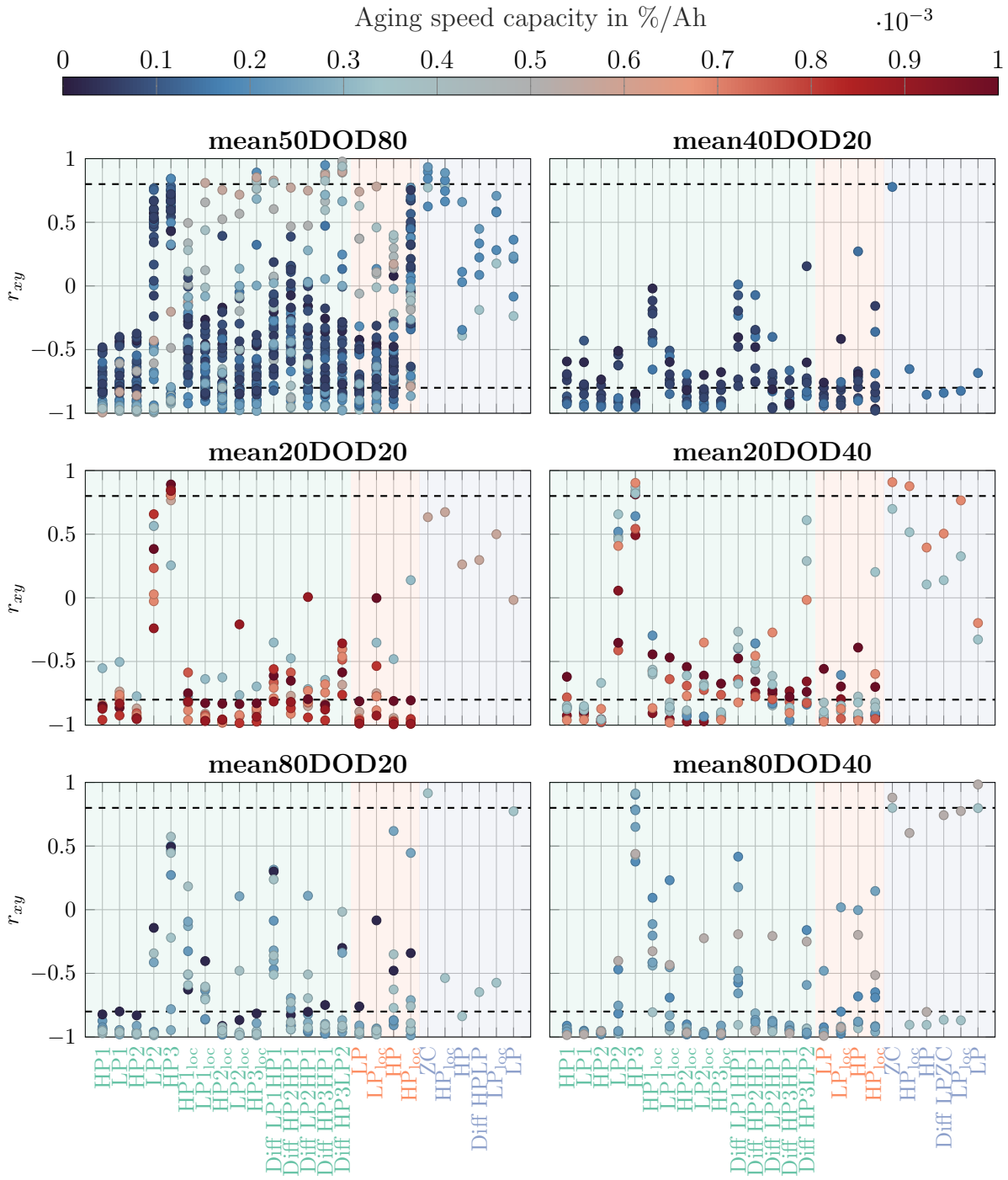

Figure 4.18: Correlation of the features with capacity loss across all six conditions. Each point represents one cell, with the color of the point corresponding to the aging speed in terms of capacity. The dashed lines at 0.8 and -0.8 indicate strong correlation. indicates features of the DVA, features of the qHysteresis, and features of EIS, respectively. Since we performed EIS measurements for 12 cells, there are fewer points, i.e. cells, illustrated for the EIS features.

In general, for the conditions that induce the most severe aging, we observe strong correlations for both the x- (SOC) and y-values (magnitude) of HP1, LP1, HP2, and HP3. It is also apparent that, for the conditions mean50DOD80 and mean40DOD20, the correlation between the value of HP3 and capacity loss is positive, meaning the peak decreases as aging progresses. In contrast, the correlation is negative under the other conditions, indicating that the peak increases with aging. Generally, the LP and HP of the qHysteresis also correlate strongly with the capacity loss of a cell except for the mean50DOD80 condition where we assume that several aging mechanisms overlap. Generally, the LP and the LP's location of the qHysteresis correlate more with capacity loss than their respective HP values. Regarding the EIS measurements, only the ZC feature shows a good correlation with the aging of the battery cells across all conditions. It is widely recognized that this feature provides an indication of aging in the current collectors or the electrolyte [165].

A quantitative representation of the most strongly correlating features for each cycling condition is shown in Table 4.4. Only cells whose relative capacity loss falls within the interval $[\mu - \sigma, \mu + \sigma]$ were considered, in order to capture typical aging behavior and minimize the influence of statistical outliers.

Condition	Feature	Avg. correlation
mean50DOD80	ZC	0.81
	HP1	-0.81
	LP1	-0.78
mean40DOD20	HP3	-0.91
	LP	-0.88
	DiffHP3HP1	-0.87
mean20DOD20	HP_{loc}	-0.98
	HP	-0.97
	$HP2_{loc}$	-0.97
mean20DOD40	HP2	-0.95
	LP	-0.92
	LP1	-0.91
mean80DOD20	HP2	-0.96
	$HP3_{loc}$	-0.96
	LP1	-0.96
mean80DOD40	$LP2_{loc}$	-0.97
	HP2	-0.97
	$HP3_{loc}$	-0.96

Table 4.4: For every condition we determine the three features that correlate the most with the relative capacity loss. It should be noted that we only consider cells whose capacity losses lie inside the interval [μ-σ, μ+σ] within a cycling condition. The cells in correspond to the features of the DVA, the cells in to the features of the qHysteresis, and the cells in to the features of EIS, respectively.

Overall, we observe that the DVA features are particularly important: the first peaks, which are associated with cathode aging, show a strong correlation with capacity loss,

both in their value and their location. Additionally, the location of HP3 serves as a strong indicator of aging under high mean SOC conditions. In general, the examined features exhibit a high correlation with cell aging, except in the case of mean50DOD80, where even the most correlated features show comparatively low correlation. For lower mean SOCs, the qHysteresis features become more relevant, suggesting that it may serve as a sensitive indicator when cells operate predominantly in the lower SOC range.

4.4 Conclusion

In this chapter, we presented the results of a large-scale aging study on commercial SIBs, data that is rarely found in the literature. All cells were cycled at a constant temperature of 25 °C and a charge/discharge rate of 2C/2C, but with varying mean SOC and DOD. After more than 4,000 EFC, they exhibited significantly different aging behavior in terms of capacity and resistance across the six cycling conditions. In contrast to typical graphite-based lithium systems, cycling around 50 % SOC with a high DOD led to minimal capacity loss. In fact, similar to the SiC-containing lithium-based cells investigated by Willenberg et al., we observe particularly strong aging at low SOC. Recent literature suggests this may be mechanically driven, which would also align with Willenberg et al.. Since both Willenberg's work and this study used 18650-type cells, this degradation might be influenced by cell geometry [147].

The large number of cells per condition provided a crucial advantage in analyzing variability in aging behavior. Even cells that initially appeared nearly identical under the same cycling conditions diverged significantly over time. For instance, in the mean20DOD40 condition, a substantial spread in capacity loss was observed: while two out of eight cells exhibited particularly high aging rates, the others aged more slowly. Such variability demonstrates that relying on only a few cells could have produced misleading conclusions. Furthermore, some features that correlate strongly with aging across the full dataset might have appeared insignificant in smaller samples, underscoring the importance of a sufficiently large number of test cells, especially when working with early-commercial SIBs.

Overall, our analyses used in this work, i.e., DVA, qHysteresis, EIS, each contribute to a non-destructive investigation of battery cell aging. Particularly, the DVA revealed dominant degradation modes for our SIB. For instance, loss of active anode material (desodiated) and LSI appear to be major degradation modes for the low mean SOC cycling. Furthermore, we capture the complex interactions between qHysteresis and the capacity and observe strong correlation of qHysteresis features with capacity loss under conditions where capacity fade is most prominent.

Moreover, the investigated SIBs exhibit very favorable aging behavior within the operating ranges described in Chapter 3, as the pronounced aging and hysteresis effects at low SOCs

are not relevant for the application. Across all cells and conditions, a median capacity loss of only 2 % is observed after approximately 4,000 EFC. Considering the most relevant operating ranges for the high-power application, the median capacity loss falls below 1 %, indicating that these SIBs offer a promising lifetime for practical deployment in our target application.

5 Sodium-Ion Diagnostics for Battery Management Systems

Battery state estimation within a BMS is becoming increasingly challenging as new cell technologies are expected to replace existing ones in specific applications [79, 170]. While SIBs share many similarities with LIBs, the differences in voltage profiles, operating ranges, and degradation patterns, analyzed in Chapter 4, can significantly impact estimation accuracy. Therefore, it is essential to quantify these effects for the specific cell and application to determine which existing BMS algorithms remain reliable and to set realistic expectations for SOC and SOH estimation, ultimately enabling rapid integration of new cells in existing systems.

In the literature, a wide array of algorithms for estimating internal battery states exist. They range from conventional coulomb counting [82, 83] and model-based techniques [84–86, 171] to data-based methods [87–91, 172], whereas each method has individual advantages and limitations [173, 174]. However, selecting the most suitable algorithm for a particular application presents a challenge due to the limited evaluation of algorithms found in literature across diverse operational scenarios, making direct performance comparisons difficult [175]. Often, algorithms are evaluated for only one specific load profile, such as the Worldwide Harmonized Light Vehicles Test Procedure (WLTP), at a single temperature [82, 84, 89, 171], assume ideal BMS measurements, and one initial SOC [82, 84, 85, 171] using a single statistical metric such as RMSE [87, 176]. Yet, in reality, batteries experience various operation scenarios, influencing the algorithm's overall performance [79, 177]. Without a comprehensive evaluation of BMS algorithms, diagnostic algorithms might fail to perform reliably in specific situations, even if they perform well on average [79]. Depending on the context, this may require compromises in accuracy to ensure greater robustness. To address these challenges, researchers have already developed methods for evaluating diagnostic algorithms. For instance, varying load profiles [177, 178] and various aging states [178] were considered for SOC algorithm assessment. Simulations were performed under the influence of disturbances such as noise, offset, or faulty initialization [86, 178]. Klee Barillas et al. [178] and Campestrini et al. [175] evaluated various SOC algorithms using a point-based system. The points achieved in different categories were graphically compared for all the algorithms investigated in a radar chart, allowing for a visual comparison based on individual criteria. However, often, the scale used lacks direct physical meaning. Moreover, existing evaluation methods typically focus only on measuring algorithm accuracy, overlooking aspects like bias and precision. This oversight can lead to misleading results and inadequate algorithm selection, as highlighted in the literature [176]. Additionally, these methods often concentrate

solely on SOC estimation, neglecting a broader evaluation across all BMS-relevant states, including SOH. Consequently, a comprehensive, systematic assessment of diagnostic algorithm performance for both SOC and SOH remains lacking, hindering the development of new algorithms and the selection of application-oriented algorithms for emerging cell technologies, such as the investigated SIB.

To address this gap, this chapter provides a systematic evaluation of real-time capable SOC and SOH algorithms for the investigated commercial SIB. It builds on the high-power application presented in Chapter 3 and the cell behavior characterized in Chapter 4. At the core of this evaluation is an open-source, multi-criteria framework [179] that assesses not only accuracy but also bias and precision. Algorithms originally developed for LIBs are tested on the targeted SIB to evaluate their transferability, while SOC performance is also compared with results from the original NMC/LTO system. This work does not seek to analyze every possible algorithm or condition in detail; instead, we demonstrate a practical method that enables rapid evaluation of algorithm performance. Our approach identifies performance limits and reveals challenges and opportunities in diagnostics, offering insights into the complex interplay of cell chemistry, algorithm design, and diagnostic quality.

The following chapter contains results that were published as a peer-reviewed article in the Journal *Batteries & Supercaps* under the title "Benchmarking the Transferability of Real-Time State of Charge Algorithms to Sodium-Ion Cells Using an Open-Source Diagnostics Framework" [180].

5.1 Evaluation Framework

Our evaluation framework, depicted in Figure 5.1, automates the assessment of diagnostic algorithm performance through a top-down data generation and bottom-up evaluation process. To generate evaluation data we first identify critical performance categories such as environmental, operational, and BMS-specific influences that might occur in the application of the high-power mobile application from Chapter 3. Scenario data (e.g. battery and BMS time-series data) is generated using a model-based simulation toolchain (Section 5.1.1). For each simulated scenario, we calculate a set of statistical metrics, described in Section 5.1.2, including measures of accuracy, bias, and precision. These metrics are then aggregated and analyzed across all scenarios within each category enabling the identification of trends and patterns in algorithm behavior associated with specific influencing factors like temperature or aging. After evaluating each category individually, a final summary of the results is provided, including average values per category and metric as well as aggregated data across all categories to assess overall algorithm performance.

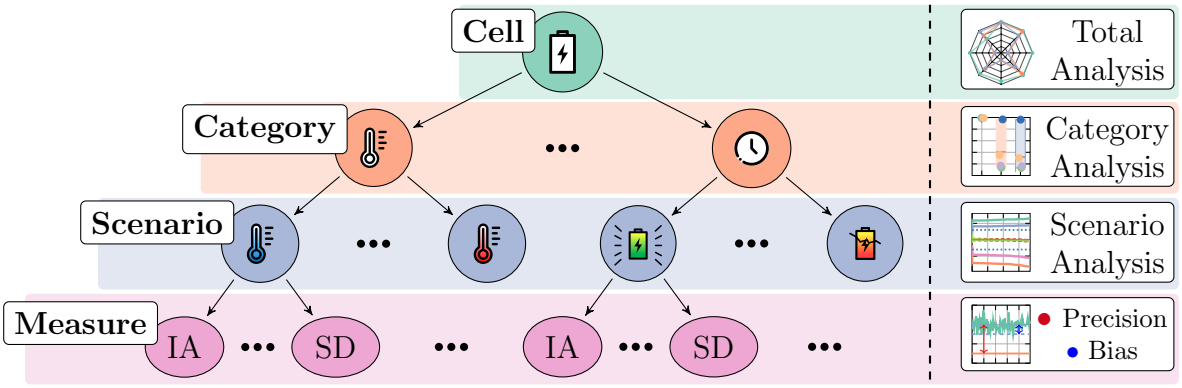

Figure 5.1: Evaluation framework consisting of a top-down data generation and a bottom-up evaluation process. We evaluate several metrics for every scenario, averaging the results for different categories (such as temperature) and cells.

5.1.1 Simulation Toolchain

Evaluating algorithms across a wide range of operating conditions using actual battery specimens would be both time-consuming and resource-intensive. As a remedy, we employ a model-based simulation toolchain, originally developed in MATLAB/Simulink, for our algorithm performance benchmarking, acting as a digital twin. This approach, depicted in Figure 5.2 adapted from Berger et al. [79], simulates the entire BMS signal path, from the load profile to the diagnostic algorithms. In addition to enabling reproducible evaluations under controlled conditions, this simulation setup provides an important initial assessment of algorithm performance and forms the basis for further validation steps, such as hardware-in-the-loop testing.

To accurately simulate battery behavior within our toolchain, we use a complex electrical model, and the aging model, both presented in Section 5.2.1. To account for different hardware designs, we emulate the BMS hardware and introduce noise, sampling effects, and offsets to the reference data based on components commonly used in modern systems [181]. These processed data serve as input for the diagnostic algorithms. The detailed steps of the BMS simulation are as follows:

1. Load profile: The simulation of a load profile that is scaled to the specific battery is the starting point of the toolchain.

2. High-precision battery model: Utilizing a high-order ECM, we simulate battery characteristics such as voltage, current, and temperature within a battery simulation toolchain. The model structure, defined in an eXtensible Markup Language (XML) file, contains the parameter values dependent on SOC and temperature. For each defined parameter, the voltage is calculated and the current state is updated. In addition to the electrical simulation, the thermal and aging behaviors are simulated.

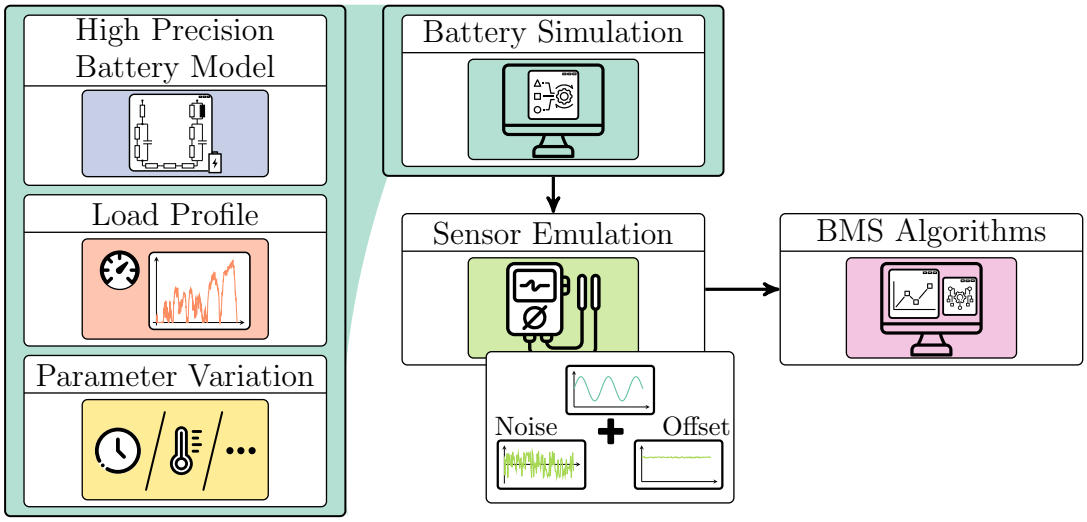

Figure 5.2: BMS simulation toolchain. A high precision battery model takes a load profile and specific environmental conditions as inputs, simulating realistic battery behavior using a battery simulation framework. The outputs are then passed through a BMS sensor emulation stage, introducing noise, offsets, and quantization to mimic real-world sensors. Finally, using different BMS algorithms we employ on-board estimation algorithms that determine the internal battery states SOC and SOH. The BMS toolchain is publicly available [179].

The thermal model divides the cell in segments and calculates the heat flow through each segment. The resulting heat is fed back to the electrical model to modify the parameters of the ECM accordingly. The independent aging simulation quantifies calendar and cyclic aging. The changes of capacity and internal resistance are calculated and fed back to the simulation framework influencing the simulation in the next time step. The reference model characteristics serve as the foundation for the establishment of the reference value, including the reference internal states such as SOC and SOH. More information about the battery simulation can be found here [110, 182].

3. Sensor emulation: The battery measurements are affected by noise, quantization, and perturbations, replicating real-world BMS hardware effects. Quantization effects are modeled based on the resolution of a BMS analogue-digital converter, with separate quantization steps for temperature, voltage (0.15 mV), and current (0.3 mA), complemented by configurable measurement noise and gain/offset parameters. The sensor system introduces for each simulation a current sensor offset of 0.025 % of the nominal capacity, a (linear) gain error of 10^{-4}, and white noise with a variance of 0.15 % relative to the nominal capacity. These values are based on a commercial sensor data sheets used in relevant applications [183].

4. BMS algorithms: The output from the BMS hardware emulation is further processed to simulate diagnostic algorithms. In this work, we evaluate commonly used, real-time capable algorithms for SOC and SOH estimation. Our focus is on evaluating these algorithms from an application-oriented perspective, emphasizing their practical performance rather than the development or tuning of the underlying BMS models. For detailed descriptions of the algorithms, we refer to the literature [184, 185].

5.1.2 Evaluation Criteria

Addressing the limitations of current evaluation practices, we introduce a set of statistical metrics for assessing diagnostic algorithm performance. They can be grouped into the following criteria. The general concept is illustrated in Figure 5.3. [176, 186, 187]

- **Accuracy** measures the difference between estimated and reference values, with maximum accuracy indicating full congruence. It combines bias (systematic error) and precision (random error).

- **Bias** describes the systematic error of a model. Measures for bias compare the position parameters of estimated and reference value, such as mean, median or mode. This allows to assess whether the algorithm systematically over- or underestimates the reference values.

- **Precision** describes the random error of a model. Measures of precision describe the variation of estimated and reference value, and allow the identification of data outliers.

When accuracy is low, distinguishing between bias and precision helps to identify the source of inaccuracy.

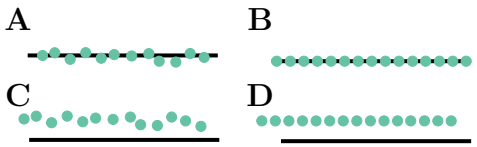

Figure 5.3: Graphical comparison of the concepts bias and precision. The black lines represent the reference values, and the dots are the estimated values.
A: Low bias, low precision.
B: Low bias, high precision.
C: High bias, low precision.
D: High bias, high precision.

In this work, we select statistical metrics for each criterion, i.e. accuracy, bias, precision, as

shown in Table 5.1. The inclusion of the Index of Agreement (IA) as an accuracy metric provides a normalized parameter, with values ranging from 0 to 1. This complements maximum error (e_{max}) and RMSE, which are well-established in the literature, offering a widely recognized basis for comparison alongside a relative measure of accuracy. The mean error (ME) is used as a measure of bias. Precision is assessed using σ. In Table 5.1, the target value denotes the metric value that should be achieved with complete freedom from errors.

Table 5.1: Statistical metrics for the evaluation of diagnostic algorithms with the indication of the target value and range of the metric. The estimated value is denoted as y while the reference value is denoted as w. e indicates the deviation of the estimated value y from the corresponding reference value w.

Criterion	Metric	Definition	Range	Target value
Accuracy	Maximum error	$e_{max} = \begin{cases} \max\limits_{i\in 1,\dots,N} e_i, & \lvert\max e_i\rvert \geq \lvert\min e_i\rvert \\ \min\limits_{i\in 1,\dots,N} e_i, & \text{otherwise} \end{cases}$	$(-\infty, +\infty)$	0
Accuracy	Root mean square error	$RMSE = \sqrt{\frac{1}{N}\sum_{i=1}^{N}(y_i - w_i)^2}$	$[0, +\infty)$	0
Accuracy	Index of agreement	$IA = 1 - \frac{\sum_{i=1}^{N}\lvert y_i - w_i\rvert}{\sum_{i=1}^{N}(\lvert y_i - \bar{w}\rvert + \lvert w_i - \bar{w}\rvert)}$	$[0, 1]$	1
Bias	Mean error	$ME = \bar{e} = \frac{1}{N}\sum_{i=1}^{N}(y_i - w_i) = \bar{y} - \bar{w}$	$(-\infty, +\infty)$	0
Precision	Standard deviation	$SD = \sqrt{\frac{1}{N}\sum_{i=1}^{N}(e_i - \bar{e})^2}$	$[0, +\infty)$	0

The metrics beyond σ and RMSE are described in more detail in the following.

Maximum error e_{max} describes the largest estimation error of all observed values and is defined by Equation (5.1).

$$e_{max} = \begin{cases} \max\limits_{i\in 1,\dots,N} e_i, & \lvert\max e_i\rvert \geq \lvert\min e_i\rvert \\ \min\limits_{i\in 1,\dots,N} e_i, & otherwise \end{cases} \tag{5.1}$$

where e_i indicates the deviation of the estimated value y_i from the corresponding reference value w_i of a single measurement. e_{max} is signed to keep the information on the direction of the error. If the absolute value of e_{max} is significantly larger than average values, it indicates the presence of data outliers.

Index of Agreement The IA developed by Willmott [188] describes not only the relationship but also the agreement between the estimated and the reference value. The IA

is a standardized metric ranging between 0 and 1, where a value of 1 indicates perfect agreement. [188] The original definition of IA [188] was refined several times, leading to the definition shown in Equation (5.2) [189].

$$IA = 1 - \frac{\sum_{i=1}^{N} |y_i - w_i|}{\sum_{i=1}^{N} (|y_i - \bar{w}| + |w_i - \bar{w}|)} \tag{5.2}$$

IA approaches the value of perfect agreement gradually, allowing nuanced comparison of relatively high-performing models [189]. As a scaled metric, IA signifies freedom from errors in the estimated values regardless of the magnitude of the value. This allows for easy comparison between different use cases and estimators and can also be interpreted without specified tolerance ranges. However, for approximately constant reference values, IA approaches values close to zero, irrespective of the estimation values, limiting the utility as a metric of accuracy in such cases.

Mean Error The ME describes the difference of the average estimated value $\bar{y}$ from the average reference value $\bar{w}$, representing the mean of the estimation error $\bar{e}$.

$$ME = \bar{e} = \frac{1}{N} \sum_{i=1}^{N} (y_i - w_i) = \bar{y} - \bar{w} \tag{5.3}$$

Unlike methods utilizing absolute values or squared differences, the ME balances positive and negative errors, providing insights into the model's bias. A ME value above or below zero reveals whether the model systematically overestimates or underestimates reference values, respectively. While an ME of zero does not imply an exact match between all values, it indicates their mean values are equal. [176, 190]

Normalized Error Metrics MPE and RMSPE In addition to the absolute error metrics, we also compute normalized error measures to better reflect relative deviations. Specifically, we calculate the mean percentage error (MPE) and the root mean square percentage error (RMSPE), as defined in Equations (5.4) and (5.5), respectively. These metrics express the errors relative to the true values, enabling a scale-independent evaluation of the estimator performance.

$$\text{MPE} = \frac{1}{N} \sum_{i=1}^{N} \frac{y_i - w_i}{w_i} \tag{5.4}$$

$$\text{RMSPE} = \sqrt{\frac{1}{N} \sum_{i=1}^{N} \left(\frac{y_i - w_i}{w_i} \right)^2} \tag{5.5}$$

5.2 Modeling Behavior of a Commercial Sodium-Ion Battery

To evaluate the transferability of lithium-based algorithms to the investigated SIB in a simulation environment, it is first necessary to model both the cell's aging behavior and its electrical characteristics. In this section, we fit two electrical models based on characterization measurements, which include capacity and pulse data as well as EIS measurements recorded at various SOC levels and temperatures. Additionally we build on the aging data from Chapter 4 as well as a previous study by Klick et al. [191] and fit a semi-empirical aging model.

5.2.1 Modeling Electrical Behavior

In the literature, a wide range of battery models can be found, which are broadly classified into empirical models, ECMs, electrochemical models, and reduced-order models [192]. Among these, ECMs are particularly popular due to their favorable balance between modeling accuracy and computational efficiency [193]. They describe the dynamic electrical behavior of battery cells using combinations of active and passive electrical components. ECMs can be divided into two main categories: simple models, which do not aim to represent the underlying electrochemical processes, such as standard RC models, and physico-chemical consistent ECMs, which are inspired by the internal electrochemical processes of the battery. [192] In this work, two different ECMs are employed: For reference within the battery simulation, a parameterized physico-chemical consistent LiIon4 ECM is used which was introduced by Bihn et al. [194]. For the on-board estimation, an R1RC model, i.e. a simple ECM consisting of a voltage source, a resistor, and one RC-Element is applied.

Structurally, the LiIon4 model comprises a combination of classical ECM components (e.g., voltage source, resistors, capacitors) and more advanced elements such as Warburg and ZARC impedances, which together reflect the underlying physics derived from the Doyle-Fuller–Newman model. The model is divided into three domains representing high-, medium-, and low-frequency dynamics. Charge-transfer resistance, R_{ct}, and double-layer capacitance, C_{dl}, are used to describe the kinetics at the electrode/electrolyte interface, while the impedance contributions from intra-particle diffusion, Z_{Diff}, are approximated using distributed RC elements to reflect spherical or planar diffusion. Additionally, the model includes migration resistances in the porous structure of both electrodes, $R_{M,P}$, and in the separator, $R_{M,Sep}$, as well as a Warburg element to capture the electrolyte diffusion impedance. A separate RC circuit (R_{LF}, C_{LF}) accounts for slow processes such as inter-particle lithium redistribution. The schematic LiIon4 model is depicted in Figure 5.4A.

RC-type models are composed of an ideal voltage source connected in series with a resistor

and one or more RC elements, each consisting of a resistor and capacitor in parallel [195]. The voltage source represents the OCV, the serial resistance R_0 captures instantaneous overpotentials, and the RC elements describe the battery's dynamic electrochemical behavior. On-board BMS algorithms typically employ simplified RC models with only one or two RC elements to balance accuracy and computational efficiency. The employed R1RC model is depicted in Figure 5.4B, which is also used in the original BMS of the targeted high-power application.

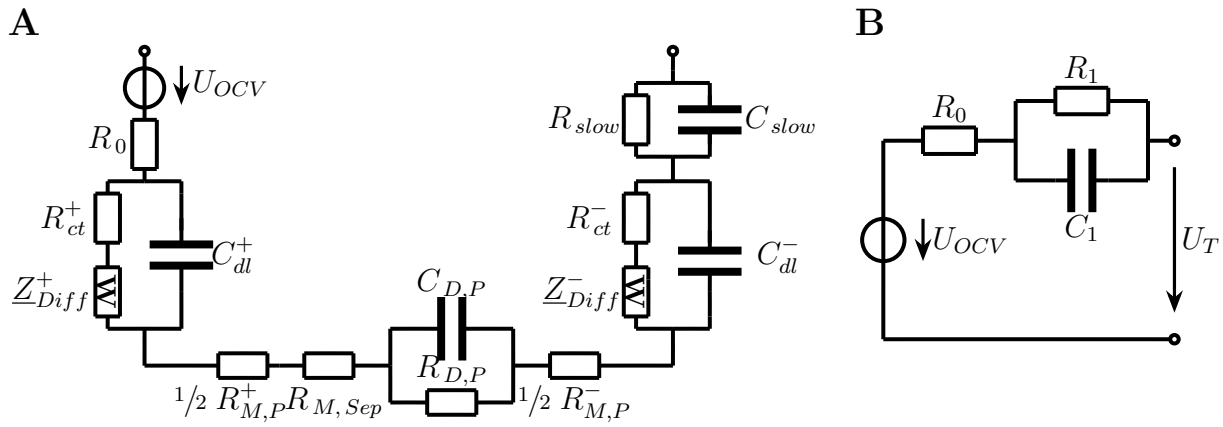

Figure 5.4: To emulate the electrical behavior of the SIB we choose two different ECMs. A: The LiIon4 model [193] is a physically-motivated ECM that replicates the behavior for low, medium, and high frequencies. The model serves as a reference for the battery simulation. For the fitting, the series connection of $\frac{1}{2}R^+_{\mathrm{M,P}}$, $R_{\mathrm{M,Sep}}$, and $\frac{1}{2}R^-_{\mathrm{M,P}}$ is combined into $R_{\mathrm{M,P}}$ to limit the number of fitting parameters.
B: For the two model-based SOC algorithms, we employ a R1RC model as this is widely used in industry for SOC estimation.

5.2.1.1 Experimental data

Once the models have been defined, a series of characterization measurements is required to parameterize the individual electrical model components as a function of temperature and SOC. These measurements are carried out using the a Digatron cycler with cells placed inside a temperature-controlled chamber similar to the aging experiments, described in Chapter 4. The characteristics of the test equipment are given in Table 4.2.

The measurement procedure is schematically depicted in Figure 5.5. Initially, two capacity tests are performed at 25 °C to determine the available capacity for the C-Rates 0.5 C and 1 C. Following this, the cell is discharged to 99 % SOC defined according to the 0.5 C capacity test. This is followed by a relaxation phase until the terminal voltage has stabilized. Then, both EIS and pulse measurements are conducted. The pulse tests are

applied at various C-Rates in both charge and discharge directions. After each pulse, the removed charge is charged back into the cell using a constant current of 0.5 C. This sequence of pulse and EIS measurements is repeated in 10 % DOD intervals, progressing stepwise down to 0 % SOC.

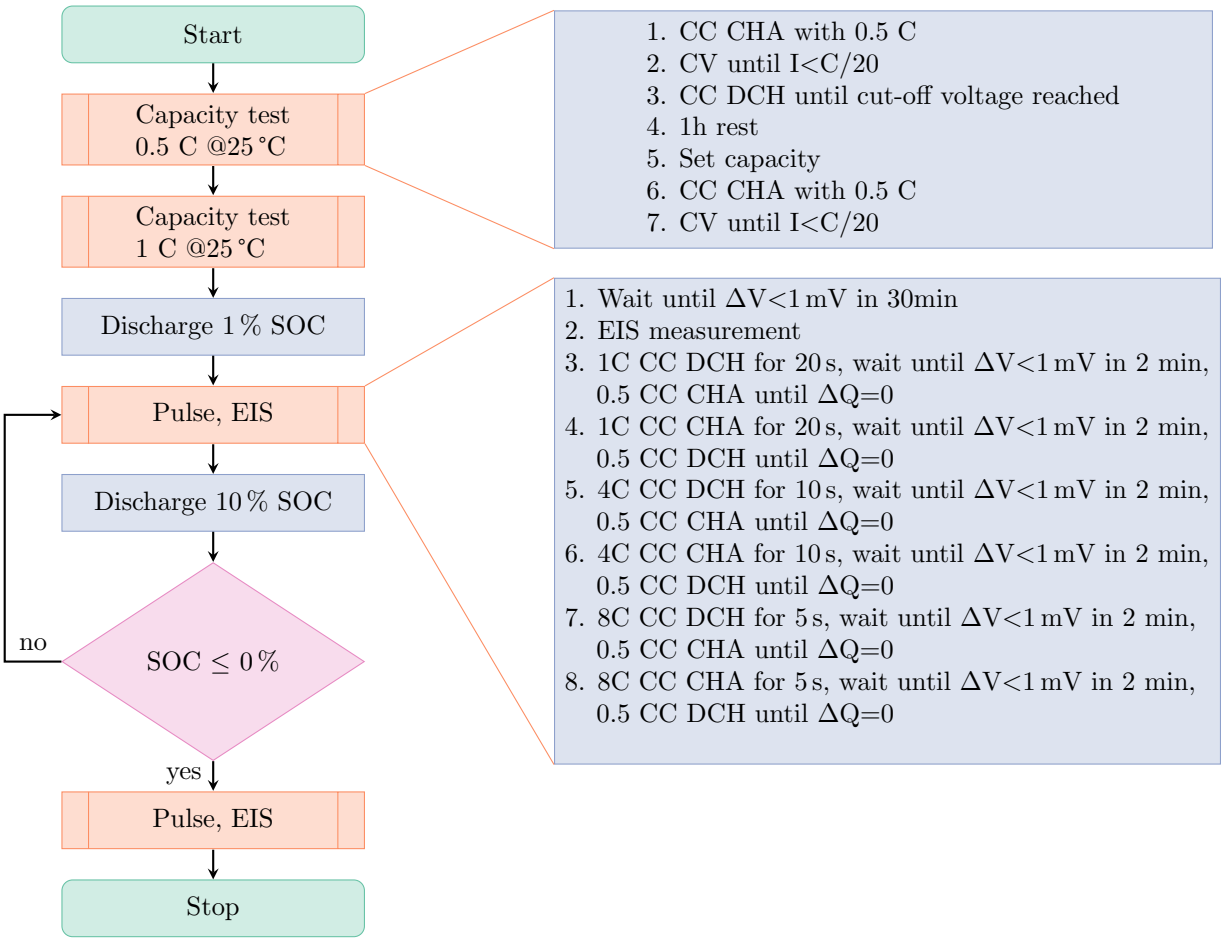

Figure 5.5: Characterization measurement at 25 °C. The procedure is repeated for the test temperatures 0 °C, 10 °C, 25 °C, and 40 °C.

The voltage and current of the characterization measurement at 25 °C are depicted in Figure 5.6. To ensure efficient testing while covering relevant operating conditions, the parameterization focuses on the temperature ranges occurring in the use case presented in Chapter 3.

The fitting of the voltage source is based on a qOCV measurement, which involves recording the voltage during very low C-Rate cycling. Despite the low C-Rate, a small but noticeable overpotential remains, particularly at lower temperatures. For the SIB, the cell is first fully charged to its maximum voltage and then discharged at C/20 to its end-of-discharge voltage, followed by a charge at C/20 to the end-of-charge voltage. Figure 5.7

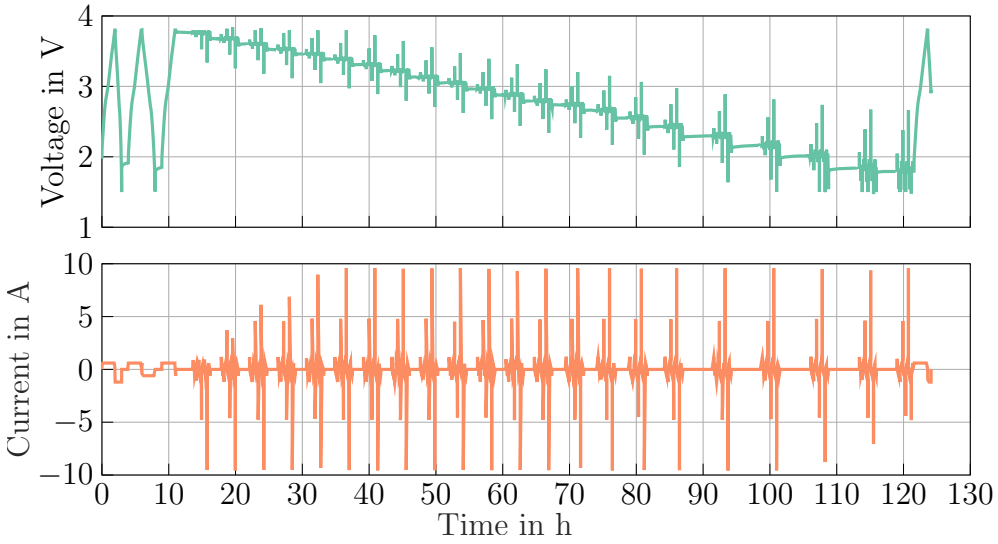

Figure 5.6: Measurement procedure used for the parameter fitting of both ECMs. The procedure is repeated for the test temperatures 0 °C, 10 °C, 25 °C, and 40 °C.

shows the resulting average qOCV curves of the SIB for different temperatures, where the spread between the curves reflects the influence of temperature-dependent overpotentials.

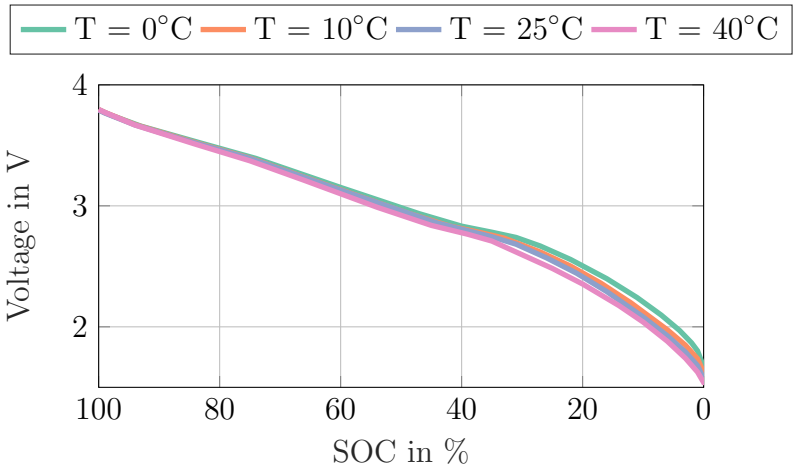

Figure 5.7: Cell qOCV as a function of SOC and temperature. The qOCV displayed here is the mean of both charge and discharge qOCV.

The EIS measurements are used for the fitting in the frequency domain and are performed before the pulse measurements for every SOC. The EIS spectrum as a function of voltage (as an indication for SOC) and temperature is shown in Figure 5.8A and B, respectively. It is clearly visible that at lower voltages and temperatures the semi-circle increases. This is primarily due to the reduced availability of charge carriers for redox reactions at the electrodes, which slows down the charge transfer kinetics [196]. This behavior is similar

to LIBs, indicating a similarity regarding the electrical properties.

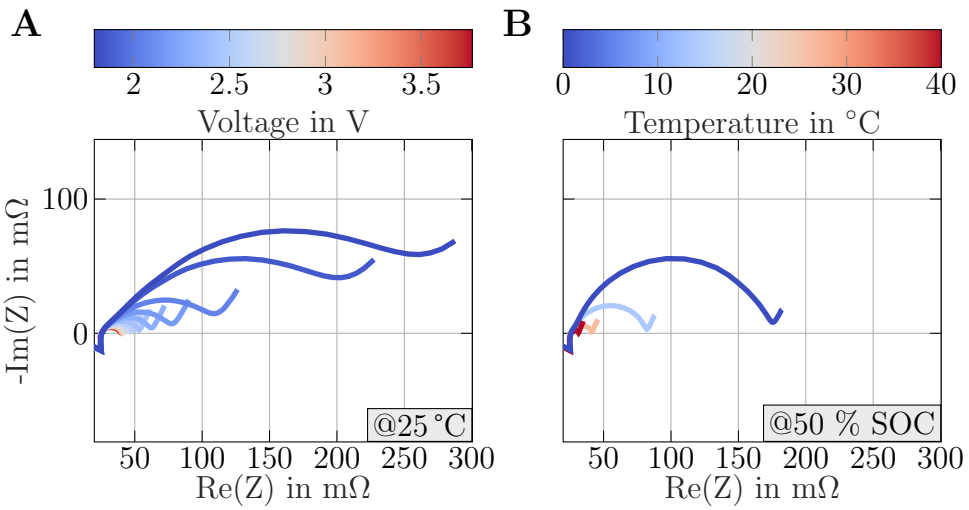

Figure 5.8: EIS spectra for the investigated SIB.
A: EIS spectra dependent on voltage for 25 °C.
B: EIS spectra dependent on different temperatures for an SOC of 50 %.

5.2.1.2 Fitting of the Electrical Models

To extract the parameters of the ECM components from the EIS and pulse measurements, we fit the model equations to the experimental data. The required steps for the procedure including their physical interpretation for the LiIon4 model are thoroughly described in [193]. For the R1RC model, we use the open-source toolbox *impedance.py* [197] to perform the fitting. Since the primary focus of this work is to evaluate the transferability of algorithms from lithium-based systems to our SIBs, we present representative fitting results and validations for the SIB without pursuing full model optimization.

An exemplary fit of the LiIon4 model at 25 °C and 3.67 V solely based on EIS measurement is displayed in Figure 5.9A. Since the LiIon4 model is composed of different time constants and electrical components reflecting different electrochemical processes we are able to accurately describe the relevant parts of the EIS spectrum. However, with a much simpler R1RC model we can only model the semi-circle behavior in the EIS Nyquist plot, so we ignore the other measurement points (e.g. the inductive part or the diffusion processes) during the fitting and end up with a less accurate, however still sufficient fit for most on-board applications. It is immediately visible in Figure 5.9B, that the EIS behavior of the cell follows a semi-elliptical shape on the medium-frequency range, which can be adequately captured with the LiIon4 model but not the R1RC model, which can only form a round semi-circle [165].

By applying the fitting procedure across all relevant temperatures and SOCs, we obtain

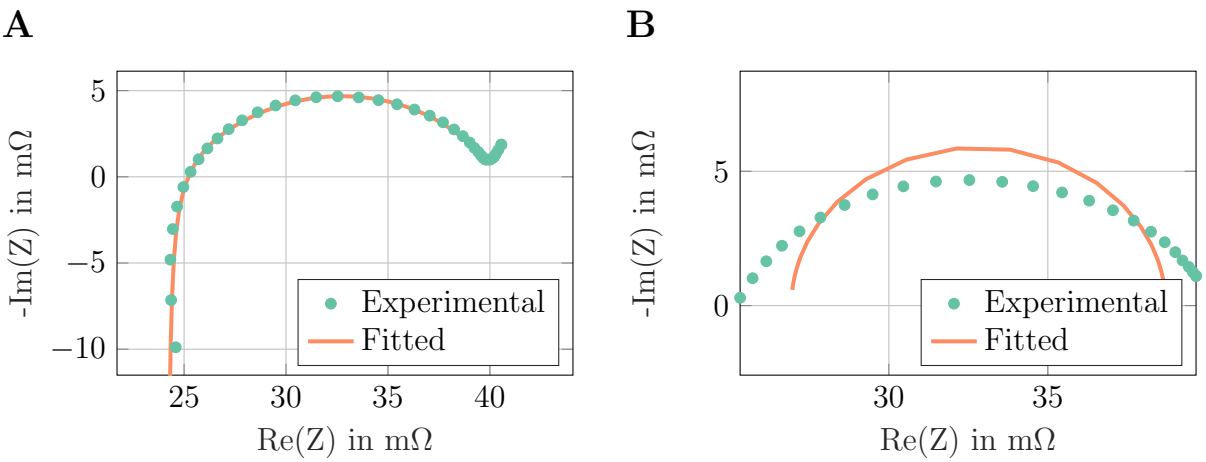

Figure 5.9: Example of an EIS measurement at 25 °C and 3.67 V and the corresponding fit.
A: LiIon4 model.
B: R1RC model. Only a limited frequency range of the measurement is used for fitting. Effects such as diffusion or multiple charge transfer processes cannot be captured by the R1RC model.

the fitted parameters shown in the Supplementary Figures A.2 and A.3 for the LiIon4 and R1RC models, respectively. As previously discussed, the extracted model parameters capture the key trends observed in the EIS spectra: most electrochemical processes slow down at lower SOCs and temperatures, leading to increased overpotentials [198]. Both parameterized models are converted into an XML format for use in the BMS simulation toolchain, where the look-up tables (LUTs) are stored as a function of SOC and temperature.

To validate the accuracy of our models, we performed a series of tests on the physical battery cells and compare the measured voltage profiles to their simulated counterparts. Since optimized fitting is not focus of this work, we refer to the Supplementary Material A.3 for exemplary fitting results.

5.2.2 Modeling Aging Behavior

A wide range of aging models can be found in the literature [118]. Generally, a distinction is made between physical, data-based and empirical models [118]. Physical models aim to derive the effects of electrochemical cycling or storage on battery capacity and impedance based on first principles [199, 200]. It enables the tracking of observed aging down to individual electrochemical processes. However, it requires extensive testing using a variety of measurement methods, ranging from material to cell level. In contrast, empirical aging models do not attempt to model electrochemical processes per se, but rather the resulting

effects of specific operating conditions on capacity and impedance. These models are significantly simpler but do not allow for detailed insights into individual degradation mechanisms.

In this work, we use an aging model based on the approach of Schmalstieg et al. [118]. It is a semi-empirical model that estimates capacity loss and resistance increase over time as functions of multiple stress factors such as temperature, SOC or voltage, DOD, and charge throughput. The overall degradation at each time step is computed by superimposing calendar and cyclic aging contributions, using empirically derived functions for capacity loss and resistance increase. To assess whether this modeling approach is sufficient for use in our battery simulation, we analyze how well one of its core assumption, a linear compression of the OCV with capacity fade, replicates realistic behavior under different aging levels. Based on the discharge curves of all tested cells from the RPTs across all cycling conditions, originally presented in Figure 4.10, we illustrate in Figure 5.10 how capacity loss leads to a compression of the discharge curve, using an exemplary BOL curve and different levels of capacity fade. The discharge voltage curves at 0 %, 3.3 %, 6.6 %, and 10 % capacity loss are shown in different colors.

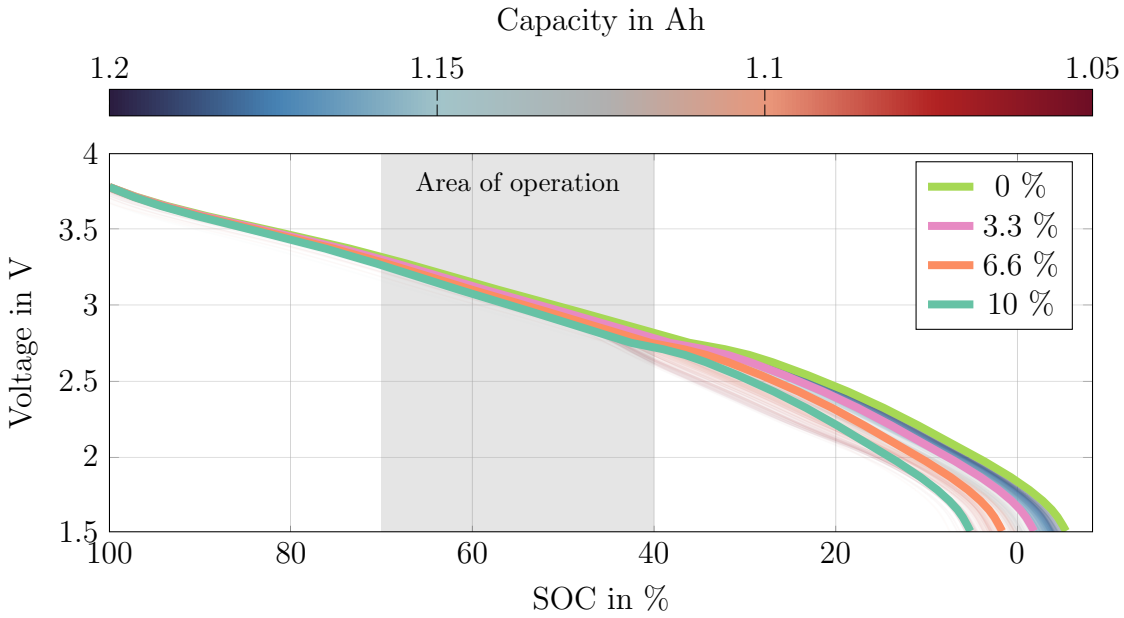

Figure 5.10: Effect of capacity fade on discharge curves through simple compression for different capacity loss levels 0 %, 3.3 %, 6.6 %, and 10 %. Within the high-power application, we only use a limited SOC range that is depicted in gray.

It is evident that in the upper SOC range ($> 43\,\%$), the curves can be reproduced very accurately by simple compression. Similarly, in the very low SOC range ($< 10\,\%$) the method remains sufficiently accurate. However, in the SOC range in between, simple compression does not fully capture the changes. For our use case, this deviation is ac-

ceptable for the purposes of this work, as the relevant area of operation in the considered use case lies in the medium SOC range.

In the following, we discuss the formulas for calendar and cyclic aging as well as the fitting of the empirical aging data.

5.2.2.1 Calendar Aging

It is well established that batteries undergo aging even in the absence of electrochemical cycling, typically referred to es calendar aging [201]. To parameterize calendar aging behavior, we have to perform storage tests at different temperatures and voltages, each corresponding to a fixed SOC. The measured capacity fade and impedance increase is fitted using empirical power-law functions. A dependency of the form $t^{0.75}$ was found to best capture the observed trends, representing the root-time relationship commonly attributed to different SEI formation mechanisms [118]. The resulting calendar aging equations for normalized capacity C and resistance R as functions of time t (in days) are:

$$C(t) = 1 - \alpha_{\text{cap}} \cdot t^{0.75} \tag{5.6}$$

$$R(t) = 1 + \alpha_{\text{res}} \cdot t^{0.75} \tag{5.7}$$

The coefficients α_{cap} and α_{res} are functions of temperature and voltage and are extracted as a result of the fitting procedure. A linear voltage dependency and Arrhenius-type temperature dependency are used:

$$\alpha(V, T) = (\alpha_1 V + \alpha_2) \cdot \exp\left(\frac{-E_a}{RT}\right) \tag{5.8}$$

where V is the storage voltage in V, T is the absolute temperature in K, R is the gas constant and E_a is the activation energy in J/mol.

5.2.2.2 Cyclic Aging

Cyclic aging refers to the degradation of battery performance caused by repeated charge and discharge cycles [202]. To describe the impact of cycling on the capacity and impedance of a battery we performed cycling tests over a variety of DOD and average SOC conditions (see Chapter 4). When performing cyclic aging tests time still passes causing calendar aging. To isolate the impact of cycling from calendar aging, degradation measured during cycling must be corrected by subtracting the calendar aging contributions in a specific timeframe. The degradation trends are then fitted using two separate empirical functions. Capacity loss is following a square root dependency on

the cumulative charge throughput Q in Ah:

$$C(Q) = 1 - \beta_{\text{cap}} \cdot \sqrt{Q} \tag{5.9}$$

Resistance increase was found to be linear with respect to Q [118]:

$$R(Q) = 1 + \beta_{\text{res}} \cdot Q \tag{5.10}$$

The coefficients β_{cap} and β_{res} were observed to vary with DOD and average SOC. A linear dependency on DOD and a quadratic dependency on SOC were found to best capture the experimental data:

$$\beta_{\text{cap}} = a(\overline{\text{SOC}} - SOC_0)^2 + b + c \cdot \text{DOD} \tag{5.11}$$

$$\beta_{\text{res}} = d(\overline{\text{SOC}} - SOC_1)^2 + e + f \cdot \text{DOD} \tag{5.12}$$

where $\overline{\text{SOC}}$ is the average SOC during cycling, and a, b, c, d, e, f, SOC_0, and SOC_1 are fitting constants determined from the experimental data.

The total aging at each time step is modeled by summing the calendar and cycle aging components:

$$C(t, Q) = 1 - \alpha_{\text{cap}}(T, SOC) \cdot \sqrt{t} - \beta_{\text{cap}}(\overline{\text{SOC}}, \text{DOD}) \cdot \sqrt{Q} \tag{5.13}$$

$$R(t, Q) = 1 + \alpha_{\text{res}}(T, SOC) \cdot \sqrt{t} + \beta_{\text{res}}(\overline{\text{SOC}}, \text{DOD}) \cdot Q \tag{5.14}$$

5.2.2.3 Fitting of the Aging Model

To fit the aging model parameters of the SIB, a series of tests are necessary. For the calendar aging tests, we rely on the work of Klick et al. [191], who conducted calendar aging experiments at 25 °C and 40 °C for the investigated SIB, using one cell per condition. Both cells were kept at 100 % SOC. To avoid repeating calendar aging experiments, we assume that calendar aging is independent of SOC for this cell type. Based on existing calendar aging experiments with cells of the same type conducted by Streck et al. [203], this assumption introduces an error of less than 1 % in the estimated aging over the course of one year, which is considered acceptable. Furthermore, no clear trend in the change of internal resistance was observed in the investigations by Klick et al. [191]. Therefore, we neglect this effect for our further analysis. These assumptions lead to the following simplified equation:

$$\alpha_{\text{cap}} = (0.6 \cdot \exp(-660.05/T)), \quad \alpha_{\text{res}} = 0 \tag{5.15}$$

The resulting simple fit for calendar aging, obtained by minimizing the RMSE, is shown in the Supplementary Figure A.7.

For fitting the cyclic aging behavior, the tests described in Chapter 4 were used. Since multiple cells were aged under identical conditions, the average aging behavior per condition was used for the fitting process. In contrast to calendar aging, clear dependencies on voltage (or SOC) and DOD are observed. In terms of capacity, this leads to particularly pronounced aging at low SOCs. As already noted in the aging study, the aging model does not capture a clear trend in the aging behavior of internal resistance: under same load conditions, internal resistance increases or decreases slightly with aging. Nevertheless, its behavior can be accurately described by the following equations, derived using the fitting approach of Schmalstieg et al. [118]:

$$\begin{aligned}\beta_{\text{cap}} = & -1.55 \cdot 10^{-4} \cdot \exp(-1.03 \cdot 10^{-2} \cdot \text{DOD}) \\ & + 2.36 \cdot 10^{-7} \cdot \left(\overline{\text{SOC}}\right)^2 \\ & - 2.61 \cdot 10^{-5} \cdot \left(\overline{\text{SOC}}\right) \\ & + 9.36 \cdot 10^{-4}\end{aligned} \tag{5.16}$$

$$\begin{aligned}\beta_{\text{res}} = & -2.10 \cdot 10^{-3} \cdot \exp(-1.04 \cdot 10^{-2} \cdot \text{DOD}) \\ & + 7.71 \cdot 10^{-7} \cdot \left(\overline{\text{SOC}}\right)^2 \\ & - 7.51 \cdot 10^{-5} \cdot \left(\overline{\text{SOC}}\right) \\ & + 2.90 \cdot 10^{-3}\end{aligned} \tag{5.17}$$

These relationships, including the averaged loads at the discrete measurement points, are illustrated in Figure 5.11. The fitting quality of both fits was comparably high with an RMSE of < 0.06.

The fitted results confirm the general trends already observed in the analyses in Chapter 4. Capacity fade is highest at low mean SOC levels, with the DOD showing minimal influence. At high mean SOC, capacity fade rises slightly, though the most pronounced degradation remains at low mean SOC. The capacity fade is the lowest for the mid mean SOC. A similar pattern is observed for resistance growth. Interestingly, under certain conditions, the fitted coefficient is negative, indicating a decrease in resistance. In contrast to capacity fade, resistance growth exhibits a clearer dependency on the DOD, with higher DOD conditions leading to a more pronounced increase. Overall, resistance growth is most significant at both low and high average SOC levels.

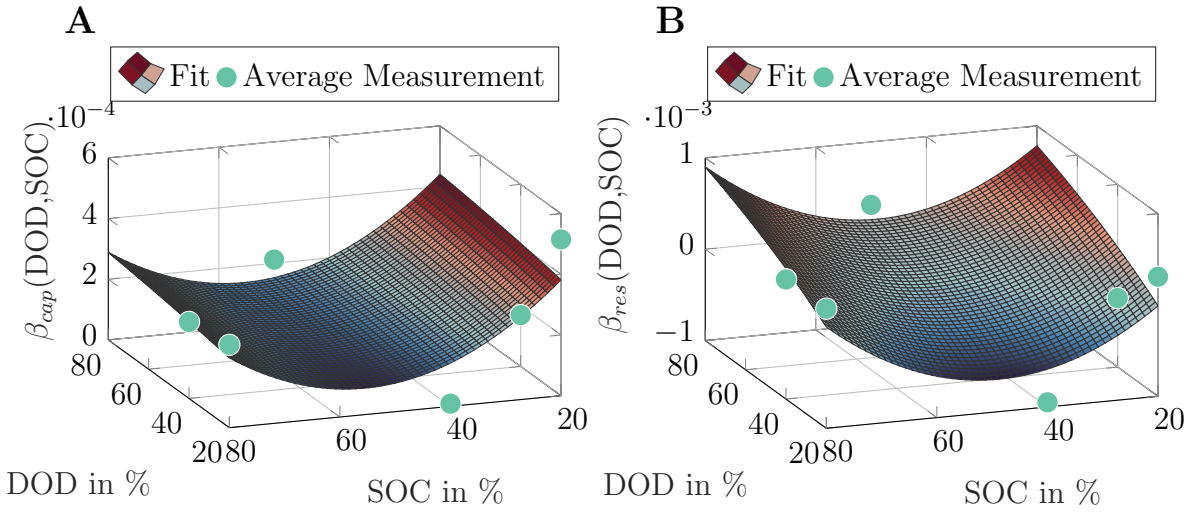

Figure 5.11: Fitting results for cyclic behavior using the model of Schmalstieg et al. [118]. Green points indicate the averaged cell aging parameters under the respective operating conditions.
A: β_{cap}.
B: β_{res}.

5.3 Transferability of SOC Algorithms

Based on the established evaluation framework and SIB models, we now benchmark three widely used, real-time capable SOC estimation algorithms. The evaluation is performed for the investigated $NaMO_2$/HC cell and, for comparison, for the original NMC/LTO cell from the target application across relevant operating conditions.

The accuracy of most diagnostic algorithms strongly depends on the shape of the OCV(SOC) and the operating window. Figure 5.12 shows the corresponding curves for both cell types. The $NaMO_2$/HC cell exhibits a substantially broader voltage window, i.e. 1.5 V – 3.8 V, and a steeper OCV(SOC) characteristic with a pronounced plateau around 40 %. In the context of control theory, the broader voltage range and the overall steeper sections of the OCV(SOC) characteristic enhance the observability of the SOC, which may positively affect the performance of real-time estimation algorithms.

5.3.1 Simulation-based Design of Experiment

We focus on seven evaluation categories to systematically analyze different factors influencing algorithm performance. These categories encompass critical environmental, operational, and BMS-specific conditions that affect estimation accuracy and are based on current literature [80, 120] and the high-power use case from Chapter 3. By isolating

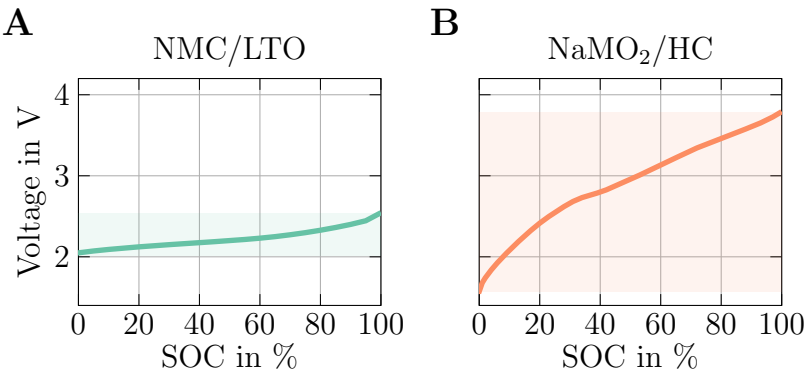

Figure 5.12: Averaged OCV in dependency of SOC across the two cell types based on qOCV measurements. The curves are characterized by different voltage ranges and slopes.
A: NMC/LTO cell that is originally applied in the high-power scenario.
B: $NaMO_2$/HC.

and varying individual features within each category, we aim to identify their specific impacts on algorithm behavior. Although the chosen scenarios do not fully cover all relevant use cases, they illustrate the methodology. A *base scenario* is established as a reference for each estimator's performance, testing the functionality of the algorithm without additional disturbances. From this base scenario, we vary one feature per category while keeping all other parameters fixed. The scenarios are depicted in Figure 5.13.

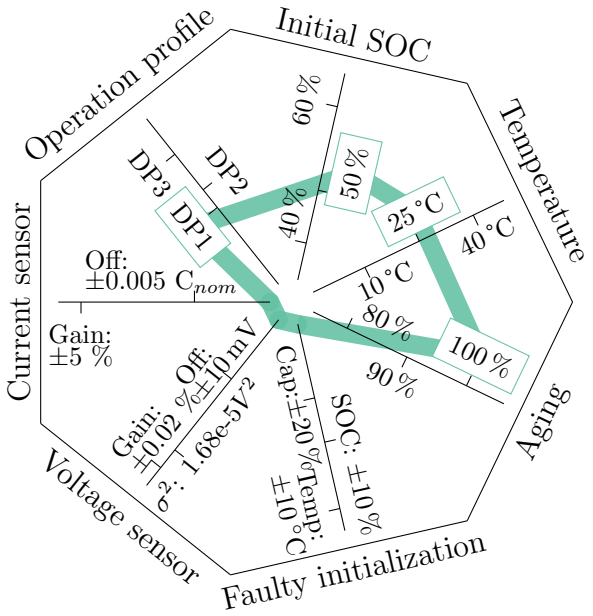

Figure 5.13: Simulation-based Design of Experiment as a base for algorithm benchmark. The green line indicates the *base scenario*. Within each category, only one feature is varied. The choice of parameters within the different categories is based on the operation range of the high-power use case from Chapter 3.

Base scenario

Within the *base scenario*, we employ a representative load profile for the high power application from Chapter 3. The profile DP1, shown in Figure 5.14B, is based on real recorded driving data of a representative European driver. It is applied at an initial SOC of 50 % to a pristine cell at an ambient temperature of 25 °C. The algorithms are correctly initialized, and no additional disturbing influences occur besides the basic sensor emulation.

Dynamic high-power profiles

Since all real-world data originates from a 48 V system with a maximum discharge rate of 25 C, the resulting power levels are not directly applicable to the SIB. Therefore, the three original profiles are scaled to match the SIB's nominal power. This process is shown in Figure 5.14, where Figure 5.14A shows the power-equivalent profile. To compress the data, pauses longer than one hour are removed, as the cell's relaxation processes are largely completed within this timeframe. The final profile used as input for simulation is shown in Figure 5.14B.

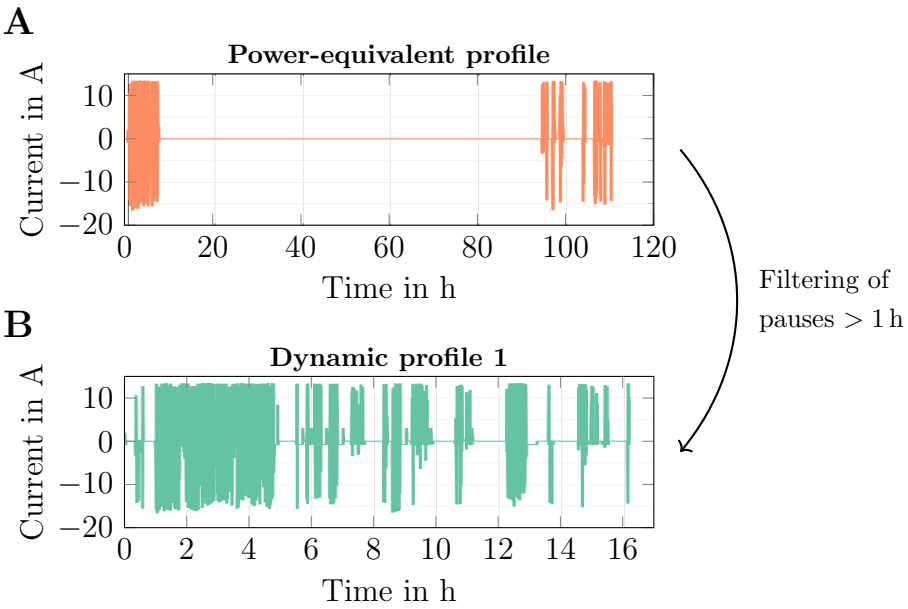

Figure 5.14: The load profile is based on real driving data from the application.
A: Power-equivalent profile, already scaled to match the power characteristics of the SIB.
B: The pauses are removed from the power-equivalent profile to compress data and reduce simulation time.

Beyond the standard drive cycle, we consider two additional high-power profiles shown in Figure 5.15, both based on real-world data from the high-power application. The profiles differ in duration and the number of rest periods. While the average currents in profiles DP2 and DP3 are slightly lower than in DP1, all three cover similar SOC ranges, as these are representative of the actual application. Further characteristics of all three high dynamic profiles for the SIB are summarized in Table 5.2.

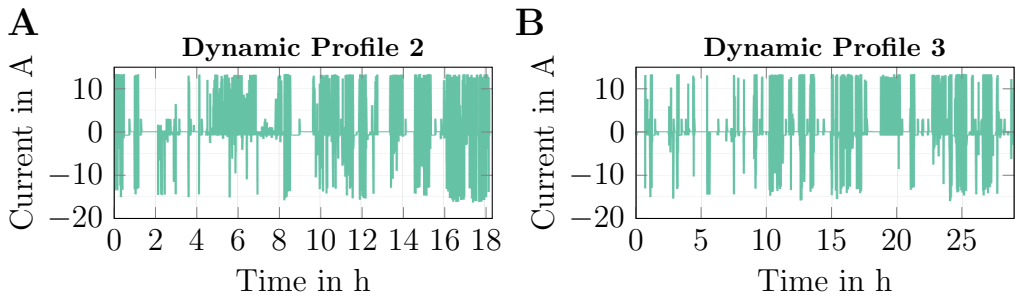

Figure 5.15: Additional load profiles in the category dynamic high-power profiles. These profiles stem from the high-power application described in Chapter 3 and are scaled to match the power of the SIB. Long pauses have been shortened similar to Figure 5.14.

Table 5.2: High dynamic profile (DP) characteristics for the commercial SIB.

	Duration	Avg. Current		Start SOC	End SOC	Max. SOC	Min SOC
		Cha	Dch				
Unit	h	A	A	%	%	%	%
Profile DP1	16.16	2.7 [σ=4.17]	-1.34 [σ=2.2]	50	55.43	73.32	42.69
Profile DP2	18.23	1.55 [σ=3.39]	-0.89 [σ=1.43]	50	52.29	70.88	42.18
Profile DP3	28.8	1.95 [σ=3.72]	-0.9 [σ=1]	50	44.87	71.3	41.9

Initial SOC
The initial SOC is varied to both 40 % and 60 % to assess the diagnostic algorithms' behavior near the initial values encountered in the high-power application.

Environmental temperature
The typical ambient temperature limits that occur in the high-power application, i.e. 10 °C and 40 °C, are considered.

Aging
To reflect the aging conditions observed in the field, we define specific aging states in addition to the fresh cell. The initial capacity is reduced to 90 % and 80 % of the nominal capacity (SOH_C) while simultaneously increasing the serial resistance to 125 % or 150 % of the BOL resistance (SOH_R), respectively. The second values stated in each case correspond the End-of-Life (EOL) of the battery and also occur in the high-power application.

Current sensor
Additional noise, offset errors, and gain errors test the influence of disturbances on the current sensor on the diagnostic algorithms. The gain error (Gain) quantifies the magnitude by which each measured value is multiplied. The offset error (Off) denotes the fixed deviation between each measured value and its reference value. Following the approach

presented by Campestrini et al. [175], the offset error was determined as a function of the nominal capacity, allowing for a cell chemistry-independent comparison. A gain error of ±5 % was selected to simulate realistic variations in the current sensor calibration. For the offset error a value of ±0.005 was chosen, as it reveals noticeable disparities among the diagnostic algorithms' estimates within this order of magnitude. The values are based on a currently used current sensor [183].

Voltage sensor
For the gain error (Gain), a value of ±0.02 % was chosen. The offset error (Off) is set to ±10 mV. Moreover, the root mean square value of the mean-free noise (Var) is set to 0.0000168 V^2. The values stem from the datasheet of a currently used voltage sensor for mobile applications [204].

Faulty initialization
In a BMS, faulty states can occur either due to algorithmic errors or hardware malfunctions. To assess their impact on algorithm performance, we introduce an SOC offset of ±10 % and vary the nominal capacity by ±0.2 C_{nom} to test algorithm convergence. Additionally, we simulate an ambient temperature offset of ±10 °C.

The individual simulation scenarios are summarized in the Supplementary Table A.1.

5.3.2 Real-time SOC Algorithms

Within this work, we investigate the operational behavior of widely used, real-time capable SOC estimation algorithms. Specifically, we benchmark an ampere-hour counter with recalibration (AhC & OCV), an Extended Kalman Filter R1RC (EKF R1RC), and an Unscented Kalman Filter R1RC (UKF R1RC).

Ampere-hour–based algorithm
A widely used and direct method to estimate the SOC is the ampere-hour counter. According to Equation (2.9), the measured battery current is integrated over time to determine the charge. However, the ampere-hour counter method is prone to errors due to inaccurate initialization, sensor inaccuracies, losses, or reduced capacity from aging. Since these errors can accumulate significantly over time, the approach has been supplemented with a recalibration mechanism during relaxation. During recalibration, when no current flows, the ΔV criterion is used to check whether the battery is in a relaxed state. If this condition is met, the voltage is measured, and the current SOC is determined via interpolation based on the OCV(SOC) relationship. To prevent abrupt changes, the SOC value is then updated gradually. Once current flows again, the SOC is initialized with the updated value. SOC is normalized to the nominal capacity of the cell.

EKF and UKF using a R1RC model
We benchmark two well-documented and commonly used KF implementations available

in MATLAB/Simulink. The parameter sets for both cell chemistries, listed in Table 5.3, were obtained through iterative tuning. While detailed optimization is not the focus here, it is important to keep in mind that it can significantly influence algorithm performance, as discussed in the literature [205].

Table 5.3: Initialization of the model-based algorithms for the two cell chemistries. In the matrices, the first diagonal element corresponds to the SOC, while the second represents the voltage of the RC element.

Parameter	NMC/LTO	$NaMO_2$/HC
α (only for UKF)	1	1
β (only for UKF)	2	2
κ (only for UKF)	0	0
Q	$\begin{bmatrix} 10^{-8} & 0 \\ 0 & 10^{-6} \end{bmatrix}$	$\begin{bmatrix} 10^{-6} & 0 \\ 0 & 10^{-10} \end{bmatrix}$
R	0.5	0.5
$P0$	$\begin{bmatrix} 10^{-10} & 0 \\ 0 & 10^{-8} \end{bmatrix}$	$\begin{bmatrix} 10^{-3} & 0 \\ 0 & 10^{-5} \end{bmatrix}$

Filter initialization involves the choice of the initial covariance matrix $P0$, the process noise matrix Q, and the measurement noise R. The covariance matrix influences the filter's convergence behavior with higher values reflecting lower confidence in the initial parameters. Q determines model uncertainty, where higher values correspond to lower confidence in model accuracy. R reflects measurement uncertainty. A high value of R results in a low Kalman Gain, reducing the impact of measurement updates on the state estimate. [206]

5.3.3 Results

Figure 5.16 presents the evaluation results of the three SOC algorithms for both cells. The left panel summarizes algorithm performance across categories using the average IA value, chosen for its direct comparability in the radar chart. Both cells show excellent performance under base conditions, with IA values above 0.97. However, performance changes under different operating conditions and these changes differ for the two chemistries.

For the $NaMO_2$/HC cell, all algorithms demonstrate notably low sensitivity to both external and BMS-specific influences. The AhC & OCV algorithm exhibits larger errors in the *aging* category. The errors in the *faulty initialization* category are relatively small, due to the algorithm's integrated recalibration. The *current sensor* category also has only a minimal impact on the performance of the AhC & OCV. The categories *temperature*, *initial SOC*, and *operation profile* show similarly minor effects on all three investigated algorithms. Interestingly, the *voltage sensor* category also has minimal impact on both model-based algorithms.

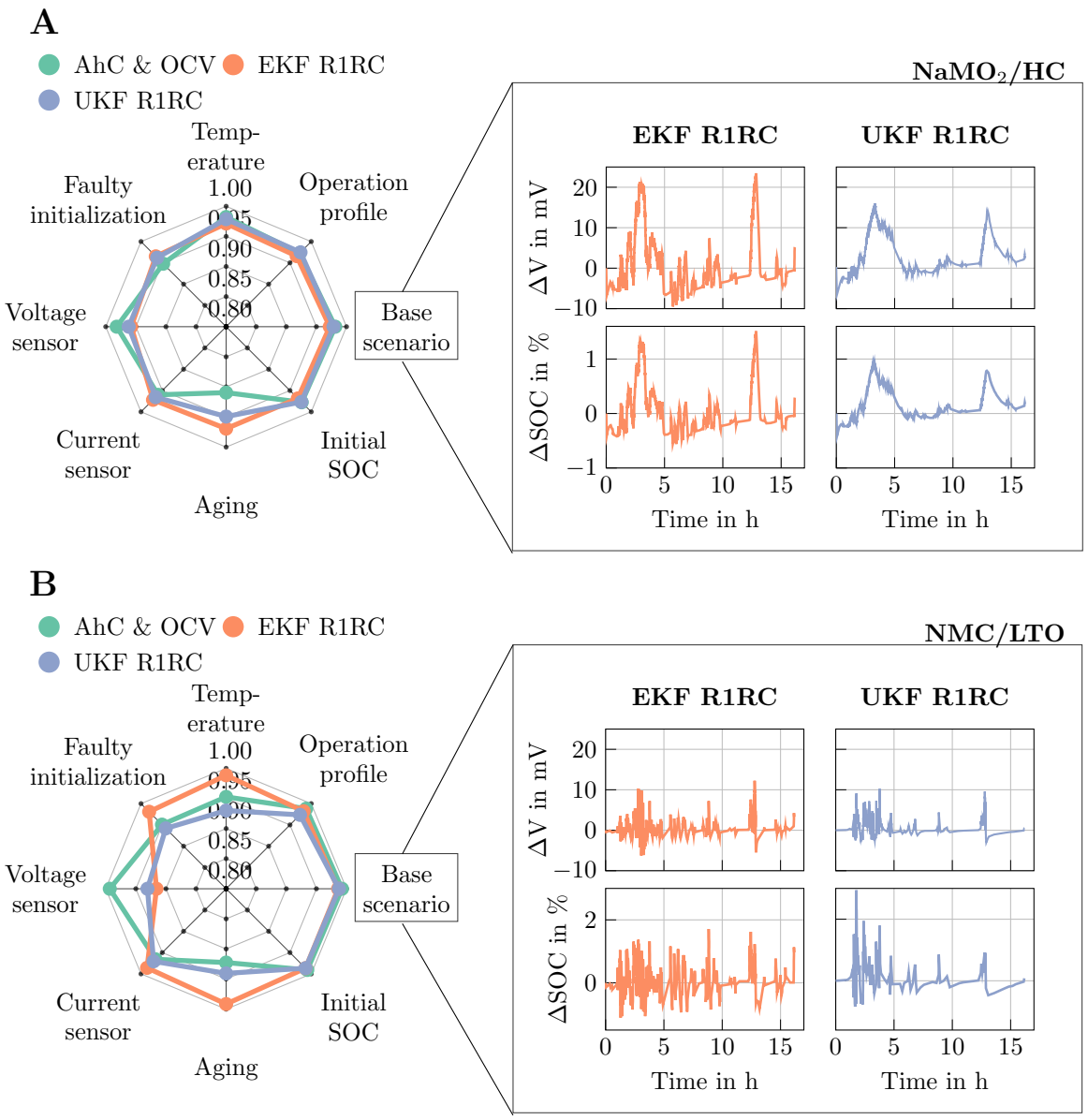

Figure 5.16: Summarized results using the IA as a measure of accuracy across the two cell chemistries. The IA provides an initial indication within the framework of which categories may exhibit irregularities. The right panel focuses on the model-based algorithms within the base scenario, presenting the voltage error and the corresponding SOC error.
A: $NaMO_2$/HC.
B: NMC/LTO.

For the NMC/LTO cell, shown in the left panel of Figure 5.16B, the AhC & OCV performs poorly in the *faulty initialization* and *aging* categories, as observed for the $NaMO_2$/HC cell. In the *voltage sensor* category, both filters perform poorly, likely due to the NMC/LTO cell's very narrow OCV range. Voltage measurement errors have a greater

impact, covering a larger portion of the operating range compared to the $NaMO_2$/HC cell. As with the SIB, the AhC & OCV performs well in the *current sensor* category, likely because recalibration minimizes current errors, leading to only minor deviations in SOC estimation. The UKF R1RC, similar to the AhC & OCV, exhibits higher deviations in the *aging* category, especially since the SOC is normalized to the nominal capacity.

The right panel in Figure 5.16 shows the SOC error of the model-based algorithms for the *base scenario*, as well as the voltage error, defined as the difference between the estimated and the reference OCV. For the $NaMO_2$/HC cell in Figure 5.16A, the EKF R1RC exhibits voltage errors of up to 20 mV, resulting in a maximum SOC error of approximately 1.5 %. The UKF R1RC, in contrast, limits the voltage error to 15 mV, which corresponds to a maximum SOC error of about 1 %. For the NMC/LTO cell, however, the voltage error of the EKF R1RC reaches up to 12 mV, leading to a maximum SOC error of approximately 1.9 %. While the UKF R1RC shows a similar voltage error in this case, the corresponding SOC error is larger. The larger SOC deviation despite the smaller voltage error for the NMC/LTO cell compared to the $NaMO_2$/HC cell can, in part, be attributed to the narrower voltage range of the NMC/LTO cell, where even a small voltage error results in a larger SOC deviation.

Figure 5.17 shows the detailed results for the metrics RMSE, e_{max}, ME, and σ across all scenarios and algorithms for the SIB, enabling an overview of the respective strengths and limitations of each algorithm. When varying the operation profiles, all estimators show very good accuracy, although the EKF R1RC exhibits the highest e_{max}, which can be attributed to larger short-term deviations. The accuracy of all algorithms also remains stable across different temperatures and initial SOC values. Changes in the initial aging state affect both the AhC & OCV and the UKF R1RC. For the AhC & OCV, using the nominal capacity as the denominator causes overestimation of relative errors when the actual capacity deviates. A similar, though smaller, effect also influences the UKF R1RC. Current sensor offsets have an impact on the accuracy of the AhC & OCV. The time-series for each scenario within the *current sensor* category are summarized in Figure 5.18. Although an offset accumulates over time, leading to a higher SOC deviation, this error is largely corrected by the algorithm's recalibration mechanism during rest periods, resulting in good overall accuracy. For the EKF R1RC, current offsets have only a minor effect, whereas gain errors lead to brief spikes in the SOC deviation. In contrast, the UKF R1RC is particularly sensitive to a positive current offset. Even with voltage corrections, this can result in a persistent deviation of the estimated mean SOC from the true value, because the filter effectively trusts the biased current too much. This error is reflected in the slightly increased ME, highlighted in light blue in the heatmap. Voltage sensor disturbances do not affect the AhC & OCV but do impact the model-based filters. A voltage offset, in particular, has the strongest effect on both filters, which are unable to compensate for it, reflected in increased ME values for these scenarios. In contrast, gain and variance errors show no noticeable impact on accuracy, bias, or precision. Incorrect initialization significantly affects the performance of all estimators.

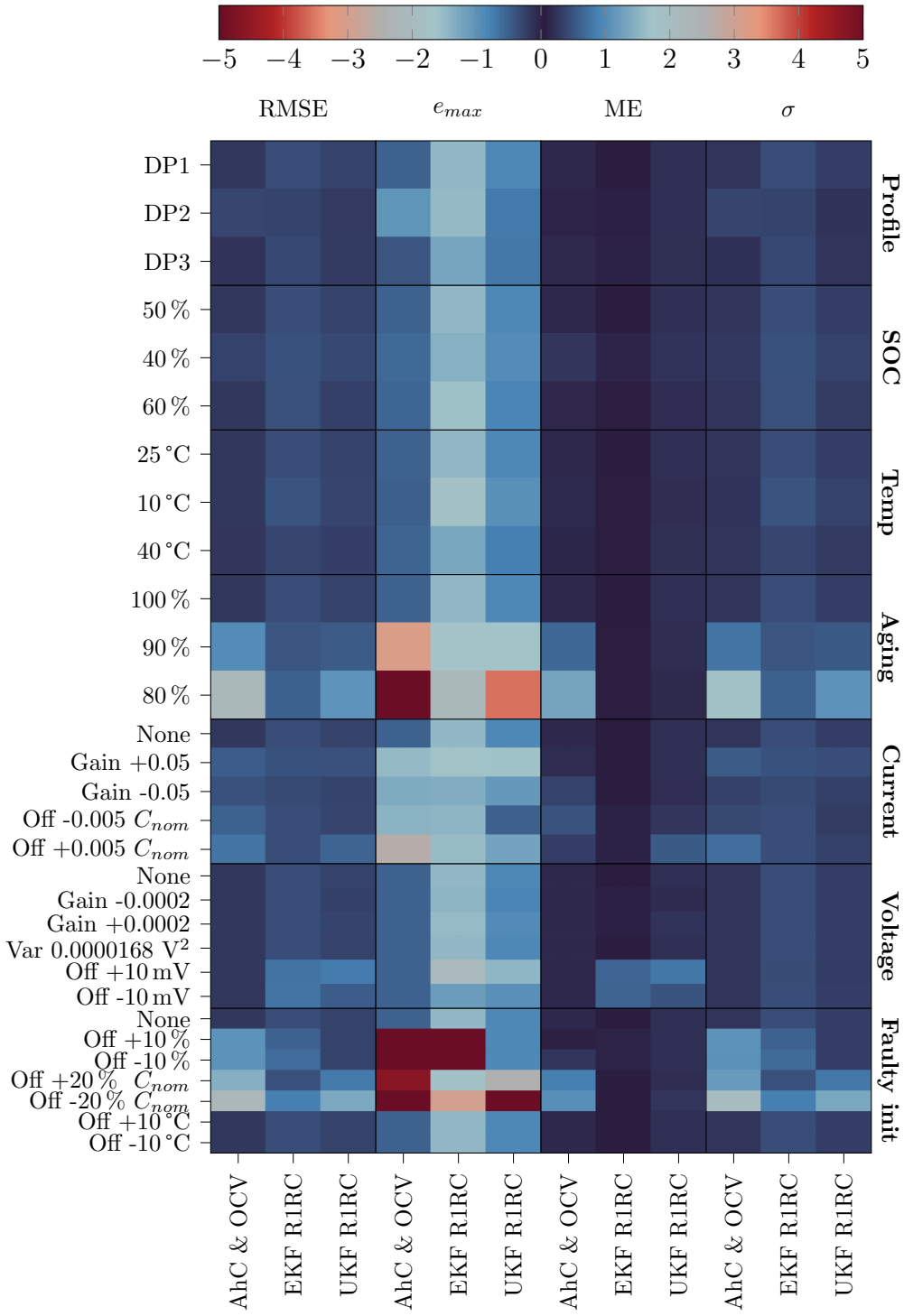

Figure 5.17: Sensitivity analysis for the SIB. The performance is evaluated across seven categories, three estimation algorithms, and four error metrics capturing accuracy, bias, and precision. Red fields indicate high metric values, i.e., poor performance, while blue fields denote low values, corresponding to high estimation quality with respect to the respective metric.

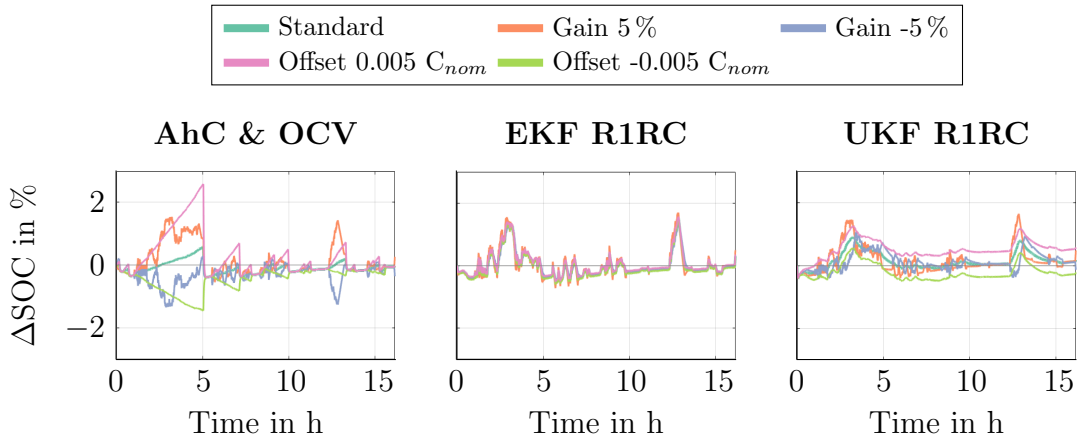

Figure 5.18: Time-series results for the *current sensor* category of the investigated SIB. The AhC & OCV consists of a recalibration mechanism during rest periods, which mitigates the effects of current offset errors. In contrast, the UKF R1RC accumulates the current error and relies heavily on the current sensor.

An initial SOC offset has a moderate impact on the AhC & OCV, as the algorithm can correct the deviation during the next rest period. Interestingly, the UKF R1RC is largely unaffected in terms of e_{max}, as it corrects the SOC offset immediately. In contrast, a capacity offset degrades the performance of the AhC & OCV, since normalization errors in SOC calculation accumulate over time. The model-based estimators are also sensitive to capacity offsets, exhibiting higher maximum errors and reduced precision, as reflected in increased standard deviations. Temperature offsets, on the other hand, have only a minor influence on all three algorithms. This indicates that the model-based estimators can tolerate moderate temperature misestimations, as they are able to compensate for the resulting errors in the LUT. To further compare the algorithm performance with the NMC/LTO cell and highlight the impact of different evaluation metrics, Supplementary Table A.2 summarizes the best and worst algorithms for each cell, based on various performance indicators. It is evident that, according to the measures of accuracy, all metrics favor the Kalman filter-based algorithms, with the UKF R1RC performing best for the $NaMO_2$/HC and the EKF R1RC for the NMC/LTO cell. However, when considering bias, different algorithms rank as the best or worst ones. For instance, the least bias for both cells, reflected by a low ME is achieved using the EKF R1RC.

Implications

Voltage measurement errors can strongly affect the performance of Kalman filter estimators, due to their reliance on voltage feedback for state correction. Interestingly, the tested SOC algorithms maintain high accuracy for the SIB even under strong voltage sensor disturbances. Detailed results for each voltage sensor scenario, based on the IA metric, are presented in Figure 5.19.

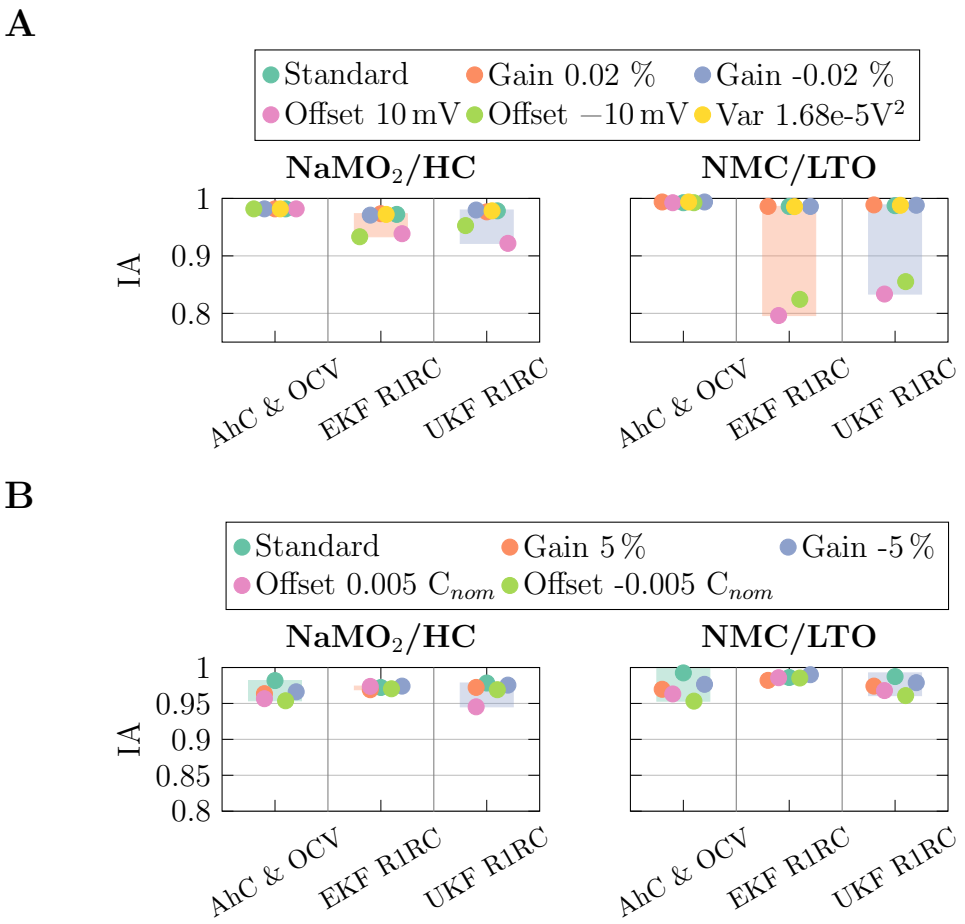

Figure 5.19: Comparison of algorithm performance considering IA across the two cell chemistries.
A: Voltage sensor.
B: Current sensor. The difference in AhC & OCV values between the two cells arises from the underlying load profile, which is power-equivalent rather than C-Rate-equivalent.

This robustness arises from the steep OCV curve of the $NaMO_2$/HC cell, whereas the NMC/LTO cell exhibits a relatively flat voltage curve and a narrow voltage window, reducing observability. As a result, absolute voltage offsets strongly influence the OCV of the NMC/LTO cell and, consequently, SOC estimation. The EKF R1RC exhibits a minimum IA below 0.8, whereas the $NaMO_2$/HC cell shows minimal sensitivity to voltage measurement errors, with the UKF R1RC maintaining a minimum IA above 0.9.

While the AhC & OCV is primarily dependent on current sensor accuracy and OCV recalibration, we observe that inaccuracies in current sensors impact both model-based algorithms and the AhC & OCV. This is due to the balance between overpotential estimation and the integrated coulomb counter in Kalman Filters, both of which are influenced by measurement errors. We observe that current sensor offset errors have the greatest

impact on SOC estimation, leading to long-term integration drift. However, the effect of current sensor errors remains mostly consistent across both cell chemistries. Furthermore, our analysis shows that, for industry-relevant sensor inaccuracies, errors in voltage sensors have a more significant impact than realistic current sensor errors, particularly in the chosen profiles.

In general, all tested algorithms perform well for the commercial SIB in the high-power use case. Even in the presence of sensor errors, the SIB achieves reliable results, largely due to the steep OCV(SOC) curve. Even when model inaccuracies lead to higher voltage deviations, the model-based estimations remain robust. In an extreme case with a positive voltage offset, the EKF R1RC for the $NaMO_2$/HC cell achieves an RMSE of approximately 0.7 %, whereas the EKF R1RC for the NMC/LTO cell achieves an RMSE value of 3.47 %, which is five times higher. Using our evaluation framework, we can quantify these behaviors precisely, confirming that SOC estimators originally developed for lithium-based systems can be applied to the targeted SIB without compromising accuracy, and even show potential for further improvements.

5.4 Transferability of SOH Algorithms

In this section, we investigate the transferability of real-time capable SOH estimation methods to the investigated SIB. We evaluate five algorithms with a focus on their operational performance under application-relevant conditions. Although resistance increase is often an important indicator in high-power systems, we concentrate on capacity estimation, as no significant resistance increase was observed in the application. Moreover, aging tests from Chapter 4 showed inconsistent trends, including decreasing values in some operation cases, rendering resistance an unreliable metric for systematic evaluation.

Unlike SOC estimation, where we relied on the IA indicator as a metric of accuracy, the same metric is not applicable for SOH estimation. The reason is that the IA tends to approach a value of 0 when the reference values are constant or vary only slowly over time, as each reference value approximates the average reference value. Therefore, we use the normalized error metric RMSPE for the overview of algorithm performance within each category.

Due to the absence of a suitable aging model for the original NMC/LTO cell in our simulation toolchain, we focus the SOH algorithm evaluation on the SIB, taking into account the implications from the high-power application presented in Chapter 3. Analogous to the SOC evaluation, this section demonstrates the methodology for operational SOH algorithm assessment using the high-power use case. Our framework serves as a foundation for application-specific algorithm selection and further optimization, while the results exemplify its practical use with established algorithms and predefined parameters.

5.4.1 Simulation-based Design of Experiment

5.4.1.1 Evaluation Categories

We focus on seven evaluation categories to systematically analyze different factors influencing SOH algorithm performance. Similar to the SOC benchmark, one simulation is carried out containing all standard settings that is referred to as the *base scenario*. The results obtained from this evaluation are used as a reference for comparison of the variance created by the different categories and their parameter variances. An overview of all simulation scenarios conducted for the SOH benchmark is given in Supplementary Table A.3.

Base scenario
The driving profile of the high-power application DP1 at an ambient temperature of 25 °C is used as the base. Similar to the *base scenario* for SOC evaluation, voltage and current sensors are not subjected to additional disturbances.

As shown in Figure 3.3, the variation in SOH becomes particularly pronounced at an energy throughput of around 2000 kWh, which is specific to the targeted application. In this region, the spread around the mean is large, and the difference between minimum and maximum SOH values is greatest. This highlights the importance of accurate SOH estimation in such use cases, especially because deviations in SOH can have more serious consequences at lower values since at reduced SOH, small estimation errors may wrongly influence performance restrictions or trigger warranty-related decisions [207]. To address this within our framework, we define a charge throughput of 4000 Ah and assume a calendar age of 2000 d in the standard case, which corresponds to this critical operating window. This ensures that the estimators are evaluated under conditions where SOH accuracy is most relevant.

Dynamic high-power profiles
Beyond the standard profile, we employ the profiles DP2 and DP3 depicted in Figure 5.15.

Environmental temperature
Similar to the SOC benchmark, in addition to the standard ambient temperature of 25 °C, two scenarios are considered at 10 °C and 40 °C. These temperatures were selected to reflect the typical operating range in our high-power application.

Initial aging state
To analyze the performance of the estimators at different initial aging states without conducting long simulations, a series of simulation scenarios were designed that represent different initial battery age conditions. The battery simulation framework allows for defining the starting point of aging through two parameters: an initial SOH factor that adjusts

the battery's capacity and impedance, and a parameter that specifies the battery's age in terms of both calendar days and charge throughput. In this work, charge throughput and age in days are used as the variables to represent aging, capturing both cyclic and calendar aging effects. To determine the specific aging state, we assume an average SOC of 50 % and an average DOD of 10 % representing common operation in our investigated high-power vehicle application. Field data indicate that batteries can experience charge throughputs exceeding 125 000 Ah, although most vehicles remain within a range of up to 80 000 Ah. Based on these insights, we evaluate the functionality of the SOH algorithms across five additional aging states: a pristine condition with no charge throughput or calendar aging, an early aging state at 1000 Ah and 1000 days, moderate aging at 2000 Ah and 2000 days, and an advanced aging condition at 8000 Ah and 4000 days, emphasizing cyclic aging.

Aging rate
To analyze the impact of varying aging rates, a time scale factor within the battery simulation toolchain is used to control how quickly aging progresses. A higher value increases the frequency of aging updates, effectively accelerating the simulation of degradation. For example, a time scale factor of 5 reduces the interval between aging steps from one day to 4.8 hours. This allows long-term effects to be simulated within a shorter real-time span. The factor influences only the pacing of updates, not the severity of each individual aging step. To efficiently simulate long-term degradation, we used time scale factors of 60 and 120, corresponding to aging updates every 24 or 12 minutes respectively, enabling the modeling of months of battery use within just a few simulation hours [110]. However, it should be noted that these high acceleration factors induce very fast degradation that are unlikely to occur to this extent in the targeted SIB application. Nevertheless, they serve to test the limits of the estimators under extreme degradation scenarios.

Voltage sensor
Similar to the SOC estimation, the simulated battery data that serves as input for the algorithms is distorted by added noise and gain errors. Three types of distortion are implemented: A gain error, an offset error, and a variance error. These errors were added separately to analyze their impact individually. For the voltage sensor, the gain error is set to ± 0.0002. With the offset error, an additive error of $\pm 10\,\mathrm{mV}$ is added to the sensor data. The variance error is added by a gaussian normally distributed error with a value of $0.000\,016\,8\,\mathrm{V}^2$ [204].

Current sensor
Similar to the SOC evaluation, the gain error is set to ± 0.05 of the nominal value of the sensor. With the offset error, an additive error of $\pm 0.005\ C_{nom}$ is added to the sensor data reflecting an extreme, but possible behavior of typical BMS sensor hardware [183].

Faulty initialization
To assess algorithm convergence, we vary the nominal capacity by $\pm 0.2\ C_{nom}$. Additionally, we simulate an ambient temperature offset of $\pm 10\,^{\circ}\mathrm{C}$.

5.4.2 Real-time SOH Algorithms

Since our evaluation framework, as outlined in Section 5.1, emulates a real-time BMS, we focus on model-based and direct methods, as in the previous SOC assessment. Specifically, we benchmark five real-time capable estimators: coulomb counting (CC), as well as four model-based algorithms, EKF, UKF, weighted ordinary least square algorithm (WOLS), and recursive approximation of total least squares algorithm (RTLS), all implemented using MATLAB/Simulink's Simscape library and documented in [185].

In model-based approaches, capacity is treated as an internal state variable and is adjusted by minimizing the SOC estimation error, rather than directly minimizing voltage error. Capacity is inferred from the relationship between charge throughput and changes in SOC, according to Equation (5.18). Accurate SOC estimation is therefore critical, as errors in SOC propagate into the capacity estimate. Conversely, an inaccurate capacity value also feeds back into the SOC estimation, potentially amplifying overall estimation errors. For all four model-based algorithms, we use the best-performing SOC estimator from Section 5.3.3, namely the UKF R1RC with the predefined initialization shown in Table 5.3. This configuration yielded the most accurate results in the context of the high-power application. An overview of the general process of capacity estimation and its connection to SOC estimation is shown in Figure 5.20.

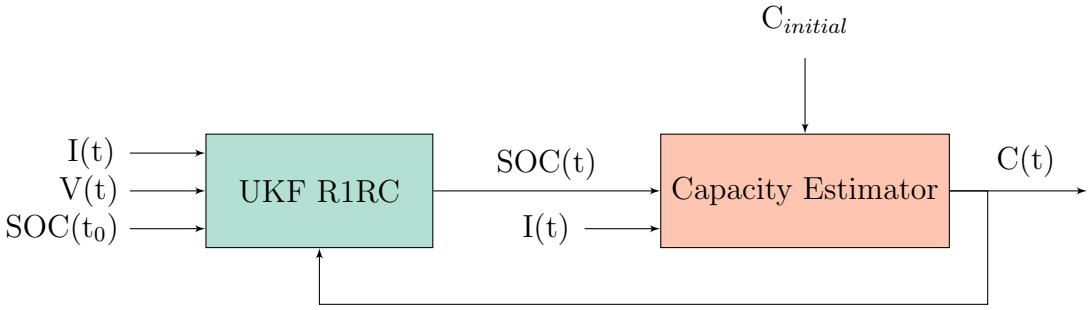

Figure 5.20: Dependency of model-based capacity estimator on SOC estimation, measured signals, and initial values.

Coulomb counting
Equation (2.9) requires the actual capacity at a given time step to calculate the SOC. Rearranging this equation yields Equation (5.18), which directly determines the capacity. The parameter η_C denotes the coulombic efficiency. In this work, the coulombic efficieny is set to 1.

$$C_{act} = \frac{\int_{t_0}^{t_1} \eta_C \cdot i(t)dt}{\mathrm{SOC}(t_1) - \mathrm{SOC}(t_0)} \tag{5.18}$$

To determine the SOC, we can either use estimated values from an algorithm or refer to the OCV(SOC) mapping. There are two common approaches to detect the relaxed state.

- Time-dependent: The cell must rest for a certain time until the cell can be considered in a relaxed state.

- Negligible voltage change: During relaxation, the voltage gradually stabilizes. If its derivative reaches zero, the cell is considered relaxed. However, due to noise and other influencing factors, this process would theoretically continue indefinitely. Therefore, a threshold is defined. Once the voltage change falls below this value, the cell is assumed to be in a relaxed state.

Accurate capacity estimation requires a sufficiently large DOD and a clear voltage difference between the start and end points. If these points are too close in voltage, even small measurement errors can significantly distort the result. For an accurate capacity estimation, several other conditions must be met. The complete process is illustrated in Figure 5.21 and consists of three stages that are described in the Supplementary Material A.7.

Least-squares algorithms
The objective of least-squares algorithms is to identify the linear function that best characterizes the relationship between the states and the measurement points by minimizing the sum of the squared residuals as shown in Figure 5.22 [208]. For capacity estimation, the relation between capacity and SOC from Equation (2.9) is used. As shown in Equation (5.19), x represents the ΔSOC and y the resulting change of charge ΔQ.

$$\begin{cases} x_n = SOC(t_1) - SOC(t_0) \\ y_n = \int_{t_0}^{t_1} i(\tau) d\tau \end{cases} \tag{5.19}$$

We can then rewrite the Equation (2.9) to

$$y_n = Q \cdot x_n \tag{5.20}$$

This equation is then used to estimate the capacity using least-squares estimation, where Δx_n and Δy_n represent the uncertainties, and $\hat{Q}$ the estimated capacity:

$$(y_n - \Delta y_n) = \hat{Q} \cdot (x_n - \Delta x_n) \tag{5.21}$$

Both y_n and x_n have sensor noise and estimation noise, respectively [209]. The WOLS minimizes the weighted sum of squared residuals Δy_n, whereas the RTLS minimizes both the sum of squared residuals Δy_n and Δx_n [209].

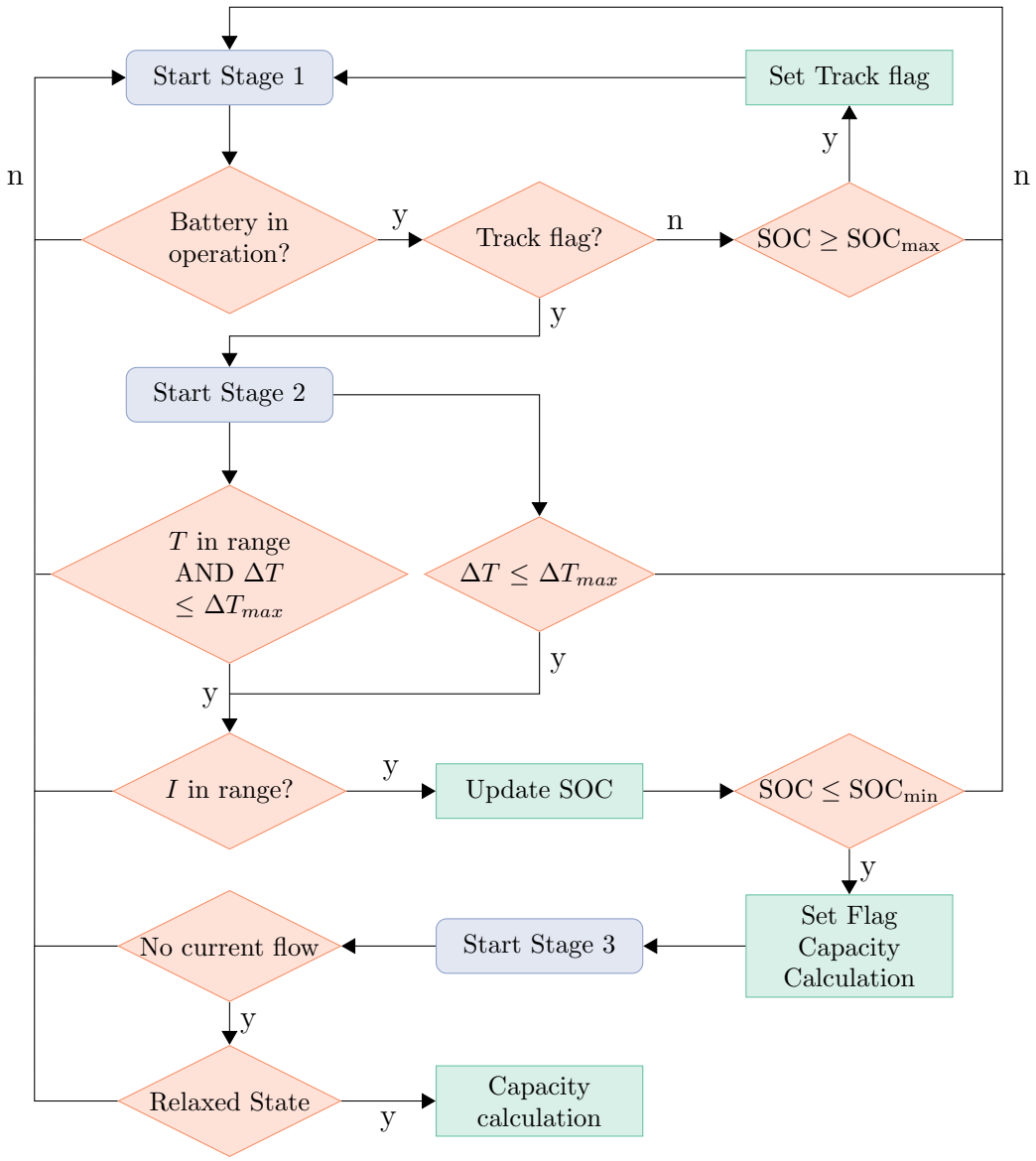

Figure 5.21: CC capacity estimation as stateflow diagram. Each block in marks the start of a new stage. Each block in represents a process. The diamond-shaped blocks in are conditions.

For the WOLS, the estimated capacity is obtained by minimizing the weighted least squares function:

$$\chi^2_{WOLS} = \sum_{n=1}^{N} \frac{(y_n - Y_n)^2}{\sigma^2_{y_n}} \tag{5.22}$$

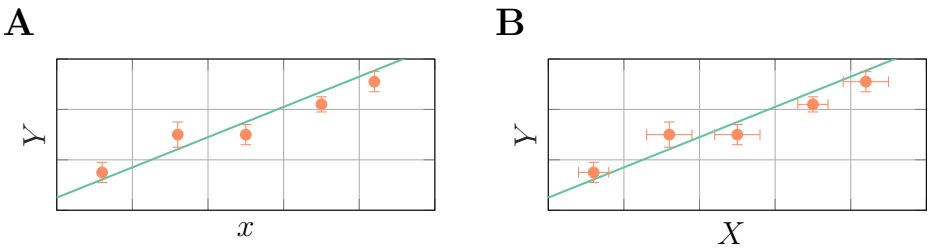

Figure 5.22: Exemplary data with estimated regression line.
A: The WOLS minimizes the squared residuals Δy.
B: The RTLS minimizes the squared residuals Δy and Δx.

The solution for the estimated capacity can be determined according to Equation (5.23).

$$\hat{Q} = \frac{\sum_{n=1}^{N} \frac{x_n y_n}{\sigma_{y_n}^2}}{\sum_{n=1}^{N} \frac{x_n^2}{\sigma_{y_n}^2}} \tag{5.23}$$

A forgetting factor $\gamma \in [0,1]$ can be introduced to gradually reduce the influence of older measurements, resulting in the solution according to Equation (5.24) [209].

$$\hat{Q} = \frac{\sum_{n=1}^{N} \gamma^{N-1} \frac{x_n y_n}{\sigma_{y_n}^2}}{\sum_{n=1}^{N} \gamma^{N-1} \frac{x_n^2}{\sigma_{y_n}^2}} \tag{5.24}$$

To additionally account for the uncertainty of x_n, the weighted total least-squares algorithm estimates the capacity by minimizing the following function:

$$\chi_{WTLS}^2 = \sum_{n=1}^{N} \frac{(x_n - X_n)^2}{\sigma_{x_n}^2} + \frac{(y_n - Y_n)^2}{\sigma_{y_n}^2} \tag{5.25}$$

For the RTLS used in this work, we set $\sigma_{xn} = k\sigma_{yn}$, leading to the estimation considering a forgetting factor:

$$\hat{Q} = \frac{-k_{1,n} + k^2 k_{3,n} + \sqrt{(k_{1,n} - k^2 k_{3,n})^2 + 4k^2 k_{2,n}^2}}{2k^2 k_{2,n}} \tag{5.26}$$

where

$$
\begin{aligned}
k_{1,n} &= \gamma k_{1,n-1} + \frac{x_n^2}{\sigma_{y_n}^2}, \\
k_{2,n} &= \gamma k_{2,n-1} + \frac{x_n y_n}{\sigma_{y_n}^2}, \\
k_{3,n} &= \gamma k_{3,n-1} + \frac{y_n}{\sigma_{y_n}^2}.
\end{aligned}
\tag{5.27}
$$

The tuning of the least-squares algorithm parameters is summarized in Supplementary Table A.5.

Kalman filters
The functionality and underlying principles of Kalman filters have been discussed in Section 2.4.1.3. In contrast to SOC estimation, the SOH estimation focuses solely on capacity, which is treated as the state to be estimated. The filter operates using the noisy, estimated SOC and current as inputs. The parameterization of the nonlinear Kalman filters, namely the EKF and UKF, follows the same iterative tuning strategy as applied for SOC estimation, with the corresponding parameters listed in Supplementary Table A.6.

5.4.3 Results

Figure 5.23 provides an overview of the performance of the five SOH estimation algorithms for the SIB, using the normalized metric RMSPE. In each category, a lower RMSPE corresponds to a more accurate average estimation.

Notably, the results for SOH estimation are generally less accurate than those for SOC, with RMSPE values exceeding 5 % in some scenarios. This is primarily due to the low observability of capacity in the available, noise-affected measurement signals. In addition, if a systematic SOC error is already present, it may be misinterpreted by the filter as a deviation in capacity. However, these general challenges are not unique to SIBs but are also present in LIBs.

The UKF and EKF estimators generally demonstrate the best performance across most categories, consistently achieving low errors. The UKF reaches an average RMSPE of 2 % across all categories, while the EKF achieves an average RMSPE of 1.7 %. Their estimates remain relatively stable even in the presence of current or voltage sensor faults, highlighting their robustness to deviations from standard operating conditions. However, performance significantly degrades in the category *faulty initialization*. The errors in this category are primarily caused by large initial capacity errors of ±20 %. Although the error gets corrected over time, the duration of the base profile is too short for the capacity estimate to converge, so significant errors remain at the end of the measurement. The WOLS also achieves good results, with an average RMSPE of 1.8 % across all categories.

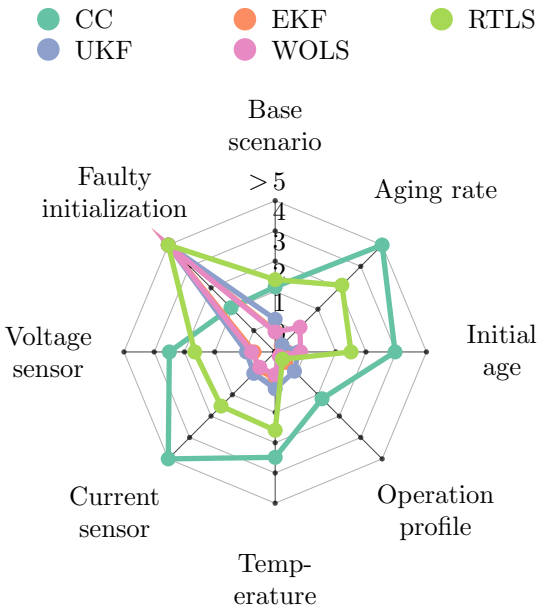

Figure 5.23: Overview of algorithm performance results across all robustness categories. Each dot represents the achieved average RMSPE value in the respective category. RMSPE values greater than five are cut off.

The only exception is large initial capacity deviations, which also cannot be corrected within the limited duration of the profile. In contrast, the RTLS estimators exhibits higher RMSPE values across most categories with an average RMSPE value of 3.3 %, indicating generally reduced estimation accuracy. Nevertheless, with the exception of the *faulty initialization* category, the errors remain below 5 % RMSPE, suggesting that their performance remains within an acceptable range for most conditions [79]. The CC algorithm lacks adaptability when it comes to current sensor faults, variation of initial age, and varying aging rates. However, it is not strongly influenced by a capacity offset yielding to an average RMSPE value of 4 % across all categories.

Figure 5.24 illustrates the time-series estimation results for each algorithm under the base scenario. The green line denotes the deviation of the estimated SOH from the reference value, while the orange line represents the deviation in SOC. The SOC for the Kalman filter and least-squares estimators is determined by the UKF R1RC, analyzed in Section 5.3.2.

The discrete nature of the CC method is evident in the step-wise behavior observed in the SOH. The estimator updates only when the DOD exceeds a certain threshold and the environmental conditions, such as current and temperature, remain within a valid range. For the *base scenario*, the algorithm triggers the capacity estimation two times. Since the nominal capacity is used for the SOC estimation, the SOC error is very dynamic and higher than for the rest of the algorithms. The SOH estimated by the EKF shows an average error of less than 1 % and converges toward a stable value. The UKF SOH estimator

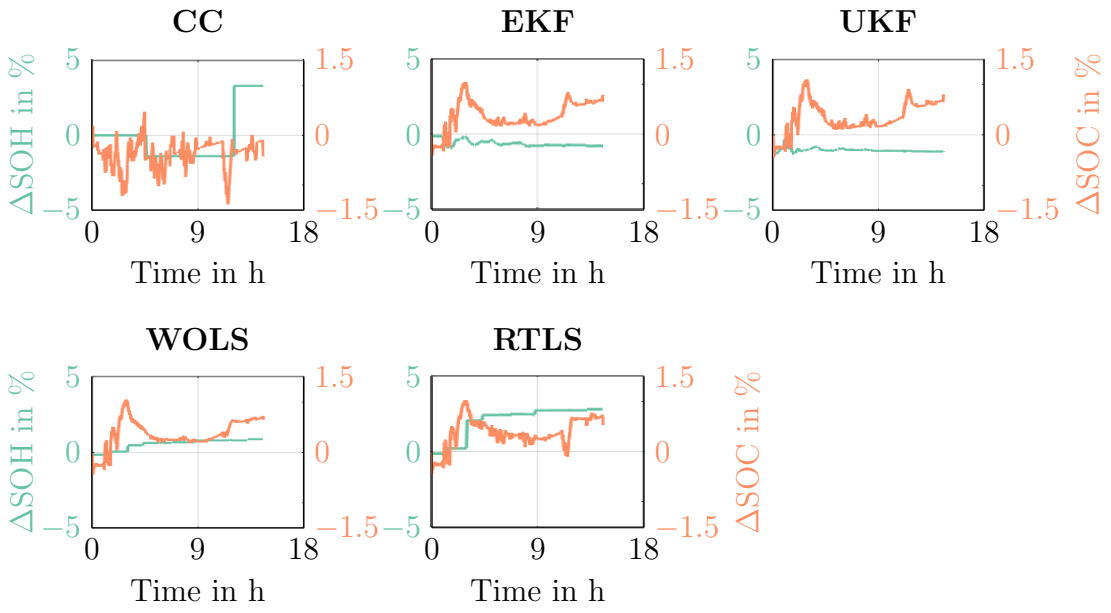

Figure 5.24: Time-series for the *base scenario* across each algorithm. The green curve depicts the SOH and the orange curve the SOC error, respectively.

exhibits similar behavior, resulting in comparable SOC errors. In contrast, the RTLS and WOLS tend to overestimate capacity and also converge to fixed values. Similar to the CC approach, both RTLS and WOLS operate as discrete estimators, which is reflected in their step-wise SOH profiles. These algorithms generally face difficulties in identifying the correct initial capacity trend. The WOLS method maintains moderate errors in both SOC and SOH, whereas the RTLS estimator yields the largest SOH deviations among all evaluated methods, despite still achieving reasonable SOC estimates. In both cases, the estimator misattributes an SOC offset to capacity drift, thereby misinterpreting the underlying source of the error. Generally, we observe that a low SOC error does not necessarily yield a low SOH error and vice versa. All algorithms perform acceptable in the *base scenario* whereas the WOLS yields the lowest SOH and SOC errors according to the RMSPE.

To enable a more detailed analysis of algorithm performance across all categories, Figure 5.25, analogous to Figure 5.17 fo SOC evaluation, shows the individual results in each robustness category for every scenario, using metrics for accuracy, bias, and precision. While all investigated high-power profiles are characterized by strong current dynamics, DP2 and DP3 exhibit lower peak currents compared to DP1, which has a positive effect especially on the CC and the RTLS. This is partly because current sensor noise increases with higher C-Rate, introducing integration errors that negatively influence estimation accuracy. For the category *initial age*, the first value indicates charge throughput in Ah and the second the calendar age in days. In general, this category has little impact on estimation accuracy, except for the CC, where larger errors are observed, particularly in the BOL scenario. This is caused by a higher offset, as reflected in the increased ME. The error arises because, although the errors in the estimated charge and SOC are small

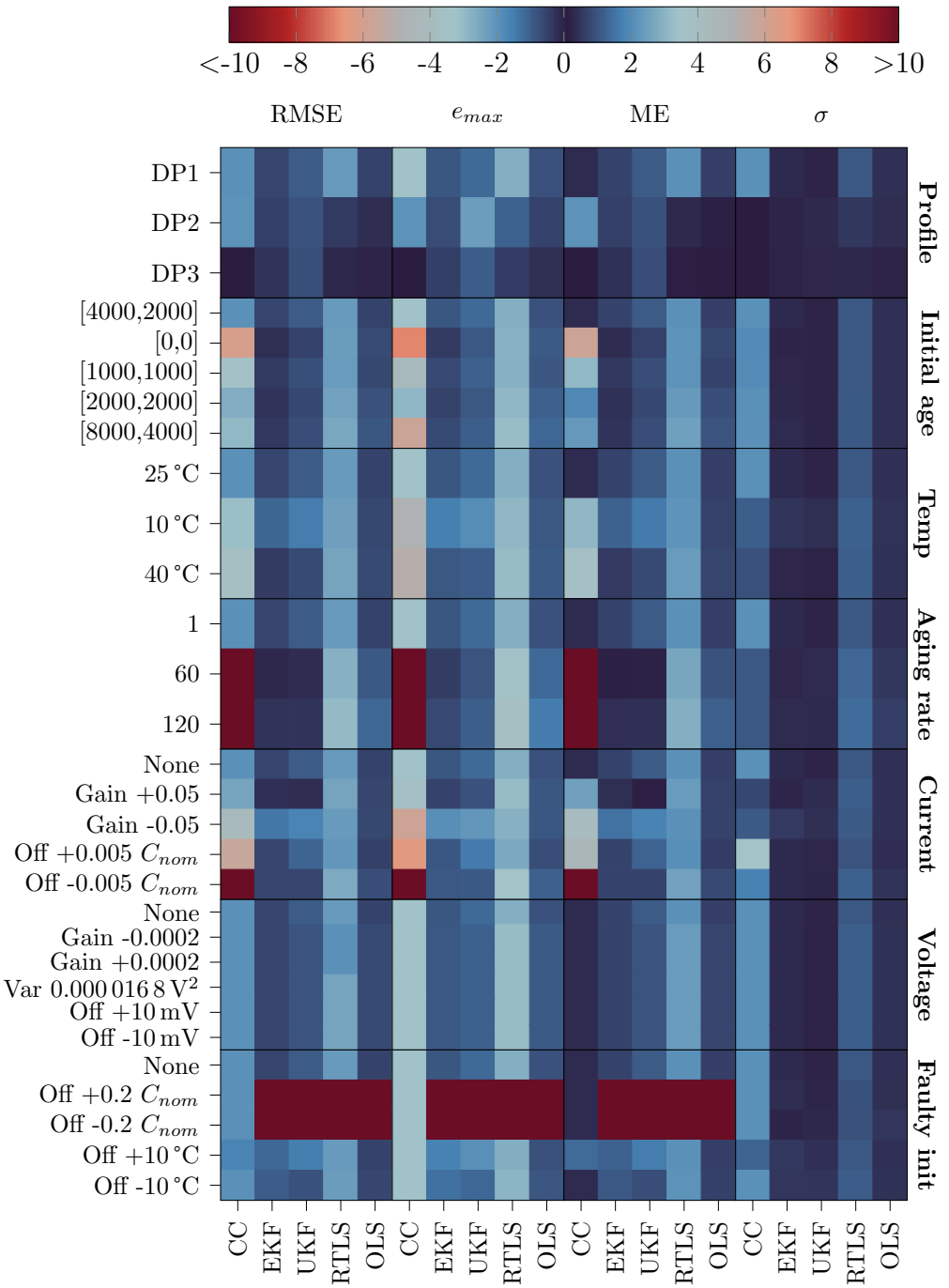

Figure 5.25: Assessment of accuracy, bias, and precision across all simulation scenarios and algorithms. A red color indicates a high error value, whereas blue indicates low errors.

individually, their ratio amplifies the resulting CC error. This behavior will be analyzed in more detail later in this section. In the *temperature* category, the CC, EKF and UKF show a sensitivity, attributable to slightly increased SOC errors at lower temperatures, while the other algorithms remain largely unaffected. In the *aging rate* category, degradation is

artificially accelerated to test algorithm performance under rapid capacity changes. CC produces large errors because it assumes constant capacity during the triggering period, while the reference capacity decreases, resulting in SOC overestimation and substantial capacity errors. Being a discrete estimator that triggers only infrequently, CC cannot properly track rapidly changing capacity. For the remaining algorithms, two trends are observed: the performance of the two Kalman filters remains largely unaffected by the accelerated capacity changes, whereas the least-squares algorithms show a slight degradation in estimation accuracy due to their initialization. A forgetting factor of 98 % was used for RTLS and WOLS. If faster aging were expected, this factor should be reduced. Since the investigated SIB does not experience significant aging during operation, the forgetting factor was set high for this study, which in turn introduces erros for these scenarios. The *current sensor* particularly affects the CC, where especially a constant offset leads to significantly reduced accuracy. As shown in Figure 5.26A this stems from a higher error in estimated Q. The offset only has a minor effect on the other algorithms. The Kalman Filters are both mainly affected by a negative gain, increasing the SOH errors. Disturbances in the *voltage sensor* have almost no effect on CC performance. The other algorithms are also minimally affected. Lastly, the *faulty initialization* category has the most significant impact on algorithm accuracy, primarily due to the initial capacity offset in the estimation algorithms. Because SOC changes are small and the profile duration is limited, the measurements provide only weak excitation for updating capacity. Additionally, the Kalman filters update their capacity estimate gradually based on the Kalman gain, while the least-squares algorithms weigh past data heavily due to the high forgetting factor. As a result, these algorithms cannot fully correct a large initial capacity error within the profile duration. The CC algorithm, in contrast, is unaffected by the capacity offset, as it always uses the nominal capacity for SOC estimation and does not necessitate an initial capacity value.

We now analyze the CC in more detail, as it exhibits the highest variability under different operating conditions as seen in Figure 5.23. Our analysis is grounded in the fundamental principles of the algorithm, focusing on how errors in ΔSOC and charge propagate to capacity, while the specific values observed for our cell and use case help us quantify the algorithm's performance under realistic operating conditions. As an open-loop estimator, the CC relies entirely on the accuracy of the estimated ΔSOC and accumulated charge Q, as described in Equation (5.18). Figure 5.26 illustrates the relationship between the estimation errors in Q and ΔSOC, with bubble size representing the capacity error, which is defined according to Equation (5.28).

$$Cap_{error} = \left(\frac{C_{ref} - C_{est}}{C_{ref}} \right) \cdot 100\ \% \tag{5.28}$$

The bubble color indicates the category of the respective scenario. Each bubble corresponds to a single SOH value at the time calculation is triggered. In the *base scenario*, this occurs twice, and both values are shown separately. As already discussed, in the *aging rate* category, the CC method is triggered while the reference capacity has already decreased during the triggering period, resulting in an increased SOC. Because the CC

method assumes that capacity remains approximately constant during this period, this assumption is violated, leading to unrealistically high capacity errors. Therefore, this category is excluded from subsequent analyses.

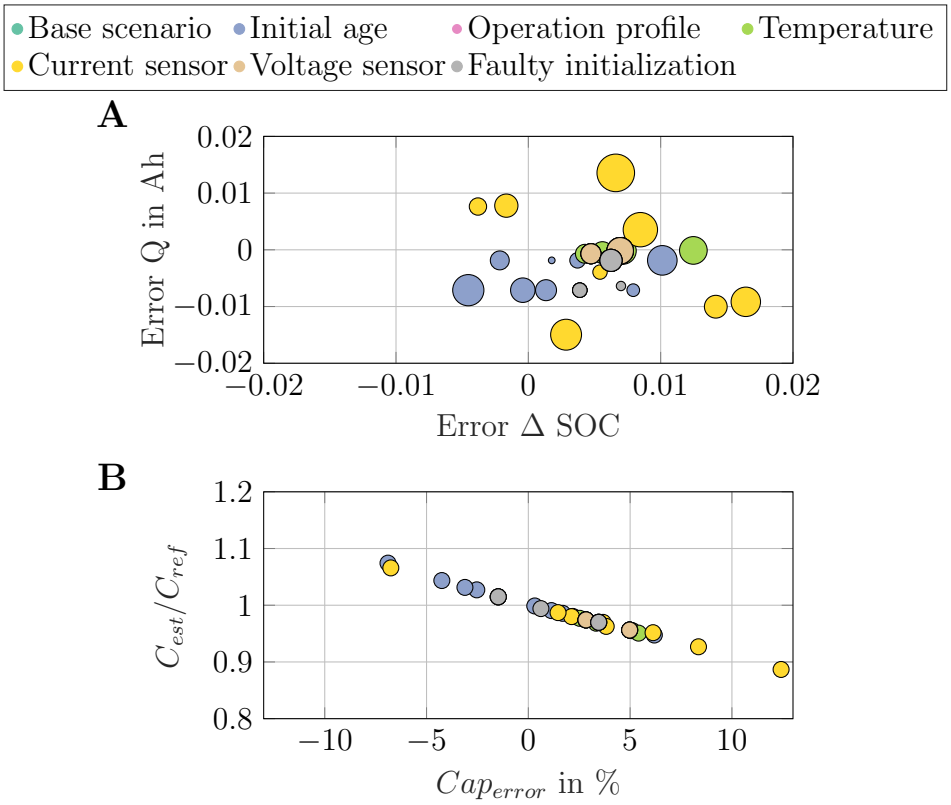

Figure 5.26: Influence of error in Q and ΔSOC on capacity error. Each point represents an estimate produced by the CC.
A: For each scenario within each category the error in Q over error in ΔSOC is plotted. The size of the bubble increases linearly with the capacity error defined according to Equation (5.28).
B: Link of capacity error, defined according to Equation (5.28), and the ratio C_{est}/C_{ref}, defined by Equation (5.29).

It is evident in Figure 5.26A that increasing deviations in ΔSOC or in Q generally lead to higher estimated capacities, although the relationship is non-linear. The dependency between these estimation errors and the ratio C_{est}/C_{ref} can be expressed mathematically as:

$$\frac{C_{est}}{C_{ref}} = \frac{1 + \frac{error_{Ah}}{\Delta Ah_{ref}}}{1 + \frac{error_{\Delta SOC}}{\Delta SOC_{ref}}} \tag{5.29}$$

Here, $error_{\mathrm{Ah}}$ denotes the deviation between the actual and estimated charge, while $error_{\Delta\mathrm{SOC}}$ represents the deviation in the SOC window. A ratio $C_{\mathrm{est}}/C_{\mathrm{ref}} > 1$ indi-

cates capacity overestimation, whereas a ratio below 1 corresponds to underestimation. Accordingly, the normalized capacity error Cap_{error} is directly proportional to $C_{\mathrm{est}}/C_{\mathrm{ref}}$. Figure 5.26B illustrates this relationship for our scenarios, providing a validation of the estimator's functionality. In particular, scenarios from the *current sensor* category exhibit capacity deviations of up to 12 %, which leads to a Cap_{error} roughly five times higher than in the standard case. Even in scenarios without disturbances, such as different initial aging states, unfavorable combinations of errors in Q and ΔSOC can still occur, producing elevated capacity errors. For most scenarios, however, capacity errors fall below 5 %, indicating that even under the demanding conditions of our application, the CC algorithm remains a suitable SOH estimator and satisfies the application requirements.

For our high-power use case, SOH estimation achieves errors below 3 % under the standard profile, demonstrating that the algorithms are suitable for the operating conditions. As expected, current sensor errors lead to the largest deviations for the CC algorithm, whereas the Kalman filters remain robust across all scenarios, exhibiting RMSPE values below 1 % for most cases. High initial capacity errors cannot be fully corrected within the profile duration, leading to RMSPE values exceeding 10 %. Overall, the main limitation for SOH accuracy in this application is the narrow SOC range, which strongly reduces the observability of capacity.

5.5 Conclusion

The drop-in potential of SIBs as complementary systems to commercial LIBs has been increasingly addressed in the literature, particularly with regard to manufacturing processes and material compositions. However, the implications for the system-level, especially for the BMS, remain unexplored. This chapter addressed this gap by systematically evaluating the transferability of real-time capable SOC and SOH algorithms from LIB systems to SIBs, utilizing a fully automated simulation toolchain that is made publicly available [179]. This toolchain replicates the entire BMS signal path, from real-world high-power load profiles to the deployment of diagnostic algorithms. Two electrical models and one aging model, parameterized with experimental data from the targeted SIB, are integrated into the simulation toolchain. The aging model captured a critical degradation pattern: capacity fade predominantly occurs at low SOC and is minimal around mid mean SOC. Importantly, we demonstrated that, for the investigated high-power use case, modeling a compression of the OCV is sufficient to reproduce aging effects, mitigating complexity requirements.

We systematically assessed three runtime-capable SOC algorithms and benchmarked them against the performance of the in the use case originally used NMC/LTO LIB. Our analysis, including industry-standard hardware considerations, identified voltage sensor errors and faulty initialization as the dominant sources of model-based SOC estimation errors. Yet, the SIB's highly linear and steeper OCV curve mitigates these effects substantially.

Even with a introduced voltage sensor offset of 10 mV, all evaluated algorithms maintained an RMSE below 1.5 %, highlighting their robustness for such cases.

A smaller SOC error provides a solid foundation for SOH estimation suggesting that SOH estimates for the SIB should be at least as accurate as those for the LIB when only considering SOC accuracy. We determined the battery capacity based on the current and the estimated SOC and fed the updated capacity estimate back into the SOC estimator. While the UKF, EKF and WOLS generally demonstrated strong performance, our analyses showed that if the initial capacity estimate is inaccurate, the investigated model-based filters have difficulty autonomously correcting it within the duration of the profile. Even though it is possible to account for this offset by further adjusting the tuning parameters, such adjustments can degrade the accuracy of the estimator under other, more basic operating conditions. For the investigated scenarios, the EKF proved to be a particularly robust choice for the high-power use case, delivering consistent and accurate performance across different operating scenarios.

Overall, we developed a flexible simulation toolchain that enables a fast, structured, and quantitative evaluation of BMS algorithms under realistic operating conditions. This framework allows users to efficiently assess algorithm performance, identify weaknesses, and adapt configurations to specific applications or cell chemistries, enabling rapid algorithm performance assessment. Applied to the investigated SIB, the results show that conventional SOC and SOH estimation methods are largely transferable. Across all tested scenarios, including extreme conditions, the SOC estimators achieved RMSE values below 2.5 %, demonstrating high robustness. The favorable shape of the OCV curve can potentially reduce demands on model accuracy and sensor quality. In contrast, SOH estimators showed slightly higher deviations, particularly under extreme conditions such as erroneous initial capacity. SOH estimation remains particularly challenging, mainly due to the operational constraints of the target application.

6 Conclusions and Outlook

In the quest for sustainable and cost-effective battery technologies, SIBs are emerging as a promising alternative to commercial lithium-based systems. While SIBs and LIBs share similar electrochemical properties that suggest potential for drop-in integration, differences in OCV characteristics and degradation behavior must be thoroughly understood and addressed.

In this work, we present a systematic approach to accelerate the integration of new cell chemistries into existing battery systems by linking aging behavior, diagnostic performance, and application requirements. As a use case, we focus on a high-power automotive application that currently employs costly NMC/LTO cells. Given that SIBs exhibit similar performance characteristics at potentially lower cost, they represent a promising candidate for replacement. The main challenge in this application lies in the combination of high currents, low DODs, and the absence of full charging during operation, all of which place increased demands on both algorithms and models. Using the field data comprising over 12 million readouts from 600,000 vehicles, we characterize typical operating conditions and requirements for lifetime and management. For rapid deployment of new cell chemistries, it is essential to have methods in place that provide timely information on battery behavior in the field. To this end, we introduce an anomaly detection framework that systematically detects batteries with unusual aging patterns, supporting manufacturers in assessing performance and guiding operational decisions such as battery replacements.

To evaluate whether SIBs can be integrated into the same application meeting the requirements of our use case, we first need to understand their specific aging behavior. Therefore, we investigated the aging behavior of a commercial SIB with a layered-oxide cathode and a HC anode across different conditions and highlighted distinctive aging behaviors through a large-scale aging study. Remarkably, even after 4,000 EFC, the capacity loss remained below 11 % for all tested conditions. Across all cells, the median capacity loss was approximately 2 %, underlining the cell's high lifetime. Interestingly, the cells exhibit the highest aging in the lower SOC range, potentially due to mechanical stress during sodium-ion storage at low SOC. By analyzing degradation behavior using experimental diagnostic techniques, we identified LSI and LAM of the negative electrode as the dominant degradation modes. Based on the experimental data, we fit a semi-empirical aging model that captures the relationship of capacity and resistance with operating conditions. Using this model and the requirements of the high-power application, we tested common real-time capable BMS algorithms in a publicly-available simulation framework.

For SOC estimation, we identified the UKF as the best-performing algorithm in terms of accuracy, bias, and precision for our use case and the chosen SIB. Compared to the originally used lithium-based cell, our results show that a robust estimation can also be achieved in demanding cases of the application: Even when the underlying BMS model showed larger voltage deviations, the resulting SOC error remained small which is due to the broad voltage window of the SIB voltage. For the investigated worst-case voltage offsets, some estimators achieve an accuracy approximately five times higher than that of the originally deployed battery, demonstrating their high robustness even under such disturbances. Moreover, we evaluated five real-time capable algorithms for their suitability in SIB SOH estimation. We demonstrated that, for the investigated SIB and use case, filter-based algorithms are well suited for SOH estimation. The best performing algorithm achieved an average error across all scenarios of approximately 1.7 %.

The main contributions of this work can be summarized as follows:

- **Analysis of a unique, extensive LIB field dataset in a high-power application as a benchmark for SIB integration:** We analyzed over 12 million readouts from 600,000 customer and prototype vehicles. By examining the influence of load history and operating scenarios on estimated battery aging, we demonstrated how statistical learning methods can be used for detecting irregular batteries. The introduced framework can support manufacturer in aging-aware fleet operation and reliability analyses.

- **Aging study of a commercial SIB under diverse conditions:** We evaluated aging behavior of 81 $NaMO_2$/HC cells over more than 4,000 EFC, covering a range of operating conditions - representing, to our knowledge, the most extensive dataset of its kind published to date. Unlike lithium-based systems, the main capacity loss occurs at low SOC, which we attribute to LAM on the desodiated anode and to LSI, based on DVA and EIS diagnostics. We quantify how features extracted from these methods relate to capacity fade, providing detailed insight into the degradation patterns of this commercial SIB. Remarkably, the median capacity loss across all cells is 2 % after approximately 4,000 EFC.

- **Simulation-based assessment of diagnostic algorithm transferability to SIB:** We developed a simulation framework to systematically evaluate real-time capable BMS algorithms for SOC and SOH estimation. While the fundamental electrochemical mechanisms of the investigated SIB are largely comparable to those of conventional LIBs, their distinct voltage profile and dynamic behavior require quantitative assessment to ensure reliable diagnostic performance. The investigated SIB benefits from a favorable OCV(SOC) curve and a broad voltage window, enabling accurate estimation performance, even exceeding that of the originally deployed lithium-based cell. The results suggest that simplified models and lower-cost voltage sensors could be employed in future BMS for SIBs without compromising algorithm accuracy. Our framework is publicly available and supports the process of BMS algorithm design and evaluation.

We are still in the early stages of understanding the degradation mechanisms of SIBs, focusing broadly on the electrochemical processes that drive aging. To validate our hypotheses regarding the dominant degradation modes, post-mortem analyses will be conducted in future work. In particular, to better understand the pronounced increase in hysteresis with aging, it is necessary to characterize the cell's pulse response and impedance over a wider range of SOC levels and C-Rates, as the observed hysteresis growth may be driven by increasing overpotentials. Our results indicate that hysteresis correlates strongly with SOH and may capture specific degradation patterns, making it a valuable source for diagnostics. Future research should therefore focus on extracting and modeling hysteresis features as functions of SOH and operating conditions, with the aim of improving both aging estimation and aging prediction. To further enhance the electrical model, incorporating model parameter's current dependencies would be beneficial within our high-power use case. Finally, to fully integrate a SIB into an application, system-level optimization, including pack design and thermal management, remain essential to ensure deployment.

A Appendix

A.1 Kalman Filter Equations

The Kalman Filter operates in two consecutive steps:

1. **Prediction:** In the prediction step, the state from the previous time step is propagated forward using the system model according to Equation A.1. This equation provides a prediction of the next state $\hat{\mathbf{x}}_{k+1|k}$ based on the previous estimate $\hat{\mathbf{x}}_{k|k}$ and the input $\mathbf{u}_k$. The associated uncertainty of the prediction is represented by the covariance matrix $\mathbf{P}$, which is updated according to Equation (A.2) [95].

$$\hat{\mathbf{x}}_{k+1|k} = \mathbf{A}\hat{\mathbf{x}}_{k|k} + \mathbf{B}\mathbf{u}_k \tag{A.1}$$

$$\mathbf{P}_{k+1|k} = \mathbf{A}\mathbf{P}_{k|k}\mathbf{A}^T + \mathbf{Q} \tag{A.2}$$

   The matrix $\mathbf{Q}$ represents the process noise covariance and quantifies how much uncertainty is introduced by model inaccuracies [210]. A larger $\mathbf{Q}$ value indicates lower trust in the model prediction.

2. **Update**: The update step corrects the prediction based on the measured voltage. In this context, the Kalman gain $\mathbf{K_{k+1}}$ determines how strongly the new measurement influences the updated state estimate and is computed according to Equation (A.3). Here, $\mathbf{R}$ is the measurement noise covariance, which reflects the reliability of the voltage measurement. A high measurement noise leads to a smaller Kalman gain, meaning that the filter relies more on the model prediction. Conversely, when the measurement is assumed to be accurate, the gain is higher, and the filter gives more weight to the measured voltage. The updated state estimate is then obtained by combining the model prediction and the new measurement according to Equation (A.4). For the case of SOC estimation, the measurement residual $(\mathbf{z}_{k+1} - \mathbf{H}\hat{\mathbf{x}}_{k+1|k})$ represents the difference between the measured and predicted terminal voltage. If the measured voltage is lower than predicted, the residual is negative, and the SOC estimate is corrected downward. The Kalman gain $\mathbf{K}_{k+1}$ determines how strongly this correction is applied. Finally, the uncertainty of the updated estimate is reduced by incorporating the new information, as expressed by Equation (A.5), where $\mathbf{I}$ is the identity matrix.

$$\mathbf{K}_{k+1} = \mathbf{P}_{k+1|k}\mathbf{H}^T(\mathbf{H}\mathbf{P}_{k+1|k}\mathbf{H}^T + \mathbf{R})^{-1} \tag{A.3}$$

$$\hat{\mathbf{x}}_{k+1|k+1} = \hat{\mathbf{x}}_{k+1|k} + \mathbf{K}_{k+1}(\mathbf{z}_{k+1} - \mathbf{H}\hat{\mathbf{x}}_{k+1|k}) \tag{A.4}$$

$$\mathbf{P}_{k+1|k+1} = (\mathbf{I} - \mathbf{K}_{k+1}\mathbf{H})\mathbf{P}_{k+1|k} \tag{A.5}$$

A.2 Sensitivity Analysis of Anomaly Detection

Figure A.1 illustrates the sensitivity of anomaly detection to different SOH deviations using various pseudo SOH values. Figure A.1A shows the case of SOH underestimation, while Figure A.1B shows overestimation. In both cases, pseudo SOHs that deviate strongly from the cluster average are consistently flagged as outliers, whereas small deviations result in significantly lower detection rates. The results highlight that reliable outlier detection requires adapting the detection threshold to both the initial cell-to-cell variation and the spread over aging. If this variation is not considered, overly narrow thresholds will lead to excessive false positives, particularly early in the battery's life, compromising the robustness of the method. A sound understanding of the degradation behavior and the expected variation is therefore essential for defining realistic and practical SOH acceptance thresholds. Choosing a higher significance level α would also raise the detection rates of outliers but also increase the accepted error of false-positive detections.

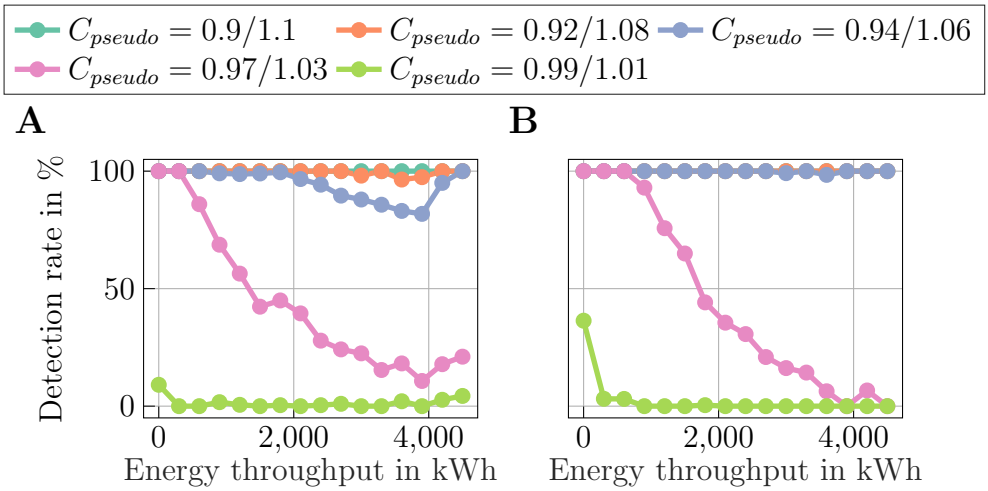

Figure A.1: Anomaly detection rate for different pseudo SOHs and $\alpha = 0.1$ across all clusters. The more the pseudo SOH deviates from the average SOH of the specific cluster, the more often the pseudo SOH is flagged as an outlier.
A: Underestimation of SOH.
B: Overestimation of SOH.

A.3 Modeling Results of the SIB

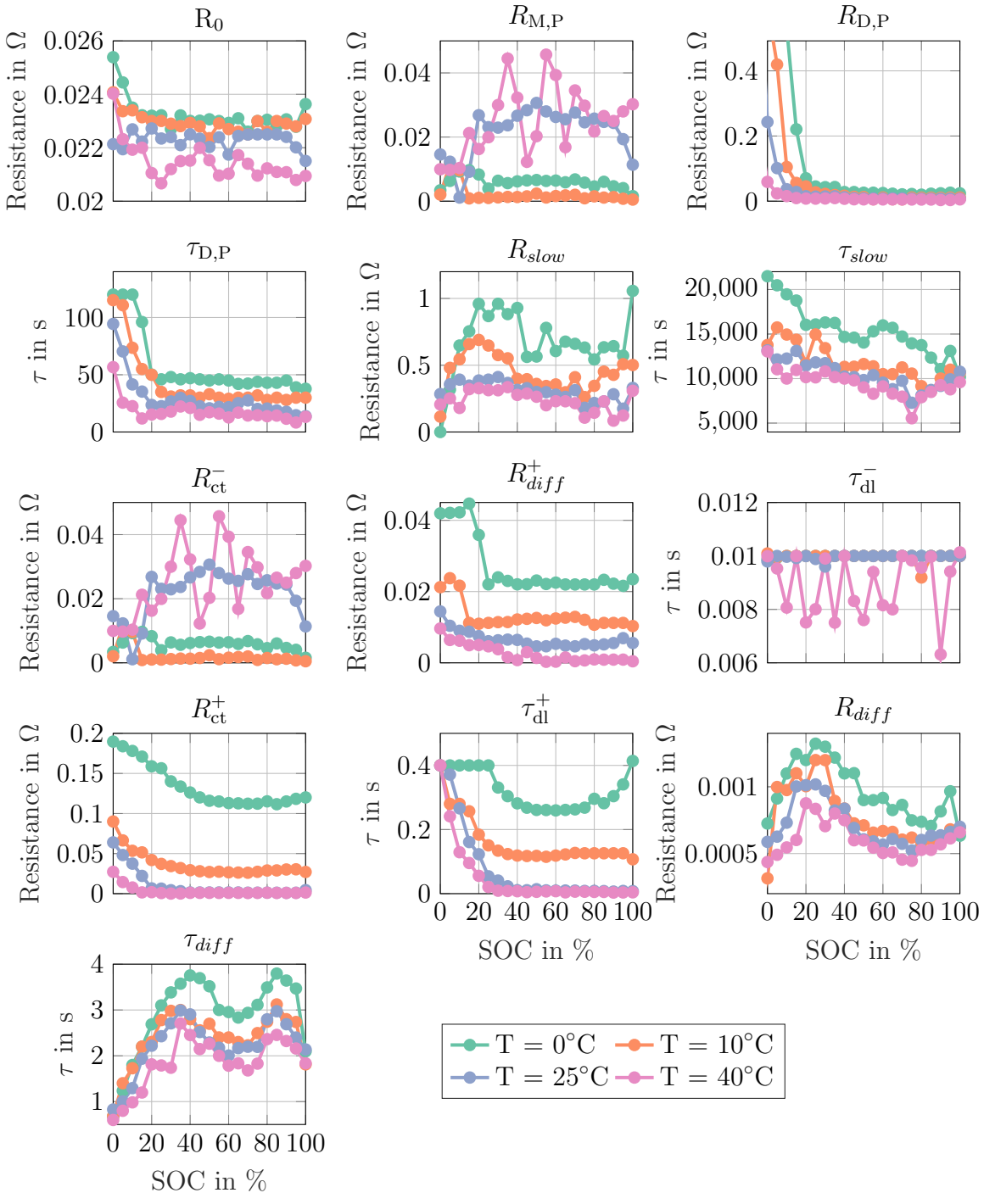

Figure A.2: Temperature and SOC dependent model parameters for the LiIon4 model based on the fitting procedure of Bihn et al. [193]. Time constants and resistances typically increase with lower temperatures and SOCs.

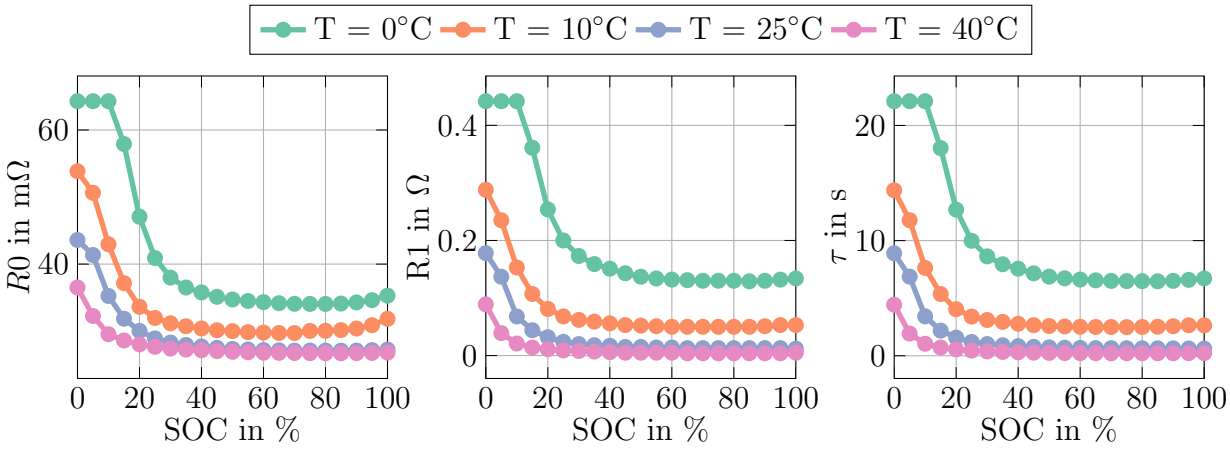

Figure A.3: Temperature and SOC dependent model parameters for the R1RC model. All parameters show a very similar trend with an increase at lower SOCs and temperatures.

For model validation, we use the profile shown in Figure A.4 and apply it to the measurement data of the SIB. The profile reaches C-Rates of more than 3 C in both charge and discharge directions, making it well-suited to reveal modeling inaccuracies.

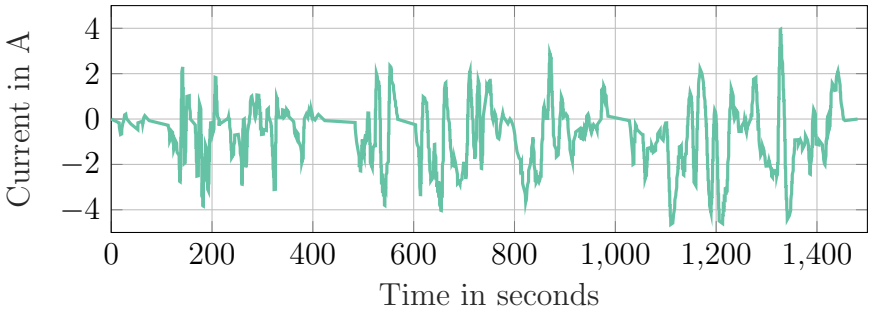

Figure A.4: Current profile used as an input for the validation of the LiIon4 and the R1RC model.

Figure A.5 compares the measured and simulated voltages obtained with the LiIon4 model, yielding an average voltage error of 3.7 mV at 10 °C. In contrast, using the simpler R1RC model, which can be implemented on real-world BMS systems, results in a higher average error of about 8.3 mV.

Figure A.6 displays the error progression of both ECMs for the SIB used in this work. A general decrease in modeling error with increasing temperature is observed, which can be attributed to the reduction of overpotentials at elevated temperatures, leading to improved agreement between simulation and measurement.

At 25 °C and 40 °C, the performance of both models is comparable, with the R1RC model exhibiting only a slightly higher accumulated error relative to the LiIon4 model. In

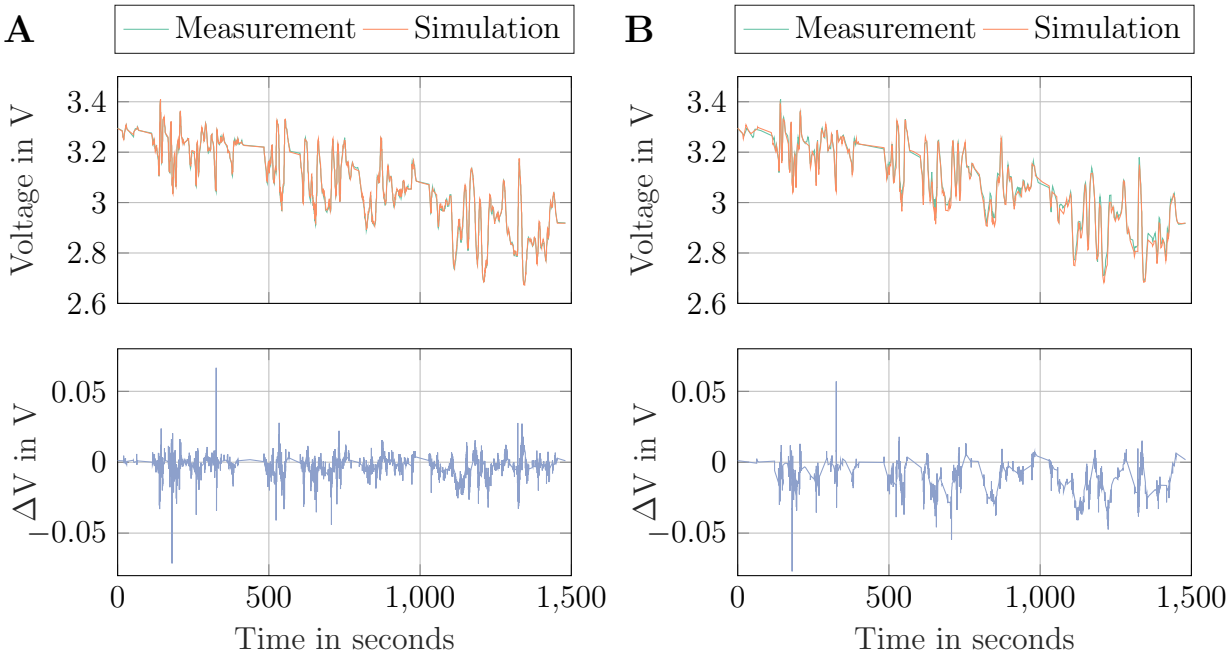

Figure A.5: Simulation error for the input profile at 10 °C and a start voltage of 3.3 V.
A: LiIon4 model.
B: R1RC model. The R1RC model exhibits a pronounced bias in voltage estimation, while the LiIon4 model offers a more accurate fit but shows increased distortion.

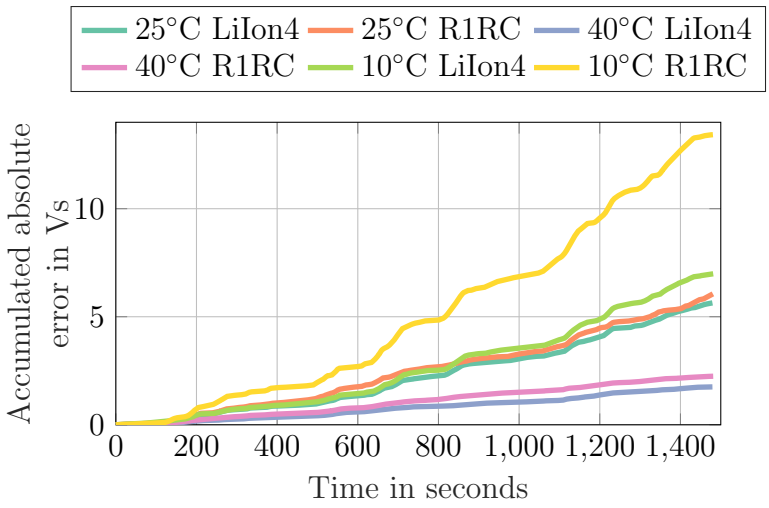

Figure A.6: Integrated voltage error over time for the profile as a function of both temperature and model. Errors increase with lower temperatures and lower model complexity.

contrast, at lower temperatures, particularly at 10 °C, a larger deviation emerges. While the LiIon4 model maintains moderate accuracy, the R1RC model shows a substantially greater error accumulation. This pronounced discrepancy at lower temperatures highlights

the limitations of the R1RC model, whose single RC element cannot sufficiently capture the broad distribution of time constants associated with slower charge transfer kinetics and increased diffusion resistances under these conditions. Consequently, the reduced model complexity leads to increasing inaccuracies as temperature decreases, emphasizing the necessity of more detailed model structures, such as the LiIon4 model, for accurate voltage simulation at low temperatures.

Figure A.7 shows the simple fitting results of the calendar aging model.

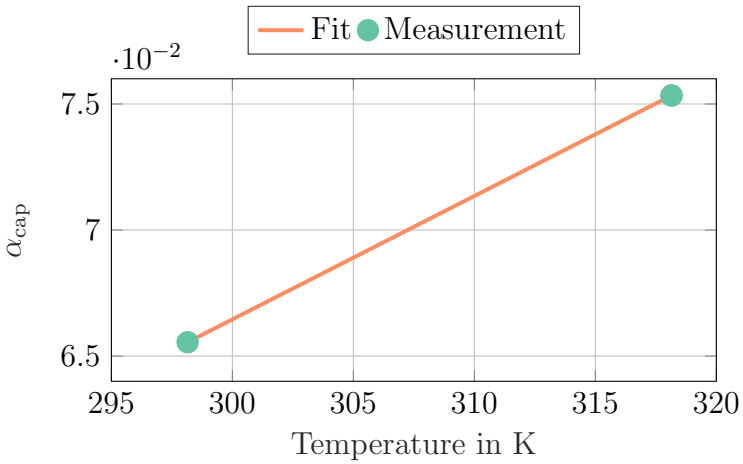

Figure A.7: Experimental and fitted data for the calendar aging coefficient. The experimental values stem from Klick et al. [191].

A.4 Simulation Scenarios for SOC Evaluation

Table A.1: Design of Experiment for the SOC benchmark.

Load profile	SOC_{init}	T	$SOHc$	$SOHr$	Current sensor	Voltage sensor	Offset
Base scenario							
DP1	50 %	25 °C	1	1	-	-	-
Dynamic Operation profile							
DP2	50 %	25 °C	1	1	-	-	-
DP3	50 %	25 °C	1	1	-	-	-
Initial SOC							
DP1	40 %	25 °C	1	1	-	-	-
DP1	60 %	25 °C	1	1	-	-	-
Environmental temperature							
DP1	50 %	10 °C	1	1	-	-	-
DP1	50 %	40 °C	1	1	-	-	-
Aging							
DP1	50 %	25 °C	0,9	1,25	-	-	-
DP1	50 %	25 °C	0,8	1.5	-	-	-
Current sensor							
DP1	50 %	25 °C	1	1	Gain: +0.05	-	-
DP1	50 %	25 °C	1	1	Gain: -0.05	-	-
DP1	50 %	25 °C	1	1	Off: $+0.005\,C_{nom}$	-	-
DP1	50 %	25 °C	1	1	Off: $-0.005\,C_{nom}$	-	-
Voltage sensor							
DP1	50 %	25 °C	1	1	-	Gain: +0.0002	-
DP1	50 %	25 °C	1	1	-	Gain: -0.0002	-
DP1	50 %	25 °C	1	1	-	Off: $+10\,mV$	-
DP1	50 %	25 °C	1	1	-	Off: $-10\,mV$	-
DP1	50 %	25 °C	1	1	-	Var: 0.0000168 V^2	-
Faulty initialization							
DP1	50 %	25 °C	1	1	-	-	+10 % SOC
DP1	50 %	25 °C	1	1	-	-	-10 % SOC
DP1	50 %	25 °C	1	1	-	-	$+0.2\,C_{nom}$
DP1	50 %	25 °C	1	1	-	-	$-0.2\,C_{nom}$
DP1	50 %	25 °C	1	1	-	-	+10 °C
DP1	50 %	25 °C	1	1	-	-	-10 °C

A.5 SOC Algorithm Results for Different Metrics

Table A.2: Comparison of the performance evaluation results for the NMC/C and the $NaMO_2$/HC cells. The best performing cell according to a specific metric is highlighted in green .

Battery	Best performance	$\overline{IA_1}$	Poorest performance	$\overline{IA_1}$
NMC/LTO	EKF R1RC	0.98	UKF R1RC	0.95
$NaMO_2$/HC	UKF R1RC	0.97	AhC & OCV	0.96

(a) Best and poorest average IA_1 values across all robustness categories.

Battery	Best performance	$\overline{RMSE}$	Poorest performance	$\overline{RMSE}$
NMC/LTO	EKF R1RC	0.55	UKF R1RC	1.16
$NaMO_2$/HC	UKF R1RC	0.36	AhC & OCV	0.63

(b) Best and poorest average RMSE values across all robustness categories.

Battery	Best performance	$\overline{e_{max}}$	Poorest performance	$\overline{e_{max}}$
NMC/LTO	EKF R1RC	2.6	UKF R1RC	4.3
$NaMO_2$/HC	UKF R1RC	1.0	AhC & OCV	2.0

(c) Best and poorest average e_{max} values across all robustness categories.

Battery	Best performance	$\overline{ME}$	Poorest performance	$\overline{ME}$
NMC/LTO	EKF R1RC	0.19	AhC & OCV	0.71
$NaMO_2$/HC	EKF R1RC	0.05	AhC & OCV	0.26

(d) Best and poorest average ME values across all robustness categories.

Battery	Best performance	$\overline{SD}$	Poorest performance	$\overline{SD}$
NMC/LTO	EKF R1RC	0.42	EKF R1RC	0.84
$NaMO_2$/HC	UKF R1RC	1.28	AhC & OCV	1.93

(e) Best and poorest average SD values across all robustness categories.

A.6 Simulation Scenarios for SOH Evaluation

Table A.3: Design of Experiment for the SOH benchmark. Besides the base scenario, we evaluate algorithm performance across seven evaluation categories.

Load Profile	T	Charge throughput	Time	Rate	Current sensor	Voltage sensor	Offset
-	°C	Ah	d	d	-	-	-
Base Scenario							
DP1	25	4000	2000	1	1	-	-
Dynamic Operation Profile							
DP2	25	4000	2000	1	1	-	-
DP3	25	4000	2000	1	1	-	-
Temperature							
DP1	10	4000	2000	1	1	-	-
DP1	40	4000	2000	1	1	-	-
Initial Age							
DP1	25	0	0	1	-	-	-
DP1	25	1000	1000	1	-	-	-
DP1	25	2000	2000	1	-	-	-
DP1	25	8000	4000	1	-	-	-
Aging rate							
DP1 long	25	4000	2000	60	-	-	-
DP1 long	25	4000	2000	120	-	-	-
Current sensor							
DP1	25	4000	2000	1	Gain: +0.05	-	-
DP1	25	4000	2000	1	Gain: -0.05	-	-
DP1	25	4000	2000	1	Off: $+0.005\,C_{nom}$	-	-
DP1	25	4000	2000	1	Off: $-0.005\,C_{nom}$	-	-
Voltage sensor							
DP1	25	4000	2000	1	-	Gain: +0.0002	-
DP1	25	4000	2000	1	-	Gain: -0.0002	-
DP1	25	4000	2000	1	-	Off: $+10\,mV$	-
DP1	25	4000	2000	1	-	Off: $-10\,mV$	-
DP1	25	4000	2000	1	-	Var: $0.0000168\,V^2$	-
Faulty initialization							
DP1	25	4000	2000	1	-	-	$+0.2\,C_{nom}$
DP1	25	4000	2000	1	-	-	$-0.2\,C_{nom}$
DP1	25	4000	2000	1	-	-	+10 °C
DP1	25	4000	2000	1	-	-	-10 °C

A.7 SOH Estimation based on Coulomb Counting

The estimation process described in Section 5.4.2 consists of three consecutive stages.

1. Initialization: The SOC must be above the upper threshold, SOC_{high}, before the process starts. This ensures that enough charge can be removed from the battery to allow for a meaningful capacity estimation. If the SOC is too low at the beginning, the discharge period would be too short, leading to increased sensitivity to measurement noise. The SOC is estimated based on the AhC & OCV. Once this condition is met, the algorithm begins tracking the charge, marking the transition to stage two.

2. Monitoring: During operation, the algorithm continuously tracks the current and temperature. The current must stay within an acceptable range to ensure that the discharge process remains stable and representative of real operating conditions. The temperature must either remain within predefined limits or have a sufficiently small gradient, as large temperature variations can change the internal resistance and affect the battery's capacity.

3. Finalization: When the SOC reaches the lower threshold, SOC_{low}, the algorithm stops counting the discharged charge and enters the third stage. The lower threshold ensures that a sufficiently large portion of the battery's capacity has been measured, reducing errors due to partial discharge cycles. At this point, the system waits for the battery to enter a relaxed state, meaning that the current is zero and transient effects have settled. If all conditions are met, the capacity is calculated according to Equation (5.18).

If, during stages two or three, temperature or current conditions are violated, the process is stopped, and the algorithm resets to stage one without producing an estimate.

A.8 Initial Parameters for SOH algorithms

Table A.4: Set-up of the coulomb counting based capacity estimation for the SIB reflecting typical conditions within the high-power mobile application discussed in Chapter 3. The SOC range is low, reflecting the small DOD occurring during operation.

Variable	Unit	Value
SOC_{low}	%	55
SOC_{high}	%	65
I_{min}	A	0.5 C
I_{max}	A	5 C
T_{min}	°C	20
T_{max}	°C	40
ΔT_{max}	°C	10
V_{eq}	mV	0.1

Table A.5: Tuning of WOLS and RTLS for SOH estimation. The SOC change threshold filters out small fluctuations to improve estimation stability. The forgetting factor determines the influence of past data on estimator updates, influencing adaptability and stability of the estimator. The current measurement variance quantifies uncertainty in current, affecting noise sensitivity in the estimation process. The scaling factor k (only for RTLS) is defined as $\sigma_{xn} = k\sigma_{yn}$ and links the measurement variance to the SOC change variance.

Parameter	WOLS and RTLS SIB
Scaling factor (only for RTLS)	2
SOC change	3 %
Forgetting Factor	0.98
σ^2 current measurement	$5{\cdot}10^{-3}$

Table A.6: Tuning of the EKF and UKF for SOH estimation. Q represents the process noise, R the measurement noise, and $P0$ the initial covariance.

Parameter	UKF and EKF SIB
α (only for UKF)	1
β (only for UKF)	2
κ (only for UKF)	0
Q	10^{-6}
R	10^{-6}
$P0$	10^{-7}

B Acronyms

σ	standard deviation
AhC & OCV	ampere-hour counter with recalibration
BMS	battery management system
BOL	Begin-of-Life
C-Rate	current rate
CAN	Controller Area Network
CC	coulomb counting
cdf	culumative distribution function
CEI	Cathode Electrolyte Interphase
CU	control unit
DOD	depth of discharge
DVA	differential voltage analysis
e_{max}	maximum error
ECM	equivalent circuit model
EFC	equivalent full cycles
EIS	electrochemical impedance spectroscopy
EKF	Extended Kalman Filter
EKF R1RC	Extended Kalman Filter R1RC
EOL	End-of-Life
HC	hard carbon
IA	Index of Agreement
ICA	incremental capacity analysis
kde	kernel density estimation
KF	Kalman Filter
KS	Kolmogorov-Smirnov test
LAM	loss of active material
LIB	lithium-ion battery

LLI	loss of lithium inventory
LSI	loss of sodium inventory
LUT	look-up table
ME	mean error
MPE	mean percentage error
OCP	open-circuit potential
OCV	open-circuit voltage
PBA	prussian blue analogs
PCA	Principal Component Analysis
PCB	printed circuit board
pdf	probability density function
qOCV	quasi open-circuit voltage
RMSE	root mean square error
RMSPE	root mean square percentage error
RPT	reference performance test
RSS	residual sum of squares
RTLS	recursive approximation of total least squares algorithm
SEI	Solid Electrolyte Interphase
SIB	sodium-ion battery
SOA	safe operating area
SOC	State of Charge
SOH	State of Health
SOH_C	State of Health capacity
SOH_R	State of Health resistance
UKF	Unscented Kalman Filter
UKF R1RC	Unscented Kalman Filter R1RC
WLTP	Worldwide Harmonized Light Vehicles Test Procedure
WOLS	weighted ordinary least square algorithm
XML	eXtensible Markup Language

List of Figures

List of Tables

Bibliography

[1] R. Newman and I. Noy, "The global costs of extreme weather that are attributable to climate change," *Nature Communications*, vol. 14, no. 1, p. 6103, Sep. 29, 2023.

[2] B. Soergel, E. Kriegler, I. Weindl, S. Rauner, A. Dirnaichner, C. Ruhe, M. Hofmann, N. Bauer, C. Bertram, B. L. Bodirsky, M. Leimbach, J. Leininger, A. Levesque, G. Luderer, M. Pehl, C. Wingens, L. Baumstark, F. Beier, J. P. Dietrich, F. Humpenöder, P. von Jeetze, D. Klein, J. Koch, R. Pietzcker, J. Strefler, H. Lotze-Campen, and A. Popp, "A sustainable development pathway for climate action within the UN 2030 agenda," *Nature Climate Change*, vol. 11, no. 8, pp. 656–664, Aug. 2021.

[3] P. Greim, A. A. Solomon, and C. Breyer, "Assessment of lithium criticality in the global energy transition and addressing policy gaps in transportation," *Nature Communications*, vol. 11, no. 1, p. 4570, Sep. 11, 2020.

[4] "Time for lithium-ion alternatives," *Nature Energy*, vol. 7, no. 6, pp. 461–461, Jun. 2022.

[5] Q. Mayemba, R. Mingant, A. Li, G. Ducret, and P. Venet, "Aging datasets of commercial lithium-ion batteries: A review," *Journal of Energy Storage*, vol. 83, p. 110 560, Apr. 1, 2024.

[6] J. T. Frith, M. J. Lacey, and U. Ulissi, "A non-academic perspective on the future of lithium-based batteries," *Nature Communications*, vol. 14, no. 1, p. 420, Jan. 26, 2023.

[7] A. Yao, S. M. Benson, and W. C. Chueh, "Critically assessing sodium-ion technology roadmaps and scenarios for techno-economic competitiveness against lithium-ion batteries," *Nature Energy*, vol. 10, no. 3, pp. 404–416, Mar. 2025.

[8] M. S. Ziegler, J. Song, and J. E. Trancik, "Determinants of lithium-ion battery technology cost decline," *Energy & Environmental Science*, vol. 14, no. 12, pp. 6074–6098, Dec. 9, 2021.

[9] M. S. Ziegler and J. E. Trancik, "Re-examining rates of lithium-ion battery technology improvement and cost decline," *Energy & Environmental Science*, vol. 14, no. 4, pp. 1635–1651, Apr. 21, 2021.

[10] S. Orangi, N. Manjong, D. P. Clos, L. Usai, O. S. Burheim, and A. H. Strømman, "Historical and prospective lithium-ion battery cost trajectories from a bottom-up production modeling perspective," *Journal of Energy Storage*, vol. 76, p. 109 800, Jan. 15, 2024.

[11] X. Cai, Y. Yue, Z. Yi, J. Liu, Y. Sheng, and Y. Lu, "Challenges and industrial perspectives on the development of sodium ion batteries," *Nano Energy*, vol. 129, p. 110 052, Oct. 1, 2024.

[12] H. Laufen, S. Klick, H. Ditler, K. L. Quade, A. Mikitisin, A. Blömeke, M. Schütte, D. Wasylowski, M. Sonnet, L. Henrich, A. Schwedt, G. Stahl, F. Ringbeck, J. Mayer, and D. U. Sauer, "Multi-method characterization of a commercial 1.2 Ah sodium-ion battery cell indicates drop-in potential," *Cell Reports Physical Science*, vol. 5, no. 5, 2024.

[13] A. Rudola, R. Sayers, C. J. Wright, and J. Barker, "Opportunities for moderate-range electric vehicles using sustainable sodium-ion batteries," *Nature Energy*, vol. 8, no. 3, pp. 215–218, Mar. 2023.

[14] K. Bischof, V. Marangon, M. Kasper, A. Aracil Regalado, M. Wohlfahrt-Mehrens, M. Hölzle, D. Bresser, and T. Waldmann, "Evaluation of commercial 18650 and 26700 sodium-ion cells and comparison with well-established lithium-ion cells," *Journal of Power Sources Advances*, vol. 27, p. 100 148, Jun. 1, 2024.

[15] L. Zhao, T. Zhang, W. Li, T. Li, L. Zhang, X. Zhang, and Z. Wang, "Engineering of sodium-ion batteries: Opportunities and challenges," *Engineering*, vol. 24, pp. 172–183, May 1, 2023.

[16] K. M. Abraham, "How comparable are sodium-ion batteries to lithium-ion counterparts?" *ACS Energy Letters*, vol. 5, no. 11, pp. 3544–3547, Nov. 13, 2020.

[17] R. R. Gaddam and X. Zhao, Eds., *Handbook of Sodium-Ion Batteries: Materials and Characterization*, Milton: Jenny Stanford Publishing, 2023.

[18] D. Linden and T. B. Reddy, Eds., *Handbook of batteries*, 3rd ed, McGraw-Hill handbooks, New York: McGraw-Hill, 2002.

[19] M. Winter and R. J. Brodd, "What are batteries, fuel cells, and supercapacitors?" *Chemical Reviews*, vol. 104, no. 10, pp. 4245–4270, Oct. 1, 2004.

[20] I. Buchberger, "Electrochemical and structural investigations on lithium-ion battery materials and related degradation processes," Ph.D. dissertation, Technische Universität München, 2016.

[21] W. Wang, X. Wei, D. Choi, X. Lu, G. Yang, and C. Sun, "Chapter 1 - electrochemical cells for medium- and large-scale energy storage: Fundamentals," in *Advances in Batteries for Medium and Large-Scale Energy Storage*, ser. Woodhead Publishing Series in Energy, C. Menictas, M. Skyllas-Kazacos, and T. M. Lim, Eds., Woodhead Publishing, Jan. 1, 2015, pp. 3–28.

[22] R. Suresh and R. Rengaswamy, "Modeling and control of battery systems. part i: Revisiting butler–volmer equations to model non-linear coupling of various capacity fade mechanisms," *Computers & Chemical Engineering*, vol. 119, pp. 336–351, Nov. 2, 2018.

[23] M. Xie, F. Wu, and Y. Huang, *Sodium-Ion Batteries: Advanced Technology and Applications*. De Gruyter, Aug. 1, 2022.

[24] H. Rubenbauer and S. Henninger, "Definitions and reference values for battery systems in electrical power grids," *Journal of Energy Storage*, vol. 12, pp. 87–107, Aug. 1, 2017.

[25] X. Lai, L. Zhou, Z. Zhu, Y. Zheng, T. Sun, and K. Shen, "Experimental investigation on the characteristics of coulombic efficiency of lithium-ion batteries considering different influencing factors," *Energy*, vol. 274, p. 127 408, Jul. 1, 2023.

[26] F. Yang, D. Wang, Y. Zhao, K.-L. Tsui, and S. J. Bae, "A study of the relationship between coulombic efficiency and capacity degradation of commercial lithium-ion batteries," *Energy*, vol. 145, pp. 486–495, Feb. 15, 2018.

[27] A. Bills, S. Sripad, W. L. Fredericks, M. Singh, and V. Viswanathan, "Performance metrics required of next-generation batteries to electrify commercial aircraft," *ACS Energy Letters*, vol. 5, no. 2, pp. 663–668, Feb. 14, 2020.

[28] J. Kersey, N. D. Popovich, and A. A. Phadke, "Rapid battery cost declines accelerate the prospects of all-electric interregional container shipping," *Nature Energy*, vol. 7, no. 7, pp. 664–674, Jul. 2022.

[29] A. Masias, J. Marcicki, and W. A. Paxton, "Opportunities and challenges of lithium ion batteries in automotive applications," *ACS Energy Letters*, vol. 6, no. 2, pp. 621–630, Feb. 12, 2021.

[30] C. M. Tan, Y. Yang, K. J. M. Kumar, D. D. Mishra, and T.-Y. Liu, "Addressing practical challenges of LiB cells in their pack applications," *Scientific Reports*, vol. 14, no. 1, p. 10 126, May 2, 2024.

[31] J.-M. Tarascon and M. Armand, "Issues and challenges facing rechargeable lithium batteries," *Nature*, vol. 414, no. 6861, pp. 359–367, Nov. 2001.

[32] X. Shen, X.-Q. Zhang, F. Ding, J.-Q. Huang, R. Xu, X. Chen, C. Yan, F.-Y. Su, C.-M. Chen, X. Liu, and Q. Zhang, "Advanced electrode materials in lithium batteries: Retrospect and prospect," *Energy Material Advances*, vol. 2021, Jan. 19, 2021.

[33] D. Guyomard and J.-M. Tarascon, "Rocking-chair or lithium-ion rechargeable lithium batteries," *Advanced Materials*, vol. 6, no. 5, pp. 408–412, 1994.

[34] J. Mitali, S. Dhinakaran, and A. A. Mohamad, "Energy storage systems: A review," *Energy Storage and Saving*, vol. 1, no. 3, pp. 166–216, Sep. 1, 2022.

[35] M. Ghiji, V. Novozhilov, K. Moinuddin, P. Joseph, I. Burch, B. Suendermann, and G. Gamble, "A review of lithium-ion battery fire suppression," *Energies*, vol. 13, no. 19, p. 5117, Jan. 2020.

[36] P. Du, J. Wan, J. Qu, H. Xie, D. Wang, and H. Yin, "Passivation and corrosion of al current collectors in lithium-ion batteries," *npj Materials Degradation*, vol. 8, no. 1, pp. 1–11, Apr. 25, 2024.

[37] M. R. Palacin, "Battery materials design essentials," *Accounts of Materials Research*, vol. 2, no. 5, pp. 319–326, May 28, 2021.

[38] R. Korthauer, Ed., *Lithium-Ion Batteries: Basics and Applications*, Berlin, Heidelberg: Springer, 2018.

[39] V. S. Bagotsky, *Fundamentals of Electrochemistry*. Wiley-VCH, Oct. 21, 2005.

[40] M. Osiak, H. Geaney, E. Armstrong, and C. O'Dwyer, "Structuring materials for lithium-ion batteries: Advancements in nanomaterial structure, composition, and defined assembly on cell performance," *Journal of Materials Chemistry A*, vol. 2, no. 25, pp. 9433–9460, Jun. 3, 2014.

[41] S. K. Sharma, G. Sharma, A. Gaur, A. Arya, F. S. Mirsafi, R. Abolhassani, H.-G. Rubahn, J.-S. Yu, and Y. K. Mishra, "Progress in electrode and electrolyte materials: Path to all-solid-state li-ion batteries," *Energy Advances*, vol. 1, no. 8, pp. 457–510, Aug. 11, 2022.

[42] R. Borah, F. R. Hughson, J. Johnston, and T. Nann, "On battery materials and methods," *Materials Today Advances*, vol. 6, p. 100 046, Jun. 1, 2020.

[43] A. Chakraborty, S. Kunnikuruvan, S. Kumar, B. Markovsky, D. Aurbach, M. Dixit, and D. T. Major, "Layered cathode materials for lithium-ion batteries: Review of computational studies on $LiNi_{1-x-y}Co_xMn_yO_2$ and $LiNi_{1-x-y}Co_xAl_yO_2$," *Chemistry of Materials*, vol. 32, no. 3, pp. 915–952, Feb. 11, 2020.

[44] H. Zhao, H. Zuo, J. Wang, and S. Jiao, "Practical application of graphite in lithium-ion batteries: Modification, composite, and sustainable recycling," *Journal of Energy Storage*, vol. 98, p. 113 125, Sep. 20, 2024.

[45] S. K. Heiskanen, J. Kim, and B. L. Lucht, "Generation and evolution of the solid electrolyte interphase of lithium-ion batteries," *Joule*, vol. 3, no. 10, pp. 2322–2333, Oct. 16, 2019.

[46] R. Mogensen, D. Brandell, and R. Younesi, "Solubility of the solid electrolyte interphase (SEI) in sodium ion batteries," *ACS Energy Letters*, vol. 1, no. 6, pp. 1173–1178, Dec. 9, 2016.

[47] V. A. Agubra and J. W. Fergus, "The formation and stability of the solid electrolyte interface on the graphite anode," *Journal of Power Sources*, vol. 268, pp. 153–162, Dec. 5, 2014.

[48] L. Zhang, C. Zhu, S. Yu, D. Ge, and H. Zhou, "Status and challenges facing representative anode materials for rechargeable lithium batteries," *Journal of Energy Chemistry*, vol. 66, pp. 260–294, Mar. 1, 2022.

[49] S. Chae, S.-H. Choi, N. Kim, J. Sung, and J. Cho, "Integration of graphite and silicon anodes for the commercialization of high-energy lithium-ion batteries," *Angewandte Chemie International Edition*, vol. 59, no. 1, pp. 110–135, 2020.

[50] T. Yuan, Z. Tan, C. Ma, J. Yang, Z.-F. Ma, and S. Zheng, "Challenges of spinel $Li_4Ti_5O_{12}$ for lithium-ion battery industrial applications," *Advanced Energy Materials*, vol. 7, no. 12, p. 1 601 625, 2017.

[51] N. Nitta, F. Wu, J. T. Lee, and G. Yushin, "Li-ion battery materials: Present and future," *Materials Today*, vol. 18, no. 5, pp. 252–264, Jun. 1, 2015.

[52] H. Oubaha, L. Fkhar, R. Cloots, F. Boschini, and A. Mahmoud, "Direct NCA cathode active materials recycling from spent li-ion batteries: Solvent-free recovery and healing by heat treatment," *ACS Sustainable Resource Management*, vol. 1, no. 8, pp. 1791–1801, Aug. 22, 2024.

[53] M. Wood, J. Li, R. E. Ruther, Z. Du, E. C. Self, H. M. Meyer, C. Daniel, I. Belharouak, and D. L. Wood, "Chemical stability and long-term cell performance of low-cobalt, ni-rich cathodes prepared by aqueous processing for high-energy li-ion batteries," *Energy Storage Materials*, vol. 24, pp. 188–197, Jan. 1, 2020.

[54] J. Hu, W. Huang, L. Yang, and F. Pan, "Structure and performance of the LiFePO4 cathode material: From the bulk to the surface," *Nanoscale*, vol. 12, no. 28, pp. 15 036–15 044, Jul. 23, 2020.

[55] Z. Peng, X. Xia, Y. Xiao, and T. Huang, "Progress on lithium manganese iron phosphate cathode materials," *Journal of Alloys and Compounds*, vol. 1016, p. 178 901, Feb. 15, 2025.

[56] Y. Huang, Y.-C. Lin, D. M. Jenkins, N. A. Chernova, Y. Chung, B. Radhakrishnan, I.-H. Chu, J. Fang, Q. Wang, F. Omenya, S. P. Ong, and M. S. Whittingham, "Thermal stability and reactivity of cathode materials for li-ion batteries," *ACS Applied Materials & Interfaces*, vol. 8, no. 11, pp. 7013–7021, Mar. 23, 2016.

[57] C. R. Birkl, M. R. Roberts, E. McTurk, P. G. Bruce, and D. A. Howey, "Degradation diagnostics for lithium ion cells," *Journal of Power Sources*, vol. 341, pp. 373–386, Feb. 15, 2017.

[58] N. Collath, B. Tepe, S. Englberger, A. Jossen, and H. Hesse, "Aging aware operation of lithium-ion battery energy storage systems: A review," *Journal of Energy Storage*, vol. 55, p. 105 634, Nov. 25, 2022.

[59] J. Vetter, P. Novák, M. R. Wagner, C. Veit, K.-C. Möller, J. O. Besenhard, M. Winter, M. Wohlfahrt-Mehrens, C. Vogler, and A. Hammouche, "Ageing mechanisms in lithium-ion batteries," *Journal of Power Sources*, vol. 147, no. 1, pp. 269–281, Sep. 9, 2005.

[60] R. Xiong, Y. Pan, W. Shen, H. Li, and F. Sun, "Lithium-ion battery aging mechanisms and diagnosis method for automotive applications: Recent advances and perspectives," *Renewable and Sustainable Energy Reviews*, vol. 131, p. 110 048, Oct. 1, 2020.

[61] J. S. Edge, S. O'Kane, R. Prosser, N. D. Kirkaldy, A. N. Patel, A. Hales, A. Ghosh, W. Ai, J. Chen, J. Yang, S. Li, M.-C. Pang, L. B. Diaz, A. Tomaszewska, M. W. Marzook, K. N. Radhakrishnan, H. Wang, Y. Patel, B. Wu, and G. J. Offer, "Lithium ion battery degradation: What you need to know," *Physical Chemistry Chemical Physics*, vol. 23, no. 14, pp. 8200–8221, Apr. 15, 2021.

[62] S. E. J. O'Kane, W. Ai, G. Madabattula, D. Alonso-Alvarez, R. Timms, V. Sulzer, J. Sophie Edge, B. Wu, G. J. Offer, and M. Marinescu, "Lithium-ion battery degradation: How to model it," *Physical Chemistry Chemical Physics*, vol. 24, no. 13, pp. 7909–7922, 2022.

[63] P. Peljo and H. H. Girault, "Electrochemical potential window of battery electrolytes: The HOMO–LUMO misconception," *Energy & Environmental Science*, vol. 11, no. 9, pp. 2306–2309, Sep. 12, 2018.

[64] B. Bitzer and A. Gruhle, "A new method for detecting lithium plating by measuring the cell thickness," *Journal of Power Sources*, vol. 262, pp. 297–302, Sep. 15, 2014.

[65] X. Lin, K. Khosravinia, X. Hu, J. Li, and W. Lu, "Lithium plating mechanism, detection, and mitigation in lithium-ion batteries," *Progress in Energy and Combustion Science*, vol. 87, p. 100 953, Nov. 1, 2021.

[66] H. Wang, X. Li, F. Li, X. Liu, S. Yang, and J. Ma, "Formation and modification of cathode electrolyte interphase: A mini review," *Electrochemistry Communications*, vol. 122, p. 106 870, Jan. 1, 2021.

[67] J. Seok, W. Lee, H. Lee, S. Park, C. Chung, S. Hwang, and W.-S. Yoon, "Aging mechanisms of lithium-ion batteries," *Journal of Electrochemical Science and Technology*, vol. 15, no. 1, pp. 51–66, Jan. 29, 2024.

[68] Y. Yu, *Sodium-Ion Batteries: Energy Storage Materials and Technologies*, 1st ed. Wiley, Apr. 25, 2022.

[69] H. Kang, Y. Liu, K. Cao, Y. Zhao, L. Jiao, Y. Wang, and H. Yuan, "Update on anode materials for na-ion batteries," *Journal of Materials Chemistry A*, vol. 3, no. 35, pp. 17 899–17 913, Aug. 25, 2015.

[70] H. Pan, Y.-S. Hu, and L. Chen, "Room-temperature stationary sodium-ion batteries for large-scale electric energy storage," *Energy & Environmental Science*, vol. 6, no. 8, pp. 2338–2360, Jul. 17, 2013.

[71] Z. Wang, J. Tang, Y. Li, J. Wang, Q. Xue, and G. Wang, "Progress of research on carbon-based anode materials for sodium-ion batteries," *Ionics*, vol. 31, no. 1, pp. 1–21, Jan. 1, 2025.

[72] B. Babu, "Carbon–based materials for li-ion battery," *Batteries & Supercaps*, vol. 7, no. 3, 2024.

[73] N. Tapia-Ruiz et al., "2021 roadmap for sodium-ion batteries," *Journal of Physics: Energy*, vol. 3, no. 3, p. 031 503, Jul. 2021.

[74] M. Titirici, P. Adelhelm, and Y.-S. Hu, Eds., *Sodium-Ion Batteries: Materials, Characterization, and Technology*, Weinheim: Wiley-VCH, 2023.

[75] F. Chen, H. Li, X. Qiao, R. Wang, C. Hu, T. Chen, Y. Niu, B. Zhong, Z. Wu, and X. Guo, "The chance of sodium titanate anode for the practical sodium-ion batteries," *Chinese Journal of Chemical Engineering*, vol. 72, pp. 226–244, Aug. 1, 2024.

[76] P. Gupta, S. Pushpakanth, M. A. Haider, and S. Basu, "Understanding the design of cathode materials for na-ion batteries," *ACS Omega*, vol. 7, no. 7, pp. 5605–5614, Feb. 22, 2022.

[77] S. Yang, X. Liu, S. Li, and C. Zhang, *Advanced Battery Management System for Electric Vehicles* (Key Technologies on New Energy Vehicles). Singapore: Springer Nature, 2023.

[78] Y. Cao, Y. Zhang, and C. Gu, Eds., *Automated and electric vehicle: design, informatics and sustainability*, Recent advancements in connected autonomous vehicle technologies volume 3, Singapore: Springer Nature, 2023, pp. 23–44, 285 pp.

[79] F. Berger, D. Joest, E. Barbers, K. Quade, Z. Wu, D. U. Sauer, and P. Dechent, "Benchmarking battery management system algorithms - requirements, scenarios and validation for automotive applications," *eTransportation*, vol. 22, 2024.

[80] M. Lelie, T. Braun, M. Knips, H. Nordmann, F. Ringbeck, H. Zappen, and D. U. Sauer, "Battery management system hardware concepts: An overview," *Applied Sciences*, vol. 8, no. 4, p. 534, Apr. 2018.

[81] N. Khan, C. A. Ooi, Shreasth, A. Alturki, M. K. M. Desa, M. Amir, A. B. Ahmad, and M. K. Ishak, "A novel active cell balancing topology for serially connected li-ion cells in the battery pack for electric vehicle applications," *Scientific Reports*, vol. 14, no. 1, p. 18 600, Aug. 10, 2024.

[82] K. S. Ng, C.-S. Moo, Y.-P. Chen, and Y.-C. Hsieh, "Enhanced coulomb counting method for estimating state-of-charge and state-of-health of lithium-ion batteries," *Applied Energy*, vol. 86, no. 9, pp. 1506–1511, Sep. 1, 2009.

[83] Y. Zhang, W. Song, S. Lin, and Z. Feng, "A novel model of the initial state of charge estimation for LiFePO4 batteries," *Journal of Power Sources*, vol. 248, pp. 1028–1033, Feb. 15, 2014.

[84] C. Lin, H. Mu, R. Xiong, and W. Shen, "A novel multi-model probability battery state of charge estimation approach for electric vehicles using h-infinity algorithm," *Applied Energy*, vol. 166, pp. 76–83, Mar. 2016.

[85] S. Yang, S. Zhou, Y. Hua, X. Zhou, X. Liu, Y. Pan, H. Ling, and B. Wu, "A parameter adaptive method for state of charge estimation of lithium-ion batteries with an improved extended kalman filter," *Scientific Reports*, vol. 11, no. 1, p. 5805, Mar. 11, 2021.

[86] C. Campestrini, T. Heil, S. Kosch, and A. Jossen, "A comparative study and review of different kalman filters by applying an enhanced validation method," *Journal of Energy Storage*, vol. 8, pp. 142–159, Nov. 2016.

[87] J. Zhu, Y. Wang, Y. Huang, R. Bhushan Gopaluni, Y. Cao, M. Heere, M. J. Mühlbauer, L. Mereacre, H. Dai, X. Liu, A. Senyshyn, X. Wei, M. Knapp, and H. Ehrenberg, "Data-driven capacity estimation of commercial lithium-ion batteries from voltage relaxation," *Nature Communications*, vol. 13, no. 1, p. 2261, Apr. 27, 2022.

[88] M. Dubarry, N. Costa, and D. Matthews, "Data-driven direct diagnosis of li-ion batteries connected to photovoltaics," *Nature Communications*, vol. 14, no. 1, p. 3138, May 30, 2023.

[89] D. Roman, S. Saxena, V. Robu, M. Pecht, and D. Flynn, "Machine learning pipeline for battery state-of-health estimation," *Nature Machine Intelligence*, vol. 3, no. 5, pp. 447–456, May 2021.

[90] S. Khaleghi, D. Karimi, S. H. Beheshti, M. S. Hosen, H. Behi, M. Berecibar, and J. Van Mierlo, "Online health diagnosis of lithium-ion batteries based on nonlinear autoregressive neural network," *Applied Energy*, vol. 282, p. 116 159, Jan. 15, 2021.

[91] M. A. Hannan, M. S. H. Lipu, A. Hussain, P. J. Ker, T. M. I. Mahlia, M. Mansor, A. Ayob, M. H. Saad, and Z. Y. Dong, "Toward enhanced state of charge estimation of lithium-ion batteries using optimized machine learning techniques," *Scientific Reports*, vol. 10, no. 1, p. 4687, Mar. 13, 2020.

[92] A. G. Stefanopoulou and Y. Kim, "10 - system-level management of rechargeable lithium-ion batteries," in *Rechargeable Lithium Batteries*, ser. Woodhead Publishing Series in Energy, A. A. Franco, Ed., Woodhead Publishing, Jan. 1, 2015, pp. 281–302.

[93] P. Shrivastava, T. K. Soon, M. Y. I. B. Idris, and S. Mekhilef, "Overview of model-based online state-of-charge estimation using kalman filter family for lithium-ion batteries," *Renewable and Sustainable Energy Reviews*, vol. 113, p. 109 233, Oct. 1, 2019.

[94] Q. Li, R. Li, K. Ji, and W. Dai, "Kalman filter and its application," in *2015 8th International Conference on Intelligent Networks and Intelligent Systems (ICINIS)*, Tianjin, China: IEEE, Nov. 2015, pp. 74–77.

[95] C. Urrea and R. Agramonte, "Kalman filter: Historical overview and review of its use in robotics 60 years after its creation," *Journal of Sensors*, vol. 2021, no. 1, p. 9 674 015, 2021.

[96] E. A. Wan and R. van der Merwe, "The unscented kalman filter," in *Kalman Filtering and Neural Networks*, S. Haykin, Ed., 1st ed., Wiley, Oct. 2001, pp. 221–280.

[97] L. Lista, *Statistical Methods for Data Analysis: With Applications in Particle Physics* (Lecture Notes in Physics). Cham: Springer International Publishing, 2023, vol. 1010.

[98] M. Plaue, "Descriptive statistics," in *Data Science: An Introduction to Statistics and Machine Learning*, M. Plaue, Ed., Berlin, Heidelberg: Springer, 2023, pp. 35–64.

[99] O. C. Ibe, "Chapter 8 - introduction to descriptive statistics," in *Fundamentals of Applied Probability and Random Processes (Second Edition)*, O. C. Ibe, Ed., Boston: Academic Press, Jan. 1, 2014, pp. 253–274.

[100] A. Celikoglu and U. Tirnakli, "Skewness and kurtosis analysis for non-gaussian distributions," *Physica A: Statistical Mechanics and its Applications*, vol. 499, pp. 325–334, Jun. 1, 2018.

[101] O. C. Ibe, "Chapter 9 - introduction to inferential statistics," in *Fundamentals of Applied Probability and Random Processes (Second Edition)*, O. C. Ibe, Ed., Boston: Academic Press, Jan. 1, 2014, pp. 275–305.

[102] T. Mouais, O. A. Kittaneh, and M. A. Majid, "Choosing the best lifetime model for commercial lithium-ion batteries," *Journal of Energy Storage*, vol. 41, p. 102 827, Sep. 1, 2021.

[103] M. Johnen, C. Schmitz, M. Kateri, and U. Kamps, "Fitting lifetime distributions to interval censored cyclic-aging data of lithium-ion batteries," *Computers & Industrial Engineering*, vol. 143, p. 106 418, May 1, 2020.

[104] V. K. Rohatgi and A. K. M. E. Saleh, *An Introduction to Probability and Statistics* (Wiley Series in Probability and Statistics), 1st ed. Wiley, Aug. 19, 2015.

[105] O. Kittaneh, "Powerful mathematica codes for goodness-of-fit tests for censored data," in *Handbook of Smart Energy Systems*, M. Fathi, E. Zio, and P. M. Pardalos, Eds., Cham: Springer International Publishing, 2023, pp. 215–245.

[106] B. K. Das, D. N. Jha, S. K. Sahu, A. K. Yadav, R. K. Raman, and M. Kartikeyan, "Chi-square test of significance," in *Concept Building in Fisheries Data Analysis*, B. K. Das, D. N. Jha, S. K. Sahu, A. K. Yadav, R. K. Raman, and M. Kartikeyan, Eds., Singapore: Springer Nature, 2023, pp. 81–94.

[107] W. Rolke and C. G. Gongora, "A chi-square goodness-of-fit test for continuous distributions against a known alternative," *Computational Statistics*, vol. 36, no. 3, pp. 1885–1900, Sep. 1, 2021.

[108] V. Steininger, K. L. Quade, K. Rumpf, S. Bihn, J. Ringler, D. U. Sauer, and W. Li, "Detection of abnormal SOH estimates in battery field data using statistical learning," *Cell Reports Physical Science*, 2025.

[109] K. Rumpf, M. Naumann, and A. Jossen, "Experimental investigation of parametric cell-to-cell variation and correlation based on 1100 commercial lithium-ion cells," *Journal of Energy Storage*, vol. 14, pp. 224–243, Dec. 1, 2017.

[110] E. Barbers, F. E. Hust, F. E. A. Hildenbrand, F. Frie, K. L. Quade, S. Bihn, D. U. Sauer, and P. Dechent, "Exploring the effects of cell-to-cell variability on battery aging through stochastic simulation techniques," *Journal of Energy Storage*, vol. 84, 2024.

[111] M. Dubarry, N. Vuillaume, and B. Y. Liaw, "Origins and accommodation of cell variations in li-ion battery pack modeling," *International Journal of Energy Research*, vol. 34, no. 2, pp. 216–231, 2010.

[112] F. Duffner, L. Mauler, M. Wentker, J. Leker, and M. Winter, "Large-scale automotive battery cell manufacturing: Analyzing strategic and operational effects on manufacturing costs," *International Journal of Production Economics*, vol. 232, p. 107 982, Feb. 2021.

[113] M. Ank, T. Kröger, M. Schreiber, and M. Lienkamp, "Experimental analysis of lithium-ion cell procurement: Quality differences, correlations, and importance of cell characterization," *Journal of Energy Storage*, vol. 66, p. 107 430, Aug. 30, 2023.

[114] D. Evans, D. M. Brieske, C. Tebruegge, and J. Kowal, "Analysis of the impact of manufacturing-induced cell-to-cell variation for high-power applications," *Journal of Power Sources*, vol. 614, p. 235 001, Sep. 2024.

[115] A. Kwade, W. Haselrieder, R. Leithoff, A. Modlinger, F. Dietrich, and K. Droeder, "Current status and challenges for automotive battery production technologies," *Nature Energy*, vol. 3, no. 4, pp. 290–300, Apr. 12, 2018.

[116] T. Baumhöfer, M. Brühl, S. Rothgang, and D. U. Sauer, "Production caused variation in capacity aging trend and correlation to initial cell performance," *Journal of Power Sources*, vol. 247, pp. 332–338, Feb. 1, 2014.

[117] T. Waldmann, M. Wilka, M. Kasper, M. Fleischhammer, and M. Wohlfahrt-Mehrens, "Temperature dependent ageing mechanisms in lithium-ion batteries – a post-mortem study," *Journal of Power Sources*, vol. 262, pp. 129–135, Sep. 15, 2014.

[118] J. Schmalstieg, S. Käbitz, M. Ecker, and D. U. Sauer, "A holistic aging model for li(NiMnCo)o2 based 18650 lithium-ion batteries," *Journal of Power Sources*, vol. 257, pp. 325–334, Jul. 1, 2014.

[119] T. Bank, S. Klamor, and D. U. Sauer, "Lithium-ion cell requirements in a real-world 48 v system and implications for an extensive aging analysis," *Journal of Energy Storage*, vol. 30, p. 101 465, Aug. 1, 2020.

[120] A. Geslin, L. Xu, D. Ganapathi, K. Moy, W. C. Chueh, and S. Onori, "Dynamic cycling enhances battery lifetime," *Nature Energy*, Dec. 9, 2024.

[121] R. D. Deshpande and K. Uddin, "Physics inspired model for estimating 'cycles to failure' as a function of depth of discharge for lithium ion batteries," *Journal of Energy Storage*, vol. 33, p. 101 932, Jan. 1, 2021.

[122] L. Song, K. Zhang, T. Liang, X. Han, and Y. Zhang, "Intelligent state of health estimation for lithium-ion battery pack based on big data analysis," *Journal of Energy Storage*, vol. 32, p. 101 836, Dec. 1, 2020.

[123] V. Steininger, P. Hüsson, K. Rumpf, and D. U. Sauer, "Customer-centric aging simulation for 48 v lithium-ion batteries in vehicle applications," *eTransportation*, vol. 16, p. 100 240, Apr. 1, 2023.

[124] G. Pozzato, A. Allam, L. Pulvirenti, G. A. Negoita, W. A. Paxton, and S. Onori, "Analysis and key findings from real-world electric vehicle field data," *Joule*, vol. 7, no. 9, pp. 2035–2053, Sep. 20, 2023.

[125] D. Geringer, P. Hofmann, J. Girard, E. Trunner, and W. Knefel, "Aging investigations and consideration for automotive high power lithium-ion batteries in a 48 v mild hybrid operating strategy," *Automotive and Engine Technology*, vol. 6, no. 3, pp. 219–234, Dec. 1, 2021.

[126] X. Li, J. Li, A. Abdollahi, and T. Jones, "Data-driven thermal anomaly detection for batteries using unsupervised shape clustering," in *2021 IEEE 30th International Symposium on Industrial Electronics (ISIE)*, Jun. 2021, pp. 1–6.

[127] Y. Zhao, P. Liu, Z. Wang, L. Zhang, and J. Hong, "Fault and defect diagnosis of battery for electric vehicles based on big data analysis methods," *Applied Energy*, Transformative Innovations for a Sustainable Future – Part II, vol. 207, pp. 354–362, Dec. 1, 2017.

[128] L. Yao, Y. Xiao, X. Gong, J. Hou, and X. Chen, "A novel intelligent method for fault diagnosis of electric vehicle battery system based on wavelet neural network," *Journal of Power Sources*, vol. 453, p. 227 870, Mar. 31, 2020.

[129] C. Sun, Z. He, H. Lin, L. Cai, H. Cai, and M. Gao, "Anomaly detection of power battery pack using gated recurrent units based variational autoencoder," *Applied Soft Computing*, vol. 132, p. 109 903, Jan. 1, 2023.

[130] W. Diao, I. H. Naqvi, and M. Pecht, "Early detection of anomalous degradation behavior in lithium-ion batteries," *Journal of Energy Storage*, vol. 32, p. 101 710, Dec. 1, 2020.

[131] C. Liu, J. Tan, H. Shi, and X. Wang, "Lithium-ion cell screening with convolutional neural networks based on two-step time-series clustering and hybrid resampling for imbalanced data," *IEEE Access*, vol. 6, pp. 59 001–59 014, 2018.

[132] S. N. Haider, Q. Zhao, and X. Li, "Data driven battery anomaly detection based on shape based clustering for the data centers class," *Journal of Energy Storage*, vol. 29, p. 101 479, Jun. 1, 2020.

[133] S. J. Harris and M. M. Noack, "Statistical and machine learning-based durability-testing strategies for energy storage," *Joule*, vol. 7, no. 5, pp. 920–934, May 17, 2023.

[134] A. Barré, B. Deguilhem, S. Grolleau, M. Gérard, F. Suard, and D. Riu, "A review on lithium-ion battery ageing mechanisms and estimations for automotive applications," *Journal of Power Sources*, vol. 241, pp. 680–689, Nov. 1, 2013.

[135] P. M. Attia, K. A. Severson, and J. D. Witmer, "Statistical learning for accurate and interpretable battery lifetime prediction," *Journal of The Electrochemical Society*, vol. 168, no. 9, p. 090 547, Sep. 2021.

[136] H. Zhang, Z. Gao, C. Du, S. Bi, Y. Fang, F. Yun, S. Fang, Z. Yu, Y. Cui, and X. Shen, "Parameter estimation of three-parameter weibull probability model based on outlier detection," *RSC Advances*, vol. 12, no. 53, pp. 34 154–34 164, Nov. 29, 2022.

[137] Z. Tian, M. Zhuo, L. Liu, J. Chen, and S. Zhou, "Anomaly detection using spatial and temporal information in multivariate time series," *Scientific Reports*, vol. 13, no. 1, p. 4400, Mar. 16, 2023.

[138] E. Schubert, J. Sander, M. Ester, H. P. Kriegel, and X. Xu, "DBSCAN revisited, revisited: Why and how you should (still) use DBSCAN," *ACM Trans. Database Syst.*, vol. 42, no. 3, 19:1–19:21, Jul. 31, 2017.

[139] C. G. Bezerra, B. Sielly Jales Costa, L. A. Guedes, and P. P. Angelov, "A comparative study of autonomous learning outlier detection methods applied to fault detection," in *2015 IEEE International Conference on Fuzzy Systems (FUZZ-IEEE)*, Aug. 2015, pp. 1–7.

[140] A. Boukerche, L. Zheng, and O. Alfandi, "Outlier detection: Methods, models, and classification," *ACM Comput. Surv.*, vol. 53, no. 3, 55:1–55:37, Jun. 12, 2020.

[141] "Percentile," in *The Concise Encyclopedia of Statistics*, New York, NY: Springer, 2008, pp. 419–421.

[142] M. Luh and T. Blank, "Comprehensive battery aging dataset: Capacity and impedance fade measurements of a lithium-ion NMC/c-SiO cell," *Scientific Data*, vol. 11, no. 1, p. 1004, Sep. 16, 2024.

[143] L. Wildfeuer, A. Karger, D. Aygül, N. Wassiliadis, A. Jossen, and M. Lienkamp, "Experimental degradation study of a commercial lithium-ion battery," *Journal of Power Sources*, vol. 560, p. 232 498, Mar. 15, 2023.

[144] M. He, R. Davis, D. Chartouni, M. Johnson, M. Abplanalp, P. Troendle, and R.-P. Suetterlin, "Assessment of the first commercial prussian blue based sodium-ion battery," *Journal of Power Sources*, vol. 548, p. 232 036, Nov. 15, 2022.

[145] L. H. B. Nguyen, P. S. Camacho, J. Fondard, D. Carlier, L. Croguennec, M. R. Palacin, A. Ponrouch, C. Courrèges, R. Dedryvère, K. Trad, C. Jordy, S. Genies, Y. Reynier, and L. Simonin, "First 18650-format na-ion cells aging investigation: A degradation mechanism study," *Journal of Power Sources*, vol. 529, p. 231 253, May 1, 2022.

[146] P. Dechent, E. Barbers, A. Epp, D. Jöst, W. Li, D. U. Sauer, and S. Lehner, "Correlation of health indicators on lithium-ion batteries," *Energy Technology*, vol. 11, no. 7, p. 2 201 398, 2023.

[147] L. Willenberg, P. Dechent, G. Fuchs, M. Teuber, M. Eckert, M. Graff, N. Kürten, D. U. Sauer, and E. Figgemeier, "The development of jelly roll deformation in 18650 lithium-ion batteries at low state of charge," *Journal of The Electrochemical Society*, vol. 167, no. 12, p. 120 502, Aug. 2020.

[148] F. Stroebl, R. Petersohn, B. Schricker, F. Schaeufl, O. Bohlen, and H. Palm, "A multi-stage lithium-ion battery aging dataset using various experimental design methodologies," *Scientific Data*, vol. 11, no. 1, p. 1020, Sep. 19, 2024.

[149] P. M. Attia, A. Bills, F. Brosa Planella, P. Dechent, G. dos Reis, M. Dubarry, P. Gasper, R. Gilchrist, S. Greenbank, D. Howey, O. Liu, E. Khoo, Y. Preger, A. Soni, S. Sripad, A. G. Stefanopoulou, and V. Sulzer, "Review—"knees" in lithium-ion battery aging trajectories," *Journal of The Electrochemical Society*, vol. 169, no. 6, p. 060 517, Jun. 2022.

[150] M. Dubarry, C. Truchot, and B. Y. Liaw, "Synthesize battery degradation modes via a diagnostic and prognostic model," *Journal of Power Sources*, vol. 219, pp. 204–216, Dec. 1, 2012.

[151] W. Xu, J. Zhu, J. Zhang, M. Tian, J. Cai, H. Wu, G. Wei, T. Chen, X. Wei, and H. Dai, "Investigation of lithium-ion battery degradation by corrected differential voltage analysis based on reference electrode," *Applied Energy*, vol. 389, p. 125 735, Jul. 1, 2025.

[152] S. Schindler and M. A. Danzer, "A novel mechanistic modeling framework for analysis of electrode balancing and degradation modes in commercial lithium-ion cells," *Journal of Power Sources*, vol. 343, pp. 226–236, Mar. 1, 2017.

[153] A. Weng, J. B. Siegel, and A. Stefanopoulou, "Differential voltage analysis for battery manufacturing process control," *Frontiers in Energy Research*, vol. 11, Mar. 22, 2023.

[154] I. Bloom, A. N. Jansen, D. P. Abraham, J. Knuth, S. A. Jones, V. S. Battaglia, and G. L. Henriksen, "Differential voltage analyses of high-power, lithium-ion cells: 1. technique and application," *Journal of Power Sources*, vol. 139, no. 1, pp. 295–303, Jan. 4, 2005.

[155] M. Schütte, H. Laufen, D. Luder, H. Ditler, J. Kern, S. Klick, M. Junker, G. Stahl, F. Frie, and D. U. Sauer, "First full cell parameterization of a commercial layered oxide/hard carbon sodium-ion 18650 battery cell for a physico-chemical model," *Journal of Energy Storage*, vol. 107, p. 114 931, Jan. 30, 2025.

[156] W. Li, I. Demir, D. Cao, D. Jöst, F. Ringbeck, M. Junker, and D. U. Sauer, "Data-driven systematic parameter identification of an electrochemical model for lithium-ion batteries with artificial intelligence," *Energy Storage Materials*, vol. 44, pp. 557–570, Jan. 1, 2022.

[157] J. Chen, M. N. Marlow, Q. Jiang, and B. Wu, "Peak-tracking method to quantify degradation modes in lithium-ion batteries via differential voltage and incremental capacity," *Journal of Energy Storage*, vol. 45, p. 103 669, Jan. 1, 2022.

[158] X. Chen, C. Liu, Y. Fang, X. Ai, F. Zhong, H. Yang, and Y. Cao, "Understanding of the sodium storage mechanism in hard carbon anodes," *Carbon Energy*, vol. 4, no. 6, pp. 1133–1150, 2022.

[159] A. Chanda, A. Pakhare, A. Alfadhli, V. A. Sethuraman, and S. P. V. Nadimpalli, "Real-time measurement of sodiation induced stress in hard carbon composite electrodes," *Journal of Power Sources*, vol. 609, p. 234 678, Jul. 30, 2024.

[160] N. Sun, J. Qiu, and B. Xu, "Understanding of sodium storage mechanism in hard carbons: Ongoing development under debate," *Advanced Energy Materials*, vol. 12, no. 27, p. 2 200 715, 2022.

[161] B. Kishore, L. Chen, C. E. J. Dancer, and E. Kendrick, "Electrochemical formation protocols for maximising the life-time of a sodium ion battery," *Chemical Communications*, vol. 56, no. 85, pp. 12 925–12 928, Oct. 27, 2020.

[162] A. Blömeke, O. Kappelhoff, D. Wasylowski, F. Ringbeck, and D. U. Sauer, "Open source online electrochemical impedance spectroscopy data analytics tool," *Journal of Power Sources*, vol. 615, p. 235 049, Sep. 30, 2024.

[163] A. C. Lazanas and M. I. Prodromidis, "Electrochemical impedance spectroscopya tutorial," *ACS Measurement Science Au*, vol. 3, no. 3, pp. 162–193, Jun. 21, 2023.

[164] S. Klink, E. Madej, E. Ventosa, A. Lindner, W. Schuhmann, and F. La Mantia, "The importance of cell geometry for electrochemical impedance spectroscopy in three-electrode lithium ion battery test cells," *Electrochemistry Communications*, vol. 22, pp. 120–123, Aug. 1, 2012.

[165] W. Hu, Y. Peng, Y. Wei, and Y. Yang, "Application of electrochemical impedance spectroscopy to degradation and aging research of lithium-ion batteries," *The Journal of Physical Chemistry C*, vol. 127, no. 9, pp. 4465–4495, Mar. 9, 2023.

[166] K. Smith, P. Gasper, A. M. Colclasure, Y. Shimonishi, and S. Yoshida, "Lithium-ion battery life model with electrode cracking and early-life break-in processes," *Journal of The Electrochemical Society*, vol. 168, no. 10, p. 100 530, Oct. 2021.

[167] T. Hodson, K. W. Knehr, and D. A. Steingart, "Studying break-in phenomena in lithium-ion batteries through acoustic and impedance measurements," *ECS Meeting Abstracts*, vol. MA2018-01, no. 1, p. 138, Apr. 13, 2018.

[168] L. Jahn, P. Mößle, F. Röder, and M. A. Danzer, "A physically motivated voltage hysteresis model for lithium-ion batteries using a probability distributed equivalent circuit," *Communications Engineering*, vol. 3, no. 1, pp. 1–11, May 30, 2024.

[169] V. J. Ovejas and A. Cuadras, "Effects of cycling on lithium-ion battery hysteresis and overvoltage," *Scientific Reports*, vol. 9, no. 1, p. 14 875, Oct. 16, 2019.

[170] Z. Huang, L. D. Couto, C. Dangwal, S. Xiao, W. Lv, D. Zhang, and S. J. Moura, "On electrochemical model-based state estimation for lithium–sulfur batteries," *IEEE Transactions on Control Systems Technology*, vol. 32, no. 3, pp. 849–861, May 2024.

[171] Q. Wang, J. Wang, P. Zhao, J. Kang, F. Yan, and C. Du, "Correlation between the model accuracy and model-based SOC estimation," *Electrochimica Acta*, vol. 228, pp. 146–159, Feb. 2017.

[172] W. Li, M. Rentemeister, J. Badeda, D. Jöst, D. Schulte, and D. U. Sauer, "Digital twin for battery systems: Cloud battery management system with online state-of-charge and state-of-health estimation," *Journal of Energy Storage*, vol. 30, p. 101 557, Aug. 1, 2020.

[173] N. Ghaeminezhad, Q. Ouyang, J. Wei, Y. Xue, and Z. Wang, "Review on state of charge estimation techniques of lithium-ion batteries: A control-oriented approach," *Journal of Energy Storage*, vol. 72, p. 108 707, Nov. 2023.

[174] W. Waag, C. Fleischer, and D. U. Sauer, "Critical review of the methods for monitoring of lithium-ion batteries in electric and hybrid vehicles," *Journal of Power Sources*, vol. 258, pp. 321–339, Jul. 2014.

[175] C. Campestrini, M. F. Horsche, I. Zilberman, T. Heil, T. Zimmermann, and A. Jossen, "Validation and benchmark methods for battery management system functionalities: State of charge estimation algorithms," *Journal of Energy Storage*, vol. 7, pp. 38–51, Aug. 1, 2016.

[176] M. W. Liemohn, A. D. Shane, A. R. Azari, A. K. Petersen, B. M. Swiger, and A. Mukhopadhyay, "RMSE is not enough: Guidelines to robust data-model comparisons for magnetospheric physics," *Journal of Atmospheric and Solar-Terrestrial Physics*, vol. 218, p. 105 624, Jul. 1, 2021.

[177] S. Tewiele, "Generierung von repräsentativen Fahr- und Lastzyklen aus realen Fahrdaten batterieelektrischer Fahrzeuge," Ph.D. dissertation, DuEPublico: Duisburg-Essen Publications online, University of Duisburg-Essen, Germany, Sep. 14, 2020.

[178] J. Klee Barillas, J. Li, C. Günther, and M. A. Danzer, "A comparative study and validation of state estimation algorithms for li-ion batteries in battery management systems," *Applied Energy*, vol. 155, pp. 455–462, Oct. 2015.

[179] "ISEA / BMS Simulation as MIL · GitLab," GitLab, Accessed: May 17, 2025. [Online]. Available: `https://git.rwth-aachen.de/isea/bms-simulation-as-mil`

[180] K. L. Quade, E. Hempen, H. van den Berg, D. Jöst, F. Berger, F. Ringbeck, and D. U. Sauer, "Benchmarking the transferability of real-time state of charge algorithms to sodium-ion cells using an open-source diagnostics framework," *Batteries & Supercaps*, 2025.

[181] S. Waldhör and M. Wenger, "foxBMS. the open source BMS development and research platform," presented at the Battery Modeling Webinar 2021, 2021.

[182] "ISEA / ISEA Framework · GitLab," GitLab, Accessed: May 17, 2025. [Online]. Available: `https://git.rwth-aachen.de/isea/framework`

[183] "Datenblätter & broschüren der produkte aus der präzisionsmesstechnik, isabellenhütte, isabellenhütte," Accessed: May 1, 2025. [Online]. Available: `https://www.isabellenhuette.de/praezisionsmesstechnik/downloads`

[184] M. Al-Gabalawy, N. S. Hosny, J. A. Dawson, and A. I. Omar, "State of charge estimation of a li-ion battery based on extended kalman filtering and sensor bias," *International Journal of Energy Research*, vol. 45, no. 5, pp. 6708–6726, 2021.

[185] "Simscape battery," Accessed: Feb. 17, 2025. [Online]. Available: `https://www.mathworks.com/products/simscape-battery.html`

[186] J. M. González Sopeña, V. Pakrashi, and B. Ghosh, "A benchmarking framework for performance evaluation of statistical wind power forecasting models," *Sustainable Energy Technologies and Assessments*, vol. 57, p. 103 246, Jun. 1, 2023.

[187] K. A. Maupin, L. P. Swiler, and N. W. Porter, "Validation metrics for deterministic and probabilistic data," *Journal of Verification, Validation and Uncertainty Quantification*, vol. 3, no. 3, p. 031 002, Sep. 1, 2018.

[188] C. J. Willmott, "ON THE VALIDATION OF MODELS," *Physical Geography*, vol. 2, no. 2, pp. 184–194, Jul. 1981.

[189] C. J. Willmott, S. M. Robeson, and K. Matsuura, "A refined index of model performance," *International Journal of Climatology*, vol. 32, no. 13, pp. 2088–2094, 2012.

[190] D. S. Wilks, "Chapter 9 - forecast verification," in *Statistical Methods in the Atmospheric Sciences (Fourth Edition)*, D. S. Wilks, Ed., Elsevier, Jan. 1, 2019, pp. 369–483.

[191] S. Klick, H. Laufen, M. Schütte, B. Qian, K. L. Quade, C. Rahe, M. Dubarry, and D. U. Sauer, "Failure mode and degradation analysis of a commercial sodium-ion battery with severe gassing issue," *Batteries & Supercaps*, 2024.

[192] P. Rahmani, S. Chakraborty, I. Mele, T. Katrašnik, S. Bernhard, S. Pruefling, S. Wilkins, and O. Hegazy, "Driving the future: A comprehensive review of automotive battery management system technologies, and future trends," *Journal of Power Sources*, vol. 629, p. 235 827, Feb. 15, 2025.

[193] S. Bihn, J. Rinner, H. Witzenhausen, F. Krause, F. Ringbeck, and D. U. Sauer, "Physics-based equivalent circuit model motivated by the doyle–fuller–newman model," *Batteries*, vol. 10, no. 9, p. 314, Sep. 4, 2024.

[194] S. Bihn, "Automatic parameterisation of electrical equivalent circuit models for virtual battery cell design," Ph.D. dissertation, RWTH Aachen University, 2024.

[195] M. Adaikkappan and N. Sathiyamoorthy, "Modeling, state of charge estimation, and charging of lithium-ion battery in electric vehicle: A review," *International Journal of Energy Research*, vol. 46, no. 3, pp. 2141–2165, 2022.

[196] F. Lou and D. Chen, "Aligned carbon nanostructures based 3d electrodes for energy storage," *Journal of Energy Chemistry*, vol. 24, no. 5, pp. 559–586, Sep. 1, 2015.

[197] "Getting started with impedance.py — impedance.py 1.7.1 documentation," Accessed: May 17, 2025. [Online]. Available: `https://impedancepy.readthedocs.io/en/latest/getting-started.html`

[198] A. Fly, B. Wimarshana, I. Bin-Mat-Arishad, and M. Sarmiento-Carnevali, "Temperature dependency of diagnostic methods in lithium-ion batteries," *Journal of Energy Storage*, vol. 52, p. 104 721, Aug. 1, 2022.

[199] W. Ai, L. Kraft, J. Sturm, A. Jossen, and B. Wu, "Electrochemical thermal-mechanical modelling of stress inhomogeneity in lithium-ion pouch cells," *Journal of The Electrochemical Society*, vol. 167, no. 1, p. 013 512, Oct. 3, 2019.

[200] J. M. Reniers, G. Mulder, and D. A. Howey, "Review and performance comparison of mechanical-chemical degradation models for lithium-ion batteries," *Journal of The Electrochemical Society*, vol. 166, no. 14, A3189, Sep. 19, 2019.

[201] V. N. Lam, X. Cui, F. Stroebl, M. Uppaluri, S. Onori, and W. C. Chueh, "A decade of insights: Delving into calendar aging trends and implications," *Joule*, vol. 9, no. 1, p. 101 796, Jan. 15, 2025.

[202] W. Agyei Appiah, J. Park, S. Byun, Y. Roh, M.-H. Ryou, and Y. M. Lee, "Time-effective accelerated cyclic aging analysis of lithium-ion batteries," *ChemElectroChem*, vol. 6, no. 14, pp. 3714–3725, 2019.

[203] L. Streck, T. Roth, H. Bosch, C. Kirst, M. Rehm, P. Keil, and A. Jossen, "Self-discharge and calendar aging behavior of li-ion and na-ion cells," *Journal of The Electrochemical Society*, vol. 171, no. 8, p. 080 531, Aug. 2024.

[204] "LTC6804-1 datasheet and product info — analog devices," Accessed: May 1, 2025. [Online]. Available: `https://www.analog.com/en/products/ltc6804-1.html`

[205] N. Wassiliadis, J. Adermann, A. Frericks, M. Pak, C. Reiter, B. Lohmann, and M. Lienkamp, "Revisiting the dual extended kalman filter for battery state-of-charge and state-of-health estimation: A use-case life cycle analysis," *Journal of Energy Storage*, vol. 19, pp. 73–87, Oct. 2018.

[206] C. Campestrini, "Practical feasibility of kalman filters for the state estimation of lithium-ion batteries," Ph.D. dissertation, Technische Universität München, 2018.

[207] S. K. Pradhan and B. Chakraborty, "Battery management strategies: An essential review for battery state of health monitoring techniques," *Journal of Energy Storage*, vol. 51, p. 104 427, Jul. 1, 2022.

[208] O. Demirci, S. Taskin, E. Schaltz, and B. Acar Demirci, "Review of battery state estimation methods for electric vehicles - part i: SOC estimation," *Journal of Energy Storage*, vol. 87, p. 111 435, May 15, 2024.

[209] G. L. Plett, "Recursive approximate weighted total least squares estimation of battery cell total capacity," *Journal of Power Sources*, vol. 196, no. 4, pp. 2319–2331, Feb. 15, 2011.

[210] G. Anagnostou and B. C. Pal, "Derivative-free kalman filtering based approaches to dynamic state estimation for power systems with unknown inputs," *IEEE Transactions on Power Systems*, vol. 33, no. 1, pp. 116–130, Jan. 2018.

[211] F. Berger, A. Ismayilov, K. L. Quade, D. Jöst, M. F. Börner, F. Ringbeck, and D. U. Sauer, "Stochastic profiles from real driving data for offline battery state estimation validation," *Transportation Research Part D: Transport and Environment*, vol. 152, 2026.

[212] D. Lyu, S. Onori, S. Tao, D. A. Howey, B. Zhang, K. L. Quade, M. Dubarry, B. Wu, and W. Li, "Next steps for battery diagnostics," *Cell Reports Physical Science*, vol. 6, no. 11, 2025.

[213] C. Ünlübayir, H. Youssfi, R. A. Khan, S. S. Ventura, D. Fortunati, J. Rinner, M. F. Börner, K. L. Quade, F. Ringbeck, and D. U. Sauer, "Comparative analysis and test bench validation of energy management methods for a hybrid marine propulsion system powered by batteries and solid oxide fuel cells," *Applied Energy*, vol. 376, 2024.

[214] D. Jöst, L. N. Palaniswamy, K. L. Quade, and D. U. Sauer, "Towards robust state estimation for LFP batteries: Model-in-the-loop analysis with hysteresis modelling and perspectives for other chemistries," *Journal of Energy Storage*, vol. 92, 2024.

[215] C. Ünlübayir, U. H. Mierendorff, M. F. Börner, K. L. Quade, A. Blömeke, F. Ringbeck, and D. U. Sauer, "A data-driven approach to ship energy management: Incorporating automated tracking system data and weather information," *Journal of Marine Science and Engineering*, vol. 11, no. 12, 2023.

[216] K. L. Quade, D. Jöst, D. U. Sauer, and W. Li, "Understanding the energy potential of lithium-ion batteries: Definition and estimation of the state of energy," *Batteries & Supercaps*, vol. 6, no. 8, 2023.

[217] W. Li, J. Chen, K. Quade, D. Luder, J. Gong, and D. U. Sauer, "Battery degradation diagnosis with field data, impedance-based modeling and artificial intelligence," *Energy Storage Materials*, vol. 53, 2022.

List of Publications

The following is a comprehensive list of all publications, presented in chronological order up to the date of this writing.

Journal Articles

1. F. Berger, A. Ismayilov, K. L. Quade, D. Jöst, M. F. Börner, F. Ringbeck, and D. U. Sauer, "Stochastic profiles from real driving data for offline battery state estimation validation," *Transportation Research Part D: Transport and Environment*, vol. 152, 2026
2. D. Lyu, S. Onori, S. Tao, D. A. Howey, B. Zhang, K. L. Quade, M. Dubarry, B. Wu, and W. Li, "Next steps for battery diagnostics," *Cell Reports Physical Science*, vol. 6, no. 11, 2025
3. K. L. Quade, E. Hempen, H. van den Berg, D. Jöst, F. Berger, F. Ringbeck, and D. U. Sauer, "Benchmarking the transferability of real-time state of charge algorithms to sodium-ion cells using an open-source diagnostics framework," *Batteries & Supercaps*, 2025
4. V. Steininger, K. L. Quade, K. Rumpf, S. Bihn, J. Ringler, D. U. Sauer, and W. Li, "Detection of abnormal SOH estimates in battery field data using statistical learning," *Cell Reports Physical Science*, 2025
5. S. Klick, H. Laufen, M. Schütte, B. Qian, K. L. Quade, C. Rahe, M. Dubarry, and D. U. Sauer, "Failure mode and degradation analysis of a commercial sodium-ion battery with severe gassing issue," *Batteries & Supercaps*, 2024
6. C. Ünlübayir, H. Youssfi, R. A. Khan, S. S. Ventura, D. Fortunati, J. Rinner, M. F. Börner, K. L. Quade, F. Ringbeck, and D. U. Sauer, "Comparative analysis and test bench validation of energy management methods for a hybrid marine propulsion system powered by batteries and solid oxide fuel cells," *Applied Energy*, vol. 376, 2024
7. F. Berger, D. Joest, E. Barbers, K. Quade, Z. Wu, D. U. Sauer, and P. Dechent, "Benchmarking battery management system algorithms - requirements, scenarios and validation for automotive applications," *eTransportation*, vol. 22, 2024
8. H. Laufen, S. Klick, H. Ditler, K. L. Quade, A. Mikitisin, A. Blömeke, M. Schütte, D. Wasylowski, M. Sonnet, L. Henrich, A. Schwedt, G. Stahl, F. Ringbeck, J. Mayer,

and D. U. Sauer, "Multi-method characterization of a commercial 1.2 Ah sodium-ion battery cell indicates drop-in potential," *Cell Reports Physical Science*, vol. 5, no. 5, 2024

9. E. Barbers, F. E. Hust, F. E. A. Hildenbrand, F. Frie, K. L. Quade, S. Bihn, D. U. Sauer, and P. Dechent, "Exploring the effects of cell-to-cell variability on battery aging through stochastic simulation techniques," *Journal of Energy Storage*, vol. 84, 2024
10. D. Jöst, L. N. Palaniswamy, K. L. Quade, and D. U. Sauer, "Towards robust state estimation for LFP batteries: Model-in-the-loop analysis with hysteresis modelling and perspectives for other chemistries," *Journal of Energy Storage*, vol. 92, 2024
11. C. Ünlübayir, U. H. Mierendorff, M. F. Börner, K. L. Quade, A. Blömeke, F. Ringbeck, and D. U. Sauer, "A data-driven approach to ship energy management: Incorporating automated tracking system data and weather information," *Journal of Marine Science and Engineering*, vol. 11, no. 12, 2023
12. K. L. Quade, D. Jöst, D. U. Sauer, and W. Li, "Understanding the energy potential of lithium-ion batteries: Definition and estimation of the state of energy," *Batteries & Supercaps*, vol. 6, no. 8, 2023
13. W. Li, J. Chen, K. Quade, D. Luder, J. Gong, and D. U. Sauer, "Battery degradation diagnosis with field data, impedance-based modeling and artificial intelligence," *Energy Storage Materials*, vol. 53, 2022

Patents

1. M. Fischer, B. Schricker, F. Steinbacher, S. Bihn, N. Kaiser, K. L. Quade, "Verfahren Zur Steuerung Einer Energiespeichereinrichtung", Patent EP4485729A1, Siemens Mobility GmbH; Rheinisch-Westfälische Technische Hochschule Aachen, 2023

Conference Contributions

1. L. Preuß, K. L. Quade, M. Schütte, D. U. Sauer, "Analysis of Aging and Cell-to-Cell Variability of Commercial Sodium-Ion Cells", Advanced Battery Power Conference, 2025
2. K. L. Quade, V. Steininger, D. U. Sauer, "Detecting Anomalous Aging Behavior in Battery Field Data", Advanced Battery Power Conference, 2025
3. N. Kaiser, S. Klick, H. Laufen, K. L. Quade, D. U. Sauer, "Potential of Sodium-ion Batteries in the context of rail-bound Mobility", 4. International Railway Symposium Aachen, 2024

4. K. L. Quade, D. Jöst, E. Barbers, D. U. Sauer, "Analysis of the Influence of Cell-to-cell Variations on BMS Algorithm Performance Indicators", Advanced Battery Power Conference, 2024
5. V. Steininger, K. L. Quade, D. U. Sauer, W. Li, "Aging Analysis of Vehicle Battery Field Data", Batterieforum, 2024
6. D. Jöst, F. Ringbeck, K. L. Quade, D.U. Sauer, "Trends in Battery Management for Lithium-Ion Batteries", 32nd Aachen Colloquium Sustainable Mobility Aachen, 2023
7. K. L. Quade, M. Baumann, A. Blömeke, D.U. Sauer, W. Li, "Aging Analysis for Lithium-Ion Batteries Using Electric Vehicle Field Data", Advanced Battery Power Conference, 2023
8. W. Li, J. Chen, K. L. Quade, D. Luder, J. Gong, D. U. Sauer, "Online Electrode-Level Aging Diagnosis for Lithium-Ion Batteries with Artificial Intelligence", Battery Safety Summit, 2022
9. A. Blömeke, K. L. Quade, D. Jöst, W. Li, F. Ringbeck, D. U. Sauer, "Properties of a Lithium-Ion Battery as a Partner of Power Electronics", 24th European Conference on Power Electronics and Applications, IEEE, 2022
10. D. Jöst, K. L. Quade, F. Berger, D. U. Sauer, "Systematic Battery State Estimation Algorithm Assessment – a Model-in-the-Loop Approach", 35th International Electric Vehicle Symposium and Exhibition, 2022
11. K. L. Quade, D. Jöst, D. U. Sauer, "Investigation, Definition, and Review of the State of Energy for Range Prediction", MRS Spring Meeting, 2022
12. K. L. Quade, D. Jöst, D. U. Sauer, "Development and Investigation of State of Energy Algorithms in a Model-in-the-Loop Toolchain", Advanced Battery Power Conference, 2022

List of Supervised Theses

Several theses were supervised over the course of this doctoral research, and the collaboration with these students has significantly contributed to its progress. I would like to extend my gratitude to the following students who completed their thesis under my supervision.

Name	**Topic**	**Year**
Christophe Thomassin	Modeling and Analysis of Battery Management Systems for Lithium-Ion Batteries in the Scope of Electromobility	2021
Araz Ismayilov	Analysis and Generation of Modular Load Profiles for Validation of BMS Algorithms	2022
Erik Breuer	Data-based Modeling of a BMS Hardware for High-Performance Lithium-Ion Battery Systems	2023
Julian Besseling	Worst-case Estimation of the Performance of Diagnostic Algorithms for Lithium-Ion Batteries	2023
Hanna van den Berg	Comparison of Modern Diagnostic Algorithms for Lithium-Ion Batteries	2023
Kai Krieger	State of Energy Determination of Modern Lithium-Ion Batteries with Machine Learning for Electromobility	2023
Marc Bastian	Closed-Loop Online Aging Prediction of Modern Lithium-Ion Cells	2023
Elias Hempen	Implementation and Evaluation of Modern Algorithms for Estimating the State-of-Health of Lithium-Ion Batteries	2024
Jan Lin	Sensitivity Analysis of Diagnostic Algorithms for Sodium-Ion Batteries	2024
Katrin Messink	Sensitivity Analysis for Holistic Evaluation of Battery Algorithms	2024
Moritz Krämer	Analysis of the Cyclic Aging Behavior of Sodium-Ion Cells at Different DoDs	2025
Ludwig Preuß	Analysis of the Aging Behavior of a Modern Battery Technology Taking Into Account Cell Variations into account	2025

Curriculum Vitae

Katharina Lilith Quade

19.12.2025	Doctoral Examination for Dr.-Ing.
since 10/2023	Chief Engineer and Head of Section CARL, RWTH Aachen University, Germany
01/2021 – 12/2025	PhD Candidate ISEA, RWTH Aachen University, Germany
05/2025 – 08/2025	Visiting PhD Candidate University of California, Berkeley, USA
01/2022 – 09/2023	Group Leader CARL, RWTH Aachen University, Germany
10/2015 – 10/2020	Bachelor and Master of Business Administration and Engineering: Electrical Power Engineering RWTH Aachen University, Germany
09/2019 – 12/2019	Visiting Student University of Alberta in Edmonton, Canada
2007 – 2015	General Higher Education Entrance Qualification (Abitur) Luise-von-Duesberg Gymnasium, Kempen, Germany
09/2013 – 12/2013	Visiting Student Lycée Jean Monnet, Vitrolles, France
08.09.1997	born in Munich, Germany

ABISEA Band 1
Eßer, Albert
Berührungslose, kombinierte Energie- und Informationsübertragung für bewegliche Systeme
1. Aufl. 1992, 129 S.
ISBN 3-86073-046-0

ABISEA Band 2
Vogel, Ulrich
Entwurf und Beurteilung von Verfahren zur Hochausnutzung des Rad-Schiene-Kraftschlusses durch Triebfahrzeuge
1. Aufl. 1992, 131 S.
ISBN 3-86073-060-6

ABISEA Band 3
Reckhorn, Thomas
Stromeinprägendes Antriebssystem mit fremderregter Synchronmaschine
1. Aufl. 1992, 128 S.
ISBN 3-86073-061-4

ABISEA Band 4
Ackva, Ansgar
Spannungseinprägendes Antriebssystem mit Synchronmaschine und direkter Stromregelung
1. Aufl. 1992, 137 S.
ISBN 3-86073-062-2

ABISEA Band 5
Mertens, Axel
Analyse des Oberschwingungsverhaltens von taktsynchronen Delta - Modulationsverfahren zur Steuerung von Pulsstromrichtern bei hoher Taktzahl
1. Aufl. 1992, 178 S.
ISBN 3-86073-069-X

ABISEA Band 6
Geuer, Wolfgang
Untersuchungen über das Alterungsverhalten von Blei-Akkumulatoren
1. Aufl. 1993, 97 S.
ISBN 3-86073-097-5

ABISEA Band 7
Langheim, Jochen
Einzelradantrieb für Elektrostraßenfahrzeuge
1. Aufl. 1993, 213 S.
ISBN 3-86073-123-8
(vergriffen)

ABISEA Band 8
Fetz, Joachim
Fehlertolerante Regelung eines Asynchron-Doppelantriebes für ein Elektrospeicherfahrzeug
1. Aufl. 1993, 136 S.
ISBN 3-86073-124-6
(vergriffen)

ABISEA Band 9
Schülting, Ludger
Optimierte Auslegung induktiver Bauelemente für den Mittelfrequenzbereich
1. Aufl. 1993, 126 S.
ISBN 3-86073-174-2
(vergriffen)

ABISEA Band 10
Skudelny, H.-Ch.
Stromrichtertechnik
4. Aufl. 1997, 259 S.
ISBN 3-86073-189-0

ABISEA Band 11
Skudelny, H.-Ch.
Elektrische Antriebe
3. Aufl. 1997, 124 S.
ISBN 3-86073-231-5

ABISEA Band 12
Schöpe, Friedhelm
Batterie-Management für Nickel-Cadmium Akkumulatoren
1. Aufl. 1994, 148 S.
ISBN 3-86073-232-3
(vergriffen)

ABISEA Band 13
v. d. Weem, Jürgen
Schmalbandige aktive Filter für Schienentriebfahrzeuge am Gleichspannungsfahrdraht
1. Aufl. 1995, 126 S.
ISBN 3-86073-233-1

ABISEA Band 14
Backhaus, Klaus
Spannungseinprägendes Direktantriebssystem mit schnelllaufender geschalteter Reluktanzmaschine
1. Aufl. 1995, 146 S.
ISBN 3-86073-234-X
(vergriffen)

ABISEA Band 15
Reinold, Harry
Optimierung dreiphasiger Pulsdauermodulationsverfahren
1. Aufl. 1996, 107 S.
ISBN 3-86073-235-8

ABISEA Band 16
Köpken, Hans-Georg
Regelverfahren für Parallelschwingkreisumrichter
1. Aufl. 1996, 125 S.
ISBN 3-86073-236-6

ABISEA Band 17
Mauracher, Peter
Modellbildung und Verbundoptimierung bei Elektrostraßenfahrzeugen
1. Aufl. 1996, 192 S.
ISBN 3-86073-237-4

ABISEA Band 18
Protiwa, Franz-Ferdinand
Vergleich dreiphasiger Resonanz-Wechselrichter in Simulation und Messung
1. Aufl. 1997, 178 S.
ISBN 3-86073-238-2

ABISEA Band 19
Brockmeyer, Ansgar
Dimensionierungswerkzeug für magnetische Bauelemente in Stromrichteranwendungen
1. Aufl. 1997, 175 S.
ISBN 3-86073-239-0

Aachener Beiträge des ISEA

ABISEA Band 20
Apeldoorn, Oscar
Simulationsgestützte Bewertung von Steuerverfahren für netzgeführte Stromrichter mit verringerter Netzrückwirkung
1. Aufl. 1997, 134 S.
ISBN 3-86073-680-9

ABISEA Band 21
Lohner, Andreas
Batteriemanagement für verschlossene Blei-Batterien am Beispiel von Unterbrechungsfreien Stromversorgungen
1. Aufl. 1998, 126 S.
ISBN 3-86073-681-7

ABISEA Band 22
Reinert, Jürgen
Optimierung der Betriebseigenschaften von Antrieben mit geschalteter Reluktanzmaschine
1. Aufl. 1998, 153 S.
ISBN 3-86073-682-5

ABISEA Band 23
Nagel, Andreas
Leitungsgebundene Störungen in der Leistungselektronik: Entstehung, Ausbreitung und Filterung
1. Aufl. 1999, 140 S.
ISBN 3-86073-683-3

ABISEA Band 24
Menne, Marcus
Drehschwingungen im Antriebsstrang von Elektrostraßenfahrzeugen - Analyse und aktive Dämpfung
1. Aufl. 2001, 169 S.
ISBN 3-86073-684-1

ABISEA Band 25
von Bloh, Jochen
Multilevel-Umrichter zum Einsatz in Mittelspannungs-Gleichspannungs-Übertragungen
1. Aufl. 2001, 137 S.
ISBN 3-86073-685-X

ABISEA Band 26
Karden, Eckhard
Using low-frequency impedance spectroscopy for characterization, monitoring, and modeling of industrial batteries
1. Aufl. 2002, 137 S.
ISBN 3-8265-9766-4

ABISEA Band 27
Karipidis, Claus-Ulrich
A Versatile DSP/ FPGA Structure optimized for Rapid Prototyping and Digital Real-Time Simulation of Power Electronic and Electrical Drive Systems
1. Aufl. 2001, 164 S.
ISBN 3-8265-9738-9

ABISEA Band 28
Kahlen, Klemens
Regelungsstrategien für permanentmagnetische Direktantriebe mit mehreren Freiheitsgraden
1. Aufl. 2002, 154 S.
ISBN 3-8322-1222-1

ABISEA Band 29
Inderka, Robert B.
Direkte Drehmomentregelung Geschalteter Reluktanzantriebe
1. Aufl. 2003, 182 S.
ISBN 3-8322-1175-6

ABISEA Band 30
Schröder, Stefan
Circuit-Simulation Models of High-Power Devices Based on Semiconductor Physics
1. Aufl. 2003, 123 S.
ISBN 3-8322-1250-7

ABISEA Band 31
Buller, Stephan
Impedance-Based Simulation Models for Energy Storage Devices in Advanced Automotive Power Systems
1. Aufl. 2003, 138 S.
ISBN 3-8322-1225-6

ABISEA Band 32
Schönknecht, Andreas
Topologien und Regelungsstrategien für das induktive Erwärmen mit hohen Frequenz-Leistungsprodukten
1. Aufl. 2004, 157 S.
ISBN 3-8322-2408-4

ABISEA Band 33
Tolle, Tobias
Konvertertopologien für ein aufwandsarmes, zweistufiges Schaltnetzteil zum Laden von Batterien aus dem Netz
1. Aufl. 2004, 148 S.
ISBN 3-8322-2676-1

ABISEA Band 34
Götting, Gunther
Dynamische Antriebsregelung von Elektrostraßenfahrzeugen unter Berücksichtigung eines schwingungsfähigen Antriebsstrangs
1. Aufl. 2004, 157 S.
ISBN 3-8322-2804-7

ABISEA Band 35
Dieckerhoff, Sibylle
Transformatorlose Stromrichterschaltungen für Bahnfahrzeuge am 16 2/3Hz Netz
1. Aufl. 2004, 147 S.
ISBN 3-8322-3094-7

ABISEA Band 36
Hu, Jing
Bewertung von DC-DC-Topologien und Optimierung eines DC-DC-Leistungsmoduls für das 42-V-Kfz-Bordnetz
1. Aufl. 2004, 148 S.
ISBN 3-8322-3201-X

ABISEA Band 37
Detjen, Dirk-Oliver
Characterization and Modeling of Si-Si Bonded Hydrophobie Interfaces for Novel High-Power BIMOS Devices
1. Aufl. 2004, 135 S.
ISBN 3-8322-2963-9

ABISEA Band 38
Walter, Jörg
Simulationsbasierte Zuverlässigkeitsanalyse in der modernen Leistungselektronik
1. Aufl. 2004, 121 S.
ISBN 3-8322-3481-0

ABISEA Band 39
Schwarzer, Ulrich
IGBT versus GCT in der Mittelspannungsanwendung - ein experimenteller und simulativer Vergleich
1. Aufl. 2005, 170 S.
ISBN 3-8322-4489-1

ABISEA Band 40
Bartram, Markus
IGBT-Umrichtersysteme für Windkraftanlagen: Analyse der Zyklenbelastung, Modellbildung, Optimierung und Lebensdauervorhersage
1. Aufl. 2006, 185 S.
ISBN 3-8322-5039-5

ABISEA Band 41
Ponnaluri, Srinivas
Generalized Design, Analysis and Control of Grid side converters with integrated UPS or Islanding functionality
1. Aufl. 2006, 163 S.
ISBN 3-8322-5281-9

ABISEA Band 42
Jacobs, Joseph
Multi-Phase Series Resonant DC-to-DC Converters
1. Aufl. 2006, 185 S.
ISBN 3-8322-5532-X

ABISEA Band 43
Linzen, Dirk
Impedance-Based Loss Calculation and Thermal Modeling of Electrochemical Energy Storage Devices for Design Considerations of Automotive Power Systems
1. Aufl. 2006, 185 S.
ISBN 3-8322-5706-3

ABISEA Band 44
Fiedler, Jens
Design of Low-Noise Switched Reluctance Drives
1. Aufl. 2007, 176 S.
ISBN 978-3-8322-5864-1

ABISEA Band 45
Fuengwarodsakul, Nisai
Predictive PWM-based Direct Instantaneous Torque Control for Switched Reluctance Machines
1. Aufl. 2007, 141 S.
ISBN 978-3-8322-6210-5

ABISEA Band 46
Meyer, Christoph
Key Components for Future Offshore DC Grids
1. Aufl. 2007, 187 S.
ISBN 978-3-8322-6571-7

ABISEA Band 47
Fujii, Kansuke
Characterization and Optimization of Soft-Switched Multi-Level Converters for STATCOMs
1. Aufl. 2008, 199 S.
ISBN 978-3-8322-6981-4

ABISEA Band 48
Carstensen, Christian
Eddy Currents in Windings of Switched Reluctance Machines
1. Aufl. 2008, 179 S.
ISBN 978-3-8322-7118-3

ABISEA Band 49
Bohlen, Oliver
Impedance-based battery monitoring
1. Aufl. 2008, 190 S.
ISBN 978-3-8322-7606-5

ABISEA Band 50
Thele, Marc
A contribution to the modelling of the charge acceptance of lead-acid batteries - using frequency and time domain based concepts
1. Aufl. 2008, 165 S.
ISBN 978-3-8322-7659-1

ABISEA Band 51
König, Andreas
High Temperature DC-to-DC Converters for Downhole Applications
1. Aufl. 2009, 154 S.
ISBN 978-3-8322-8489-3

ABISEA Band 52
Dick, Christian Peter
Multi-Resonant Converters as Photovoltaic Module-Integrated Maximum Power Point Tracker
1. Aufl. 2010, 182 S.
ISBN 978-3-8322-9199-0

ABISEA Band 53
Kowal, Julia
Spatially resolved impedance of nonlinear inhomogeneous devices: using the example of lead-acid batteries
1. Aufl. 2010, 203 S.
ISBN 978-3-8322-9483-0

ABISEA Band 54
Roscher, Michael Andreas
Zustandserkennung von LiFeP04-Batterien für Hybrid- und Elektrofahrzeuge
1. Aufl. 2011, 186 S.
ISBN 978-3-8322-9738-1

ABISEA Band 55
Hirschmann, Dirk
Highly Dynamic Piezoelectric Positioning
1. Aufl. 2011, 146 S.
ISBN 978-3-8322-9746-6

ABISEA Band 56
Rigbers, Klaus
Highly Efficient Inverter Architectures for Three-Phase Grid Connection of Photovoltaic Generators
1. Aufl. 2011, 244 S.
ISBN 978-3-8322-9816-9

ABISEA Band 57
Kasper, Knut
Analysis and Control of the Acoustic Behavior of Switched Reluctance Drives
1. Aufl. 2011, 205 S.
ISBN 978-3-8322-9869-2

Aachener Beiträge des ISEA

ABISEA Band 58
Köllensperger, Peter
The Internally Commutated Thyristor - Concept, Design and Application
1. Aufl. 2011, 214 S.
ISBN 978-3-8322-9909-5

ABISEA Band 59
Schoenen, Timo
Einsatz eines DC/DC-Wandlers zur Spannungsanpassung zwischen Antrieb und Energiespeicher in Elektro-und Hybridfahrzeugen
1. Aufl. 2011, 128 S.
ISBN 978-3-8440-0622-3

ABISEA Band 60
Hennen, Martin
Switched Reluctance Direct Drive with Integrated Distributed Inverter
1. Aufl. 2012, 141 S.
ISBN 978-3-8440-0731-2

ABISEA Band 61
van Treek, Daniel
Position Sensorless Torque Control of Switched Reluctance Machines
1. Aufl. 2012, 144 S.
ISBN 978-3-8440-1014-5

ABISEA Band 62
Bragard, Michael
The Integrated Emitter Turn-Off Thyristor. An Innovative MOS-Gated High-Power Device
1. Aufl. 2012, 164 S.
ISBN 978-3-8440-1152-4

ABISEA Band 63
Gerschler, Jochen B.
Ortsaufgelöste Modellbildung von Lithium-Ionen-Systemen unter spezieller Berücksichtigung der Batteriealterung
1. Aufl. 2012, 334 S.
ISBN 978-3-8440-1307-8

ABISEA Band 64
Neuhaus, Christoph R.
Schaltstrategien für Geschaltete Reluktanzantriebe mit kleinem Zwischenkreis
1. Aufl. 2012, 133 S.
ISBN 978-3-8440-1487-7

ABISEA Band 65
Butschen, Thomas
Dual-ICT- A Clever Way to Unite Conduction and Switching Optimized Properties in a Single Wafer
1. Aufl. 2012, 168 S.
ISBN 978-3-8440-1771-7

ABISEA Band 66
Plum, Thomas
Design and Realization of High-Power MOS Turn-Off Thyristors
1. Aufl. 2013, 113 S.
ISBN 978-3-8440-1884-4

ABISEA Band 67
Kiel, Martin
Impedanzspektroskopie an Batterien unter besonderer Berücksichtigung von Batteriesensoren für den Feldeinsatz
1. Aufl. 2013, 226 S.
ISBN 978-3-8440-1973-5

ABISEA Band 68
Brauer, Helge
Schnelldrehender Geschalteter Reluktanzantrieb mit extremem Längendurchmesserverhältnis
1. Aufl. 2013, 192 S.
ISBN 978-3-8440-2345-9

ABISEA Band 69
Thomas, Stephan
A Medium-Voltage Multi-Level DC/DC Converter with High Voltage Transformation Ratio
1. Aufl. 2014, 226 S.
ISBN 978-3-8440-2605-4

ABISEA Band 70
Richter, Sebastian
Digitale Regelung von PWM Wechselrichtern mit niedrigen Trägerfrequenzen
1. Aufl. 2014, 126 S.
ISBN 978-3-8440-2641-2

ABISEA Band 71
Bösing, Matthias
Acoustic Modeling of Electrical Drives - Noise and Vibration Synthesis based on Force Response Superposition
1. Aufl. 2014, 188 S.
ISBN 978-3-8440-2752-5

ABISEA Band 72
Waag, Wladislaw
Adaptive algorithms for monitoring of lithium-ion batteries in electric vehicles
1. Aufl. 2014, 232 S.
ISBN 978-3-8440-2976-5

ABISEA Band 73
Sanders, Tilman
Spatially Resolved Electrical In-Situ Measurement Techniques for Fuel Cells
1. Aufl. 2014, 126 S.
ISBN 978-3-8440-3121-8

ABISEA Band 74
Baumhöfer, Thorsten
Statistische Betrachtung experimenteller Alterungsuntersuchungen an Lithium-Ionen Batterien
1. Aufl. 2015, 157 S.
ISBN 978-3-8440-3423-3

ABISEA Band 75
Andre, Dave
Systematic Characterization of Ageing Factors for High-Energy Lithium-Ion Cells and Approaches for Lifetime Modelling Regarding an Optimized Operating Strategy in Automotive Applications
1. Aufl. 2015, 196 S.
ISBN 978-3-8440-3587-2

ABISEA Band 76
Merei, Ghada
Optimization of off-grid hybrid PV-wind-diesel power supplies with multi-technology battery systems taking into account battery aging
1. Aufl. 2015, 184 S.
ISBN 978-3-8440-4148-4

ABISEA Band 77
Schulte, Dominik
Modellierung und experimentelle Validierung der Alterung von Blei-Säure Batterien durch inhomogene Stromverteilung und Säureschichtung
1. Aufl. 2016, 165 S.
ISBN 978-3-8440-4216-0

ABISEA Band 78
Schenk, Mareike
Simulative Untersuchung der Wicklungsverluste in Geschalteten Reluktanzmaschinen
1. Aufl. 2016, 126 S.
ISBN 978-3-8440-4282-5

ABISEA Band 79
Wang, Yu
Development of Dynamic Models with Spatial Resolution for Electrochemical Energy Converters as Basis for Control and Management Strategies
1. Aufl. 2016, 188 S.
ISBN 978-3-8440-4303-7

ABISEA Band 80
Ecker, Madeleine
Lithium Plating in Lithium-Ion Batteries:
An Experimental and Simulation Approach
1. Aufl. 2016, 154 S.
ISBN 978-3-8440-4525-3

ABISEA Band 81
Zhou, Wei
Modellbasierte Auslegungsmethode von Temperierungssystemen für Hochvolt-Batterien in Personenkraftfahrzeugen
1. Aufl. 2016, 175 S.
ISBN 978-3-8440-4589-5

ABISEA Band 82
Lunz, Benedikt
Deutschlands Stromversorgung im Jahr 2050
Ein szenariobasiertes Verfahren zur vergleichenden Bewertung von Systemvarianten und Flexibilitätsoptionen
1. Aufl. 2016, 187 S.
ISBN 978-3-8440-4627-4

ABISEA Band 83
Hofmann, Andreas G.
Direct Instantaneous Force Control: Key to Low-Noise Switched Reluctance Traction Drives
1. Aufl. 2016, 228 S.
ISBN 978-3-8440-4715-8

ABISEA Band 84
Budde-Meiwes, Heide
Dynamic Charge Acceptance of Lead-Acid Batteries for Micro-Hybrid Automotive Applications
1. Aufl. 2016, 157 S.
ISBN 978-3-8440-4733-2

ABISEA Band 85
Engel, Stefan P.
Thyristor-Based High-Power On-Load Tap Changers Control under Harsh Load Conditions
1. Aufl. 2016, 156 S.
ISBN 978-3-8440-4986-2

ABISEA Band 86
Van Hoek, Hauke
Design and Operation Considerations of Three-Phase Dual Active Bridge Converters for Low-Power Applications with Wide Voltage Ranges
1. Aufl. 2017, 231 S.
ISBN 978-3-8440-5011-0

ABISEA Band 87
Diekhans, Tobias
Wireless Charging of Electric Vehicles - a Pareto-Based Comparison of Power Electronic Topologies
1. Aufl. 2017, 151 S.
ISBN 978-3-8440-5048-6

ABISEA Band 88
Lehner, Susanne
Reliability Assessment of Lithium-Ion Battery Systems with Special Emphasis on Cell Performance Distribution
1. Aufl. 2017, 184 S.
ISBN 978-3-8440-5090-5

ABISEA Band 89
Käbitz, Stefan
Untersuchung der Alterung von Lithium-Ionen-Batterien mittels Elektroanalytik und elektrochemischer Impedanzspektroskopie
1. Aufl. 2016, 258 S.
DOI: 10.18154/RWTH-2016-12094

ABISEA Band 90
Witzenhausen, Heiko
Elektrische Batteriespeichermodelle: Modellbildung, Parameteridentifikation und Modellreduktion
1. Aufl. 2017, 266 S.
DOI: 10.18154/RWTH-2017-03437

ABISEA Band 91
Münnix, Jens
Einfluss von Stromstärke und Zyklentiefe auf graphitische Anoden
1. Aufl. 2017, 171 S.
DOI: 10.18154/RWTH-2017-01915

ABISEA Band 92
Pilatowicz, Grzegorz
Failure Detection and Battery Management Systems of Lead-Acid Batteries for Micro-Hybrid Vehicles
1. Aufl. 2017, 212 S.
DOI: 10.18154/RWTH-2017-09156

ABISEA Band 93
Drillkens, Julia
Aging in Electrochemical Double Layer Capacitors: An Experimental and Modeling Approach
1. Aufl. 2017, 179 S.
DOI: 10.18154/RWTH-2018-223434

Aachener Beiträge des ISEA

ABISEA Band 94
Magnor, Dirk
Globale Optimierung netzgekoppelter PV-Batteriesysteme unter besonderer Berücksichtigung der Batteriealterung
1. Aufl. 2017, 210 S.
DOI: 10.18154/RWTH-2017-06592

ABISEA Band 95
Iliksu, Merve
Elucidation and Comparison of the Effects of Lithium Salts on Discharge Chemistry of Nonaqueous Li-O_2 Batteries
1. Aufl. 2018, 160 S.
DOI: 10.18154/RWTH-2018-223782

ABISEA Band 96
Schmalstieg, Johannes
Physikalisch-elektrochemische Simulation von Lithium-Ionen-Batterien: Implementierung, Parametrierung und Anwendung
1. Aufl. 2017, 168 S.
DOI: 10.18154/RWTH-2017-04693

ABISEA Band 97
Soltau, Nils
High-Power Medium-Voltage DC-DC Converters: Design, Control and Demonstration
1. Aufl. 2017, 176 S.
DOI: 10.18154/RWTH-2017-04084

ABISEA Band 98
Stieneker, Marco
Analysis of Medium-Voltage Direct-Current Collector Grids in Offshore Wind Parks
1. Aufl. 2017, 144 S.
DOI: 10.18154/RWTH-2017-04667

ABISEA Band 99
Masomtob, Manop
A New Conceptual Design of Battery Cell with an Internal Cooling Channel
1. Aufl. 2017, 167 S.
DOI: 10.18154/RWTH-2018-223281

ABISEA Band 100
Marongiu, Andrea
Performance and Aging Diagnostic on Lithium Iron Phosphate Batteries for Electric Vehicles and Vehicle-to-Grid Strategies
1. Aufl. 2017, 222 S.
DOI: 10.18154/RWTH-2017-09944

ABISEA Band 101
Gitis, Alexander
Flaw detection in the coating process of lithium-ion battery electrodes with acoustic guided waves
1. Aufl. 2017, 109 S.
DOI: 10.18154/RWTH-2017-099519

ABISEA Band 102
Neeb, Christoph
Packaging Technologies for Power Electronics in Automotive Applications
1. Aufl. 2017, 132 S.
DOI: 10.18154/RWTH-2018-224569

ABISEA Band 103
Adler, Felix
A Digital Hardware Platform for Distributed Real-Time Simulation of Power Electronic Systems
1. Aufl. 2017, 156 S.
DOI: 10.18154/RWTH-2017-10761

ABISEA Band 104
Becker, Jan
Flexible Dimensionierung und Optimierung hybrider Lithium-Ionenbatterie-speichersysteme mit verschiedenen Auslegungs-zielen
1. Aufl., 2017, 157 S.
DOI: 10.18154/RWTH-2017-09278

ABISEA Band 105
Warnecke, Alexander J.
Degradation Mechanisms in NMC Based Lithium-Ion Batteries
1. Aufl. 2017, 158 S.
DOI: 10.18154/RWTH-2017-09646

ABISEA Band 106
Taraborrelli, Silvano
Bidirectional Dual Active Bridge Converter using a Tap Changer for Extended Voltage Ranges
1. Aufl. 2017, 94 S.
DOI: 10.18154/RWTH-2018-228242

ABISEA Band 107
Sarriegi, Garikoitz
SiC and GaN Semiconductors: The Future Enablers of Compact and Efficient Converters for Electromobility
1. Aufl. 2017, 106 S.
DOI: 10.18154/RWTH-2018-227548

ABISEA Band 108
Senol, Murat
Drivetrain Integrated Dc-Dc Converters utilizing Zero Sequence Currents
1. Aufl. 2017, 134 S.
DOI: 10.18154/RWTH-2018-226170

ABISEA Band 109
Kojima, Tetsuya
Efficiency Optimized Control of Switched Reluctance Machines
1. Aufl. 2017, 142 S.
DOI: 10.18154/RWTH-2018-226697

ABISEA Band 110
Lewerenz, Meinert
Dissection and Quantitative Description of Aging of Lithium-Ion Batteries Using Non-Destructive Methods Validated by Post-Mortem-Analyses
1. Aufl. 2018, 139 S.
DOI: 10.18154/RWTH-2018-228663

ABISEA Band 111
Büngeler, Johannes
Optimierung der Verfügbarkeit und der Lebensdauer von Traktionsbatterien für den Einsatz in Flurförderfahrzeugen
1. Aufl. 2018, 171 S.
DOI: 10.18154/RWTH-2018-226569

ABISEA Band 112
Wegmann, Raphael
Betriebsstrategien und Potentialbewertung hybrider Batteriespeichersysteme in Elektrofahrzeugen
1. Auflage 2018, 184 S.
DOI: 10.18154/RWTH-2018-228833

ABISEA Band 113
Nordmann, Hannes
Batteriemanagementsysteme unter besonderer Berücksichtigung von Fehlererkennung und Peripherieanalyse
1. Aufl. 2018, 222 S.
DOI: 10.18154/RWTH-2018-228763

ABISEA Band 114
Engelmann, Georges
Reducing Device Stress and Switching Losses Using Active Gate Drivers and Improved Switching Cell Design
1. Aufl. 2018, 195 S.
DOI: 10.18154/RWTH-2018-228973

ABISEA Band 115
Klein-Heßling, Annegret
Active DC-Power Filters for Switched Reluctance Drives during Single-Pulse Operation
1. Aufl. 2018, 166 S.
DOI: 10.18154/RWTH-2018-231030

ABISEA Band 116
Burkhart, Bernhard
Switched Reluctance Generator for Range Extender Applications - Design, Control and Evaluation
1. Aufl. 2018, 194 S.
DOI: 10.18154/RWTH-2019-00025

ABISEA Band 117
Biskoping, Matthias
Discrete Modeling and Control of a versatile Power Electronic Test Bench with Special Focus on Central Photovoltaic Inverter Testing
1. Aufl. 2018, 236 S.
DOI: 10.18154/RWTH-2019-03346

ABISEA Band 118
Schubert, Michael
High-Precision Torque Control of Inverter-Fed Induction Machines with Instantaneous Phase Voltage Sensing
1. Aufl. 2019, 221 S.
DOI: 10.18154/RWTH-2018-231364

ABISEA Band 119
Van der Broeck, Christoph
Methodology for Thermal Modeling, Monitoring and Control of Power Electronic Modules
1. Aufl. 2019, 290 S.
DOI: 10.18154/RWTH-2019-01370

ABISEA Band 120
Hust, Friedrich Emanuel
Physico-chemically motivated parameterization and modelling of real-time capable lithium-ion battery models – a case study on the Tesla Model S battery
1. Aufl. 2019, 203 S.
DOI: 10.18154/RWTH-2019-00249

ABISEA Band 121
Ralev, Iliya
Accurate Torque Control of Position Sensorless Switched Reluctance Drives
1. Aufl. 2019, 154 S.
DOI: 10.18154/RWTH-2019-03071

ABISEA Band 122
Ayeng'o, Sarah Paul
Optimization of number of PV cells connected in series for a direct-coupled PV system with lead-acid and lithium-ion batteries
1. Aufl. 2019, 114 S.
DOI: 10.18154/RWTH-2019-01843

ABISEA Band 123
Koschik, Stefan Andreas
Permanenterregte Synchronmaschinen mit verteilter Einzelzahnsteuerung - Regelkonzepte und Betriebsstrategien für hochintegrierte Antriebssysteme
1. Aufl. 2019, 158 S.
DOI: 10.18154/RWTH-2019-03446

ABISEA Band 124
Farmann, Alexander
A comparative study of reduced-order equivalent circuit models for state-of-available-power prediction of lithium-ion batteries in electric vehicles
1. Aufl. 2019, 214 S.
DOI: 10.18154/RWTH-2019-04700

ABISEA Band 125
Mareev, Ivan
Analyse und Bewertung von batteriegetriebenen, oberleitungsversorgten und brennstoffzellengetriebenen Lastkraftwagen für den Einsatz im Güterfernverkehr in Deutschland
1. Aufl. 2019, 158 S.
DOI: 10.18154/RWTH-2019-04698

ABISEA Band 126
Qi, Fang
Online Model-predictive Thermal Management of Inverter-fed Electrical Machines
1. Aufl. 2019, 154 S.
DOI: 10.18154/RWTH-2019-08304

ABISEA Band 127
Kairies, Kai-Philipp
Auswirkungen dezentraler Solarstromspeicher auf Netzbetreiber und Energieversorger
1. Aufl. 2019, 140 S.
DOI: 10.18154/RWTH-2019-06706

Aachener Beiträge des ISEA

ABISEA Band 128
Fleischer, Michael
Traction control for Railway Vehicles
1. Aufl. 2019, 162 S.
DOI: 10.18154/RWTH-2019-10570

ABISEA Band 129
Teuber, Moritz
Lifetime Assessment and Degradation Mechanisms in Electric Double-Layer Capacitors
1. Aufl. 2019, 150 S.
DOI: 10.18154/RWTH-2019-10071

ABISEA Band 130
Bußar, Christian
Investigation of Optimal Transformation Pathways towards 2050 for the Successful Implementation of a Sustainable Reduction of Carbon Emissions from Power Generation
1. Aufl. 2019, 204 S.
DOI: 10.18154/RWTH-2019-09975

ABISEA Band 131
Wienhausen, Arne Hendrik
High Integration of Power Electronic Converters enabled by 3D Printing
1. Aufl. 2019, 146 S.
DOI: 10.18154/RWTH-2019-08746

ABISEA Band 132
Kwiecien, Monika
Electrochemical Impedance Spectroscopy on Lead-Acid Cells during Aging
1. Aufl. 2019, 138 S.
DOI: 10.18154/RWTH-2019-09480

ABISEA Band 133
Titiz, Furkan Kaan
A Three-phase Low-voltage Grid-connected Current Source Inverter
1. Aufl. 2019, 128 S.
DOI: 10.18154/RWTH-2020-00458

ABISEA Band 134
Wünsch, Martin
Separation der Kathoden-alterung in Lithium-Ionen-Batteriezellen mittels elektrochemischer Impedanzspektroskopie
1. Aufl. 2019, 177 S.
DOI: 10.18154/RWTH-2019-11017

ABISEA Band 135
Badeda, Julia
Modeling and Steering of Multi-Use Operation with Uninterruptible Power Supply Systems - utilizing the example of lead-acid batteries
1. Aufl. 2020, 282 S.
DOI: 10.18154/RWTH-2020-05456

ABISEA Band 136
Kleinsteinberg, Björn
Energy Efficiency Increase of a Vanadium Redox Flow Battery with a Power-Based Model
1. Aufl. 2020, 163 S.
DOI: 10.18154/RWTH-2020-06092

ABISEA Band 137
Cai, Zhuang
Optimization of dimension and operation strategy for a wind-battery energy system in German electricity market under consideration of battery ageing process
1. Aufl. 2020, 144 S.
DOI: 10.18154/RWTH-2020-06525

ABISEA Band 138
Sabet, Pouyan Shafiei
Analysis of Predominant Processes in Electrochemical Impedance Spectra and Investigation of Aging Processes of Lithium-Ion Batteries with Layered Oxide Cathodes and Graphitic Anodes
1. Aufl. 2020, 136 S.
DOI: 10.18154/RWTH-2020-07683

ABISEA Band 139
Angenendt, Georg
Operation, Optimization and Additional Market Participation of Households with PV Battery Storage System and Power-to-Heat Application
1. Aufl. 2020, 221 S.
DOI: 10.18154/RWTH-2020-05200

ABISEA Band 140
Oberdieck, Karl Friedrich
Measurement and Mitigation of Electromagnetic Emissions of Propulsion Inverters for Electric Vehicles
1. Aufl. 2020, 181 S.
DOI: 10.18154/RWTH-2020-09215

ABISEA Band 141
Bubert, Andreas Martin
Optimierung des elektrischen Antriebsstrangs von Elektrofahrzeugen mit Betrachtung parasitärer Ströme innerhalb der elektrischen Maschine
1. Aufl. 2020, 215 S.
DOI: 10.18154/RWTH-2020-09556

ABISEA Band 142
Fleischer, Christian Georg
Model-Driven Software Development and Verification Solutions for Safety Critical Battery Management Systems
1. Aufl. 2021, 356 S.
DOI: 10.18154/RWTH-2021-00436

ABISEA Band 143
Arzberger, Arno
Thermografische Methoden zur zerstörungsfreien Messung der anisotropen Wärmeleitfähigkeit von Lithium-Ionen Zellen
1. Aufl. 2020, 131 S.
DOI: 10.18154/RWTH-2021-00479

ABISEA Band 144
Lange, Tobias
Oberwellenbasierte Modellierung, Regelung und Auslegung von Permanentmagnet- und Reluktanz-Synchronmaschinen
1. Aufl. 2020, S.
DOI: 10.18154/RWTH-2021-02537

ABISEA Band 145
Weiss, Claude
Fault Tolerant Switched Reluctance Machines with Distributed Inverters – Modeling and Control
1. Aufl. 2020, S.
DOI: 10.18154/RWTH-2021-02327

ABISEA Band 146
Huck, Moritz
Modelling the Transient Behaviour of Lead-Acid Batteries: Electrochemical Impedance of Adsorbed Species
1. Aufl. 2020, 151 S.
DOI: 10.18154/RWTH-2020-08362

ABISEA Band 147
Willenberg, Lisa
Volumenausdehnung und ihre Auswirkungen auf die Alterung einer zylindrischen Lithium-Ionen-Batterie
1. Aufl. 2020, S.
DOI: 10.18154/RWTH-2021-01906

ABISEA Band 148
Rogge, Matthias
Electrification of Public Transport Bus Fleets with Battery Electric Busses
1. Aufl. 2020, 161 S.
DOI: 10.18154/RWTH-2021-02146

ABISEA Band 149
Münderlein, Jeanette
Numerische Methodik zur Auslegung eines Hybriden Speichersystems mit Multinutzen“
1. Aufl. 2020, 221 S.
DOI: 10.18154/RWTH-2021-00867

ABISEA Band 150
Merten, Michael
Participation of Battery Storage Systems in the Secondary Control Reserve Market
1. Aufl. 2020, 187 S.
DOI: 10.18154/RWTH-2021-01029

ABISEA Band 151
Ge, Lefei
Performance Enhancement of Switched Reluctance Machines for High-speed Back-up Generators
1. Aufl. 2020, 152 S.
DOI: 10.18154/RWTH-2020-11546

ABISEA Band 152
Neubert, Markus
Modeling, Synthesis and Operation of Multiport-Active Bridge Converters
1. Aufl. 2020, 227 S.
DOI: 10.18154/RWTH-2020-10814

ABISEA Band 153
Schülting, Philipp
Optimierte Auslegung von hochintegrierten und bidirektionalen Onboard GaN-Ladegeräten
1. Aufl. 2020, 158 S.
DOI: 10.18154/RWTH-2020-09771

ABISEA Band 154
Sewergin, Alexander
Design Challenges and Solutions for the Practical Application of SiC Power Moduls – Exemplified by an Automotive DC-DC Converter. 1. Aufl. 2021, 154 S.
DOI: 10.18154/RWTH-2021-04498

ABISEA Band 155
Stippich, Alexander
Exploiting the Full Potential of Silicon Carbide Devices via Optimized Highly Integrated Power Modules
1. Aufl. 2021, 188 S.
DOI: 10.18154/RWTH-2021-08122

ABISEA Band 156
Gottschlich, Jan
Hilfsspannungsversorgungskonzepte für Mittelspannungs-DC/DC-Wandler
1. Aufl. 2021, 178 S.
DOI: 10.18154/RWTH-2021-11881

ABISEA Band 157
Hollstegge, Philipp
Injektion raumzeigerzerlegter Stromharmonischer zur Minderung tonaler Geräuschanteile in asymmetrisch sechsphasigen Permanentmagnetsynchronmaschinen
1. Aufl. 2021, 191 S.
DOI: 10.18154/RWTH-2021-11040

ABISEA Band 158
Grau, Vivien
Development of a Test Bench to Investigate the Impact of Steep Voltage Slopes on the Lifetime of Insulation Systems for Coil Windings
1. Aufl. 2021, 182 S.
DOI: 10.18154/RWTH-2021-09577

ABISEA Band 159
Ringbeck, Florian
Optimized Charging of Lithium-Ion Batteries with Physico-Chemical Models
1. Aufl. 2021, 174 S.
DOI: 10.18154/RWTH-2021-11038

ABISEA Band 160
Bank, Thomas
Performance and Aging Analysis of High-Power Lithium Titanate Oxide Cells for Low-Voltage Vehicle Applications
1. Aufl. 2021, 148 S.
DOI: 10.18154/RWTH-2021-10369

Aachener Beiträge des ISEA

ABISEA Band 161
Aupperle, Felix
Realizing High-Performance Silicon-Based Lithium-Ion Batteries
1. Aufl. 2022, 138 S.
DOI: 10.18154/RWTH-2022-05155

ABISEA Band 162
Schröer, Philipp A.
Entwicklung einer adaptiven Leistungsprognosefunktion für Starterbatterien mit Lithium-Titanat-Oxid-Anode als Grundlage zur sicheren Energieversorgung im Fahrzeug
1. Aufl. 2021, 187 S.
DOI: 10.18154/RWTH-2021-10819

ABISEA Band 163
Dechent, Philipp
Simulation and Real-Life assessment of cell-to-cell variation of ageing lithium-ion batteries
1. Aufl. 2022, 149 S.
DOI: 10.18154/RWTH-2022-09298

ABISEA Band 164
Li, Weihan
Battery Digital Twin with Physics-Based Modeling, Battery Data and Machine Learning
1. Aufl. 2022, 234 S.
DOI: 10.18154/RWTH-2022-02292

ABISEA Band 165
Thien, Tjark G. C.
Optimaler Betrieb von stationären Hybrid-Batteriespeichern am Beispiel des Projekts M5BAT
1. Aufl. 2022, 172 S.
DOI: 10.18154/RWTH-2022-00997

ABISEA Band 166
Lüdecke, Christoph
Compensating Asymmetries of Parallel-Connected SiC MOSFETs Using Intelligent Gate Drivers
1. Aufl. 2022, 166 S.
DOI: 10.18154/RWTH-2022-09587

ABISEA Band 167
Rahe, Christiane
Untersuchung von Batterieelektroden mit optischen Verfahren
1. Aufl. 2022, 214 S.
DOI: 10.18154/RWTH-2022-08794

ABISEA Band 168
Weber, Felix Martin
Stability of lithium electrolyte interphase enabling rechargeable lithium-metal batteries
1. Aufl. 2023, 168 S.
DOI: 10.18154/RWTH-2023-03565

ABISEA Band 169
Henn, Jochen
Gate Driver Integrated Closed-Loop Control for Electromagnetic Emissions and Switching Losses of Wide Bandgap Power Electronic Converters
1. Aufl. 2023, 169 S.
DOI: 10.18154/RWTH-2023-07726

ABISEA Band 170
Quabeck, Stefan
Modeling of Parasitic Currents and Fault Detection in Electrical Traction Drives
1. Aufl. 2023, 133 S.
DOI: 10.18154/RWTH-2023-10920

ABISEA Band 171
Hecht, Christopher
Usage overview, prediction, and siting optimization for electric vehicles public charging infrastructure with machine learning and big data methods
1. Aufl. 2023, 185 S.
DOI: 10.18154/RWTH-2024-01156

ABISEA Band 172
Kuipers, Matthias L. U.
Development of a Virtual Cell Design Tool for Objective Comparisons between State-of-the-Art Battery Cells and Next Generation Technologies
1. Aufl. 2023, 203 S.
DOI: 10.18154/RWTH-2023-11897

ABISEA Band 173
Brieske, Daniel Martin
Anwendungsbezogene Modellierung und Zustandsbestimmung von Lithium-Schwefel-Batterien
1. Aufl. 2023, 146 S.
DOI: 10.18154/RWTH-2023-10905

ABISEA Band 174
Teichert, Philipp
Einfluss der Degradation von nickelreichen $Li[Ni_xMn_yCo_z]O_2$ (NMC) Elektroden (mit $x \geq 0.6$) auf Vollzellalterung von Lithium-Ionen-Zellen
1. Aufl. 2023, 159 S.
DOI: 10.18154/RWTH-2024-01059

ABISEA Band 175
Kühnle, Hannes Sebastian
Optical and electrochemical investigations of fundamental lithium metal deposition processes on lithium surfaces
1. Aufl. 2023, 218S.
DOI: 10.18154/RWTH-2024-05806

ABISEA Band 176
Epp, Alexander
Multiphysical Models and Optimization for Conceptual Design of High-Voltage Battery Systems
1. Aufl. 2024, 256 S.
DOI: 10.18154/RWTH-2024-00430

ABISEA Band 177
Figgener, Jan
Data-driven battery aging analysis of home storage systems based on high-resolution field measurements
1. Aufl. 2024, 208 S.
DOI: 10.18154/RWTH-2024-10709

ABISEA Band 178
Meishner, Fabian
Untersuchung eines direktnetzgekoppelten stationären LTO-Speichersystems in einem 750 V DC Stadtbahnnetz
1. Aufl. 2024, 116 S.
DOI: 10.18154/RWTH-2024-06358

ABISEA Band 179
Frambach, Tobias
Anwendungsgerechte Dimensionierung und Betriebsstrategien von 48 V Plug-In-Hybridfahrzeugen
1. Aufl. 2024, 154 S.
DOI: 10.18154/RWTH-2024-03411

ABISEA Band 180
Goldbeck, Rafael
Model-Based Control of Three-Phase Dual-Active Bridge Converters for Dynamic Operation and Adaptive Compensation of Parameter Deviations
1. Aufl. 2024, 194 S.
DOI: 10.18154/RWTH-2025-00288

ABISEA Band 181
Götz, Georg Tobias
Bidirectional DC-to-DC Converter with Integrated Switched Reluctance Generator
1. Aufl. 2024, 192 S.
DOI: 10.18154/RWTH-2024-03854

ABISEA Band 182
Harries, Martin
Aktive Reduzierung der Vibrationen von Permanentmagnet-Synchronmaschinen durch adaptive Regler
1. Aufl. 2024, 144 S.
DOI: 10.18154/RWTH-2025-00626

ABISEA Band 183
Börner, Martin Florian
Ein prozessbasiertes Modell zur Berechnung der Kosten von Lithium-Ionen-Batteriezellen
1. Aufl. 2024, 163 S.
DOI: 10.18154/RWTH-2024-07853

ABISEA Band 184
Bihn, Stephan
Automatic Parameterisation of Electrical Equivalent Circuit Models for Virtual Battery Cell Design
1. Aufl. 2024, 226 S.
DOI: 10.18154/RWTH-2024-10636

ABISEA Band 185
Xu, Huihui
Thermal Modeling and Control of an Oil-Cooled Permanent Magnet Synchronous Machine: Initialization, Nonlinearity, and Controllability
1. Aufl. 2025, 156 S.
10.18154/RWTH-2025-01683

ABISEA Band 186
Fritz, Niklas
Generalized Control Methodology for Modular DC-DC Converters
1. Aufl. 2025, 222 S.
DOI: 10.18154/RWTH-2025-04395

ABISEA Band 187
Kalker, Sven
Toward Robust Monitoring of Power Electronic Devices: Challenges and Efficient Solutions
1. Aufl. 2025, 167 S.
DOI: 10.18154/RWTH-2025-06121

ABISEA Band 188
Wasylowski, David
Accelerating Battery Cell Design, Manufacturing, and Testing through Ultrasound Imaging
1. Aufl. 2025, 116 S.
DOI: 10.18154/RWTH-2025-00940

ABISEA Band 189
Steininger, Valentin
Aging analysis of lithium-ion batteries with field data
1. Aufl. 2025, 136 S.
DOI: 10.18154/RWTH-2025-00625

ABISEA Band 190
Jacqué, Kevin
Analyse der Belastungsprofile, der Alterung und der Wirtschaft-lichkeit eines Batteriespeichers im Primärregelleistungsmarkt aus realen Feldmessdaten
1. Aufl. 2025, 244 S.
DOI: 10.18154/RWTH-2025-04328

ABISEA Band 191
Hamzelui, Niloofar
Investigation of active materials and polymeric binders in silicon-based negative electrodes for lithium-ion batteries
1. Aufl. 2025, 148 S.
DOI: 10.18154/RWTH-2025-06437

ABISEA Band 192
Klever, Severin
High-Bandwidth Current Probing Techniques for the Dynamic Characterization of Wide-Bandgap Semiconductor Devices
1. Aufl. 2025, 158 S.
DOI: 10.18154/RWTH-2025-03518

ABISEA Band 193
von Hoegen, Anne
Precise and Instantaneous Flux-Linkage Sensing Methods in PWM Voltage-Source Inverters
1. Aufl. 2025, S.
DOI: 10.18154/RWTH-2025-

Aachener Beiträge des ISEA

ABISEA Band 194
Koltermann, Lucas
Analyse und Optimierung der Zuverlässigkeit und Effizienz von hybriden Batteriespeichern am Beispiel von M5BAT
1. Aufl. 2025, 229 S.
DOI: 10.18154/RWTH-2025-06200

ABISEA Band 195
Jöst, Dominik
Modellbasierte Bewertung von Algorithmen zur Zustandsbestimmung von Batterien: Analyse von Betriebs-, Zell- und Messtechnik-Parametern
1. Aufl. 2025, 276 S.
DOI: 10.18154/RWTH-2025-10245

ABISEA Band 196
Pegel, Hendrik
Optimal Concept Design of Battery Systems with Tabless Cylindrical Lithium-Ion Cells
1. Aufl. 2025, 309 S.
DOI: 10.18154/RWTH-2025-05204

ABISEA Band 197
Ünlübayir, Cem
Intelligent operating methods and their influence on components for hybrid marine propulsion systems
1. Aufl. 2025, S.
DOI: 10.18154/RWTH-2025-09689

ABISEA Band 198
Van Quwerkerk, Jonas
Integrating a battery value stacking approach into an energy system modelling framework to decarbonise a glassworks
1. Auf. 2026, S.
DOI: 10.18154/RWTH-2026-

ABISEA Band 199
Krause, Florian
Faseroptische Messtechniken zur ortsaufgelösten Temperaturmessung: Innovative Methode zur Optimierung von Batteriesystemen und deren Überwachung
1. Auf. 2026, S.
DOI: 10.18154/RWTH-2026-

ABISEA Band 200
Ünal, Leyla
Prelithiated Carbon Nanotubes-Containing Silicon/Graphite Negative Electrodes for High-Performance Lithium-Ion Batteries
1. Auf. 2026, S.
DOI: 10.18154/RWTH-2026-

ABISEA Band 201
Gong, Jingyu
Battery Aging-Aware Vehicle-to-Grid Control in Home Charging Systems via Deep Reinforcement Learning
1. Auf. 2026, S.
DOI: 10.18154/RWTH-2026-

Sodium-ion batteries are gaining attention as a cost-effective and sustainable complementary technology to their lithium counterpart. However, fully realizing their drop-in potential and integrating them into applications requires a deeper understanding of their aging behavior, as well as the implications for the overall system. A high-power, cost-sensitive application is selected, where lithium-ion cells could potentially be replaced by a cheaper complementary technology with similar power characteristics and energy density. An extensive field dataset from this application is then analyzed to determine the operational requirements that such a technology must meet in terms of lifetime and management. Following this analysis, a unique aging study on sodium-ion cells with layered-oxide cathode and hard-carbon anode is conducted. The results show that while there are distinct aging patterns in the sodium-ion cells, the lifetime is high with an average capacity loss of 2.8% after approximately 4000 equivalent full cycles across different operating conditions. The parameterized models, derived from the experimental data, and application-specific requirements are implemented in a simulation framework to evaluate real-time algorithms commonly used for lithium-ion batteries. We analyze that the favorable voltage range and steep open-circuit voltage curve of the investigated sodium-ion cells allow the use of simpler models and lower-cost sensors without affecting algorithm performance. By quantifying degradation and algorithm performance, this work guides the integration of sodium-ion batteries into applications, shortening the time to market for these technologies as viable alternatives to lithium-ion batteries when economic or political factors make it necessary.

ISSN 1437-675X